Department of Applied Physics

Piezoelectrically transduced temperature compensated silicon resonators for timing and frequency reference applications

Antti Jaakkola

DOCTORAL DISSERTATIONS

Aalto University publication series
DOCTORAL DISSERTATIONS 6/2016
VTT SCIENCE 122

Piezoelectrically transduced temperature compensated silicon resonators for timing and frequency reference applications

Antti Jaakkola

A doctoral dissertation completed for the degree of Doctor of Science (Technology) to be defended, with the permission of the Aalto University School of Science, at a public examination held at the lecture hall AS1 of the TUAS building (Otaniementie 17, Espoo, Finland), on 29 January 2016 at 12.

Aalto University
School of Science
Applied Physics

Supervising professor
Prof. Matti Kaivola, Aalto University, Finland

Thesis advisor
Dr. Tuomas Pensala, VTT, Finland

Preliminary examiners
Prof. Jeevak Parpia, Cornell University, USA
Prof. Jan Westerholm, Åbo Akademi University, Finland

Opponent
Dr. Jan H. Kuypers, TriQuint Semiconductor GmbH, Germany

Aalto University publication series
DOCTORAL DISSERTATIONS 6/2016

VTT SCIENCE 122

© Antti Jaakkola

ISBN 978-952-60-6615-8 (printed)
ISBN 978-952-60-6616-5 (pdf)
ISSN-L 1799-4934
ISSN 1799-4934 (printed)
ISSN 1799-4942 (pdf)
http://urn.fi/URN:ISBN:978-952-60-6616-5

ISBN 978-951-38-8388-1 (printed)
ISBN 978-951-38-8387-4 (pdf)
ISSN-L 2242-119X
ISSN 2242-119X (printed)
ISSN 2242-1203 (pdf)
http://urn.fi/URN:ISBN:978-951-38-8387-4

Unigrafia Oy
Helsinki 2016

Finland

Abstract

Aalto University, P.O. Box 11000, FI-00076 Aalto www.aalto.fi

Author
Antti Jaakkola

Name of the doctoral dissertation
Piezoelectrically transduced temperature compensated silicon resonators for timing and frequency reference applications

Publisher School of Science

Unit Department of Applied Physics

Series Aalto University publication series DOCTORAL DISSERTATIONS 6/2016

Field of research Applied Physics

Manuscript submitted 11 September 2015 **Date of the defence** 29 January 2016

Permission to publish granted (date) 2 November 2015 **Language** English

☐ **Monograph** ☒ **Article dissertation (summary + original articles)**

Abstract

Reference oscillators are used in a wide range of electronic devices for timing and for providing the frequency reference signals for wireless communications. Typically, an oscillator has to be based on a mechanical resonator, and for many decades, quartz crystals have served for this purpose. With the progress of microelectromechanical system (MEMS) technologies, silicon resonators have been developed for providing similar functionality as quartz. A silicon MEMS resonator can offer several advantages over quartz, such as smaller device size, decreased costs, and integration with other electronics.

This work focuses on two challenges in silicon resonators: First, electromechanical transduction of silicon resonators has typically been achieved with electrostatic coupling, which is inherently quite weak and requires DC biasing of the devices and tends to complicate fabrication. Transduction based on a piezoelectric thin film on top of the resonator has been investigated as an alternative. Second, the resonance frequency of a silicon resonator is orders of magnitude more sensitive to temperature variations than that of a quartz crystal. Degenerate doping of silicon can be used to drastically reduce this effect.

The first part of the work concentrates on the design, fabrication and characterization of piezoelectrically transduced silicon resonators. An oscillator based on a width extensional resonator operating at a frequency 24 MHz is demonstrated to have a phase noise -128 dBc/Hz at a 1-kHz offset from the carrier. An experimental test is conducted on piezoelectrically transduced square extensional mode resonators, whose dimensions are varied so that the main resonance mode occurs at a frequency range of f = 13 ... 30 MHz. As a result, an anchor coupling effect is identified and a subharmonic nonlinear coupling mechanism is discovered.

In the second part of the work, the effect of degenerate doping on the elastic parameters of silicon is investigated experimentally, with a focus on temperature compensation. Resonance modes that can be temperature compensated using doping are identified, and design rules for the optimization of the frequency stability are developed. The elastic parameters of silicon are determined as a function of temperature and n-type doping up to a level of $n = 7.5 \times 10^{19} cm^{-3}$, enabling modelling of the frequency-vs-temperature characteristics of an arbitrary resonator design. Extrapolation from the results yields a prediction of full second order temperature compensation in optimally designed resonators for n-type doping level above $10^{20} cm^{-3}$. The prediction is experimentally verified by the demonstration of piezoelectrically transduced resonators with frequency stability within +/- 10 ppm on a temperature range of T = -40 ... +85C, on par with the best quartz crystals.

Keywords MEMS, silicon resonators, temperature compensation, doping, AlN

ISBN (printed) 978-952-60-6615-8 **ISBN (pdf)** 978-952-60-6616-5

ISSN-L 1799-4934 **ISSN (printed)** 1799-4934 **ISSN (pdf)** 1799-4942

Location of publisher Helsinki **Location of printing** Helsinki **Year** 2016

Pages 153 **urn** http://urn.fi/URN:ISBN:978-952-60-6616-5

Aalto-yliopisto, PL 11000, 00076 Aalto www.aalto.fi

Tiivistelmä

Tekijä
Antti Jaakkola

Väitöskirjan nimi
Pietsosähköisesti herätetyt lämpötilakompensoidut piiresonaattorit ajastin- ja taajuusreferenssisovelluksiin

Julkaisija Perustieteiden korkeakoulu

Yksikkö Teknillisen fysiikan laitos

Sarja Aalto University publication series DOCTORAL DISSERTATIONS 6/2016

Tutkimusala Teknillinen fysiikka

Käsikirjoituksen pvm 11.09.2015 **Väitöspäivä** 29.01.2016

Julkaisuluvan myöntämispäivä 02.11.2015 **Kieli** Englanti

☐ **Monografia** ☒ **Yhdistelmäväitöskirja (yhteenveto-osa + erillisartikkelit)**

Tiivistelmä
Referenssioskillaattoreita käytetään monissa elektronisissa laitteissa ajastukseen ja langattomassa kommunikoinnissa tarvittavina taajuusreferensseinä. Yleensä oskillaattorissa on mekaaninen värähtelijä, ja vuosikymmenien ajan tähän tarkoitukseen on käytetty kvartsikiteitä. Mikroelektromekaanisten systeemien (MEMS) valmistusteknologian kypsyessä piiresonaattoreita on kehitetty kvartsikiteen korvaajaksi. Piistä tehdyllä MEMS-resonaattorilla on kvartsiin nähden useita etuja, kuten pienempi koko, pienemmät valmistuskustannukset ja parempi integroitavuus muuhun elektroniikkaan.
Tässä työssä keskitytään piiresonaattorin kahteen kehitystarpeeseen. Ensimmäiseksi, piiresonaattorin sähkömekaaninen transduktio järjestetään tyypillisesti sähköstaattisella kytkennällä, joka on luonnostaan melko heikko, vaatii DC-biasoinnin ja on valmistusnäkökulmasta monimutkainen. Vaihtoehtoisena tapana on kehitetty resonaattorin päälle kasvatetun pietsosähköisen ohutkalvon avulla tapahtuvaa transduktiota. Toiseksi, piistä valmistetun resonaattorin taajuus on suuruusluokkia herkempi lämpötilanvaihteluille kuin mitä kvartsikiteillä saavutetaan. Hyvin voimakasta seostusta voidaan käyttää tehokkaasti piin lämpötilaherkkyyden pienentämiseen.
Työn ensimmäisessä osassa suunnitellaan, valmistetaan ja karakterisoidaan pietsosähköisesti herätettyjä piiresonaattoreita. Taajuudeltaan 24 MHz:n leveysvenymämoodiresonaattoriin perustuvalle oskillaattorille mitataan -128 dBc/Hz vaihekohina 1 kHz:n päässä kantoaallosta. Neliövenymämoodiresonaattoreille tehdään koesarja, jossa resonaattorin kokoa varioidaan siten, että pääresonanssin taajuus on alueella f = 13 ... 30 MHz. Tuloksena löydetään ankkurikytkentäefekti sekä aliharmoninen epälineaarinen kytkentämekanismi.
Työn toisessa osassa tutkitaan kokeellisesti hyvin vahvan seostuksen vaikutusta piin elastisiin vakioihin keskittyen seostuksen sovellettavuuteen lämpötilakompensoinnissa. Lämpötilakompensoitavia resonanssimoodeja identifioidaan, ja esitetään suunnittelusäännöt optimaalisen taajuusstabiilisuuden saavuttamiseksi. Piin elastiset vakiot määritetään lämpötilan ja seostustason funktiona seostukseen $n = 7.5\text{x}10^{19}\text{cm}^{-3}$ asti, mikä mahdollistaa mielivaltaisen resonaattorin taajuuden lämpötilariippuvuuden mallintamisen. Tulosten ekstrapolointiin perustuen ennustetaan, että toisen kertaluvun lämpötilakompensointi on mahdollista optimaalisesti suunnitelluissa resonaattoreissa, kun n-tyypin seostustaso on yli 10^{20}cm^{-3}. Ennustuksen paikkansapitävyys varmistetaan kokeellisesti pietsosähköisesti herätetyillä resonaattoreilla, joiden taajuusstabiilisuus saavuttaa lämpötila-alueella T = -40 ... 85C arvon +/- 10 ppm, mikä vastaa parhaita kvartsikiteitä.

Avainsanat MEMS, piiresonaattorit, lämpötilakompensointi, seostus, AlN

ISBN (painettu) 978-952-60-6615-8 **ISBN (pdf)** 978-952-60-6616-5

ISSN-L 1799-4934 **ISSN (painettu)** 1799-4934 **ISSN (pdf)** 1799-4942

Julkaisupaikka Helsinki **Painopaikka** Helsinki **Vuosi** 2016

Sivumäärä 153 **urn** http://urn.fi/URN:ISBN:978-952-60-6616-5

Preface

This dissertation is a summary of the research work on silicon micromechanical resonators that I have been involved with while working at VTT Technical Research Centre of Finland Ltd during years 2007–2015. At VTT, research on the topic began already in 1999, and I have had a unique opportunity to build on this foundation. For me, VTT has been a great environment to grow as a researcher and I am thankful for that. This work has given me much joy of discovery.

Writing this preface was a pleasant task: it felt good to look back and think of all the people with whom I have had the privilege to work with and from whom I have always received lots of help. First, I wish to thank my colleagues in our resonator research group: Tuomas Pensala, Mika Prunnila, Panu Pekko, James Dekker, Jyrki Kiihamäki and Aarne Oja. It was Tuomas who took the time to systematically search for ways around the problematically high thermal sensitivity of silicon and initiated our investigations on using heavy doping for temperature compensation.

I am grateful to Tomi Mattila and Ari Alastalo especially for their mentorship during my early years at VTT. I am thankful to Sergey Gorelick, Jerome Lamy, Piia Rosenberg, Samuli Asmala, Arto Nurmela, Aapo Varpula, Pekka Rantakari, Tapani Makkonen and Markku Ylilammi for their assistance in design, measurements and simulations, and I appreciate the technical help from Paula Holmlund, Ari Häärä, Harri Pohjonen, Hannu Hakojärvi, Meeri Partanen, Teija Häkkinen and Kirsi Järvi. Heini Saloniemi, Tommi Riekkinen, Jyrki Molarius, Tommi Suni and Jaakko Salonen are acknowledged for sharing their expertise in MEMS fabrication.

I want to thank Heikki Seppä and Ilkka Suni for sharing their technological experience. Arto Rantala, David Martins Gomes and Jacek Flak are acknowledged for their work in circuit design and measurements. I have received much support from my teammates Teuvo Sillanpää, Jukka Kyynäräinen, Panu Kop-

pinen, Henry Rimminen, Feng Gao, Bin Guo and Jaakko Saarilahti, and from my team leader Anu Kärkkäinen. Technology Managers Timo Varpula, Hannu Kattelus and Philippe Monnoyer are acknowledged.

I wish to thank Kimmo Kokkonen, Lauri Lipiäinen and Olli Holmgren from the Department of Applied Physics of Aalto University for sharing their optical measurement expertise and for good discussions. Prof. Matti Kaivola is acknowledged for supervising this work.

Industrial collaboration has been an integral part of the research work. I wish to thank Heikki Kuisma and Ville Kaajakari from VTI Technologies (now Murata Electronics Oy) for cooperation and for sharing their insights. Markku Tilli and Jari Mäkinen from Okmetic Oyj, and Juha Majakulma from Micro Analog Systems Oy are acknowledged.

Finally, I want to thank my wife Hanna, my daughter Veera and my son Johannes for their love and for being there. And, an extra thank you goes to my parents and Irja for childcare help during the last phases of writing this book.

Financial support from Tekes and Finnish Academy is appreciated. The research has resulted in a set of patents, listed in Appendix D.

Hollola, September 6, 2015

Antti Jaakkola

Contents

Preface i

Contents iv

List of Papers vii

Author's Contribution ix

1. Introduction 1
   - 1.1 Motivation . . . 1
   - 1.2 Background . . . 2
   - 1.3 Silicon as a resonator material . . . 4
   - 1.4 Fabrication . . . 5
   - 1.5 Oscillator specifications . . . 6
   - 1.6 Objectives and scope of the work . . . 8

2. Characteristics of silicon resonators 9
   - 2.1 Resonance modes . . . 9
   - 2.2 Temperature dependent resonance frequency . . . 12
   - 2.3 Equivalent circuit representation . . . 13
   - 2.4 Electrostatic and piezoelectric transduction . . . 15
   - 2.5 Tunability . . . 17
   - 2.6 Resonator as a part of an oscillator circuit . . . 18
     - 2.6.1 Requirements for sustained oscillation . . . 18
     - 2.6.2 Phase noise of an oscillator . . . 19
   - 2.7 Quality factor . . . 20
   - 2.8 Power handling capability . . . 21
   - 2.9 Design objectives for resonators . . . 22

3. Piezoelectrically transduced silicon resonators 23

3.1 Piezoelectically transduced LE, WE and SE resonators 24
3.2 Statistical study of size-varied SE resonators 26
3.2.1 Introduction 26
3.2.2 Characteristics of modal branches 27
3.2.3 Splitting effect caused by a coupled anchor resonance . 30
3.2.4 Excitation of a subharmonic rotational mode 32
3.2.5 Discussion 33
3.3 Oscillator characterization 35

4. Temperature compensation by degenerate doping of silicon 37
4.1 Theoretical background and early experiments 38
4.2 First Experiments at VTT 38
4.3 Determination of doping dependent elastic parameters 40
4.3.1 Experimental approach 41
4.3.2 Extracted elastic parameters 43
4.3.3 Discussion 44
4.4 Temperature compensated resonance modes 47
4.4.1 Simulations 47
4.4.2 Classes of temperature compensated modes 48
4.4.3 Detailed temperature behavior 50
4.4.4 Discussion 53
4.5 Possibility of 2nd order temperature compensation 54
4.6 Long term stability and quality factors of heavily doped Si . . . 55
4.7 Experimental verification of 2nd order temperature compensation: ±10 ppm Si resonators 56

5. Conclusions 60
5.1 Physical origin of temperature compensation 60
5.2 Progress towards a MEMS-based TCXO 60
5.3 Outlook 62

6. Summary 63

A. Methods 65
A.1 Electrical characterization measurements 65
A.1.1 Frequency sweeps and $f-$vs$-T$ curve determination . 65
A.1.2 Automatization 66
A.1.3 Parameter fitting and data analysis 67
A.2 Solving for elastic parameters from resonance frequencies . . . 67
A.3 Test design for measuring an angular alignment error 68

A.4 Finite element modelling 68

B. Numerical data **70**

B.1 Specifications for wafers used for $c_{ij}(n, T)$ determination . . . 70

B.2 Measured TCFs of resonators on wafers with varied doping . . 71

B.3 Values of temperature coefficients of the elastic parameters c_{ij} as a function of doping level 72

B.4 Interpolation of elastic parameter data 73

C. Derivations **74**

C.1 Change in density vs. thermal expansion 74

C.2 Model for piezoelectric transduction 75

C.3 Lamé mode and piezoelectric transduction 76

D. List of Patents & Public Patent Applications **77**

Bibliography **78**

Papers I—X **85**

List of Papers

I A. Jaakkola, M. Prunnila, T. Pensala, J. Dekker and P. Pekko, “Design Rules for Temperature Compensated Degenerately n-type Doped Silicon MEMS Resonators”, IEEE Journal of Microelectromechanical Systems, 24(6), pp. 1832—1839, 2015.
http://dx.doi.org/10.1109/JMEMS.2015.2443379

II A. Jaakkola, P. Pekko, J. Dekker, M. Prunnila, T. Pensala, “Second Order Temperature Compensated Piezoelectrically Driven 23 MHz Heavily Doped Silicon Resonators with ±10 ppm Temperature Stability”, Proc. IEEE International Frequency Control Symposium, 2015, pp. 420—422.
http://dx.doi.org/10.1109/FCS.2015.7138871

III A. Jaakkola, M. Prunnila, T. Pensala, J. Dekker, and P. Pekko, “Determination of Doping and Temperature Dependent Elastic Constants of Degenerately Doped Silicon from MEMS Resonators”, IEEE Transactions on Ultrasonics Ferroelectrics and Frequency Control, 61(7), pp. 1063—1074, 2014.
http://dx.doi.org/10.1109/TUFFC.2014.3007

IV A. Jaakkola, S. Gorelick, M. Prunnila, J. Dekker, T. Pensala, P. Pekko, ”Long term stability and quality factors of degenerately n-type doped silicon resonators”, Proc. IEEE International Frequency Control Symposium, 2014, pp. 1—5.
http://dx.doi.org/10.1109/FCS.2014.6859866

V L. Lipiäinen, A. Jaakkola, K. Kokkonen, M. Kaivola, ”Frequency splitting of the main mode in a microelectromechanical resonator due to coupling with an anchor resonance”. Applied Physics Letters, 100(1), 013503, pp. 013503-1—3, 2012.
http://dx.doi.org/10.1063/1.3673558

VI L. Lipiäinen, A. Jaakkola, K. Kokkonen, M. Kaivola, ”Nonlinear excitation of a rotational mode in a piezoelectrically excited square-extensional mode resonator”. Applied Physics Letters, 100(15), pp. 153508-1—4, 2012.
http://dx.doi.org/10.1063/1.3703119

VII T. Pensala, A. Jaakkola, M. Prunnila, J. Dekker, “Temperature compensation of silicon MEMS resonators by heavy doping”, Proc. IEEE International Ultrasonics Symposium, 2011, pp. 1952—1955.
http://dx.doi.org/10.1109/ULTSYM.2011.0486

VIII A. Jaakkola, J. Lamy, J. Dekker, T. Pensala, L. Lipiäinen, K. Kokkonen, “Experimental study of the effects of size variations on piezoelectrically transduced MEMS resonators”, Proc. IEEE International Frequency Control Symposium, 2010, pp. 410—414.
http://dx.doi.org/10.1109/FREQ.2010.5556299

IX A. Jaakkola, P. Rosenberg, S. Asmala, A. Nurmela, T. Pensala, T. Riekkinen, J. Dekker, T. Mattila, A. Alastalo, O. Holmgren, K. Kokkonen, “Piezoelectrically transduced single-crystal-silicon plate resonators”, Proc. IEEE International Ultrasonics Symposium, 2008, pp. 717—720.
http://dx.doi.org/10.1109/ULTSYM.2008.0171

X A. Jaakkola, P. Rosenberg, A. Nurmela, T. Pensala, T. Riekkinen, J. Dekker, T. Mattila, A. Alastalo, “Piezotransduced Single-Crystal Silicon BAW Resonators”, Proc. IEEE International Ultrasonics Symposium, 2007, pp. 1653—1656.
http://dx.doi.org/10.1109/ULTSYM.2007.416

Author's Contribution

In Papers **I-IV** and **VII-X**, the author has designed the MEMS components and has been responsible for their electrical characterization and data analysis. Additionally, the author has contributed to planning of the fabrication process, and has been responsible for all device modelling in the papers, with the exception of the free electron model of doped silicon of Paper **VII** (worked out by M. Prunnila). The author has written Papers **I-IV** and **VIII-X** and contributed to the text of Papers **V**, **VI** and **VII**.

Papers **V** and **VI** have been done in collaboration with the Department of Applied Physics of Aalto University. In both of the papers, the author was responsible for planning of the experimental set of devices, for the design of the MEMS devices, and contributed to planning of the fabrication process. The author performed the electrical measurements, where the unexpected splitting of the main resonance mode was found (Paper **V**), and where the unexpected nonlinear behavior was observed (Paper **VI**). The author contributed to the planning of the optical measurements and to the text of both of the papers. The interferometric imaging results in all of the papers **V**, **VI**, **VIII** and **IX**, respectively, have been produced by Department of Applied Physics, Aalto University.

In addition, the author has presented the results of the work at international conferences including the IEEE International Ultrasonics Symposium in 2007 and 2008, and the IEEE International Frequency Control Symposium in 2010 and 2012 — 2015.

1. Introduction

1.1 Motivation

Reference oscillators are everywhere. They are needed in almost any electronic device for keeping track of time, for clocking of digital electronics, and for providing the frequency reference signal needed in wireless communications. Wristwatches, cell phones, bluetooth radios, GPS modules, and computers in general are some examples of applications to name but a few. The volume of the annual oscillator market is approximately $4 billion [1], and considerable growth is expected through drivers such as the Internet of Things and the continuous expansion of wireless communications.

For most needs, an all-electronic implementation of an oscillator is not sufficient for producing a stable enough signal, and a mechanical frequency-setting element is needed. Quartz crystal resonators have been used for the purpose for over five decades. Quartz is piezoelectric, which enables straightforward electrical interfacing, and it is exceptionally stable: the mechanical resonance frequency of a single crystal quartz resonator changes very little in the long term and it is also very independent of temperature.

Use of microelectromechanical system (MEMS) technologies has been rapidly expanding during the latest decades. MEMS technologies leverage the batch fabrication methods of the semiconductor device industry for fabrication of small components with a mechanical function, such as accelerometers, pressure sensors and gyroscopes. Tens of thousands of components can be processed on a single wafer. Research on silicon MEMS resonators started in the 1990s, as it was identified that silicon MEMS resonators could offer several advantages [2] over quartz crystals such as

- Miniaturization: a MEMS resonator can be considerably smaller than a

quartz crystal.

- Decreased fabrication costs can be reached by using batch fabrication methods combined with the smaller size of the component itself.

- A silicon MEMS component could be eventually integrated with other electronics.

Silicon has many of the qualities needed for a good mechanical resonator, but, when compared to quartz, there are two key challenges:

- Silicon is not piezoelectric, and hence another means of electrical interfacing is needed. Typically this has been achieved with electrostatic coupling, which results in relatively weak transduction and/or is challenging for fabrication.

- The temperature sensitivity of the frequency of a silicon resonator is orders of magnitude larger than that of quartz. While a quartz resonator is stable to within ± 10 ppm on a temperature range from $-40°$C to $+85°$C, the frequency of a silicon resonator changes over ± 1500 ppm, see Fig. 1.1. This feature can be fundamentally problematic for a device whose purpose is to provide a stable output under varying conditions.

The focus of this PhD thesis is at the heart of these challenges: in developing silicon resonators that are transduced using a piezoelectric thin film layer added to the resonator, and in tailoring of the material properties of silicon for better frequency stability under varying ambient temperature.

1.2 Background

The concept of a MEMS resonator, and of a MEMS component in general, dates back to the seminal paper by Nathanson et al. [3], which often is said to have been ahead of its time when published in 1967. The attractive mechanical properties of silicon started to find widespread use in MEMS components 1980s [4], and with maturing of the fabrication technologies, MEMS resonator research started to take off at the turn of the millennium. Active research groups on the field were, for example, in the US in Berkeley [5, 2] and in Michigan [6], which work led to founding of the first companies, SiTime and Discera, for commercialization of the silicon resonator technology. VTT had a

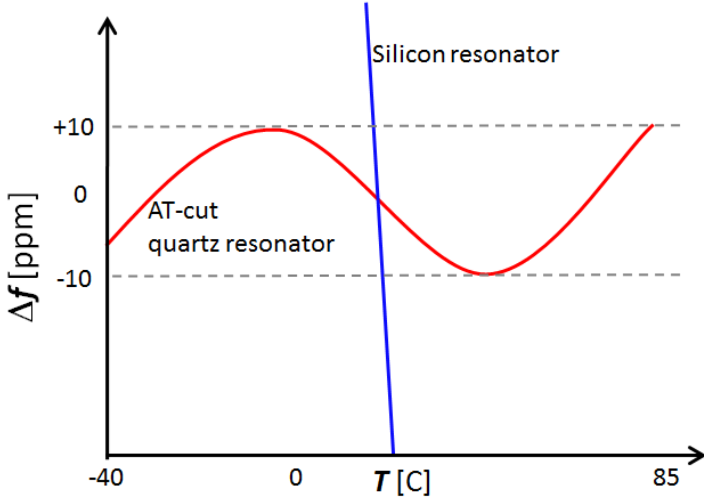

Figure 1.1. Temperature dependency of the frequency of an AT-cut quartz crystal resonator vs. that of a silicon resonator.

central role in MEMS resonator research right from the beginning. Electrostatically coupled beam resonators with record high quality factors [7, 8, 9] were an important step towards radiofrequency reference oscillators, and the tight wireless communication noise specifications were met first with the square-extensional mode resonators reported in 2004 [10]. Resonator nonlinearities [11] and the theoretical limits of MEMS-based oscillator phase noise were thoroughly investigated [12]. Also the stability of silicon resonators was measured to be at good enough level for most frequency reference applications [13].

Commercial silicon MEMS resonators of today typically rely on active temperature compensation: temperature is measured very accurately close to the resonator and the frequency error is corrected in frequency synthesis with phase-locked-loop (PLL) techniques [14]. This approach, however, degrades the noise performance of an oscillator, adds cost and increases power consumption. Also, addition of amorphous SiO_2 thin film layers to resonator structures has been used to reduce the temperature drift approximately by an order of magnitude [15], but the achieved frequency stability remains still inferior to that of quartz.

The fact that the elastic properties of silicon are affected by doping was known already in the 1960's through the theoretical work by Keyes [16] and experiments by Hall [17], but this understanding and its applicability to silicon MEMS resonators had not reached the MEMS community until 2010 [18]. This topic is central to this dissertation and it is discussed further in Chapter 4, where also parallel progress by other research groups is referred to.

Piezoelectrically transduced silicon resonators, assessed in Chapter 3 of this dissertation, has attracted attention as an alternative to electrostatically trans-

duced bare silicon resonators. In the earlier investigations, transduction was based on a piezoelectric ZnO thin film grown on top of the resonator [19, 20, 21], but later aluminum nitride as the piezoelectric thin film material was found to ensure better resonator performance [22, 23]. Commercialization of piezoelectrically coupled silicon resonators has been pursued by companies such as IDT [24] and Sand9 [25].

Several review papers on MEMS resonators have been published during the latest ten years. The early capacitively coupled silicon resonators have been reviewed in [2], and the business aspects of MEMS oscillators have been assessed by Lam in [1]. A recent review on resonant MEMS devices has been given by Beek and Puers [26]. A book by Fedder et al. assesses most recent developments [27], and also the books by Kaajakari [28] and by Senturia [29] are good sources of information. In addition, the PhD theses by Ho [30], Samarao [31], Tabrizian [32] and Harrington [33] are noted, as they deal with similar themes as this dissertation.

As the whole field of timing and frequency control devices is closely tied to the evolution of quartz-based technology, a few references of this area are highlighted as well. Introductions to quartz devices are, for example, included in the review by Vig and Ballato [34], the book by Neubig and Briese [35], and the tutorial by Vig [36], all with open online access. The IEEE UFFC society learning site is a source of additional reviews and tutorials [37].

1.3 Silicon as a resonator material

Single crystalline silicon is a very attractive material to be used in resonators. Its intrinsic mechanical losses are very low , it can be fabricated in such a way that its material properties are repeatable and well known, and, importantly, it is a very stable material (over time) [38, 4, 28]. The elasticity of single crystal silicon is anisotropic, i.e., the elastic properties are dependent on which crystal direction the material is deformed. Silicon belongs to the m3m class of the cubic crystal system, and three independent elastic constants c_{11}, c_{12} and c_{44} fully characterize it.

The frequency of a resonator should be as immune to temperature variations as possible. In general, most materials get softer when heated, and this is true for moderately doped silicon as well — the way that silicon has been typically used in MEMS resonators thus far. Moderately doped silicon behaves "normally" with temperature: its stiffness decreases with temperature and, despite anisotropy, its temperature coefficient is near $-60\,\mathrm{ppm/^{\circ}C}$, which results in

the temperature coefficient of frequency for any resonance mode being around $-30\,\mathrm{ppm}/^{\circ}\mathrm{C}$.

However, heavy doping of silicon, in particular with n-type dopants, changes its elastic characteristics drastically. It turns out that the temperature sensitivity of certain elastic constants can be made positive with suitable doping: silicon starts to behave anomalously by getting stiffer when heated. As a result, very stable behavior of the resonance frequency of a resonance mode can be obtained by balancing the negative and positive contributions from different elastic parameters to the temperature sensitivities. This is an analogous effect to what is utilized in temperature stabilized quartz crystals [39] [1].

In this work, doped silicon is divided into three categories, which will be denoted followingly:

- **n-Si** refers to "normal" silicon, which is moderately doped to a level of $n < 10^{18}\mathrm{cm}^{-3}$.
- **HD-Si** stands for heavily doped silicon, having a dopant concentration $1 \times 10^{19}\mathrm{cm}^{-3} < n < 8 \times 10^{19}\mathrm{cm}^{-3}$.
- **UHD-Si** refers to ultra-heavily doped silicon with doping level above $10^{20}\mathrm{cm}^{-3}$.

Doping level of UHD-Si corresponds to approximately 0.2% of the silicon atoms of the crystal lattice being replaced by the dopant elements. While n-Si and HD-Si wafers are commercially available, a proprietary process was developed at VTT for producing UHD-Si material.

1.4 Fabrication

Two fabrication technologies were used in this work. Electrostatically coupled (bare silicon) resonators were fabricated on SOI wafers with typically 20-μm-thick silicon device layers (Fig. 1.2(a),(b)). The resonator structures and transduction gaps were defined by deep reactive ion etching (DRIE). Two versions of the process were used: In the first one, the devices were released by etching the buried oxide with hydrofluoric acid (HF). In the second process version, the SOI wafers included pre-etched cavities [40] at the device sites, so that the devices were released immediately by the DRIE process step. Results

[1] The same effect is behind the anomalous behavior (positive temperature coefficient of stiffness) of polycrystalline SiO_2. Quartz is the single crystal form of SiO_2.

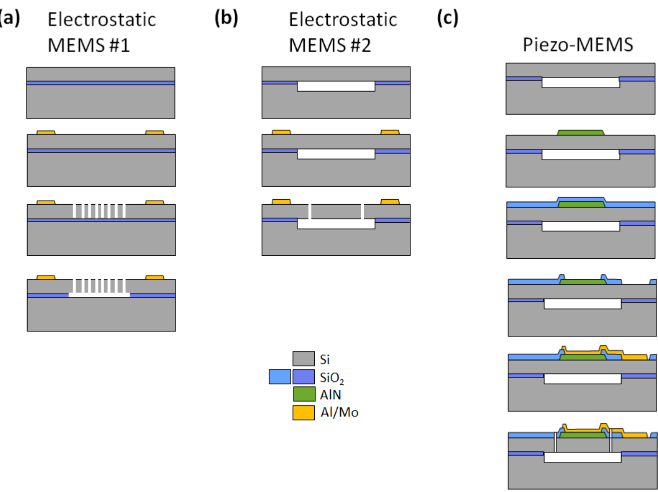

Figure 1.2. Schematic illustrations of the VTT process platforms for fabricating electrostatically and piezoelectrically coupled MEMS devices.

of vacuum encapsulated capacitively coupled resonators are discussed in Section 4.6. These devices were vacuum encapsulated on wafer level using anodic bonding with a glass/silicon cap wafer [13].

Piezoelectrically transduced resonators were fabricated using the VTT cavity-SOI PiezoMEMS process platform, see Fig. 1.2(c). The process started here, as well, with SOI wafers with pre-etched cavities. AlN, with a typical thickness of ~1 μm, was deposited and patterned right onto the Si device layer, which acted as a substrate and as the bottom electrode for device operation. An insulating layer of SiO_2 was deposited on the wafer. AlN was located only on top of the resonator, while SiO_2 was used as the insulator between the top and bottom electrodes elsewhere. Openings were etched to the SiO_2 layer, one onto the AlN layer and another onto the place where the bottom electrode contact would be formed. Molybdenum (in some cases aluminum) was deposited and patterned as the top electrode material. DRIE was used to define the device geometry and to release the resonator.

Details of the VTT process for electrostatically coupled devices are described in the dissertation by Kiihamäki [41]. General references to microfabrication technologies are books by Franssila [42] and by Madou [43].

1.5 Oscillator specifications

There is a variety of oscillator specifications depending on the specific end application, including kHz to MHz crystal resonators (Xtal), crystal oscillators (XO) and temperature compensated crystal oscillators (TCXO) [44]. The TCXO specification is of most relevance for this work. This kind of oscillators

are used, e.g., in the 2G/3G/4G/LTE phones of today. Typical TCXO specifications are collected in Table 1.1 — the exact numbers depend on the specific application. TCXOs of today are realized with an AT cut quartz crystal having a passive temperature dependent frequency stability of ±10 ppm at best, and a temperature dependent tuning capacitor is used to enhance the stability to ±2.5 ppm or better. It should be noted that all error sources are contained in the specification for the frequency stability: aging, initial accuracy (initial frequency error), and temperature dependent frequency variation.

Table 1.1. General TCXO specifications. Exact specifications may vary slightly according to the application.

frequency	frequency stability (T = -40 ... +85C, and aging effects)	phase noise at 1kHz offset from a 13 MHz carrier	current consumption
10 ... 50 MHz	± 2.5 ppm	-130 dBc/Hz	< 5 mA

As discussed, current commercially available silicon MEMS products rely on the active correction of the temperature dependent frequency drift with a PLL-synthesizer circuit. Also the initial frequency error associated with manufacturing tolerances is corrected with the PLL. This approach is associated with a penalty in a degraded noise performance and/or an increased current consumption, which has made it challenging for silicon MEMS to compete with quartz-based oscillators on the TCXO market with tight specifications.

Complementary to the MEMS approach on the market today, the goal of this work was to target a quartz-like silicon MEMS resonator, enabling performance good enough for fulfilling TCXO specifications. Key elements for realizing this vision were:

- Operating frequency in the range of 10 . . . 50 MHz.
- No frequency synthesis used at all, no PLL.
- Phase noise, oscillator power consumption and long term stability good enough to meet the TCXO specifications.
- High enough electromechanical coupling, so that the frequency adjustment needed for the correction of the initial frequency error (as well as the remaining temperature dependency of frequency) could be realized with tuning

capacitors (see Section 2.5).

1.6 Objectives and scope of the work

The objective of the work was to pursue a TCXO based on a silicon MEMS resonator by

1. investigating the achievable performance of silicon resonators whose transduction mechanism is based on a piezoelectric AlN thin film grown on top of the resonator, and by

2. investigating the possibility of passive temperature compensation of silicon resonators through heavy doping of silicon.

Chapter 2 introduces the necessary characteristics of silicon resonators needed for the discussion in subsequent chapters. Chapters 3 and 4 on piezoelectrically transduced silicon resonators and on doping-based temperature compensation, respectively, are the key chapters of this dissertation, and they contain a summary of the results published in Papers **I**—**X** as well as some non-published results[2] that are considered relevant for the discussion. Implications of the findings are discussed in Chapter 5, and a summary is presented in Chapter 6. Appendices A and B contain methodological details and numerical tables, respectively, and some relevant derivations are collected in Appendix C.

Aspects such as (wafer-level) chip packaging, fabrication cost issues, device manufacturability, and application of the free electron theory (Section 4.1) for comparison with the experimental results are left outside the scope of this dissertation. It is acknowledged that Paper **II** on our latest results of UHD-Si resonators with ±10 ppm stability does not fully comply with the standards of transparent scientific reporting, since the details of the resonator design as well as a description of the doping process are not entirely disclosed due to IPR protection reasons. Even so, the UHD-Si results are contained in this dissertation in Section 4.7, since they provide the evidence for the applicability of the findings and predictions made in Section 4.5.

[2]These results include the simulation result of Fig. 3.4(c), the oscillator characterization results of Section 3.3, and the quality factor measurement of an UHD-silicon resonator, Fig. 4.13(a).

2. Characteristics of silicon resonators

2.1 Resonance modes

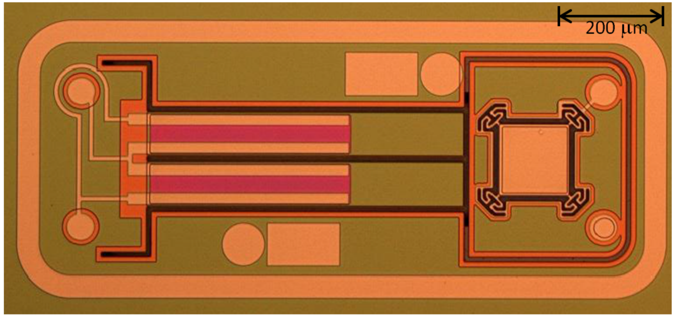

Figure 2.1. A micrograph of a chip, fabricated at VTT, containing two piezoelectrically transduced silicon resonators. On the left is a 200-kHz tuning fork resonator, and on the right is a 26-MHz square extensional mode resonator.

A silicon MEMS resonator can be designed to operate in various resonance modes, spanning a frequency range from ∼10 kHz to ∼100 MHz and having other differences in characteristics such as

- temperature-vs-frequency characteristics
- achievable strength of electromechanical transduction by using electrostatic actuation or piezoelectric actuation
- power handling capability
- tolerance to manufacturing inaccuracies
- dissipation mechanisms limiting the quality factor of the resonator

- possibility of low-loss-anchoring
- linearity
- appearance of spurious modes.

An example micrograph of two MEMS resonators are shown in Fig. 2.1, and Fig. 2.2 illustrates some examples of mode shapes encountered in this work (see also Fig. 4.7(c)): length extensional (LE) and width extensional (WE) modes of a beam resonator, Lamé and square extensional (SE) modes of a square plate, and a flexural mode of a beam resonator - which in practice is realized with the well-known tuning fork geometry. The flexural modes are suitable for use in kHz-range resonators, while the others of the above mentioned resonance modes are suitable for frequencies above $\sim 5\,\mathrm{MHz}$, when fabricated in lateral dimensions of $\sim 500\,\mu\mathrm{m}$ or less. Some descriptive qualities of LE, WE, Lamé and SE modes are discussed in the following.

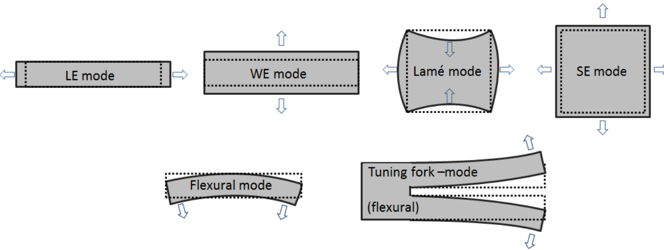

Figure 2.2. Top view schematic illustrations of the mode shapes of the length extensional (LE), Lamé, square extensional (SE), width extensional (WE), flexural, and tuning fork modes, respectively.

First reports on MEMS resonators operated in the LE mode include [8]. While demonstrated to have a high quality factor, this mode has the disadvantage of relatively low electromechanical coupling with both electrostatic actuation as well as with piezoelectric actuation. In this dissertation, it is found that the LE mode is very well suited for doping-based temperature compensation (Section 4.4.2). From the point of view of temperature compensation, flexural modes behave in a very similar way to the LE mode.

Width extensional mode resonators have been reported, e.g., in Ref. [30]. The WE mode can be better electromechanically coupled than the LE mode, and can be anchored with very low losses, since nodal points of the resonance mode shape are located at the perimeter of the resonator, when the aspect ratio of the resonator geometry fulfils certain conditions [45]. The SE mode is closely related to the WE mode (see Section 4.4.2), and has been at the focus

of many studies at VTT, starting with [10].

The Lamé mode of a plate resonator geometry can exist, when the plate sides are aligned with the [100] or [110] directions, respectively. It can be anchored at the corners of the plate with very low losses. The Lamé mode has the specific limitation in that it cannot be piezoelectrically transduced at all using the approach presented in Section 2.4, see Appendix C.3.

In general, the frequency of a resonator is given by

$$f = \frac{v}{2L}, \tag{2.1}$$

where L is the characteristic dimension for the resonator and the resonance mode in question, and

$$v = \sqrt{c/\rho} \tag{2.2}$$

is the generalized acoustic velocity, given by the material density ρ and by the characteristic stiffness c. Importantly, the characteristic stiffness c is a function of the three elastic coefficients c_{11}, c_{12} and c_{44} of silicon (see Section 1.3), which depends on the resonator geometry and on the resonance mode. For most of the resonance modes the frequency-vs-c_{ij} relation cannot be expressed in a closed form, and numerical methods are needed. The following special cases are highlighted:

- The Lamé mode can be solved in closed form, since the mode can be described as superpositions of two in-plane polarized standing shear waves propagating along the diagonals of the resonator. The acoustic velocities of the shear waves along the [100] and [110] directions are given by

$$v_{100} = \sqrt{\frac{c_{44}}{\rho}},\ v_{110} = \sqrt{\frac{(c_{11} - c_{12})/2}{\rho}}, \tag{2.3}$$

respectively [46]. The related modal frequencies are given by

$$f_{110} = \frac{1}{\sqrt{2}L}\sqrt{\frac{c_{44}}{\rho}},\ f_{100} = \frac{1}{\sqrt{2}L}\sqrt{\frac{(c_{11} - c_{12})/2}{\rho}} \tag{2.4}$$

for the Lamé mode resonators whose *sides* are aligned with the [110] and [100] directions, respectively.

- The characteristic stiffness for an LE or flexural mode of a beam resonator is given by the Young's modulus in the direction of the beam, which, for example, in the [100] direction can be approximated [28] by

$$Y_{[100]} = c_{11} - 2c_{12}^2/(c_{11} + c_{12}). \tag{2.5}$$

2.2 Temperature dependent resonance frequency

The temperature dependent resonance frequency of a resonator is customarily expanded as a power series (up to the second order)

$$f(T) = f_0[1 + TCF_1 \times \Delta T + TCF_2 \times \Delta T^2], \tag{2.6}$$

where $\Delta T = T - T_0$ is the temperature difference and f_0 is the resonance frequency at the reference temperature T_0[1]. The parameters TCF_1 and TCF_2 are the first and second order temperature coefficients of frequency[2], respectively, defined also at the reference temperature T_0. In this work, the temperature dependencies are studied over the extended industrial temperature range of $T = -40... + 85°\mathrm{C}$, and the convention of selecting $T_0 = +25°\mathrm{C}$ is followed. Higher-order temperature coefficients of frequency are neglected. Mostly the relative frequency changes are of interest, given by

$$\frac{\Delta f}{f_0} = \frac{f - f_0}{f_0} = TCF_1 \times \Delta T + TCF_2 \times \Delta T^2, \tag{2.7}$$

and typically expressed in units of ppm. As a figure of merit for the frequency stability of a resonator, the total relative frequency deviation over the full temperature range is used:

$$\Delta f_{\mathrm{total}} = \max_T (\Delta f / f_0) - \min_T (\Delta f / f_0) \,. \tag{2.8}$$

When the temperature dependence of the elastic parameters $c_{ij}(T)$ is known and, assuming that the thermal expansion is known, the temperature dependence of the resonance frequency can be calculated. The relative frequency change due to a change in the elastic parameters $\delta c_{ij}(T)$, thermal expansion $\delta L(T)/L$ and change in density $\delta\rho(T)/\rho$ can be denoted as

$$\frac{\delta f}{f}(T) = \frac{1}{f} \sum_{ij=11,12,44} \frac{\partial f}{\partial c_{ij}} \delta c_{ij}(T) - \frac{\delta L}{L}(T) - \frac{1}{2}\frac{\delta\rho}{\rho}(T). \tag{2.9}$$

For the calculations in this work, it is accurate enough to evaluate the effects from thermal expansion up to second order:

$$\frac{\delta L}{L}(T) = (\alpha_1 \Delta T + \alpha_2 \Delta T^2). \tag{2.10}$$

The last term in Eq. (2.9) can be expressed through thermal expansion (see the detailed derivation in Appendix C.1) , and the relative frequency change

[1] Variation of f_0 among a population of devices, caused by fabrication tolerances, is referred to as the initial accuracy, as the frequency scatter or as the frequency repeatability.

[2] When TCF is discussed without any subscript in this work, it refers to TCF_1.

can be written as

$$\frac{\delta f}{f}(T) \approx \frac{1}{f} \sum_{ij=11,12,44} \frac{\partial f}{\partial c_{ij}} \delta c_{ij}(T) + \frac{1}{2}(\alpha_1 \Delta T + \alpha_2 \Delta T^2). \tag{2.11}$$

The temperature dependency of the elastic parameters for a given doping level n is given by a second order expansion such that

$$c_{ij}(T,n) = c_{ij}^0(n)[1 + a_{ij}(n)\Delta T + b_{ij}(n)\Delta T^2], \tag{2.12}$$

where $a_{ij}(n)$ and $b_{ij}(n)$ are the first- and second-order temperature coefficients of the elastic parameters, respectively, and $c_{ij}^0(n)$ is the constant term. The linear temperature coefficient of frequency, TCF_1, is defined as the first derivative of Eq. (2.11)

$$TCF_1 = \frac{1}{f} \left.\frac{\mathrm{d}f}{\mathrm{d}T}\right|_{T=T_0} = \frac{1}{f} \sum_{ij} \frac{\partial f}{\partial c_{ij}} c_{ij}^0 a_{ij} + \alpha_1/2, \tag{2.13}$$

and the second order temperature coefficient of frequency, TCF_2, is obtained as

$$TCF_2 = \frac{1}{2f} \left.\frac{\mathrm{d}^2 f}{\mathrm{d}T^2}\right|_{T=T_0} = \frac{1}{f} \sum_{ij} \frac{\partial f}{\partial c_{ij}} c_{ij}^0 b_{ij} + \alpha_2/2. \tag{2.14}$$

2.3 Equivalent circuit representation

A generic mechanical resonator with distributed vibrations can be represented with a lumped model, where the physical properties of the resonator, such as mass, stiffness (spring), damping, and displacement are represented by single elements [47, 28]. The lumped spring-mass model of a generic resonator and its electrical equivalent circuit are shown in Fig. 2.3(a). A detailed derivation of the electrical equivalent circuit, commonly referred to as the BVD equivalent circuit [48], can be found, e.g., in [28], in [47] or in [26]. An intuitive and easy-to-reproduce derivation is given here.

Assume that there is a transduction mechanism, which relates the force F applied on the mass m to the electrical voltage U through a transduction factor η, and that the same transduction factor relates the output current I to the velocity,

$$F(t) = \eta U(t), \tag{2.15}$$

$$I(t) = \eta \dot{X}(t). \tag{2.16}$$

The transduction factor η itself is discussed in the following Section. Assuming a harmonic motion at angular frequency $\omega_0 = 2\pi f_0$, and neglecting any phase information, we obtain

$$F = \eta U,\ I = \eta \omega_0 X, \tag{2.17}$$

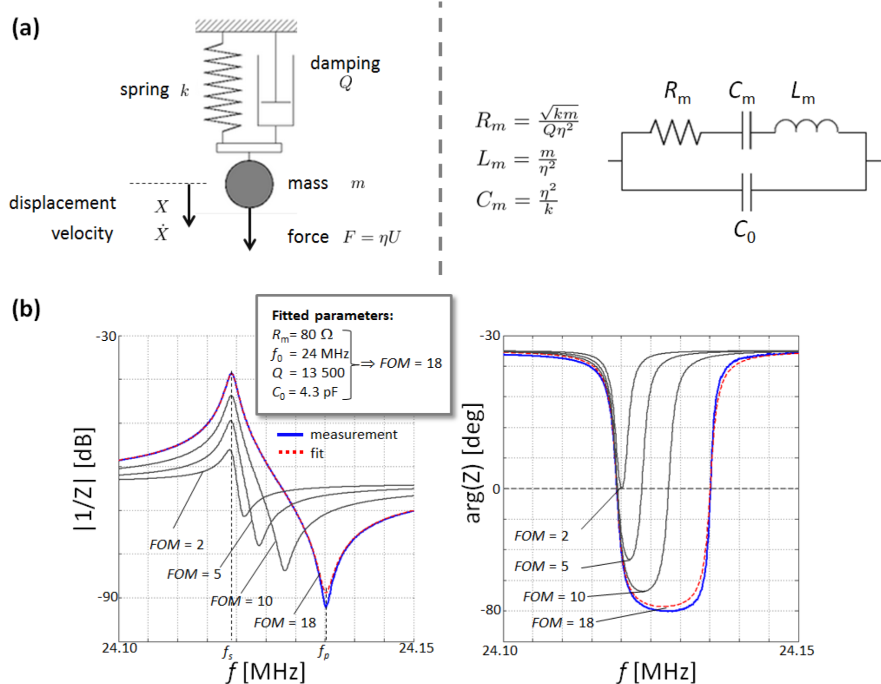

Figure 2.3. (a) The lumped spring-mass model of a mechanical resonator and its electrical equivalent circuit. (b) An example of the frequency response of a measured 24-MHz resonator, and the fitted response of an equivalent circuit. Additional calculated responses with figure of merit $FOM = 1/(2\pi f C_0 R_m) = 10, 5, 2$ illustrate how the response would be modified if the motional resistance R_m would be increased through decreased electromechanical coupling factor η (see Eq. (2.20).

where F, U, X and I denote the amplitudes of the force, voltage, displacement and current, respectively. At resonance, the electrical impedance of the system is purely resistive. Thus, the motional resistance R_m of the resonator is given as the ratio of the input voltage and output current,

$$R_m = U/I = \frac{F}{\eta^2 \omega_0 X}. \tag{2.18}$$

Now, at resonance the vibration amplitude X of the resonator is the static displacement multiplied by the quality factor Q,

$$X = \frac{F}{k} Q. \tag{2.19}$$

Using this in Eq. 2.18 we can relate the motional resistance with the mechanical parameters and the transduction factor,

$$R_m = \frac{m\omega_0}{\eta^2 Q} = \frac{\sqrt{km}}{\eta^2 Q}. \tag{2.20}$$

The latter form has been obtained by applying the relation $\omega_0 = \sqrt{k/m}$. The reactive components L_m and C_m are obtained through the knowledge that the quality factor of an RLC-circuit is given as the fraction of the capacitive or inductive reactance and the resistivity,

$$Q = \frac{X_C}{R_m} = \frac{1}{\omega_0 C_m R_m}, \tag{2.21}$$

$$Q = \frac{X_L}{R_m} = \frac{\omega_0 L_m}{R_m}, \tag{2.22}$$

respectively. Hence, we obtain

$$\begin{aligned} L_m &= m/\eta^2 \\ C_m &= \eta^2/k. \end{aligned} \tag{2.23}$$

In a typical electrical transduction scheme, there is always a direct electrical feedthrough path between the input and output, represented by capacitance C_0. The four equivalent circuit parameters R_m,C_m, L_m and C_0 characterize a micromechanical resonator. Often, when discussing resonator characteristics, f_0 and Q are referred to instead of C_m, L_m. These can be mapped back to C_m and L_m by

$$\begin{aligned} C_m &= 1/(2\pi f_0 R_m Q) \\ L_m &= R_m Q/(2\pi f_0). \end{aligned} \tag{2.24}$$

Figure 2.3(b) shows an example of the measured frequency response of a resonator together with a response of a equivalent circuit fitted to the measured data.

2.4 Electrostatic and piezoelectric transduction

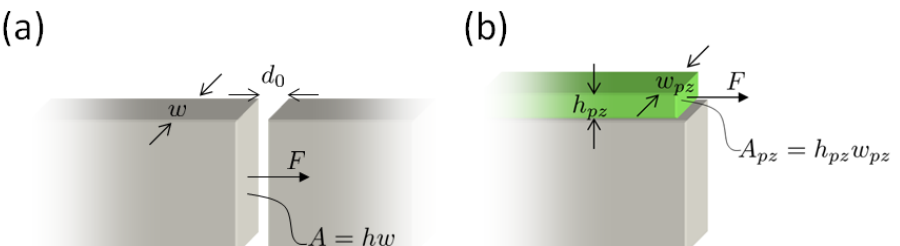

Figure 2.4. Illustrations of (a) electrostatic parallel-plate transduction of an LE mode resonator and (b) piezoelectric transduction of a similar resonator.

Electrostatic and piezoelectric transduction methods, and the related transduction factors η_{ES} and η_{pz}, respectively, are introduced here with a simplified example of an LE mode resonator. Equations (2.15) and (2.16) relate the force F with voltage U, and current I with velocity $\dot{X}$, respectively, through the transduction factor η. In general, the voltage-to-force and velocity-to-current transduction mechanisms do not have to be symmetric, but for this introduction it suffices to assume so. The transduction factors are derived for the

electrostatic and piezoelectric cases, respectively, through Eq. (2.15), i.e., by examining how the drive voltage U is converted to actuation force F.

Let us investigate a parallel plate capacitor at the end(s) of an LE beam resonator, Fig. 2.4(a). The capacitance is given by

$$C = \epsilon_0 \frac{A}{d_0 - x}, \tag{2.25}$$

where the gap is given by $d = d_0 - x$ and area by $A = hw$. The force between the capacitor plates is given by the derivative of the energy stored in the capacitor

$$F = -\frac{\partial}{\partial x}(\frac{1}{2}CU^2) = \frac{1}{2}U^2\frac{\partial}{\partial x}C(x) = \frac{1}{2}(U_{DC} + U_{AC})^2\frac{\partial}{\partial x}C(x) \tag{2.26}$$

where U is the voltage over the capacitor, consisting of a DC biasing term U_{DC} as well as of the harmonic AC drive voltage U_{AC}. Expanding the squared voltage term yields

$$F = \frac{1}{2}(U_{DC}^2 + 2U_{DC}U_{AC} + U_{AC}^2)\frac{\partial}{\partial x}C(x). \tag{2.27}$$

Of relevance is here only the harmonic component at the frequency of the drive signal, i.e., $2U_{DC}U_{AC}$. The derivative of the capacitance can be linearized to obtain

$$F \approx U_{DC}\epsilon_0\frac{A}{d_0^2}U_{AC}, \tag{2.28}$$

and a comparison to Eq. 2.15 gives for the electrostatic transduction factor

$$\eta_{ES} = U_{DC}\epsilon_0\frac{A}{d_0^2}. \tag{2.29}$$

Focus now on the case of an LE resonator, on top of which is a piezoelectric thin film of thickness h_{pz}, Fig. 2.4(b). The x-directed strain S_1, stress $T_1 = F/A_{pz}$, and a z-directed electric field E_3 are coupled together through the simplified constitutive relation [28]

$$T_1 = e_{31}E_3 + YS_1, \tag{2.30}$$

where e_{31} is a piezoelectric coefficient, and Y is the Young's modulus of the piezoelectric material. Assuming that the piezoelectric film is rigidly clamped to the underlying silicon beam is equivalent to having $S_1 = 0$. Expressing the stress T_1 through the force per cross-sectional area, and writing the electric field as $E_z = U/h_{pz}$ yields

$$\frac{F}{w_{pz}h_{pz}} = e_{31}\frac{U}{h_{pz}}, \tag{2.31}$$

from which the piezoelectric transduction factor is obtained as

$$\eta_{pz} = we_{31}. \tag{2.32}$$

A three-dimensional derivation in Appendix C.2 shows that the vertical electric field contributes to a lateral force also through the piezoelectric constant e_{33}, making the effect slightly stronger.

2.5 Tunability

Figure 2.3(b) shows that there is one resonance peak and one anti-resonance peak, or valley, in the frequency response of a resonator. These are referred to as the series and parallel resonances with frequencies

$$f_s = \frac{1}{2\pi}\sqrt{\frac{k}{m}} = \frac{1}{2\pi}\sqrt{\frac{1}{L_m C_m}} \tag{2.33}$$

and

$$f_p = \frac{1}{2\pi}\sqrt{\frac{C_m + C_0}{L_m(C_m C_0)}}. \tag{2.34}$$

For f_s, resonance is formed in the mechanical $R_m C_m L_m$ -branch, while for f_p, the resonance forms over the loop with the mechanical branch and C_0 connected in series. The separation between the two peaks, $f_p - f_s$, is of importance, since, by using a loading capacitor in an oscillator circuit [49], it is possible to tune the resonance frequency by a fraction of this distance. Typically in MEMS resonators, the relative frequency separation is a few thousand ppm at most; through a series of approximations, this metric can be expressed with equivalent circuit parameters C_0 and C_m, or with the transduction factor η as

$$\frac{f_p - f_s}{f_p} \approx \frac{1}{2}\frac{f_p^2 - f_s^2}{f_p^2} \approx \frac{1}{2}\frac{f_p^2 - f_s^2}{f_s^2} \approx \frac{1}{2}\frac{C_m}{C_0} = \frac{1}{2}\frac{\eta^2}{kC_0}. \tag{2.35}$$

It is clear that the distance between the parallel and series frequencies increases with stronger coupling. It is customary to define a coupling coefficient k_{eff}^2 as

$$k_{eff}^2 = \frac{f_p^2 - f_s^2}{f_p^2}, \tag{2.36}$$

through which the relative frequency separation is expressed as

$$\frac{f_p - f_s}{f_p} \approx \frac{1}{2}k_{eff}^2. \tag{2.37}$$

Given that the real tunability in a practical oscillator is typically $\sim 30\%$ of the distance between the two resonances, $k_{eff}^2 \times 1/6$ is used as a metric for the resonator tunability in this work (e.g. in Table 3.1).

2.6 Resonator as a part of an oscillator circuit

2.6.1 Requirements for sustained oscillation

An oscillator is a combination of an active drive circuit (amplifier) and a frequency-setting resonator element. In an idealized form, the amplifier can be a transimpedance amplifier (TIA) characterized by its negative resistance R_{TIA}, see Fig 2.5(a). For sustained oscillation, the two Barkhausen criteria [50] need to be fulfilled.

1. First, the loop gain needs to equal unity, thus the negative resistance R_{TIA} needs to cancel the motional resistance R_m, i.e., $R_{TIA} = R_m$.

2. The phase shift around the loop needs to be zero (or an integer multiple of 2π).

The first criterion relates to the power consumption of the oscillator: realizing higher R_{TIA} requires more power.

The second criterium is fulfilled if the phase swing of the response of a resonator is large enough so that a zero phase shift is reached (or crossed) at the resonance. This can be examined in the calculated example responses of Fig. 2.3(b), where the coupling factor η has been varied so as to vary the resonator's figure of merit FOM, defined as the ratio of the impedance Z_0 of the shunt capacitance C_0 to the motional resistance R_m:

$$FOM = \frac{Z_0}{R_m} = \frac{1}{2\pi f_0 C_0 R_m}. \tag{2.38}$$

An equivalent expression for Eq. (2.38) is

$$FOM = k_{eff}^2 \times Q. \tag{2.39}$$

Deducing from the plots with varied FOM, it is seen that FOM needs to be above 2 for sufficient phase swing. In practical oscillators, a rule of thumb of having a FOM of over 5 is often used for increased robustness for fulfilling the phase condition[3]. An in-depth treatment of TIA topology is found in Ref. [26], and other commonly used oscillator topologies have been analyzed by Vittoz et al. in Ref. [51].

[3] Parasitic capacitances typically add in parallel with C_0, and thus decrease FOM as well as tunability, see Eq. (2.35).

Figure 2.5. (a) Idealized oscillator topology based on a transimpedance amplifier. (b) Qualitative behavior of oscillator phase noise according to Eq. (2.40). The red and green lines illustrate how phase noise would be modified if the signal power P or the quality factor Q were increased, respectively.

2.6.2 Phase noise of an oscillator

The short term instability of an oscillator is quantified by the phase noise. The output of an ideal oscillator would be a pure sine wave, and its power would be concentrated at the oscillator frequency f_0, represented as a spectrum by the Dirac delta function. In real oscillators, this power is spread around the carrier frequency f_0. The expression for the phase noise, originally derived by Leeson [52], can be given in a simplified form [26] as

$$L(\Delta f) = \frac{F k_B T}{2P} \left(\left(\frac{f_0}{2Q\Delta f} \right)^2 + 1 \right), \tag{2.40}$$

where f_0 is the carrier frequency, Δf is the deviation from the carrier frequency, $k_B T$ is the thermal noise, F is the noise figure of the amplifier, Q is the quality factor of the resonator, and P is the signal power at the amplifier input. The phase noise is seen to consist of a Δf^{-2} -decay near the carrier component and a constant noise floor, qualitatively illustrated in Fig. 2.5(b). The following general conclusions can be made on the factors affecting the noise performance of an oscillator:

- An increased quality factor Q results in lower near carrier noise (Section 2.7).

- The near carrier noise and the noise floor can be decreased if the signal power P is increased. This is ultimately limited by the power handling capability of the resonator (Section 2.8).

In reality, factors like nonlinearities [12], coupling of other external noise sources such as a DC bias generator, and details of the oscillator topology

and its amplifier circuit often complicate the picture and make optimization of the phase noise a nontrivial task. Although typical quartz crystal quality factors are well over 100 000 at ~20 MHz, decent phase noise can be reached with a considerably lower quality factor, such as seen in Section 3.3.

To compare the phase noise performance $L_{f_H}(\Delta f)$ of an oscillator at frequency f_H to the phase noise $L_{f_L}(\Delta f)$ of another oscillator (or specification) at a lower frequency f_L, a scaling law

$$L_{f_L}(\Delta f) = L_{f_H}(\Delta f)(\frac{f_L}{f_H})^2 \tag{2.41}$$

applies [26].

2.7 Quality factor

The dissipations in a resonator are quantified by the quality factor Q, affected by several independent loss mechanisms such as anchoring (clamping) losses, thermoelastic dissipation (TED), air damping, intrinsic (material related) damping and possible other sources of damping:

$$Q = [Q_{anchor}^{-1} + Q_{TED}^{-1} + Q_{air}^{-1} + Q_{intrinsic}^{-1} + Q_{other}^{-1}]^{-1}. \tag{2.42}$$

A high quality factor implies a better short-term frequency stability (phase noise) of an oscillator (Section 2.6.2).

In MEMS resonators, the anchoring losses play an important role. The resonator has to be mechanically attached to the surrounding substrate in one way or another, and the anchoring tethers always lead to some level of leakage of the acoustic energy trapped in the resonator. However, appropriate selection of the resonance mode shape, and a proper anchoring design can reduce these losses to a very low level. As a practical rule of thumb, anchoring should be done at nodal points of the resonance mode shape, such as the corners of the Lamé mode plate (Fig. 2.2), but this may not always be possible due to other design constraints. High quality factor without nodal anchoring can still be achieved, such as demonstrated for the SE mode resonator in [28], where anti-nodally attached very flexible anchors were used. A new finding of this dissertation, related to this type of anchoring is discussed in Section 3.2.3.

Thermoelastic dissipation [53] originates from density gradients within the resonator during the oscillation, and it can be the dominating dissipation mechanism for low frequency (flexural) resonators. In bulk mode resonators, such as the extensional mode resonators in Fig. 2.2, TED can usually be neglected.

Air damping [54] can be a very strong dissipation mechanism for resonators operating at frequencies up to ~ 100 MHz. As a result, resonators typically need to be encapsulated to a vacuum below 1 mbar to ensure high quality factor operation.

The factor $Q_{intrinsic}$ captures the intrinsic dissipations of the resonator material, which in silicon are caused by phonon-phonon interactions [55]. The Lamé mode resonator is a rather ideal special case from the point of view of low losses: it can be nodally anchored at the plate corners, and TED is wholly absent, since the shear mode character causes no local density variations at all in the device during oscillation. A $Q \times f$ product of the order of 10^{13} of Lamé mode resonators reflects the low level of intrinsic dissipation in silicon[4] [56]. In this dissertation, Lamé mode resonators were used for verifying the low level of intrinsic dissipations in heavily doped silicon, see Section 4.6 (Paper **IV**).

Finally, Q_{other} stands for any other sources of dissipation, which in some cases may not be entirely known. For example, in the case of piezoelectrically actuated silicon resonators, the origin of the mechanisms limiting the quality factor are not fully understood, see Section 3.1.

2.8 Power handling capability

As seen in Eq. (2.40), the phase noise of an oscillator circuit is inversely proportional to the oscillator drive power P. Hence, for optimal performance, the energy stored in the resonator needs to be maximized. At first sight, competing with larger quartz crystals with miniaturized silicon MEMS appears very challenging from the energy storage aspect, but it has been shown that the maximum energy density in silicon resonators can be $1000\times$ higher than that in quartz [11]. The maximum vibration amplitude of a resonator is dictated by the limit at which a nonlinear effect would cause problems to oscillator operation. Typically, this limit is associated with the nonlinearity of the transduction method (piezoelectric or capacitive), nonlinear geometrical effects caused by dynamic shape variations, or, ultimately, the nonlinearity of the resonator material itself. In these cases, after the bifurcation point, i.e., at high enough vibration amplitude, the resonance frequency is not any more single valued and this threshold is considered to be the limit for the vibration amplitude. These limits are thoroughly discussed in Refs. [11] and [57]. Another way that nonlinearities can limit the power handling capability of resonators is through coupling between resonance modes. The desired res-

[4] For reference, the $Q \times f$ product of quartz is of similar magnitude.

onance mode can "leak" energy to other modes at higher (super-) harmonic frequencies, or even to modes at lower (sub-) harmonic frequencies, thus limiting the vibration amplitude of the main mode [58]. In this dissertation, a new subharmonic nonlinear coupling mechanism was identified (Paper **VI**) and it is discussed in Section 3.2.4.

2.9 Design objectives for resonators

Synthesis of the oscillator specifications (Section 1.5) and the above discussed resonator characteristics yields the following design objectives for resonators:

1. The total frequency variation due to temperature variations, Δf_{total}, should be minimized.

2. To maintain good phase noise properties, the quality factor and power handling capability of the resonator should be maximized.

3. FOM, given by Eq. (2.38) or (2.39), needs to be at least 5 for operation as a part of an oscillator circuit.

4. The motional resistance R_m should be minimized for low oscillator power consumption (Section 2.6.1)

5. Electromechanical coupling needs to be sufficiently large to allow for enough tuning of the frequency (Section 2.5), in order to correct for the initial frequency error as well as for the temperature-induced frequency error.

The design objectives can be interdependent: for example, the needed level of tunability is dependent on the achievable level of temperature stability (objective 1). Optimization of a resonator with all these design objectives is a complex optimization task with "fuzzy"[5] boundary conditions.

[5] The (technological) boundary conditions may not be accurately known at a given time, and they may be changing constantly.

3. Piezoelectrically transduced silicon resonators

Piezoelectric transduction, as an alternative to electrostatic transduction, is motivated by the design objective of achieving a strong electromechanical coupling of a silicon resonator. The ratio of the electrostatic and piezoelectric transduction factors, given by Eqs. (2.29) and (2.32), is

$$\frac{\eta_{ES}}{\eta_{pz}} = U_{DC}\frac{h}{d^2}\frac{\epsilon_0}{e_{31}}, \tag{3.1}$$

where h and d are the height and width of the capacitive gap, and U_{DC} is the DC biasing voltage. A numerical example illustrates the relatively strong transduction factor that can be obtained using aluminum nitride with piezoelectric coefficient $e_{31} = -0.58$ Cm^{-2} [59]: To match the transduction factor achieved with AlN, a bias voltage higher than 34V is needed for a capacitive gap of width $d = 0.1\,\mu$m and height $h = 20\,\mu$m. A trench this narrow is very challenging to fabricate reliably, and a DC voltage larger than 3 volts can be considered out of question for most of low-cost CMOS fabrication processes that would be used for a commercial oscillator. A clear advantage of piezoelectric transduction is that no DC bias voltage is needed at all. In this Chapter, the results obtained with piezoelectrically transduced silicon resonators are discussed.

3.1 Piezoelectically transduced LE, WE and SE resonators

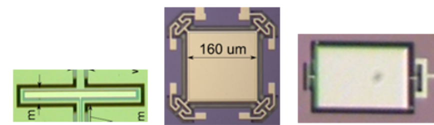

	units	**LE resonator** (Paper 1)	**SE resonator** (Papers 2,3)	**HD-Si WE-resonator**	**UHD-Si extensional mode resonator** (Paper 9)
Silicon type (doping)		n-Si $n < 10^{18}\text{cm}^{-3}$	n-Si $n < 10^{18}\text{cm}^{-3}$	HD-Si $n \sim 5\times 10^{19}\text{cm}^{-3}$	UHD-Si $n > 10^{20}\text{cm}^{-3}$
AlN thickness	µm	0.3	0.3	1	-
f_0	MHz	14	26	24	23
Frequency stability (T= - 40...+85°C)	ppm	±1500	±1500	±150	±10
Q		18 000	18 000	15 000 (*)	4000 (*)
R_m	Ω	3300	120	50	100
C_0	pF	4	9	4	10
$k^2\times 1/6$ (tunability)	ppm	10	50	370	250
FOM		0.9	5.6	33 (*)	6.3 (*)

(*): *Q* value characterized in open air.

Table 3.1. Performance summary of generations of piezoelectrically transduced silicon resonators fabricated at VTT.

The progress of the performance of different generations of piezoelectrically driven resonators fabricated at VTT is summarized in Table 3.1[1]. Our initial experiments are reported in Papers **IX** and **X**. First, 14-MHz beam resonators operating in the LE mode were fabricated. A very modest performance with FOM less than 1 was observed, due to the weak coupling implying a tunability of only 10 ppm. An in-vacuum quality factor approaching 20 000 was measured. The dependence of the quality factor on resonator in-plane orientation was investigated. It was found out that the anchor losses (see discussion in Section 2.7) for a [100]-aligned LE mode resonator were greatly increased due to the anisotoropic behavior of the silicon poisson ratio, limiting the quality factor to $Q \sim 3500$. A qualitative match with the result was obtained with FEM modelling in two dimensions.

The fabrication process was accommodated to allow for the flexible meander-

[1] The measurement data presented in Paper **IX** contains a calibration error leading to underestimation of device admittance by approximately 50%. Therefore, parameters R_m and C_0 reported in Paper **IX** have been be halved and doubled, respectively, to obtain the values for the SE resonator shown in the table. $FOM \sim 1/(C_0 R_m)$ is not affected by this calibration error. Characterization results in subsequent papers were obtained with the approach described in Appendix A.1, where the above described calibration error was eliminated.

spring anchors needed by the square plate resonator operating in the SE mode, see Fig. 3.1(b). In comparison with the LE mode, much more efficient coupling was achieved and the performance was increased to $FOM \sim 5.6$. Interferometric imaging was used for getting more insight to device operation; the optical method reveals the full vibration field of the device, which cannot be deduced from the electrical measurements. It was verified that the SE mode was cleanly excited without unwanted out-of-plane vibration components. Before this verification there was no direct evidence of whether breaking the symmetry in the out-of-plane direction by introducing of the AlN/Mo thin films on top of the resonator could lead to perturbation of the resonance mode. It was found out that excitation by the piezoelectric thin film on top of the resonator may excite also unwanted parasitic modes more easily than with capacitive transduction. Anchoring and dimensioning of the SE mode resonator was studied in fine detail, with an experimental parametric study discussed in Section 3.2.

The performance of the LE and SE mode resonators was compromised by the relatively thin AlN layer of 0.3 μm, whose effect was seen in increased static capacitance C_0 (over the this piezoelectric layer) and, correspondingly, in decreased figure of merit FOM (note that FOM, given by Eq. (2.38) scales as $R_m/C_0 \sim \eta^2/C_0$, where η is thickness independent as seen in Eq. (2.32)). A performance increase was achieved through a sputtering system upgrade, which enabled thicker AlN film deposition. The boosted WE resonator performance (Table 3.1) reflects this change. The WE designs were fabricated at a time when the temperature compensation properties of resonators fabricated on HD-silicon were understood (Section 4.4.2), and a transition from the SE mode design to the WE mode resonator was done to reach an optimal (first order compensated) frequency stability of $\pm$150 ppm. Similar work was published by [60]. Discussion on the results with the UHD-Si resonator design of the best temperature stability is presented in Section 4.7.

The quality factor of piezoelectrically driven silicon high-frequency resonators in the range of 10 000 . . . 20 000 is seen to be clearly reduced from the quality factor in excess of 100 000 of capacitively coupled bare silicon resonators operating in similar resonance modes [7, 10]. Addition of the piezoelectric (AlN) and top metal (Mo or Al) thin film layers onto the silicon resonator structure degrades the quality factor, but there is currently no consensus on what the exact mechanisms for the quality factor degradation are. The losses cannot be related to the AlN/metal stack alone, as higher $Q \times f$ products have been demonstrated for such resonators [61]. Interfacial dissipation mechanisms have been suggested [62], but recently, some counterevidence against this ex-

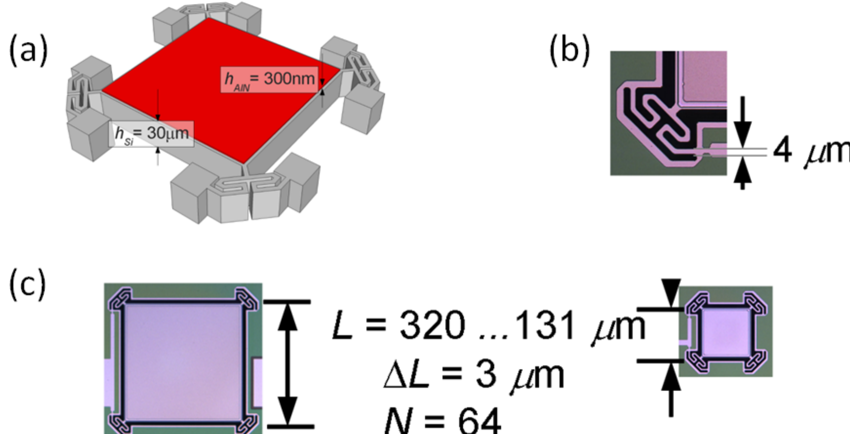

Figure 3.1. (a) An illustration of a SE plate resonator (SiO_2 and Mo layers have been excluded from the image). (b) Corner anchor design used in all of the variations. (c) Micrographs of the largest and smallest SE resonator variation. (Paper **VIII**)

planation has been presented [63]. We also hypothesize increased anchoring losses: addition of the AlN/metal stack breaks the out-of-plane symmetry of the resonator, which can lead to increased acoustic energy leakage through the anchors. Nevertheless, despite the quality factor degradation, $Q \sim$10 000 can be enough for frequency reference applications, see the phase noise result in Section 3.3.

3.2 Statistical study of size-varied SE resonators

3.2.1 Introduction

A statistical parametric study was done with a set SE mode plate resonators, whose lateral dimensions were varied so that the main resonance mode occurred at a frequency range of $f = 13\ldots30$ MHz. Findings of these experiments are reported in Papers **VIII**, **V** and **VI**. The objective was to experimentally probe the limits of the resonator design by mapping the resonance mode branches and their properties as a function of the resonator size, and, in particular, to investigate whether the in-plane extensional modes of the resonators are excited "cleanly", i.e., with a relatively low frequency scatter. Furthermore, the extensive experimental data set allowed a comprehensive comparison with simulated data. The wafer level characterization infrastructure was at the time of the study developed to a state, which enabled measurement and analysis of large amounts of data - see Appendix A.1. The investigated

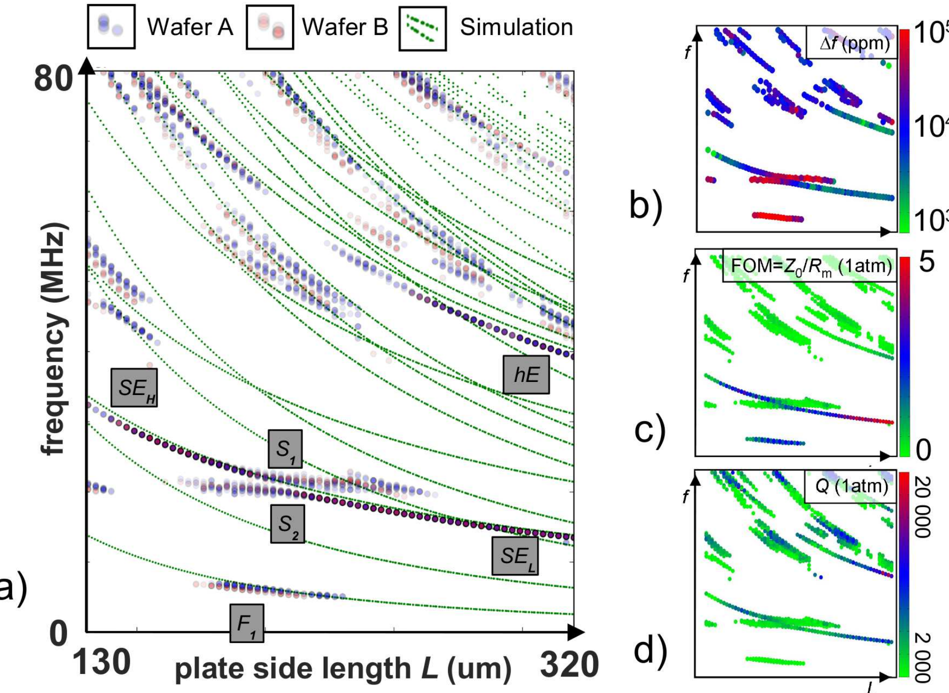

Figure 3.2. (a) Dispersion of the resonance frequency as a function of square resonator size: experimental data and simulation. To simplify the simulation models, the corner anchors were not included. Note that the data points are semi-transparent, and hence the colors are stronger for data points stacked on top of each other. For the same reason, the blue and red colors mix to make purple for overlying data from wafers A and B. (b) Frequency scatter of the resonances modes. We have defined the frequency scatter Δf as the full range of frequencies measured for the mode under investigation. (c) Resonator figure of merit $FOM = Z_0/R_m$. (d) Quality factors of the measured resonances. The measurements have been done at atmospheric pressure. (Paper **VIII**)

set of devices consisted of 64 variations, where the lateral dimension L of the resonator plate was varied from 131 μm to 320 μm with 3-μm steps, see Fig. 3.1(c). Each variation had similar corner anchors (Fig. 3.1(b)).

3.2.2 Characteristics of modal branches

The dispersion curves of the measured and simulated resonance frequencies as a function of the resonator size are shown in Figure 3.2(a). Circa 1200 devices from two wafers were characterized, and five of the largest resonances were measured for each device. For most of the measured modal branches the frequency scatter is noticeable, typically more than 15 000 ppm. This was interpreted to be attributed to the flexural character of such modes: The resonance frequency of a flexural mode is sensitive to the device thickness, and the SOI device layer thickness variation across a wafer results in corresponding variations of the resonance frequency. Additionally, a systematic difference of resonance frequencies is observed for the high-scatter branches between wafers A and B. Wafer A resonance frequencies tend to be slightly lower than

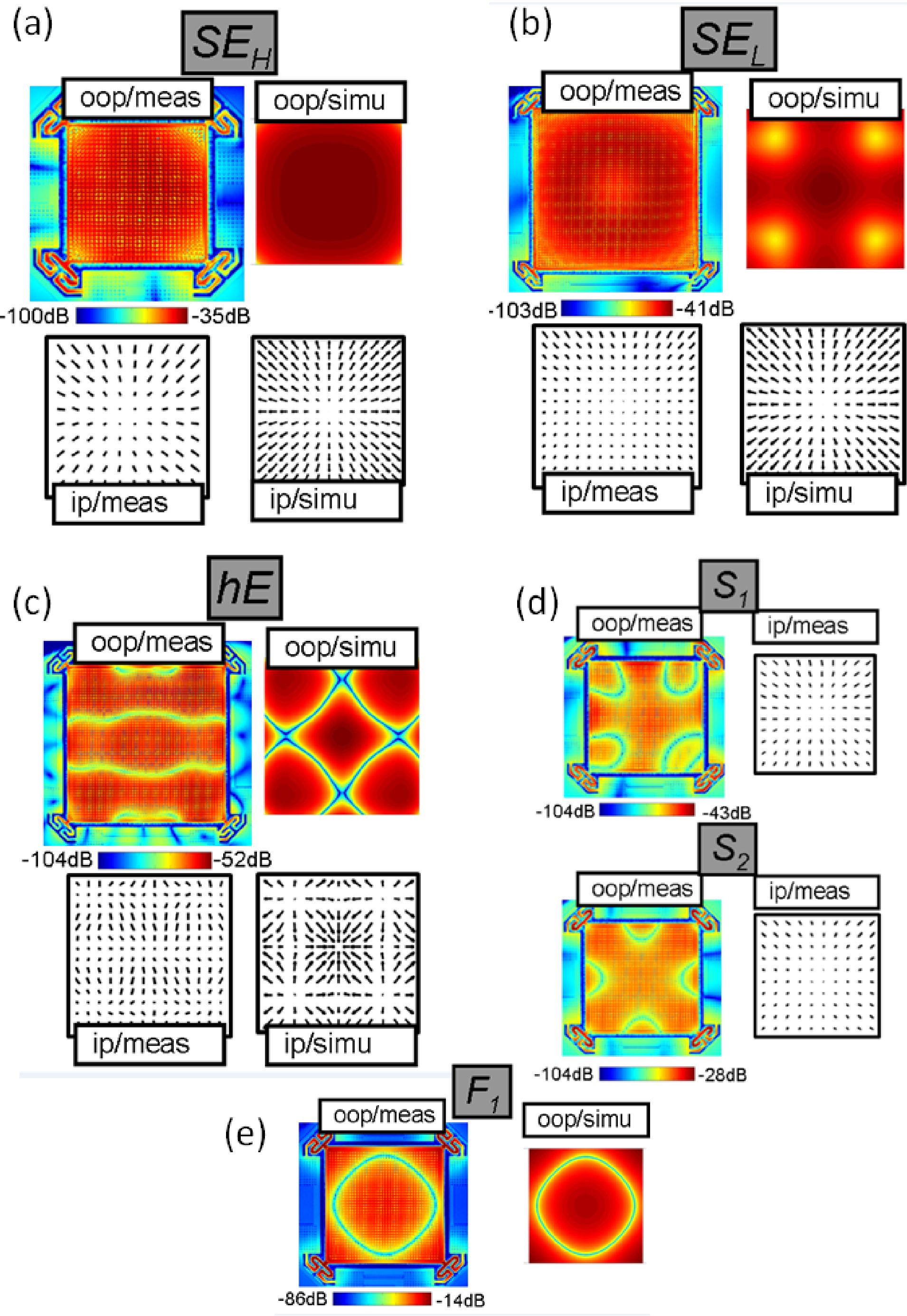

Figure 3.3. Measured and simulated out-of-plane (oop) and in-plane (ip) vibration fields of the resonance modes of selected resonance modes labelled in Fig. 3.2(a). (a)-(b) high- and low frequency tails of the SE mode branch SE_H and SE_L, (c) higher-order extensional mode hE, (d) modes S_1 and S_2 at the splitting region of the SE mode branch, and (e) flexural mode F_1. Optical measurements were done by Department of Applied Physics, Aalto University. (Papers **V** and **VIII**)

those for devices from wafer B, which can be attributed to a device layer thickness difference between wafers A and B. Figure 3.2(b) illustrates the frequency scatter in more detail. Figure 3.3(e) shows the mode shape of the low-frequency flexural mode F_1. For this mode, the match between simulation and measurement is excellent.

On the other hand, it is evident from the dispersion plot that the spread of measured resonance frequencies is relatively small for certain resonances. Comparing with data from simulation, one finds that the low-scatter branches correspond to the SE mode and to a higher-order extensional mode — we have labeled these branches as SE_H , SE_L and hE according to their mode type (subindices H and L denote the high/low-frequency region of the SE branch, respectively). The frequency scatter within the SE_H , SE_L and hE branches is typically $\Delta f \sim 2000$ ppm. We have defined the frequency scatter Δf as the full range of frequencies measured for the mode under investigation. The relatively small frequency scatter was interpreted to indicate that these extensional modes have been excited "cleanly", i.e., with a very small flexural component. The frequency of an extensional mode is only weakly dependent on the resonator thickness, and the SOI device layer thickness variations do not contribute much to the resonator frequency repeatability. It was hypothesized that the frequency scatter of these modes originates mainly from variations of the resonator lateral dimensions. Figures 3.3(a)-(c) show the in-plane and out-of-plane vibration fields of these low-scatter modes. Side-to-side comparison of the experimental and simulated data yields a relatively good match for the vibration fields.

For certain branches, such as F_1, SE_H , SE_L and hE, simulated modal frequencies and the experimental data match well with each other (Fig. 3.2(a)). The few percent difference in the resonance frequencies can be explained by the difference in real stiffness parameters and those used in the simulation, and by the exclusion of the top metal layer from simulation model. However, some of the experimentally observed resonances do not overlap with the simulated data. Most strikingly, the simulation fails to capture the SE resonance branch splitting at intermediate plate dimensions (regions S_1 and S_2): each sample from the splitting region has two separate resonances, instead of a single SE resonance peak. Optical probing data of these resonance modes (Figure 3.3(d)) reveals that the in-plane vibration field of both of the modes has the SE resonance characteristics, while the out-of-plane vibration pattern is somewhat different for the two modes. The origin of the splitting is discussed in the following Section.

Figure 3.2(d) illustrates the quality factors of the resonances. The losses are observed to increase, when approaching the splitting region along the SE resonance branches. At the SE_L and SE_H regions we observe Q ~10 000. Interestingly, the highest quality factors of $Q \sim 20\,000$ are measured at the hE region. Air damping in atmospheric pressure limits the quality factor of all resonances. Figure 3.2(c) indicates that $FOM \sim 5$ is reached for the SE resonance. It is also observed, that at intermediate dimensions also the flexural mode F_1 is relatively strongly coupled, and that at the SE resonance splitting region the performance degrades. All other modes appear to be weakly coupled with $FOM < 1$.

3.2.3 Splitting effect caused by a coupled anchor resonance

Based on the optical characterization of the vibration fields, the observed splitting of the main resonance mode was suspected to be caused by coupling of the main resonance with an in-plane flexural resonance mode of the anchors. A parametric FEM model including the corner anchors reproduced the splitting effect, Fig. 3.4(c). The coupling effect could be explained with a simple analytic model of two coupled spring-masses, Fig. 3.4(a).

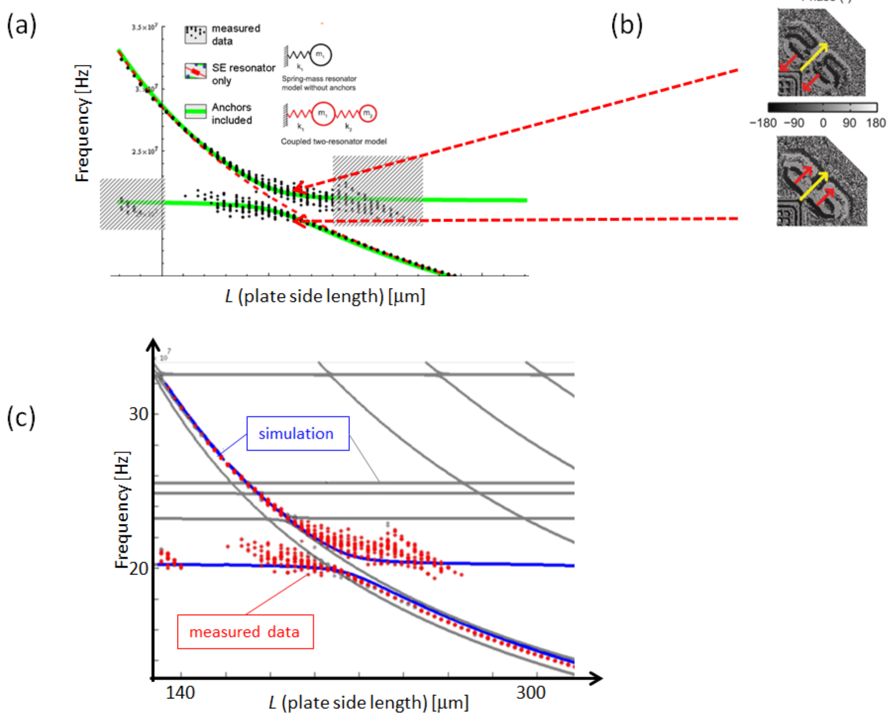

Figure 3.4. (a) A model of two coupled spring-masses (green line) captures the splitting effect seen in the SE mode branch. (b) Phase sensitive imaging covering a corner of the plate and an anchor shows that the relative vibrations of the edge of the resonator plate are in phase/antiphase for the lower/higher frequency resonances at the splitting region, respectively. Optical measurements were done by Department of Applied Physics, Aalto University. (Paper **V**) (c) Modal analysis of a FEM model including the anchors shows the splitting effect.

A spring-mass system with an effective mass m_1 and a spring constant k_1 describes the SE mode of the resonator plate. When another spring-mass system (k_2, m_2), representing all four corner anchors as a single entity, is introduced in the model, this coupled resonator model results in a good fit to the electrically measured resonance frequency data. In the upper branch the two resonators move in antiphase with each other, and the lower branch is the case when the two parts move in unison[2]. Phase-sensitive imaging of the vibration fields confirmed the in-phase/antiphase vibration between the resonator plate and the anchor on the two branches, respectively, as seen in Fig. 3.4(b). Splitting, or anti-crossing behavior of modal frequencies, is a characteristic fingerprint of strongly coupled systems, encountered in various classical and quantum mechanical systems [64].

[2]This is analogous to optical and acoustic branches of lattice vibrations.

3.2.4 Excitation of a subharmonic rotational mode

Measurements of the set of size varied plate resonators revealed an interesting non-linear phenomenon having the potential to degrade the power handling capability (see Section 2.8) of a SE resonator. It was found in electrical measurements under vacuum, that the frequency response of one 257-μm-sized SE resonator turned nonlinear when the drive was higher than U_{drive} ∼140 mV (rms), see Fig. 3.5(a). The effect was not found on all devices of similar size, so it was hypothesized that an unidentified mode coupling mechanism, sensitive to process-variation-induced frequency changes could be causing the effect.

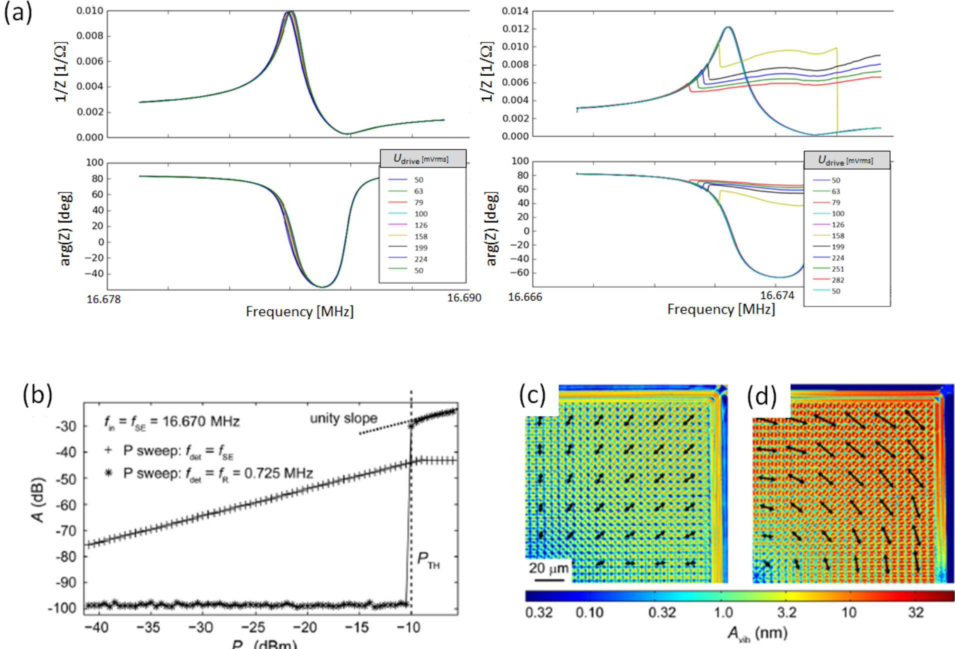

Figure 3.5. (a) Frequency responses of two plate resonators from different parts of the same wafer. One of the devices showed a severe nonlinearity (amplitude compression) after a drive amplitude threshold of $U_{\text{drive}} \sim 140\,\text{mV}_{\text{rms}}$, while the other was seen to have only a minor drive level dependency of frequency. (b) Measured relative in-plane vibration amplitude A at $f_{\text{SE}} = 16.670\,\text{MHz}$ and at $f_R = 0.725\,\text{MHz}$ as a function of the input drive power at frequency $f_{\text{in}} = f_{\text{SE}} = 16.670\,\text{MHz}$.(c) IP vibration amplitude A_{vib} and vector fields of the SE mode and the (d) rotational mode. Optical measurements were done by Department of Applied Physics, Aalto University. (Paper **VI**)

Optical measurements, presented in Paper **VI**, revealed that the nonlinearity was caused by the fact that a rotational in-plane mode was excited at a significantly lower frequency (0.725 MHz) than the SE mode (16.670 MHz), see Figs. 3.5(c), (d). When driving the resonator at 16.670 MHz with increasing drive level, the SE mode vibration amplitude increased until it saturated at a threshold value of ∼ 10 nm, after which all additional excitation energy

was inserted into the rotational mode (Fig. 3.5(b)). The 1:23 frequency ratio between the rotational and the SE modes suggests a subharmonic nonlinear coupling between these two modes. The exact coupling mechanism was not modelled. It is worth noting that the rotational resonance mode was not seen at all in the electrical measurements, so it could not be directly excited at all through the piezoelectric transduction mechanism.

3.2.5 Discussion

Findings such as the splitting of the main resonance branch and the subharmonic nonlinear effect, respectively, illustrate a delicate aspect in resonator design: it is not enough for a good resonator to have a well-designed main resonance mode - other (parasitic) modes have the potential to degrade the resonator performance in many ways. Device dimensions need to be accurately selected to avoid harmful coupling and/or degeneracies of the main resonance mode with other resonances and with its super-/subharmonics.

Anchoring

Undoubtedly the best way to anchor a resonator is at the locations that are nodal points of the resonance mode shape. Understanding of the splitting experiment yielded new understanding for anchoring of resonators. When nodal anchoring is not possible, low-loss anchoring can be achieved with flexible enough anchor bridges. In this type of anchoring, special care needs to be taken in order not to have any of the anchor's resonances close to the frequency of the main resonance. If the frequencies of the main mode and that of an anchor are brought too near to each other, resonator performance can be severely compromised:

- Resonator performance (FOM) as well as the quality factor of the main mode can be decreased.
- The frequency scatter can be increased as the anchor resonance frequency is typically more sensitive to process variations.
- At worst, the main resonance can be split into two weak resonances around the intended resonance frequency.

In general, as flexible as possible an anchor appears at first sight to provide the lowest anchoring losses for a resonator. However, there is an important tradeoff: the more flexible an anchor is, the lower the frequency of the first

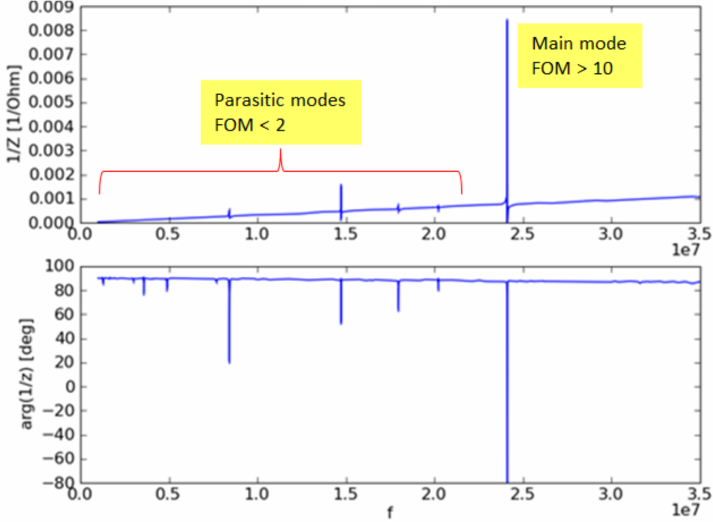

Figure 3.6. Frequency response of a 24-MHz WE mode resonator on a wide frequency range of $f = 0.1 \ldots 35\,\text{MHz}$.

resonance mode of the anchor is, and the more densely its overtones are spaced in the frequency space. It is increasingly hard to avoid degeneracy of an anchor resonance with the main mode, in particular when process variations are taken into account. Anchors also need to be stiff enough to prevent stiction during fabrication and device operation, and to provide high enough tolerance against external shocks.

Subharmonic or superharmonic nonlinear coupling

The nonlinear excitation of the rotational mode through the SE mode showed an adverse effect of frequency degeneracy of the main mode to an unwanted mode at 1/23 frequency of the main mode. Nonlinear coupling to a subharmonic mode is a known phenomenon [65], but also *super*harmonic nonlinear coupling (although not demonstrated in our experiments) can occur to a resonance mode at that occurs at the 2nd or 3rd harmonic frequency of the drive frequency [66, 67]. Figure 3.6 illustrates the response of a 24-MHz WE mode resonator on a wide frequency range, revealing the appearance of some parasitic resonances at frequencies below the main resonance mode. Although FOM of the parasitic resonances is clearly lower than that of the main mode, thus preventing an oscillator from locking into any of the parasitics, subharmonic coupling could potentially cause harmful effects if the relative frequencies match unfavorably. As seen in the context of the rotational mode excited by the SE resonance, a parasitic mode can be fully absent in the electrical frequency response of the device, and still potentially cause unwanted coupling.

It can be concluded that it is wise to design resonators in such a way that the resonator frequency is not an integer multiple of any of the parasitic modes at a lower frequency and that the frequencies of the parasitic modes are not 2nd or 3rd harmonics of the frequency of the main mode[3]. In practice, the challenge in following this design rule is enlarged by two factors: 1) processing variations will cause the frequencies of the main mode and those of the parasitics to be varied and 2) the temperature dependencies of different modes can be very different (See Section 4.4.2 to see how the temperature dependencies can vary), and, as a result, a device performing well at room temperature may experience problems at some other temperature. This is, actually, a well-known problem in quartz devices, known as "activity dips" [68]: modal frequencies (or their harmonics) cross at some point in temperature and the coupling between modes can adversely affect resonator performance. MEMS resonators, having more design freedom due to their different fabrication approach when compared to quartz manufacturing, are often considered to have better possibilities for avoiding such activity dip effects [15].

Looking from another perspective, coupling between resonances could be also be taken advantage of: our experiment revealing the subharmonic nonlinearity demonstrated the possibility of driving a resonance mode that otherwise could not be directly excited with a piezoelectric thin film at all. Superharmonic coupling of modes could potentially be exploited in a same manner. Also coupling of resonances at the same frequency can be employed to tailor resonator properties. A good example of this approach is the resonator design of Ho et al. in [69], where extensional and flexural resonance modes were coupled together to create a compound resonance mode having a better tunability of the resonance frequency than the original extensional mode.

3.3 Oscillator characterization

In this work, resonators were mostly characterized as passive components (frequency sweep based characterization, see Appendix A.1). However, simple oscillators leveraging a standard drive circuit intended for quartz crystals were constructed for demonstrating that the resonators operated in their intended operation mode as desired. Figure 3.7 shows the phase noise of an oscillator consisting of a piezoelectrically driven HD-silicon 24-MHz WE mode MEMS resonator (see Table 3.1) and a Seiko 5016 drive circuit [70]. A noise floor near

[3]This design rule does not fully protect against unwanted nonlinear coupling, since the main mode can couple simultaneously to multiple parasitic modes, see Ref. [65].

-150 dBc/Hz and a near carrier phase noise of almost -128.5 dBc/Hz at 1 kHz offset was measured. Scaling the noise for a 13-MHz carrier according to Eq. (2.41) yields a result of -134 dBc/Hz at 1kHz offset for the near carrier phase noise, which clearly meets the TCXO specification (Table 1.1). The measurement was done under atmospheric pressure, so even better performance is expected in vacuum or reduced pressure.

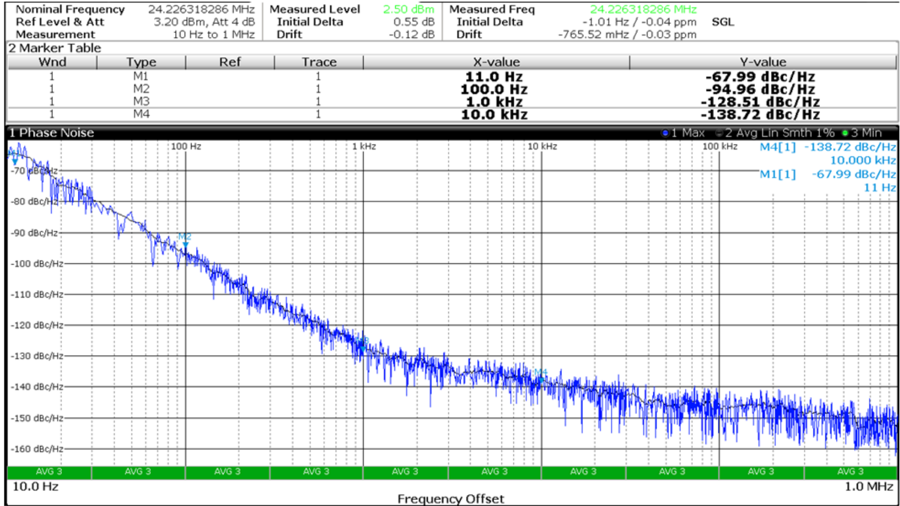

Figure 3.7. Phase noise of an oscillator based on a piezoelectrically actuated HD-Silicon resonator at 24 MHz and a Seiko 5016 driver circuit (intended for quartz crystals). The measurement was done with a Rohde&Schwartz FSW8 signal and spectrum analyzer. (Circuit design and measurements performed by Arto Rantala, VTT)

4. Temperature compensation by degenerate doping of silicon

The content with the main focus of this dissertation is presented in this Chapter. The generic effect of the elastic properties of silicon being influenced by doping was known already in the 1960's [16, 17], but this knowledge had not been applied in the field of MEMS resonators until in recent years. For temperature compensation of MEMS resonators, the effect of doping on the thermal dependencies of the elastic constants becomes of value for very high doping levels above $n \sim 2 \times 10^{19}\text{cm}^{-3}$, which has been unknown territory. First experiments of heavily doped silicon resonators were published by Samarao et al. in 2010 [18], who demonstrated first-order temperature compensation in p-type doped WE mode resonators. The effect was extended to resonators containing alternating p/n doped layers [71]. N-type doped first order temperature compensated resonators were reported by Hajjam et al. in 2010 [72], and piezoelectrically activated first order temperature compensated resonators by Shahmohammadi et al. in 2012 [60]. Similar results to those of Paper **III** were later published by Ng et al. in [73], supporting our findings. Our publications (Papers **I**—**IV**, **VII**) on the topic date to years 2011 - 2015, and their content is discussed in this Chapter.

In the following Sections, first the theoretical background is discussed, and the early experimental results are introduced. Our first experimental findings on this topic are reviewed. The experimental determination of the temperature dependent elastic properties of silicon on a wide doping range is described, and modelling and identification of classes of resonance modes that can be temperature compensated is presented. The qualitative prediction of a possibility of full 2nd-order temperature compensation in silicon MEMS resonators is introduced, and the recently achieved experimental evidence for the validity of the prediction is presented by reviewing our results of ultra-heavily doped silicon resonators with ±10 ppm frequency stability .

4.1 Theoretical background and early experiments

In a many-valley semiconductor such as Si, certain strain components lift the conduction band valley degeneracy, which changes the energy of the free electron system. The elastic constants c_{ij} are strain derivatives of the Gibbs free energy G,

$$c_{ij} = \frac{1}{V_0}\frac{\partial^2 G}{\partial S_i \partial S_j}, \tag{4.1}$$

where V_0 is the volume of the non-deformed crystal, and S_i and S_j are the strain components. Since the Gibbs free energy is affected by the charge carrier concentration, a coupling of the carrier concentration to the elastic constants is formed. For free electrons, Keyes [16] presents an expression for the free energy, from which the electronic contributions to the elastic constants can be derived. In the case of n-type Si these are

$$\begin{aligned} \delta c_{11} &= -\Phi\frac{4}{3}\Xi_u^2 \\ \delta c_{12} &= \Phi\frac{2}{3}\Xi_u^2 \\ \delta c_{44} &= 0, \end{aligned} \tag{4.2}$$

where Ξ_u is the uniaxial deformation potential constant [74], Φ is defined as

$$\Phi = -\int dE N_i(E)\frac{\partial}{\partial E}f_0(E), \tag{4.3}$$

where $N_i(E)$ is the density of states for valley i, and where the temperature dependence arises from the Fermi-Dirac distribution

$$f_0(E) = \left[e^{(E-E_F)/(k_B T)} + 1\right]^{-1}. \tag{4.4}$$

The theory [75] for p-type doped silicon is more involved due to the different nature (holes) of the charge carriers and will not be introduced here.

As for the experimental research on the topic, Hall [17] investigated the acoustic velocities of n-type doped silicon, and found out that the absolute value and the temperature dependency of the shear elastic constant $(c_{11} - c_{12})/2$ was notably affected by doping at a carrier concentration of $n \sim 2 \times 10^{19}\mathrm{cm}^{-3}$. Wang et al. [76] observed temperature compensated behavior in composite ZnO/Si and AlN/Si shear mode resonators, where silicon was p-type doped to a level of $n \sim 10^{20}\mathrm{cm}^{-3}$.

4.2 First Experiments at VTT

Paper **VII** highlights the results of the first set of experiments at VTT with heavily n- and p-type doped silicon resonators. The results are illustrated in

Fig. 4.1. Resonators were fabricated on commercially available SOI wafers with three different types of heavily boron/phosphorus doped silicon device layers from Okmetic oyj. The most heavily boron doped wafer contained also germanium to relieve the stress associated with the very high boron concentrations.

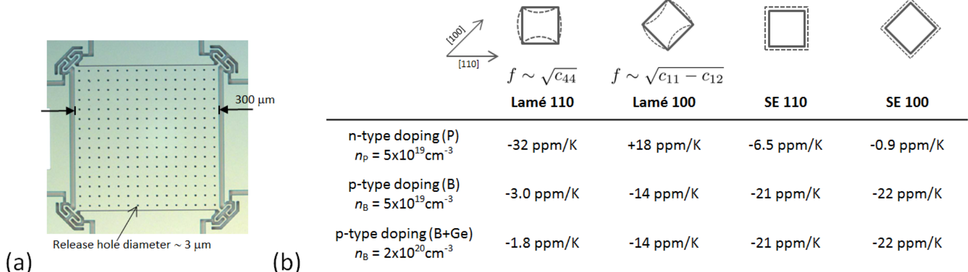

	$f \sim \sqrt{c_{44}}$ Lamé 110	$f \sim \sqrt{c_{11} - c_{12}}$ Lamé 100	SE 110	SE 100
n-type doping (P) $n_P = 5\times10^{19}\,\mathrm{cm}^{-3}$	-32 ppm/K	+18 ppm/K	-6.5 ppm/K	-0.9 ppm/K
p-type doping (B) $n_B = 5\times10^{19}\,\mathrm{cm}^{-3}$	-3.0 ppm/K	-14 ppm/K	-21 ppm/K	-22 ppm/K
p-type doping (B+Ge) $n_B = 2\times10^{20}\,\mathrm{cm}^{-3}$	-1.8 ppm/K	-14 ppm/K	-21 ppm/K	-22 ppm/K

Figure 4.1. (a) A micrograph of a square plate resonator, which can resonate both in the Lamé and SE resonance mode. (b) Measured linear temperature coefficients of frequency for the Lamé and SE resonance modes of resonators fabricated on n/p-type heavily doped wafers in two different orientations (resonator plate side aligned either to [100] or [110] direction). (Paper **VII**)

The devices were electrostatically actuated and fabricated with the 1st variant of the VTT Electrostatic MEMS process (see section 1.4) in order to investigate the characteristics of doped silicon alone, and to keep the fabrication process as simple as possible. As a side effect of this simplicity, however, the resonator plates had to be perforated with a grid of release etch holes. The etch hole grid was assumed to cause a minor perturbation to the c_{ij} dependencies of the resonance modes, which would have been hard to model due to the size of the needed FEM model, and due to the fact that the dimensions of the realized holes were not accurately known. Despite this inaccuracy, the main effects to the temperature characteristics of the resonators, caused by n- or p-type doping were identified:

- The n-type (phosphorus) doped resonators showed remarkable thermal compensation effects. The high overcompensation ($TCF_1 = +18\,\mathrm{ppm/K}$) of the [100]-oriented Lamé mode at n-type doping level of $n = 5 \times 10^{19}\,\mathrm{cm}^{-3}$ indicated that there had to be an intermediate doping level at which TCF_1 for the very same mode crosses zero (knowing that $TCF_1 \sim -30$ ppm/K at very low doping levels). Any shear modes with a similar $c_{11} - c_{12}$ (see Eq. 2.4) dependence on the elastic parameters were expected to behave similarly.

- It was seen that TCF_1 of the c_{44} characterized (see Eq. 2.4) Lamé$_{110}$ resonance mode was practically unaffected by n-type doping with its value

staying at -30ppm/K, which was in line with theory (Eq. 4.2). This observation led to the hypothesis that there had to be such resonance modes for which the dependencies on the elastic constants c_{ij} would be balanced in such a way that TCF_1 would be zero. This notion is studied in detail in Section 4.4. The SE_{100} mode with its temperature coefficient of -0.9 ppm/K turns out to be close to such optimal mode at the tested doping level. The thermal drift of a SE resonator had been reduced from over 3000 ppm over the temperature range of $T = -40 \ldots + 85°C$ to less than 300 ppm.

- In the case of p-type (boron) doped resonators, it was seen that the c_{44} characterized $Lamé_{110}$ mode resonators were affected the most. However, even with the heaviest p-type doping, the linear coefficient stayed negative, and thus the applicability to temperature compensation appeared more limited than with n-type doping.[1]

4.3 Determination of doping dependent elastic parameters

Motivated by the results of our first experiments, a systematic effort was undertaken to find out how the elastic constants of doped silicon behave as a function of doping and temperature. The study is reported in Paper **III**[2]. The objectives were:

- To eliminate the inaccuracy of the first experiments related with the release etch holes.

- To test the effects of as high doping as possible (using commercially available wafers).

- To try to see doping-dependent trends in the behavior of the elastic properties. In particular, sufficiently accurate extraction of the second order temperature coefficients was of interest, since understanding of these effects was the key for approaching quartz-level temperature stability.

[1] Patent families A-C (Appendix D) are related to designs that are amenable to temperature compensation by p-type doping.
[2] Initially published as a conference paper of narrower scope [77]

The error source associated with the release etch holes in the resonator plates was eliminated by fabricating monolithic resonators using the second variation of the VTT electrostatic MEMS process (Section 1.4). With this process choice, the angular alignment of the resonators with respect to the silicon crystal orientation was somewhat degraded, but this could be characterized with dedicated test resonator designs (see Appendix A.3) and taken into account in the analysis.

An n-type doping range up to a carrier concentration of $n = 7.5 \times 10^{19}\text{cm}^{-3}$ was covered by fabricating resonators on five arsenic/phosphorus doped wafers. Results for p-type doped silicon were obtained from two boron doped wafers, up to a concentration of $n = 3 \times 10^{19}\text{cm}^{-3}$. Wafers were grown with the Czochralski method and provided by Okmetic oyj. Specifications for the wafers are given in Appendix B.1, and they are referred to with shorthands B3, B0.6, As1.7, As2.5, P4.3, P4.7 and P7.5, indicative of the dopant element and level, respectively.

4.3.1 Experimental approach

All the fabricated wafers included seven different types of resonator variations, each of which had a different functional dependency on the elastic parameters. The variations consisted of five LE mode resonators and two Lamé mode resonators, each having different in-plane orientation and their main resonance mode around 10 MHz, see Fig. 4.2. Importantly, the air damping of the resonators was low enough ($Q \sim 10\,000$ for all designs) so that the resonance frequencies could be measured under atmospheric pressure with sufficient resolution, see Appendix A.1 for details.

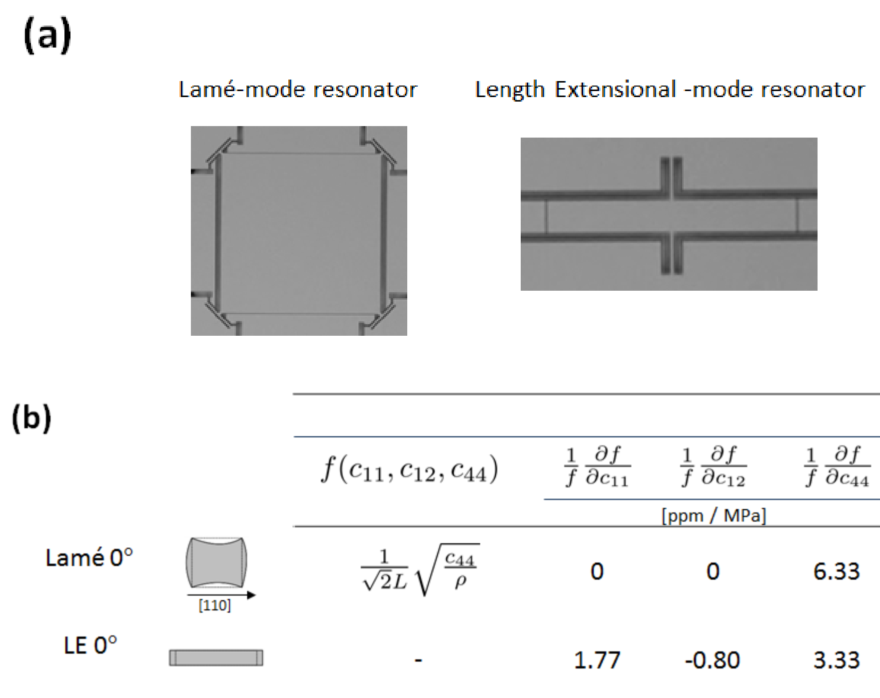

Mode	$f(c_{11}, c_{12}, c_{44})$	$\frac{1}{f}\frac{\partial f}{\partial c_{11}}$ [ppm / MPa]	$\frac{1}{f}\frac{\partial f}{\partial c_{12}}$ [ppm / MPa]	$\frac{1}{f}\frac{\partial f}{\partial c_{44}}$ [ppm / MPa]
Lamé 0° [110]	$\frac{1}{\sqrt{2}L}\sqrt{\frac{c_{44}}{\rho}}$	0	0	6.33
LE 0°	-	1.77	-0.80	3.33
LE 11.25°	-	2.30	-1.37	2.72
LE 22.5°	-	3.37	-2.53	1.46
LE 33.75°	-	4.27	-3.50	0.40
LE 45° [100]	-	4.61	-3.87	0
Lamé 45°	$\frac{1}{\sqrt{2}L}\sqrt{\frac{(c_{11}-c_{12})/2}{\rho}}$	5.10	-5.10	0

Figure 4.2. Determination of the elastic constants c_{11}, c_{12} and c_{44} was based on seven resonance modes, whose frequencies have different dependencies on the c_{ij} parameters. Alignment of the resonators was varied from [110] to [100]. The table contains the analytical formulas for the resonance frequency $f(c_{11}, c_{12}, c_{44})$ – which exist only for the two Lamé modes – and the sensitivities $1/f \times \partial f/\partial c_{ij}$ for each mode. These exemplary sensitivities have been calculated at a linearization point of $(c_{11}, c_{12}, c_{44}) = (163, 65, 79)$ GPa using the finite element approach outlined in Section A.2 (zero angular alignment error and device layer thickness of 15 μm has been assumed). The listed numbers only illustrate the character of the variation of the sensitivities within the set of modes. For individual wafers, the sensitivities differ due to different linearization points, device layer thicknesses and angular misalignments, respectively, and these effects were taken into account in the analysis. (Paper III)

By measuring the frequency-vs-temperature curves of the resonators, the three unknown elastic parameters could be determined from the seven measured data points at each temperature using a least squares fit. Details of the method are described in Appendix A.2.

4.3.2 Extracted elastic parameters

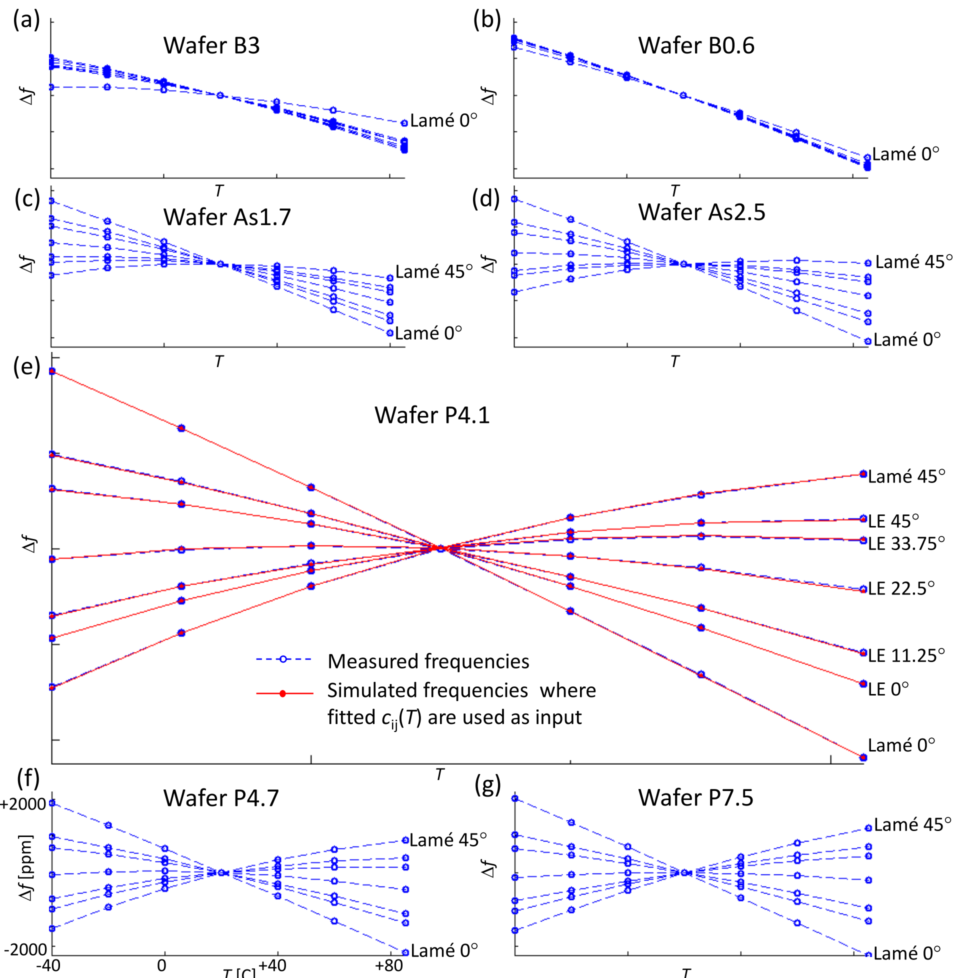

Figure 4.3. (a)–(g): Measured f vs. T data of all resonance modes on all wafers is shown with blue open circles. Dashed blue lines are second order polynomial fits to the data; fit coefficients are collected in Table B.2. All plots have a similar scaling of axes. (e): Experimental data from wafer P4.1 have been overlaid with corresponding numerical estimates $f_k^{\mathrm{th}}(T)$ which use the fitted parameters $c_{ij}(T)$ as an input (red lines with dots). (Paper **III**)

The measured frequency vs. temperature curves are shown for all modes on all wafers in Fig. 4.3, and the related temperature coefficients of frequency are collected in Table B.2.On the weakest doped wafer B0.6, all f vs. T curves lie almost on top of each other, and the linear temperature coefficients are near -30 ppm/K. On wafer B3, the slopes of the curves are decreased in magnitude, and the biggest change is observed for the Lamé-0° mode. On the n-type doped wafers larger effects are observed. The slope of the f vs. T curve of the Lamé-45° mode is gradually increased with increasing doping, and above 2×10^{19} cm^{-3} the slopes are positive. Lamé-0° mode is almost unaffected by doping, and the f vs. T curves of the LE modes span the region between the two Lamé modes. The elastic parameters $c_{ij}(T)$ were extracted from the

measured frequency data. Results are shown in Fig. 4.4. The magnitude of the elastic constants is observed to decrease upon increased doping, except for the c_{12} elastic constant which gets larger with increasing n-type doping. For closer investigation of the thermal dependency of the $c_{ij}(T)$ curves, second-order polynomials centered at $T_0 = 25°C$ were fitted to the elastic parameter data as

$$c_{ij}(T) = c_{ij}^0[1 + a_{ij}(T - T_0) + b_{ij}(T - T_0)^2], \tag{4.5}$$

where a_{ij} and b_{ij} are the first-order and second-order temperature coefficients, respectively, and c_{ij}^0 is the constant term. A second-order expansion of $c_{ij}(T)$ was found to be valid to within ± 20 ppm for all $c_{ij}(T, n)$. The results are collected in Figs. 4.5(a)–(l) and in Table B.3. One should note that, in Fig. 4.5, we have chosen to accommodate data points from both n- and p-type doped wafers within same axes by representing p/n type doping with negative/positive carrier concentrations. A detailed error analysis is provided in Paper **III**.

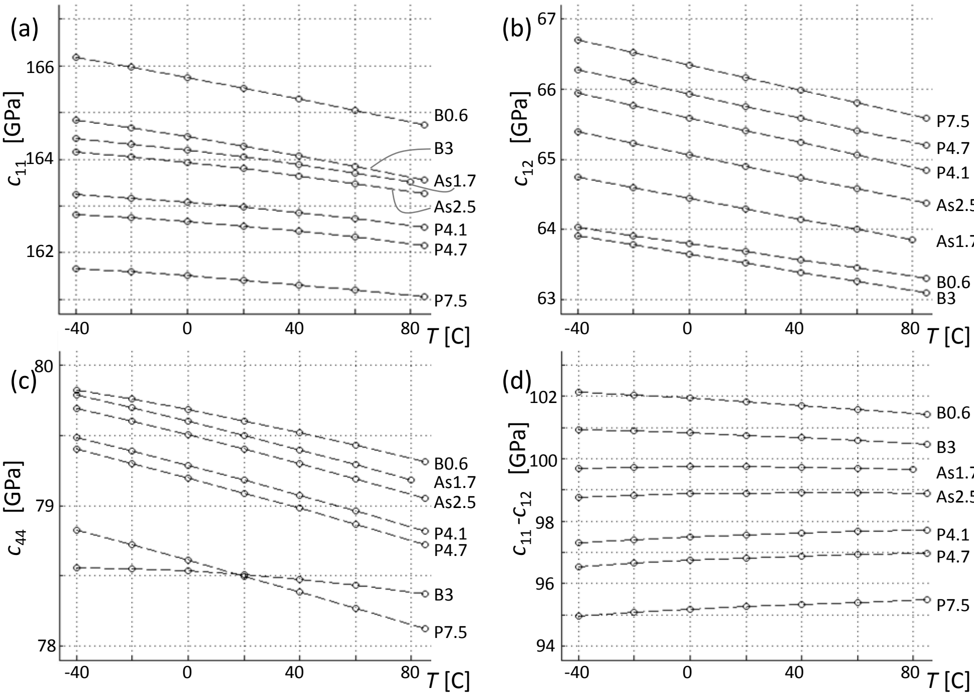

Figure 4.4. Elastic parameters c_{11}, c_{12}, c_{44}, and $c_{11} - c_{12}$ as a function of temperature and doping. The legends denote the dopant elements and the doping level, see Table B.1. Dashed lines are second-order fits to the c_{ij} vs. T data, and the fit coefficients are displayed in Fig. 4.5 and in Table B.3. (Paper **III**)

4.3.3 Discussion

Extracted temperature coefficients of the elastic constants correspond rather well to the previously published results at low dopant levels [78, 17]. Overall,

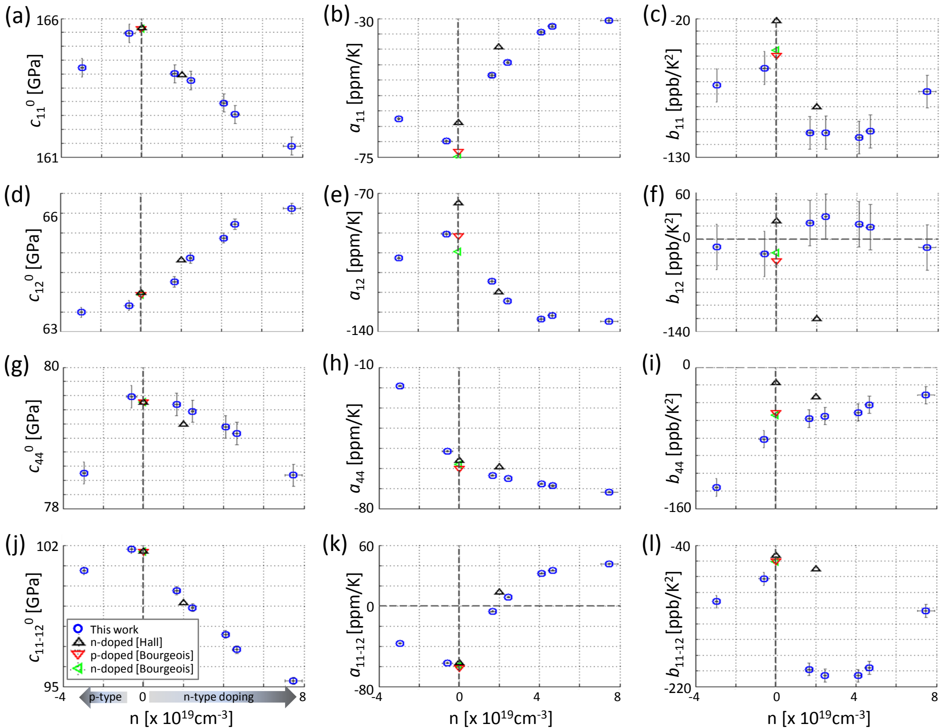

Figure 4.5. Temperature coefficients of the elastic parameters c_{ij} as a function of carrier concentration n. Data from p-type doped wafers are represented with negative carrier concentrations. The first, second and third columns represent the constant terms c^0_{ij}, linear coefficients (a_{ij}), and second-order coefficients (b_{ij}) at $T = 25°C$, respectively, see (4.5). c^0_{11-12}, a_{11-12} and b_{11-12} are shorthands for the coefficients of $c_{11} - c_{12}$. Open blue circles are the experimentally determined values of this work. Numerical values are given in Table B.3. Values reported Bourgeois in [78] are shown as red triangles pointing down (weak p-type doping) and as green triangles pointing left (weak n-type doping). Data reported by Hall in Ref. [17] was used for calculating data points shown as black triangles pointing up. Horizontal error bars indicate the carrier concentration ranges calculated from the resistivity specification for each wafer (see Table B.1). Vertical error bars are based on the error analysis presented in Paper **III**. (Paper **III**)

the data points in Fig. 4.5 show clearly detectable trends. In general, it is seen that arsenic (data points with $0 < n < 4 \times 10^{19}\,\text{cm}^{-3}$) and phosphorus ($n > 4 \times 10^{19}\,\text{cm}^{-3}$) as dopants do not stand out from the plots as separate groups, which supports the view of the effects being of mainly electronic origin[16]. The magnitudes of the elastic parameters, i.e., the constant terms c^0_{ij}, are affected to within a few percent by increased doping over the tested wafers with a decreasing trend for parameters c_{11}, c_{44} and $c_{11} - c_{12}$.

The effects on the elastic properties of silicon from n-type doping are best observed in the shear elastic constant $c_{11}-c_{12}$ and, in particular, in its temperature coefficients a_{11-12} and b_{11-12}. Figure 4.5(k) shows that the linear temperature coefficient a_{11-12} crosses zero at approximately $n = 2 \times 10^{19}$ cm^{-3}. When doping is further increased, a_{11-12} reaches a level of over $+40\,\text{ppm/K}$. The effect appears to saturate with increasing doping. Figure 4.5(l) shows that

the second order coefficient b_{11-12} is negative for all studied doping levels, with a maximum deviation from zero of approximately $-200\,\mathrm{ppb/K^2}$. This would translate to a 250 ppm frequency deviation over a range of 100°C[3]. Importantly, one finds that the second order coefficient b_{11-12} appears to approach zero when the n-type doping level is above $n = 4.1 \times 10^{19}$ cm^{-3}. This suggests a possibility of a flat or positive second order response at high enough doping, strongly motivating further investigation of n-type doping beyond $10^{20}\,\mathrm{cm^{-3}}$, see Sections 4.5 and 4.7.

The main effect to temperature compensation with p-type doping is observable in Fig. 4.5(h). The linear temperature coefficient a_{44} approaches zero with increasing p-type dopant concentration. However, zero level is not crossed even with the highest doping level of 3×10^{19} cm^{-3}. The second-order coefficient b_{44} is seen to grow in magnitude with increased p-type doping[4]. N-type doping is observed to have a relatively small effect on coefficients a_{44} and b_{44}. Ideally, according to Keyes' theory, there should be no effect at all, see Eq. (4.2).

It was estimated that using the extracted elastic parameters, one can simulate the frequency of an arbitrary resonance mode, fabricated on a wafer with similar carrier concentration as in our experiments, with following accuracies:

- The absolute frequency of a resonator can be predicted with $\pm1000\,\mathrm{ppm}$ accuracy.

- The $f-\mathrm{vs}-T$ curve can be predicted with $\pm25\,\mathrm{ppm}$ accuracy over a temperature range of $T = -40\ldots+85$°C

[3] For a resonance mode whose frequency is purely dependent on $c_{11} - c_{12}$.

[4] Later work by Ng et al. [73] included p-type doped wafers with doping level exceeding $10^{20}\,\mathrm{cm^{-3}}$, where $a_{44} \sim +2\,\mathrm{ppm/K}$ was observed. The second-order coefficient b_{44} remained clearly negative still at this (high) concentration level.

4.4 Temperature compensated resonance modes

4.4.1 Simulations

Finite element modelling of parametrically varied beam and plate resonator geometries was used to identify classes of resonance modes that can be temperature compensated by n-type doping. This study is presented in Paper **I** (a less detailed treatment was published at an earlier point as a conference paper [79]). Linear sensitivities $\partial f/\partial c_{ij}$ of the resonance frequencies to the elastic parameters were calculated through eigenfrequency analyses, and the first and second order temperature coefficients TCF_1 and TCF_2were calculated using Eqs. (2.13) and (2.14), respectively, based on the extracted elastic parameters of Section 4.3 (interpolation data are presented in Appendix B.4). Details of simulations are given in Appendix A.4. Two types of parametric sweeps for geometry variation were performed to reveal modes amenable to temperature compensation. The starting point for the parametric variations was a beam resonator having dimensions of $W \times L \times H = 40 \times 320 \times 10\,\mu\text{m}^3$ on a <100> oriented silicon wafer with its length aligned along the [100] direction (see Fig. 4.6(a)). In simulation S1, the in-plane rotation angle θ of the beam was varied from 0° to 45° so that the beam alignment changed from [100] to [110] (Fig. 4.6(b)). In simulation S2 (Fig. 4.6(c)), the beam width W was increased from $40\,\mu$m to $640\,\mu$m so that the aspect ratio W/L changed from ~ 0.1 to 2. No boundary conditions were applied to the model in order to allow for an unrestricted appearance of resonance modes in the modal analysis.

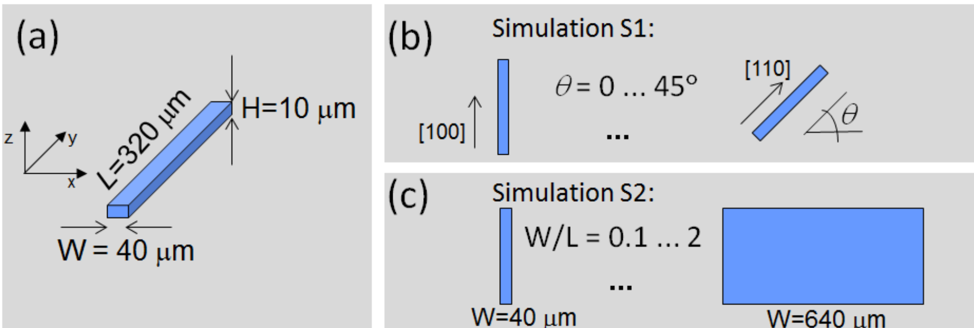

Figure 4.6. Parametrically varied resonator geometry used for finite element modelling. (a) Basic geometry used as a starting point of the simulations. (b) In simulation S1, the orientation of the beam was varied from [100] to [110]. (c) The in-plane aspect ratio was varied from ~0.1 to 2 in simulation S2. (Paper **I**)

4.4.2 Classes of temperature compensated modes

The analysis first concentrated on identifying the resonance modes that have a potential for (at least) first order temperature compensation. This was achieved by evaluating TCF_1 for all resonance modes that were obtained from simulations S1 and S2. Evaluation of TCF_1 was done at $n = 7.5 \times 10^{19}\text{cm}^{-3}$, where the elastic parameters are changed the most from their values at low doping levels. Resonance modes with $TCF_1 \geq 0$ were searched for, since they can be temperature compensated to first order by decreasing the doping level to a level at which TCF_1 reaches zero.

Figure 4.7(a) shows the dispersion of the modal frequencies as a function of the parametric variations. Results of simulations S1 and S2 are combined in the same plot. The linear temperature coefficient TCF_1, calculated at the doping level of $n = 7.5 \times 10^{19}\text{cm}^{-3}$, is illustrated with color coding for each resonance mode. The coefficient TCF_1 of selected resonance mode branches are plotted in detail in Fig. 4.7(b), and representative mode shapes from important branches are shown in Fig. 4.7(c).

The following modal families fulfilling the criterion $TCF_1 \geq 0$ can be identified in the dispersion plot[5]. The branch labels in parentheses correspond to those in Fig. 4.7, and the subscript indices stand for overtones of the modal branches.

- Out-of-plane flexural modes ($OPF_1 \dots OPF_5$): At $\theta = 0$, $W/L \sim 0.1$ these modes have their TCF_1 in the range of +8 ppm/K...+14 ppm/K (decreasing with increasing overtone order). Within the OPF_1 branch, TCF_1 is observed to peak at +20 ppm/K near $W/L = 1$, where the mode shape has evolved into a saddle mode.

- In-plane flexural modes ($IPF_1 \dots IPF_2$): The behavior of these modes in terms of TCF_1 is largely similar to the OPF modes.

[5] Patent application family D (Appendix D) covers embodiments of these resonance modes.

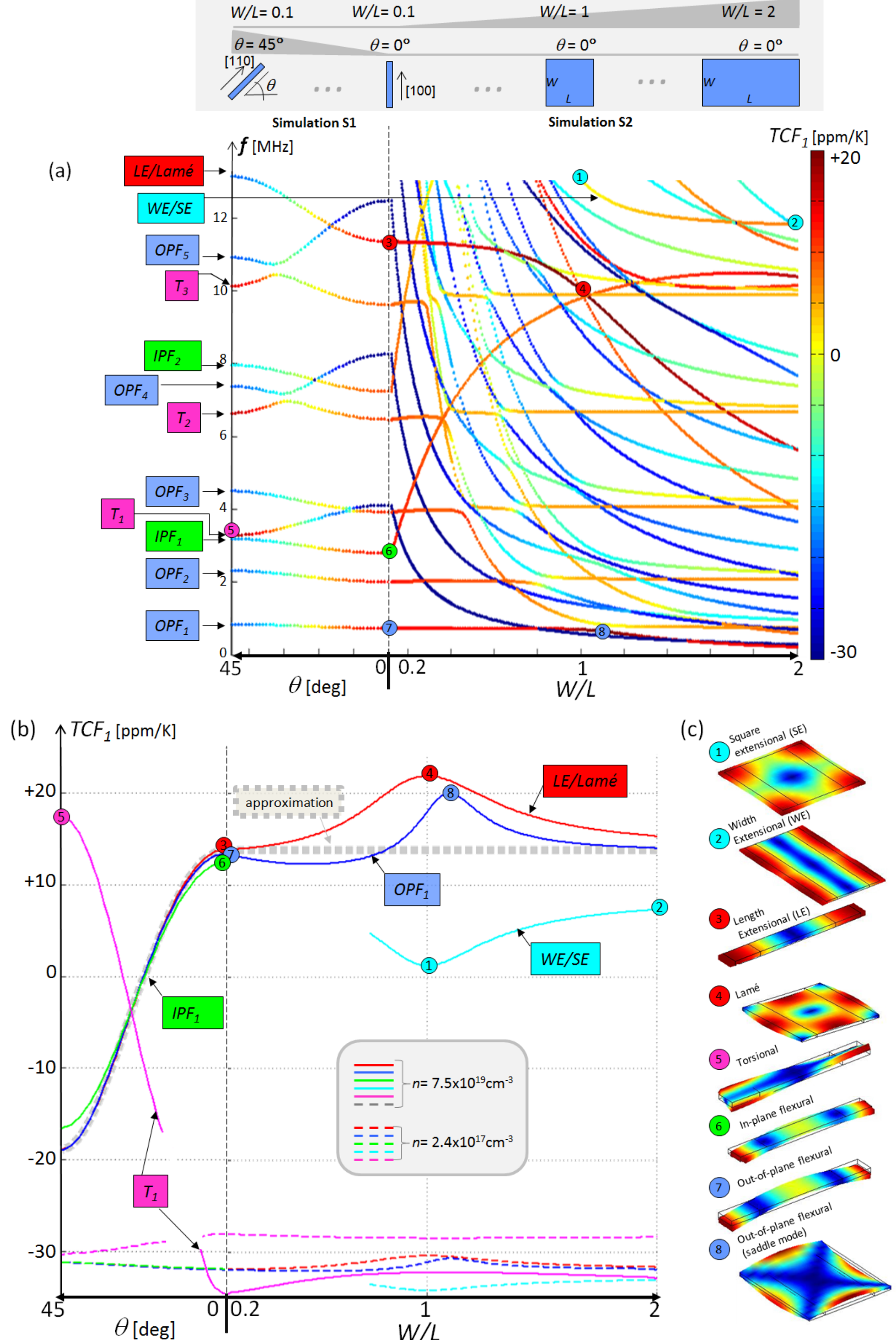

Figure 4.7. (a) Resonance frequencies and their linear temperature coefficients TCF_1 (color coding) as a function of the resonator orientation θ (Simulation S1) and in-plane aspect ratio W/L (Simulation S2). The top illustrations show how the geometry is modified in the parametric simulations S1 and S2, respectively. Dopant concentration of $7.5\times10^{19}\text{cm}^{-3}$ has been assumed for evaluating TCF_1. Modes with $TCF_1 \geq 0$ (from yellow to red) are the desired ones, since their TCF_1 can be set to zero by lowering the doping. Following modal branches and their overtones (denoted by subscripts) are identified in the plot: out-of-plane flexural modes (OPF), in-plane flexural modes (IPF), torsional modes (T), width extensional / square extensional modes (WE/SE), and length extensional / Lamé modes. ($LE/Lamé$). (b) TCF_1 for selected branches plotted in detail. Solid lines show TCF_1 evaluated at a doping level of $n = 7.5\times10^{19}\text{cm}^{-3}$, while their dashed counterparts denote the corresponding TCF_1 evaluated at $n = 2.4 \times 10^{17}\text{cm}^{-3}$. The grey dashed line represents the TCF_1 based on the approximation discussed in the context of Eq. (2.5). (c) Illustrations of the mode shapes of selected modes from the modal branches. Labels 1-8 correspond to those found in plots (a) and (b). (Paper **I**)

- Torsional modes ($T_1 \dots T_3$): These modes have a clearly positive TCF_1 with a maximum value of +18 ppm/K, which is attained when the resonator beam is aligned with the [110] direction. TCF_1 slightly decreases with increasing overtone order. Branch T_1 is coupled to OPF_3, resulting in branch splitting near $\theta = 10°$. Therefore, the T_1 curve in plot 4.7(b) is missing at the splitting region. Similar coupling occurs between T_2/OPF_4 and T_3/OPF_5 branches, respectively.

- Width-Extensional / Square Extensional mode resonance branch (WE/SE): the mode shape evolves from an x-directed WE mode at low in-plane aspect ratios W/L (not shown in the dispersion plot due to the high modal frequency) to an SE mode of a square plate ($W = L$), and then again to a y-directed WE mode at $W/L > 1$. The WE modes approach a TCF_1 value of approximately +8 ppm/K, while TCF_1 of the SE mode is close to zero.

- Length-extensional / Lamé mode resonance branch ($LE/Lamé$): This branch has a clearly positive TCF_1 for all aspect ratios and for θ deviating from zero by less than approximately 20°. The mode shape evolves from a y-directed length extensional (LE) mode into the Lamé (or wineglass) mode of a square resonator ($W/L = 1$), and then further to an x-directed LE mode as the resonator's in-plane aspect ratio is further increased. For [100] alignment, maximal TCF_1 of slightly more than +20 ppm/K occurs with the pure Lamé mode, while TCF_1 of the length extensional modes approaches +14 ppm/K when the resonator geometry becomes more beam-like.

4.4.3 Detailed temperature behavior

The $LE/Lamé$, T_1 and WE/SE branches were investigated in more detail. First, results from simulation S1 were used to find optimal configurations, which minimize the total frequency deviation Δf_{total} (Eq. (2.8)) on the $LE/Lamé$ and T_1 branches, when the resonator orientation θ and doping n are varied (simulation S1). Then, optimal combinations of the in-plane aspect ratio W/L and doping n were searched from the WE/SE and $LE/Lamé$ branches using data from simulation S2.

Figure 4.8 shows the results for the $LE/Lamé$ and torsional T_1 branches, respectively, when θ is varied. It was found in Figs. 4.8(a),(e) that the lowest carrier concentration that yields $TCF_1 = 0$ within the $LE/Lamé$ branch is $n_{0,\text{LE}} \sim 2.4 \times 10^{19}\text{cm}^{-3}$, while the corresponding limit for the T_1 branch is

slightly smaller, $n_{0,\mathrm{T}_1} \sim 2.1 \times 10^{19}\mathrm{cm}^{-3}$. Above these carrier concentration limits, there always exists an angle at which $TCF_1 \approx 0$ can be obtained. The second order coefficient TCF_2 (Figs. 4.8(b),(f)) is most negative between $n \sim 2 \ldots 4 \times 10^{19}\mathrm{cm}^{-3}$ for both modal branches, and its magnitude is decreased towards low and high doping concentrations. The total frequency deviation $\Delta f_{\mathrm{total}}$ is dominated by the non-zero linear coefficient TCF_1 below the limits $n_{0,\mathrm{LE}}$ or n_{0,T_1}, respectively. At higher doping levels, travelling along the "valleys" of Figs. 4.8(c),(g), it is found that the total frequency variation deviation $\Delta f_{\mathrm{total}}$ steadily decreases on both branches to ~150 ppm, reached at the maximal doping level of $n_{max} = 7.5 \times 10^{19}\mathrm{cm}^{-3}$. Optimal orientations at this doping level are $\theta \sim 23°$ and $\theta \sim 28°$ degrees for the *LE/Lamé* and T_1 branches, respectively. The paths for minimum total frequency variation coincide with the $TCF_1 = 0$ curves. As discussed in the previous section, the behavior of the IPF_1 and OPF_1 branches is very similar to the *LE/Lamé* branch characteristics when θ is varied. Therefore, one can expect the results of Fig. 4.8(a)-(d) to describe the behavior of these modes as well.

Figure 4.9 illustrates TCF_1, TCF_2 and $\Delta f_{\mathrm{total}}$ for the *LE/Lamé* and WE/SE branches, respectively, when the aspect ratio W/L is varied. The value $TCF_1 = 0$ is reached at first at the doping level of $n_{0,Lamé} \sim 1.9 \times 10^{19}\mathrm{cm}^{-3}$ for the *LE/Lamé* branch, and on the WE/SE branch the corresponding limit is $n_{0,WE} \sim 3.1 \times 10^{19}\mathrm{cm}^{-3}$. The second order coefficient TCF_2 stays below zero for all n and W/L, and its magnitude is again most negative for $n \sim 2 \ldots 4 \times 10^{19}\mathrm{cm}^{-3}$. Since the zero-$TCF_1$ region for the *LE/Lamé* branch is limited to the doping range of $n \sim 1.9 \ldots 2.3 \times 10^{19}\mathrm{cm}^{-3}$(which coincides with the most negative region for TCF_2), the minimum total frequency deviation remains at a comparatively high level of ~380 ppm. For the WE/SE branch, the region with $TCF_1 = 0$ is found at a doping range of $n \sim 3.1 \ldots 5.1 \times 10^{19}\mathrm{cm}^{-3}$, and a minimum total frequency deviation of ~250 ppm is reached with a square geometry ($W/L = 1$) at the upper limit of this doping range.

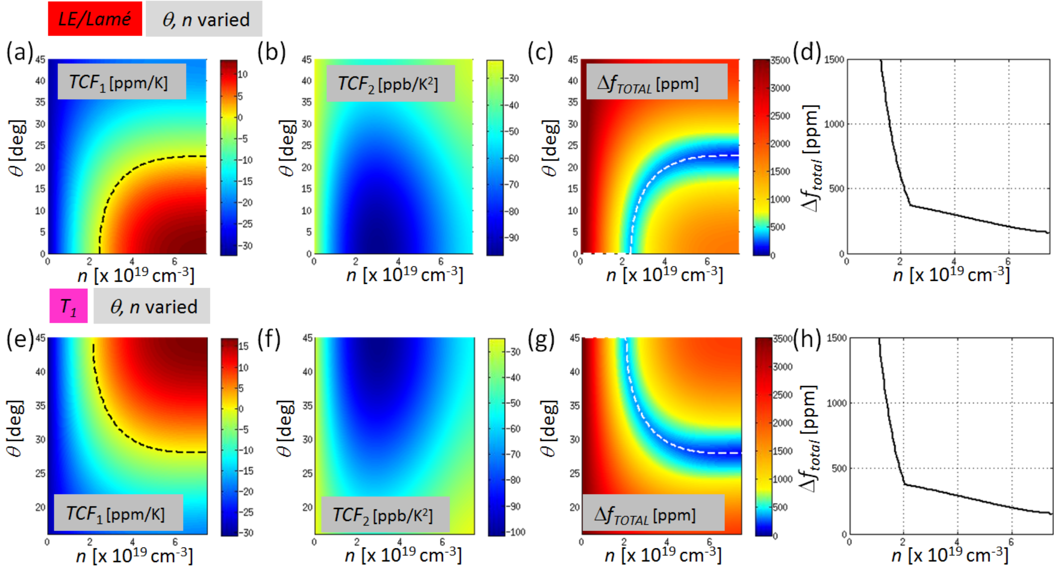

Figure 4.8. Details of temperature dependent behavior of the *LE/Lamé* branch (top row) and the T_1 branch (bottom row) as a function of doping level n and resonator orientation θ. The angles $\theta = 0°/45°$ correspond to alignment with [100]/[110]. Color coding of (a)/(e) and (b)/(f) illustrate the first and second order temperature coefficients of frequency. The dashed lines of (a)/(e) denote the locus of points (n, θ) for which TCF_1 equals zero. The total frequency variation Δf_{total} over the full temperature range of $T = -40 \ldots +85°\text{C}$ is shown in (c)/(g). The dashed lines of (c)/(g) denote the in-plane rotation angle θ, which minimizes Δf_{total} for each n. Figures (d)/(h) are plots of Δf_{total} along this line. Note that orientations of θ below 16° have been omitted for the T_1 branch due to coupling with the OPF_3 branch (see discussion in Section 4.4.2). (Paper **I**)

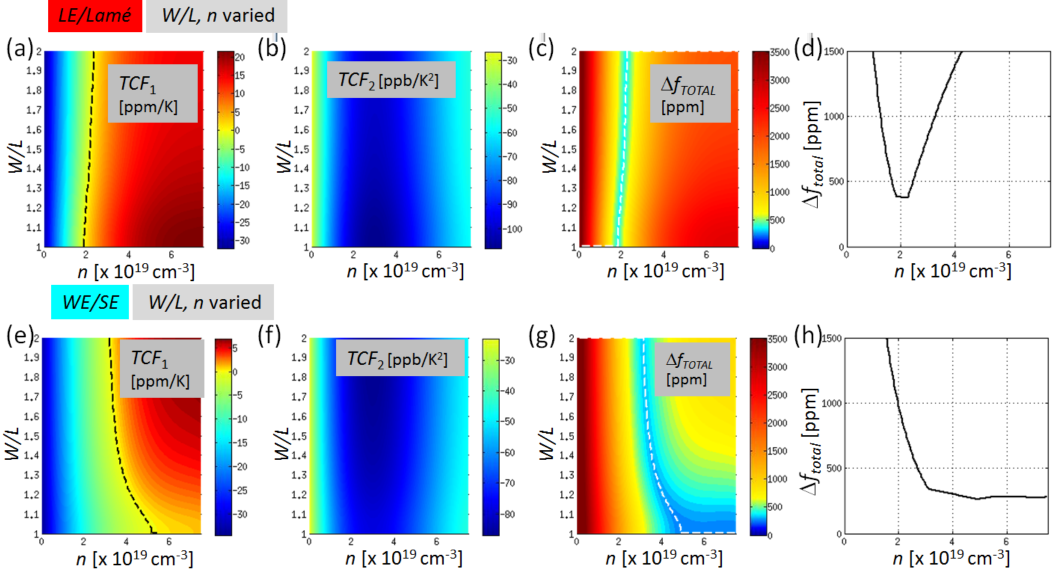

Figure 4.9. Details of temperature behavior within the *LE/Lamé* branch (top row) and the WE/SE branch (bottom row) as a function of doping level n and the resonator's in-plane aspect ratio W/L. The plots are similar to that of Fig. 4.8 with the exception that here the ordinate θ has been replaced by W/L. (Paper **I**)

4.4.4 Discussion

It was seen in Section 4.3 that the shear term $c_{11} - c_{12}$ was most affected by n-type doping, and that it could be overcompensated with a good margin. The simulation results of Fig. 4.7 show that many modes have this shear character. Most intuitive of these modes are the torsional modes of a beam resonator. Also the Lamé mode of a square plate resonator is a pure shear mode, as was discussed in Section (2.1), since the following relationship holds for the [100] aligned geometry,

$$f_{\text{Lamé}} \sim \sqrt{c_{11} - c_{12}}. \tag{4.6}$$

Figure 4.7 provides insight into as why also the length extensional mode has a dominant shear mode character: it belongs to the same branch as the Lamé mode, and much of the shear character is preserved even when the geometry of the resonator is deviated from the shape of a square. Using the approximation of Eq. (2.5) to evaluate the resonance frequency of an LE mode resonator, and linearizing it with respect to the changes in the elastic parameters δc_{ij}, one finds the relationship

$$\delta f_{LE} \sim (\delta c_{11} - \delta c_{12}) + 0.2\delta c_{12}. \tag{4.7}$$

It is apparent that the functional dependence of the LE mode on the c_{ij} parameters is to a large part similar to that of the Lamé mode - except for the added term $0.2\delta c_{12}$. The same reasoning applies also to the IPF and OPF flexural modes, as the approximation based on Eq. (2.5) applies for these modes as well.

The WE/SE branch is of special practical interest due to the fact that the WE and SE bulk mode silicon resonators have shown good performance in terms of phase noise as well as good electromechanical coupling, as seen in Section 3.3 and Table 3.1. These modes, with their TCF_1 in the range 0...+ 8 ppm/K, can still benefit from n-doping for temperature stabilization, although the WE/SE bulk modes have clearly less shear-mode character than the LE/Lamé modes. The lessons of Section 3.2.5 may become of value when resonators with optimal temperature compensated behavior are designed. It may occur that a design with the best frequency stability does not have any nodal points at its perimeter, and flexible non-nodal anchoring has to be used.

In addition to the five highlighted modal families, one can pinpoint other branches in Fig. 4.7(a) that fulfil the $TCF_1 \geq 0$ criterion. Typically these are overtone modes of the five identified modal families or coupled modes having combined characteristics.

Temperature compensated behavior of the presented modal branches can be found also in resonators fabricated on <110> oriented wafers. The presented parametric geometry sweeps on a <100> oriented silicon wafer were chosen, since they portrayed the temperature compensated behavior of all five modal families. A calculation similar to simulation S2 was presented in [79], but with geometry aligned with the [110] direction. There it was observed that neither the *LE*/*Lamé* branch nor the WE/SE branch could be temperature compensated by n-type doping when using this alignment. Interestingly, the elastic properties are isotropic in the plane of <111> oriented silicon wafers [80], and thus temperature compensated behavior similar to that discussed above cannot be found.

4.5 Possibility of 2nd order temperature compensation

It was seen in Section 4.4.3 that the total frequency deviation Δf_{total} can be minimized down to a level of $\sim 150\,\text{ppm}$ for certain modal branches. The decreasing nature of the total frequency deviation Δf_{total} of Figs. 4.8(d),(h) raises the question of whether this trend would continue at even increased doping. Most of the contribution to the remaining (non-zero) second order coefficient TCF_2 comes from the second order temperature coefficient b_{11-12}, which has a decreasing magnitude for $n > 4 \times 10^{19}\text{cm}^{-3}$ (see Fig. B.1(f)). To illustrate the possible existence of a resonance mode with full second order temperature compensation, $b_{11-12}(n)$ was assumed to grow linearly so that it crosses zero at $n \sim 11 \times 10^{19}\text{cm}^{-3}$, Fig. 4.10(f). To simplify the treatment, all other temperature constants c^0_{ij}, a^0_{ij} and b^0_{ij} of Fig. B.1 were assumed to remain unchanged from their values at $n = 7.5 \times 10^{19}\text{cm}^{-3}$. Using these assumptions, calculations for the *LE*/*Lamé* mode branch (Fig. 4.8(a)-(d)) for $\theta = 0° \ldots 45°$ were repeated, now extending the doping level to $n = 13 \times 10^{19}\text{cm}^{-3}$. The results are shown in Figs. 4.10(a)-(e).

It was found in Fig. 4.10(b) that TCF_2 approaches zero with increasing doping, and finally reaches it at $n \sim 11.3 \times 10^{19}\text{cm}^{-3}$. Figure 4.8(e) shows that the curves for $TCF_1 = 0$ and $TCF_2 = 0$ intersect each other at $\theta = 22.5°$ when the doping level is $n \sim 12 \times 10^{19}\text{cm}^{-3}$. At this point the total frequency deviation Δf_{total} reaches zero, as seen in Fig. 4.8(d).

Again, due to the similarity of the IPF, OPF and *LE*/*Lamé* branches (with θ variation), the qualitative result obtained here can be expected to apply among all of these branches. Analogously, there is a possibility of a similar optimum (with regard to the in-plane aspect ratio W/L) on the WE/SE

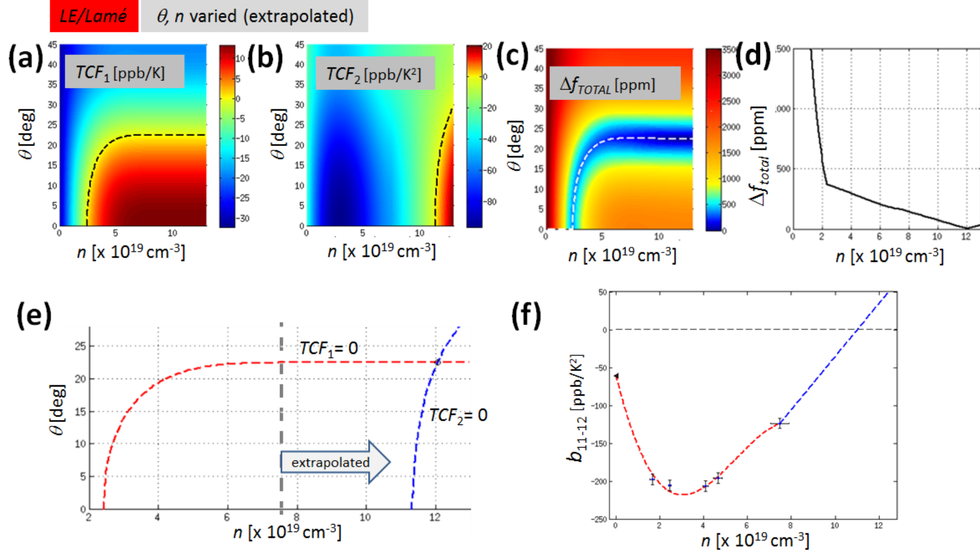

Figure 4.10. Extrapolated temperature behavior of the *LE/Lamé* branch, when orientation θ and doping n are varied. (a)-(d) are similar to Fig.4.8(a)-(d). (e) reproduces $TCF_1 = 0$ and $TCF_2 = 0$ curves from plots (a) and (b) and highlights their crossing. (f) Used extrapolation (blue dashed line) for $b_{11-12}(n)$ for calculation of the result. (Paper **I**)

branch[6].

4.6 Long term stability and quality factors of heavily doped Si

The long-term stability of a resonator is of high importance for its applicability as a frequency reference. It was a justified concern, whether heavy doping of silicon with phosphorus atoms might degrade the stability of silicon. It also had to be verified if the low level of dissipations in silicon (see Section 2.7) would be preserved with high doping levels. These aspects had the potential to act as show stoppers for the whole concept of doping based temperature compensation in Si MEMS.

Results presented in Paper **IV** remove the concerns. For HD-silicon, a long term stability of better than ~ 1 ppm/year was demonstrated (Fig. 4.11), and the intrinsic material losses were shown to stay at a very low level, maintaining the resonator $Q \times f$ product at the 10^{13} level (Fig. 4.12).

[6] Patent family E (Appendix D) relates to second-order temperature compensated resonators.

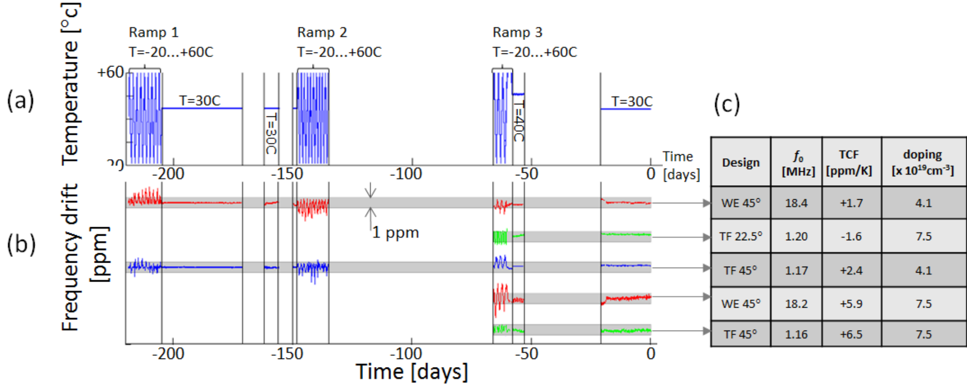

Design	f_0 [MHz]	TCF [ppm/K]	doping [x 10^{19}cm^{-3}]
WE 45°	18.4	+1.7	4.1
TF 22.5°	1.20	-1.6	7.5
TF 45°	1.17	+2.4	4.1
WE 45°	18.2	+5.9	7.5
TF 45°	1.16	+6.5	7.5

Figure 4.11. (a) Temperature of the climate chamber during the stability measurement. The profile consisted of repeated temperature ramps on a range of $T = -20 \ldots + 60°\text{C}$ and sections where the temperature was held constant at $T = +30/+40°\text{C}$. Samples were removed from the climate chamber for periods with no data (for example $t = -130 \ldots - 70$ days). (b) Frequency drift of the resonators. The greyed out regions represent 1-ppm corridors. Rows of data have been ordered according to the magnitude of the TCF of the resonators. (c) Design type, resonance frequency, TCF and doping level of the resonators. (Paper **IV**)

4.7 Experimental verification of 2nd order temperature compensation: ± 10 ppm Si resonators

After the prediction presented in Section 4.5, there was a strong incentive to search for full second order temperature compensated behavior of a resonator, by doping silicon ultra-heavily to (n-type) carrier concentration levels above $n \sim 10^{20}\text{cm}^{-3}$. In commercially available (Czochralski grown) silicon wafers, the attainable doping level was practically limited to $n \sim 7.5 \times 10^{19}\text{cm}^{-3}$. In semiconductor processing, ion implantation can routinely be used for regions with doping levels above 10^{20}cm^{-3}, but typically the penetration depths are very small [42]. A proprietary process was developed at VTT for doping the silicon device layer of SOI/cavity-SOI wafers with phosphorus well beyond 10^{20}cm^{-3}. The results of ultra-heavily doped (UHD) silicon resonators are summarized in Paper **II**. Details of the VTT UHD fabrication process as well as the used resonator designs are excluded from the scientific scope of this dissertation.

First, electrostatically coupled (bare UHD-silicon) resonators were fabricated. Figure 4.13(a) shows that the intrinsic material losses (See Section 2.7) stay at a very low level even at extreme doping levels, although the $Q \times f$ product appears to be reduced to $\sim 30\%$ of that seen for HD-silicon (Fig. 4.12). The prediction of the possibility of full second-order temperature compensation was shown to be true: TCF_2 of extensional mode resonators was

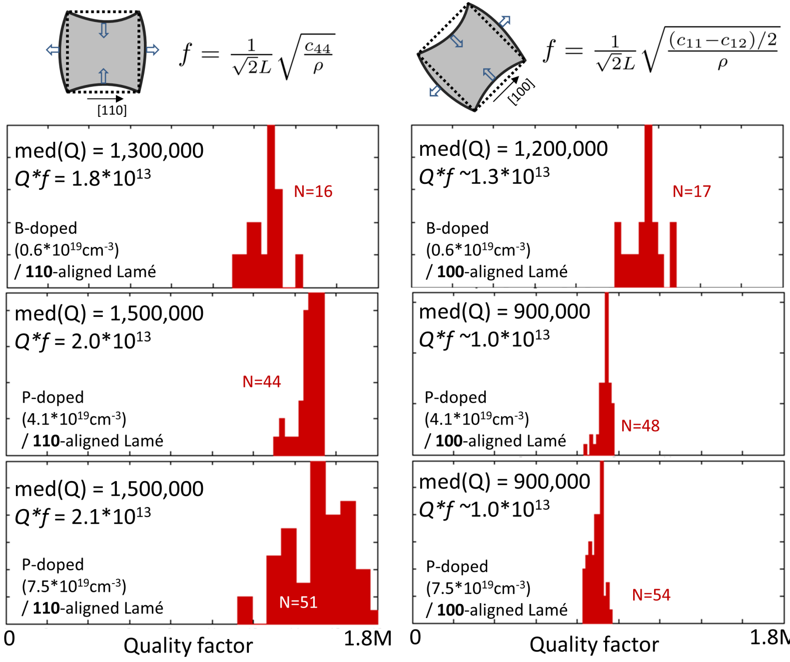

Figure 4.12. Quality factors of sets of two types of Lamé mode resonators on a moderately boron-doped wafer and on two heavily phosphorus-doped wafers. (Paper **IV**)

indeed observed to cross zero, when the doping level was high enough. The results of Fig. 4.13(b) indicated that

1. There is an optimal doping level which, together with a correct design, yields $TCF_1 \sim TCF_2 \sim 0$ simultaneously, which results in quartz level frequency stability. The best experimentally demonstrated level of stability was ±10 ppm for a temperature range of $T = -20 \ldots + 85°\text{C}$.

2. The initially negative second order temperature coefficient TCF_2 could be made positive, up to $TCF_2 \sim +15\,\text{ppb}/°C^2$.

Observation 1 leads to attractive possibilities for realizing various types of passively temperature compensated bare silicon resonators, but observation 2 is the key for realizing *piezoelectrically* transduced silicon MEMS resonators with quartz class frequency stability: Piezoelectric actuation requires addition of piezoelectric and metal (electrode) layers to the resonator device, and, practically all such materials (typically AlN + Mo/Al) have negative first- and second-order temperature coefficients TCF_1 and TCF_2, respectively [81, 82, 83]. By balancing the positive contribution from the UHD-Si resonator body and the negative effect from the piezoelectric and metallic layers to both

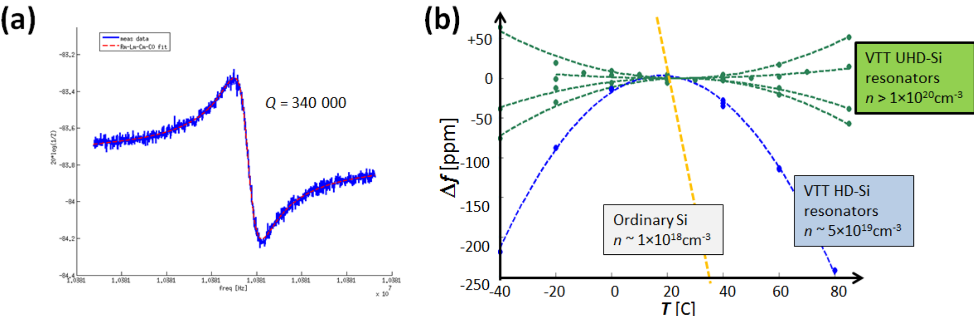

Figure 4.13. (a) Quality factor of a bare UHD-Si ($n > 10^{20}\mathrm{cm}^{-3}$) 10-MHz Lamé mode resonator with [100] alignment under vacuum of $p < 0.1\,\mathrm{mbar}$. (b) Temperature characteristics of electrostatically coupled (bare silicon) extensional mode resonators made at VTT. Resonators made of ordinary silicon ($n \sim 10^{18}\mathrm{cm}^{-3}$), heavily doped silicon (HD-Si, $n \sim 5 \times 10^{19}\mathrm{cm}^{-3}$), and ultra heavily doped silicon (UHD-Si, $n > 10^{20}\mathrm{cm}^{-3}$) are compared. With optimized doping and resonator design, a stability of ±10 ppm was reached. In UHD-Si devices, the initially negative second order temperature coefficient can be made positive, up to $TCF_2 \sim +15\,\mathrm{ppb}/°C^2$. (Paper **II**)

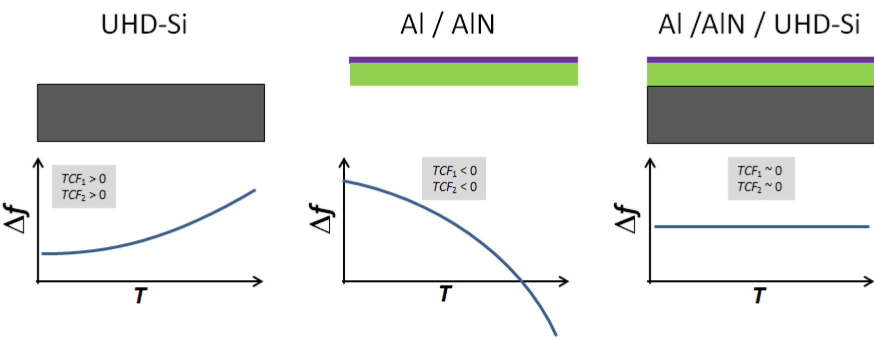

Figure 4.14. Illustration of matching the thicknesses of the UHD-Si/AlN/Al layers for an optimally flat f-vs-T curve. (Paper **II**)

TCF_1 and TCF_2 by correct composition of the resonator, it is possible to reach quartz level frequency stability, see Fig. 4.14.

The PiezoMEMS process flow (Section 1.4) was made compatible with UHD silicon device layer fabrication, and Si/AlN/Al stack thicknesses were optimized for minimizing TCF_1 and TCF_2. At best, this optimization resulted in resonators having a frequency stability of $\pm 10\,\mathrm{ppm}$ over $T = -40 \ldots + 85°\mathrm{C}$, see Fig. 4.15[7].

[7]It should be noted that the quality factor of $Q \sim 4200$ was limited here by suboptimal anchoring of the resonator. Low intrinsic dissipation in UHD-Si allows for orders of magnitude higher quality factor, see Fig. 4.13(a).

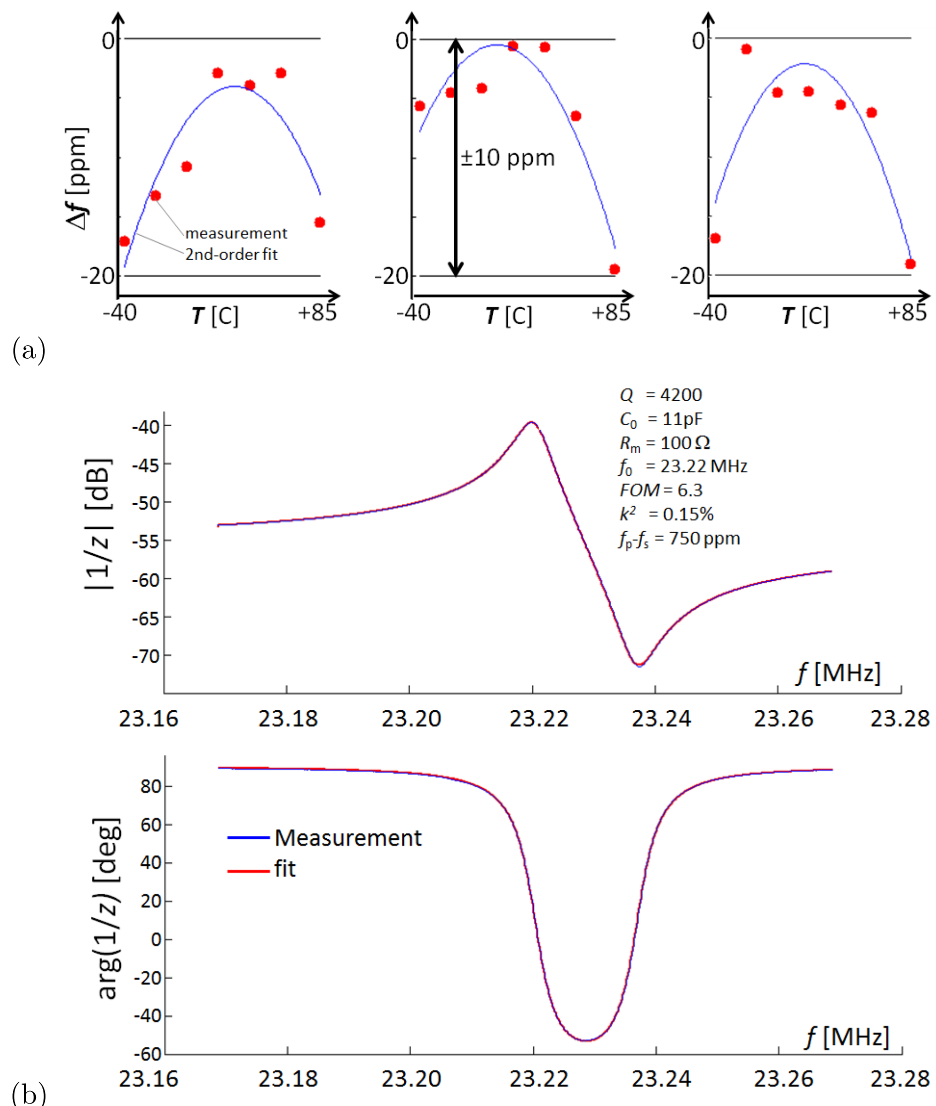

Figure 4.15. a) $f-$vs$-T$ curves of three 23 MHz PiezoMEMS extensional mode resonators. Data points are shown as red dots, and the blue line is a 2nd order polynomial fit. The scatter between measured data and the fit is expected to be caused by the fact that the measured resonators were non-packaged and measured in open-air. (b) Example frequency response of the resonator. (Paper **II**)

5. Conclusions

Some of the consequences of the findings with piezoelectrically transduced silicon resonators have already been presented in Section 3.2.5, and the results on the elastic parameter extraction and identification of classes of temperature compensated modes were discussed in Sections 4.3.3 and 4.4.4, respectively. In this Chapter, these conclusions are summarized on a more general level and extended with a few new ones.

5.1 Physical origin of temperature compensation

The physics behind the elastic constants of silicon being affected by the doping level is mainly electronic in origin, and can be described qualitatively in the following way. The density of charge carriers n, or doping level, affects how the (multiple) conduction bands are filled. The distribution of the charge carriers within the band structure is also affected by the temperature through the Fermi-Dirac distribution, Eq. (4.4). As a result, the Gibbs free energy $G(n, T)$ is a function of both doping level n as well as temperature T, and this is propagated to the behavior of the elastic constants $c_{ij}(n, T)$ as they are the strain derivatives of G, see Eq. (4.1). It was seen in this work that these mechanisms can act together very favorably for temperature compensation of silicon resonators.

5.2 Progress towards a MEMS-based TCXO

Realization of a quartz-like silicon MEMS resonator, enabling performance good enough for fulfilling TCXO specifications has moved much closer to reality through the results achieved in this work.

- Achieving the required noise performance with piezoelectrically transduced

silicon resonators was shown to be possible.

- The result of ± 10 ppm frequency stability shows that passively temperature compensated piezoelectrically coupled silicon MEMS resonators can reach a similar performance to quartz crystals of best possible frequency stability. Tunability of the resonator is enough for correcting the remaining temperature dependent variation in the same way as is done in today's quartz based TCXOs. For oscillators with slightly more relaxed frequency stability specifications, a temperature sensor might not be needed at all.

Manufacturability, or repeatability of the resonator characteristics, is a key challenge to overcome for commercial applicability of the approach pursued in this work. Figure 5.1 illustrates the scatter between the f-vs-T curves as well as the initial accuracy error of resonators on a wafer of piezoelectrically transduced UHD-Si resonators. For approximately two thirds of the resonators,

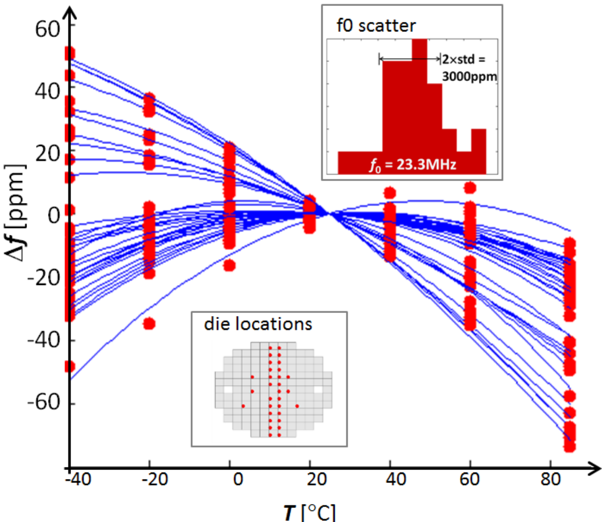

Figure 5.1. f-vs-T curves from $\sim$ 30 resonators spanning the wafer on the south-north direction. Note that the Δf is given in relative units, and hence the initial frequency error is absent. The top inset shows the initial frequency f_0 error, which has a standard deviation of 1500 ppm. Bottom inset illustrates the location of the measured dies on the wafer. (Paper **II**)

the frequency stability is within ± 20 ppm. The distribution of the initial accuracy has a standard deviation of 1500 ppm. The tunability of approximately 250 ppm (See Table 3.1) of these resonators is clearly not enough for correcting an initial accuracy error of this size. However, one of the advantages of the piezoelectric transduction scheme is that it sensitizes the frequency (and its temperature dependency) to the thicknesses of the material layers of the composite resonator. Both the temperature characteristics as well as the frequency of the resonator are functions of the thicknesses of the layers in the

Si/AlN/Al stack. Thus, selective addition or removal of material can be used for the correction of the initial accuracy and/or tuning of the f-vs-T curves for better overlap with each other. Mapped ion beam trimming, used in the microacoustic filter (SAW, BAW, FBAR) industry, is a technique that could potentially be used for achieving this goal [84].

5.3 Outlook

The findings of this work are applicable to timing and frequency references outside the TCXO specification as well. The frequency stability of ±10 ppm, although currently demonstrated with devices at ~ 20 MHz, can be straightforwardly realized e.g. with low frequency (typically 32 KHz) flexural resonators — the best quartz resonators for kHz-frequencies perform at ±50 ppm.

There is a possibility that the achievable frequency stability of UHD-Si resonator can be optimized to be remarkably less than the currently demonstrated level of ±10 ppm. The results obtained thus far suggest that the 3rd order temperature coefficient of frequency TCF_3 could be considerably smaller than that in quartz crystals. To study this possibility, more accurate characterization of UHD-Si devices is needed, where the perturbations caused by open air effects are removed.

There is some indication that the mechanical nonlinearities of HD-silicon can be affected by doping [85]. The mechanical nonlinear limits of UHD-Si are unknown, and they pose a relevant topic for investigation. Also the long term stability characteristics have not yet been studied for UHD-silicon resonators.

The demonstration of making silicon as temperature insensitive as quartz can have general significance outside the field of frequency references - silicon belongs now to the rare selection of materials that can be very temperature stable. The steps demonstrated in this work may help silicon MEMS resonators to increase their penetration on the timing and frequency control market. Considering the inertia, speed of development and scalability of silicon based MEMS fabrication, it is tempting to predict that quartz is going to face tougher competition in the times ahead.

6. Summary

In this dissertation, new scientific understanding was achieved on the design and fabrication of piezoelectrically transduced silicon resonators that are passively temperature compensated with heavy doping. The research was motivated by the two challenges silicon resonators were known to need improvement on: the electrostatic transduction method was problematic due to the requirement for a high bias voltage and narrow-gap fabrication process, and the temperature stability of silicon resonators was orders of magnitude worse than that of quartz crystals.

Chapter 3 discussed generations of piezoelectrically transduced silicon resonators that were designed, fabricated and characterized. The electrical performance of the resonators progressed to a point at which an oscillator, based on a width extensional mode resonator operating at 24 MHz, was demonstrated to have a phase noise -128 dBc/Hz at 1 kHz offset from the carrier frequency, which is good enough to meet the specification for a TCXO (temperature compensated crystal oscillator). An experimental study was conducted on piezoelectrically transduced square extensional mode resonators, whose dimensions were varied so that the main resonance mode occurred at a frequency range of $f = 13 \ldots 30$ MHz. As a result, an anchor coupling effect was identified, and design rules were developed for avoiding it. Also a subharmonic nonlinear coupling mechanism was discovered, coupling a rotational resonance mode to the main mode of the resonator at certain dimensions.

The effect of degenerate n- and p-type doping on the elastic parameters of silicon was investigated experimentally, with a focus on the applicability to temperature compensation, Chapter 4. It was identified that n-type doping was more applicable for the purpose. Families of resonance modes that can be temperature compensated using doping were identified, and design rules for the optimization of the frequency stability were developed. The elastic parameters of silicon $c_{ij}(n, T)$ were determined as a function of temperature

($T = -40 \ldots +85°$C) and of n-type doping level up to $n = 7.5 \times 10^{19}\mathrm{cm}^{-3}$, enabling modelling of the frequency-vs-temperature characteristics of an arbitrary resonator design with good accuracy. Extrapolation from the results resulted in a prediction of full second order temperature compensation in optimally designed resonators when the n-type doping level is above $10^{20}\mathrm{cm}^{-3}$. The prediction was experimentally verified with demonstration of piezoelectrically transduced resonators, whose frequency stability was measured to be within $\pm 10\,\mathrm{ppm}$ on a temperature range of $T = -40 \ldots +85°$C, on par with the best quartz crystals.

A. Methods

A.1 Electrical characterization measurements

A.1.1 Frequency sweeps and $f-\text{vs}-T$ curve determination

Electrical characterization of the resonators discussed in this thesis was based on measuring the frequency response (frequency dependent complex impedance) of the devices. Typically the resonators were measured on wafer level in atmospheric pressure on a Cascade Summit probe station using a HP 4294A impedance analyzer. A two-needle probe card was used for the measurements, and an open-short-load calibration was performed in the beginning of the measurement. Measurements were done in the four-terminal pair configuration with four 2-m BNC cables, and the two end connections to the probe needles were $\sim 15\,\text{cm}$ long. In the case of electrostatically transduced resonators, a DC bias voltage (up to 40 V) was applied between the resonator and the electrodes.

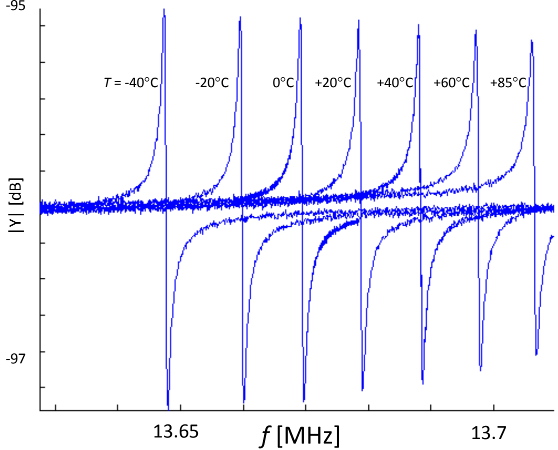

Figure A.1. Measured admittance traces of the Lamé-45° resonators on wafer P7.5 measured at different temperatures. (Paper **III**)

Determination of the frequency-vs-temperature behavior of resonators was a routine measurement needed for example in Papers **II**, **III** and **VII**. For this, the frequency responses at the resonance peaks were recorded at temperatures from -40°C to +85°C with seven steps using the temperature-controlled wafer chuck. Example traces are shown in Fig. A.1. A 15 minute stabilization period followed after each temperature step before probing of the resonators was started; the chuck temperature was well stabilized in less than 10 minutes for all temperature steps. Clean dry air flow at a rate of 30 l/min was used for purging. The effect from room temperature gas flow to resonator temperature was found to be smaller than the specified uncertainty of ±0.5°C of the temperature control system (see Paper **III**).

A.1.2 Automatization

A measurement that is based on frequency sweeps is relatively slow: a full $f-\mathrm{vs}-T$ characterization measurement for a set of 100 devices could take 12 hours[1]. Automatization of the measurements was implemented so that long measurements could be performed during nights and weekends with minimal intervention.

A LabView frontend for controlling the movements (stepping) of the probe station chuck and selection of the devices to be measured was implemented[2], and both the temperature controller as well as the impedance analyzer were steered over GPIB by an external Python program launched by the LabView frontend. A typical measurement algorithm on the impedance analyzer would first scan for resonance peaks on a wide frequency range around the expected peak frequency (the resonance frequency would vary with temperature and from device to device due to initial frequency scatter), and then zoom into a detected resonance peak at a narrower frequency span. A web interface was implemented to enable remote monitoring and control of the measurement. The measurement data (including the measurement conditions such as the chuck temperature and the impedance analyzer parameters), log files and microscope images of the devices were stored into a hierarchy of files and pushed also to a MySQL database for later analysis.

[1] Probing should be done much faster in a production environment. This is possible, e.g., by measuring the resonators as oscillators while probed, by connecting them with an oscillator drive circuit integrated on a probe card.

[2] The first version of was created by Jerome Lamy, VTT.

A.1.3 Parameter fitting and data analysis

The measured frequency responses were fitted to the $R_m - L_m - C_m - C_0$ equivalent circuit (Fig. 2.3(a)). A Matlab algorithm, based on nonlinear optimization (FMINSEARCH), was implemented for running the fits for a large set of recorded frequency responses in a batch. Typically, the fits were very good for well-behaved resonances, see Fig. 2.3(b).

The measurement data was pulled from the measurements database to Matlab using the mYm MySQL connector for Matlab [86]. Using SQL queries made it possible to filter the data with, e.g., a device type or a measurement condition, which enabled fast retrieval of the data sets of interest. This approach made it flexible to write data analysis procedures, and to produce outputs such as that in Fig. 4.3, for example.

A.2 Solving for elastic parameters from resonance frequencies

Section 4.3.1 (Paper **III**) introduced the experiment, where the values of the elastic parameters were solved from the resonance frequencies of seven different resonators, each having a different functional dependency on the elastic parameters. The details of the extraction procedure are given here. The approach was influenced by that used by Bourgeois in Ref. [78].

The experimental data consists of measured resonance frequencies at different temperatures for all seven resonance modes $f_k^{\mathrm{exp}}(T)$ $(k = 1, \ldots, 7)$. Denote the corresponding theoretical estimates containing the c_{ij} dependencies – obtained through finite element modelling (see Appendix A.4) – as $f_k^{\mathrm{th}}(c_{11}, c_{12}, c_{44})$. We use an approach of first matching f_k^{exp} and f_k^{th} at a reference temperature T_0 (here $T_0 = 20°\mathrm{C}$) by numerical minimization of a cost function

$$g(c_{ij}) = \sum_k [f_k^{\mathrm{exp}} - f_k^{\mathrm{th}}(c_{ij})]^2 \tag{A.1}$$

to find elastic parameters $c_{ij}(T_0)$. Then, Eq. (2.11) can be written for each of the individual modes,

$$\frac{\delta f_k^{\mathrm{exp}}(T)}{f_{k0}^{\mathrm{exp}}} = \frac{1}{f_{k0}^{\mathrm{th}}} \sum_{ij} \frac{\partial f_k^{\mathrm{th}}}{\partial c_{ij}} \delta c_{ij}(T) + \frac{1}{2}(\alpha_1 \Delta T + \alpha_2 \Delta T^2), \tag{A.2}$$

where, f_{k0}^{exp} and f_{k0}^{th} refer to the measured and theoretical frequencies at the reference temperature T_0. In matrix form, Eq. (A.2) can be denoted as

$$\delta \mathbf{f}^{\mathrm{exp}}(T) = A \cdot \delta \mathbf{c}(T) + \beta(T). \tag{A.3}$$

where the vector $\delta\mathbf{f}^{\text{exp}}$ contains the relative frequency changes, $\beta(T)$ is a shorthand for the thermal expansion part, and the elements of the sensitivity matrix A are defined as

$$a_{kn} = \frac{1}{f_{k0}^{\text{th}}}\frac{\partial f_k^{\text{th}}}{\partial c_n},\ n = 11, 12, 44;\ k = 1, ..., 7. \tag{A.4}$$

Sensitivity matrix elements are illustrated in Fig. 4.2. One should note that Eq. (A.4) depends on the linearization point at which it is evaluated. The changes in elastic parameters $\delta\mathbf{c}(T)$ can be solved as a least squares fit from Eq. (A.3),

$$\delta\mathbf{c}(T) = (A^T A)^{-1} A^T[\delta\mathbf{f}^{\text{exp}}(T) - \beta(T)]. \tag{A.5}$$

A.3 Test design for measuring an angular alignment error

In the study described in Section 4.3 (Paper **III**), fabrication of the devices resulted in a small deviation of the resonator orientation from the intended alignment with the crystal axes, which could have affected the accuracy of the extraction of the elastic parameters. For the determination of the elastic parameters, it was of importance to take into account the angular misalignment $\Delta\theta$ of the devices that had occurred during the fabrication. This deviation was determined using the method illustrated in Fig. A.2. Due to anisotropy of silicon, the resonance frequency of an LE mode beam resonator increases by ~10% when the resonator alignment is rotated from [100] to [110]. Between these directions, i.e., at $\pm 22.5°$ from [110], the resonance frequency is most sensitive to angular misalignment with $\Delta f/\Delta\theta \sim \pm 460\,\text{ppm}/0.1\,\text{deg}$. Copies of two LE resonators identical in dimensions, but oriented 45° to each other, both at the most sensitive orientation of $\pm 22.5°$ were included on the wafers. The angular misalignment could be deduced from the up/down frequency shifts $\pm\Delta f$ of these resonators.

A.4 Finite element modelling

Comsol Multiphysics (version 3.6) was used for finite element modelling of the resonators. In Paper **III**, numerical estimates of the modal frequencies $f_k^{\text{th}}(c_{11}, c_{12,}, c_{44})$ were calculated. Resonance frequencies were obtained with modal analysis of full 3D geometries of the devices including the anchoring regions. The calculations were performed for parameters c_{11}, c_{12} and c_{44} spanning ranges of [$160 \ldots 168$ GPa], [$63 \ldots 68$ GPa] and [$78 \ldots 80$ GPa], respectively, discretized to a grid of $5 \times 5 \times 5$ points. Values were stored in

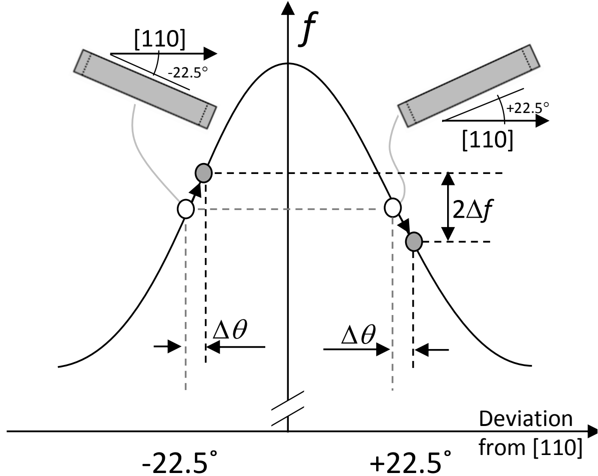

Figure A.2. In-plane angular misalignment of the wafers can be deduced from the difference of the resonance frequencies of two types of LE beam resonators, which are designed at an angle of ±22.5° from [110] direction. In-plane rotation of the resonators shifts the resonance frequencies up/down by ±460 ppm/0.1 deg. (Paper **III**)

lookup tables, and later retrieved for evaluation of Eqs. A.1 and A.4. Cubic interpolation was used for evaluation of $f_k^{\text{th}}(c_{11}, c_{12},, c_{44})$ between the grid points. The discretization was verified to be dense enough for accurate evaluation of the linear sensitivity terms $\partial f_k^{\text{th}}/\partial c_{ij}$ in Eq. (A.4).

Similarly, the sensitivities were calculated for evaluation of the temperature coefficients TCF_1 and TCF_2 in Section 4.4.2 (Paper **I**). For parametric simulations such as those of Fig. 4.6, a scripted procedure was developed to vary the simulation geometries: i) The 2D starting geometry was read from a mask file by a Python program in which a geometry object was constructed. This object had methods for deformation of the geometry with operations such as scaling, rotation or overetch of the geometries. ii) The final mesh was defined in the Gmsh 3D finite element mesh generator [87], and finally, iii) the mesh was imported into Comsol for running the final analysis[3]. Simulation data objects were stored into a MySQL database in the same manner as described in Section A.1.3, enabling flexible analyses and fast generation of plots such as those in Fig. 4.7.

The two-dimensional simulations of Paper **X** for modelling of the anchoring losses were performed with the HiQLAB simulation package [88].

[3]In Comsol version 4.0 the scripting capabilities were upgraded, and, it appears that now the procedure for parametric simulations could be implemented fully inside Comsol.

B. Numerical data

B.1 Specifications for wafers used for $c_{ij}(n, T)$ determination

Table B.1. Details of the wafers for the silicon device layers used for elastic parameter determination (Section 4.3). Wafers were grown with the Czochralski method and provided by Okmetic oyj. Carrier concentrations were calculated from the resistivity specification using Ref. [89]. Carrier concentration ranges are included as error bars in Fig. 4.5. Angular misalignment was measured using the method described in Appendix A.3. (Paper **III**)

wafer id	dopant	specified resistivity [mOhm cm] min	max	calculated carrier concentration [10^{19} cm^{-3}] min	max	avg	angular alignment error [deg]	device layer thickness [μm]	total thickness variation [μm]
B3	B	3.49	3.66	2.88	3.04	2.96	-0.6	23.8	3.1
B0.6	B	10	20	0.33	0.86	0.60	-0.1	15.6	3.5
As1.7	As	3.96	4.36	1.55	1.77	1.66	0.3	15.4	2.7
As2.5	As	2.94	3.08	2.39	2.52	2.46	-0.6	14.5	2.5
P4.1	P	1.67	1.76	3.98	4.22	4.10	0.0	14.6	2.6
P4.7	P	1.47	1.59	4.45	4.86	4.66	1.6	14.5	3.7
P7.5	P	0.95	1.05	7.05	7.89	7.47	0.5	14.5	1.7

B.2 Measured TCFs of resonators on wafers with varied doping

Table B.2. Temperature coefficients of frequency TCF_1, TCF_2 and f_0 of the resonance modes of Fig. 4.3. The fits reproduced the f vs. T curves to within ±10 ppm for all cases. (Paper **III**)

	Wafer B3			Wafer B0.6			Wafer As1.7			Wafer As2.5		
Mode	f_0 [MHz]	TCF_1 [ppm/K]	TCF_2 [ppb/K^2]	f_0 [MHz]	TCF_1 [ppm/K]	TCF_2 [ppb/K^2]	f_0 [MHz]	TCF_1 [ppm/K]	TCF_2 [ppb/K^2]	f_0 [MHz]	TCF_1 [ppm/K]	TCF_2 [ppb/K^2]
Lamé 0	13.68	-8.3	-64	13.77	-24.5	-37	13.76	-30.4	-25	13.75	-31.1	-23
LE 0°	9.02	-16.6	-52	9.07	-27.8	-33	9.04	-24.0	-44	9.03	-22.2	-43
LE 11.25°	8.81	-17.3	-50	8.87	-28.0	-33	8.85	-20.8	-49	8.80	-17.9	-53
LE 22.5°	8.39	-18.8	-49	8.45	-28.3	-34	8.41	-14.4	-66	8.36	-9.9	-69
LE 33.75°	8.04	-19.9	-47	8.09	-28.6	-34	8.03	-8.9	-78	7.99	-3.0	-83
LE 45°	7.92	-20.4	-47	7.95	-28.7	-34	7.88	-6.7	-85	7.86	-0.8	-85
Lamé 45°	10.96	-17.2	-52	11.02	-27.1	-37	10.91	-1.8	-94	10.86	5.6	-98

	Wafer P4.1			Wafer P4.7			Wafer P7.5		
Mode	f_0 [MHz]	TCF_1 [ppm/K]	TCF_2 [ppb/K^2]	f_0 [MHz]	TCF_1 [ppm/K]	TCF_2 [ppb/K^2]	f_0 [MHz]	TCF_1 [ppm/K]	TCF_2 [ppb/K^2]
Lamé 0	13.74	-32.5	-20	13.72	-32.7	-17	13.68	-34.5	-12
LE 0°	9.00	-19.5	-42	8.99	-19.0	-39	8.95	-18.9	-26
LE 11.25°	8.79	-14.1	-51	8.83	-14.7	-46	8.75	-13.2	-31
LE 22.5°	8.34	-3.0	-68	8.39	-3.7	-62	8.30	-0.8	-41
LE 33.75°	7.96	5.8	-82	7.98	6.4	-77	7.89	9.6	-48
LE 45°	7.81	9.4	-87	7.80	10.6	-84	7.74	13.7	-52
Lamé 45°	10.79	17.2	-98	10.75	18.6	-94	10.66	22.1	-57

B.3 Values of temperature coefficients of the elastic parameters c_{ij} as a function of doping level

Table B.3. Values of temperature coefficients of the elastic parameters $c_{ij}(T) = c_{ij}^0[1 + a_{ij}(T - T_0) + b_{ij}(T - T_0)^2]$. Corresponding data points are plotted in Fig. 4.5. Confidence intervals Δc_{ij}^0, Δa_{ij} and Δb_{ij} are based on the error analysis presented in Paper **III**. (Paper **III**)

dopant	n [$*10^{19}$cm^{-3}]	c_{11}^0 [GPa]	a_{11} [ppm/K]	b_{11} [ppb/K^2]	c_{12}^0 [GPa]	a_{12} [ppm/K]	b_{12} [ppb/K^2]	c_{44}^0 [GPa]	a_{44} [ppm/K]	b_{44} [ppb/K^2]	c_{11}^0-c_{12}^0 [GPa]	a_{11-12} [ppm/K]	b_{11-12} [ppb/K^2]
B	3.0	164.2	-62.5	-73	63.5	-102.9	-11	78.5	-19.3	-136	100.7	-37.1	-112
B	0.6	165.5	-69.9	-59	63.7	-90.6	-22	79.6	-51.7	-81	101.8	-56.9	-83
As	1.7	164.0	-48.5	-111	64.3	-114.7	25	79.5	-63.7	-58	99.7	-5.8	-198
As	2.5	163.8	-44.2	-111	64.9	-124.6	34	79.4	-65.1	-55	98.9	8.5	-206
P	4.1	163.0	-34.5	-115	65.4	-133.7	22	79.2	-67.8	-51	97.6	31.9	-206
P	4.7	162.5	-32.5	-110	65.7	-131.8	18	79.1	-68.7	-43	96.8	34.9	-196
P	7.5	161.4	-30.7	-78	66.1	-134.9	-12	78.5	-71.9	-31	95.3	41.6	-124
		Δc_{11}^0	Δa_{11}	Δb_{11}	Δc_{12}^0	Δa_{12}	Δb_{12}	Δc_{44}^0	Δa_{44}	Δb_{44}	$\Delta(c_{11}^0$-$c_{12}^0)$	Δa_{11-12}	Δb_{11-12}
Total uncertainty (rms sum)		±0.3	±0.7	±12	±0.1	±1.5	±33	±0.2	±0.4	±10	±0.2	±0.3	±7
E_1: frequency error		±0.3	±0.39	±9.4	±0.1	±1.20	±28.5	±0.2	±0.16	±3.6	±0.2	±0.16	±3.5
E_2: temperature error			±0.26	±6.6		±0.64	±17.1		±0.34	±9.1		±0.20	±5.6
E_3: linearization point error			±0.54	±0.8		±0.69	±1.1		±0.01	±0.0		±0.02	±0.0
E_4: thermal expansion error			±0.09			±0.09			±0.09			±0.09	
E_5: thickness variation error			±0.02	±0.0		±0.04	±0.0		±0.00	±0.0		±0.00	±0.0

B.4 Interpolation of elastic parameter data

The temperature coefficients of the elastic constants of silicon for n type doping range of $n = 0 \dots 7.5 \times 10^{19}\text{cm}^{-3}$ were interpolated using third order polynomials fitted to the data of Table B.3 (also presented in Fig. 4.5). The data points, the interpolation functions used in the simulations and the associated coefficients are shown in Fig. B.1(a)–(j).

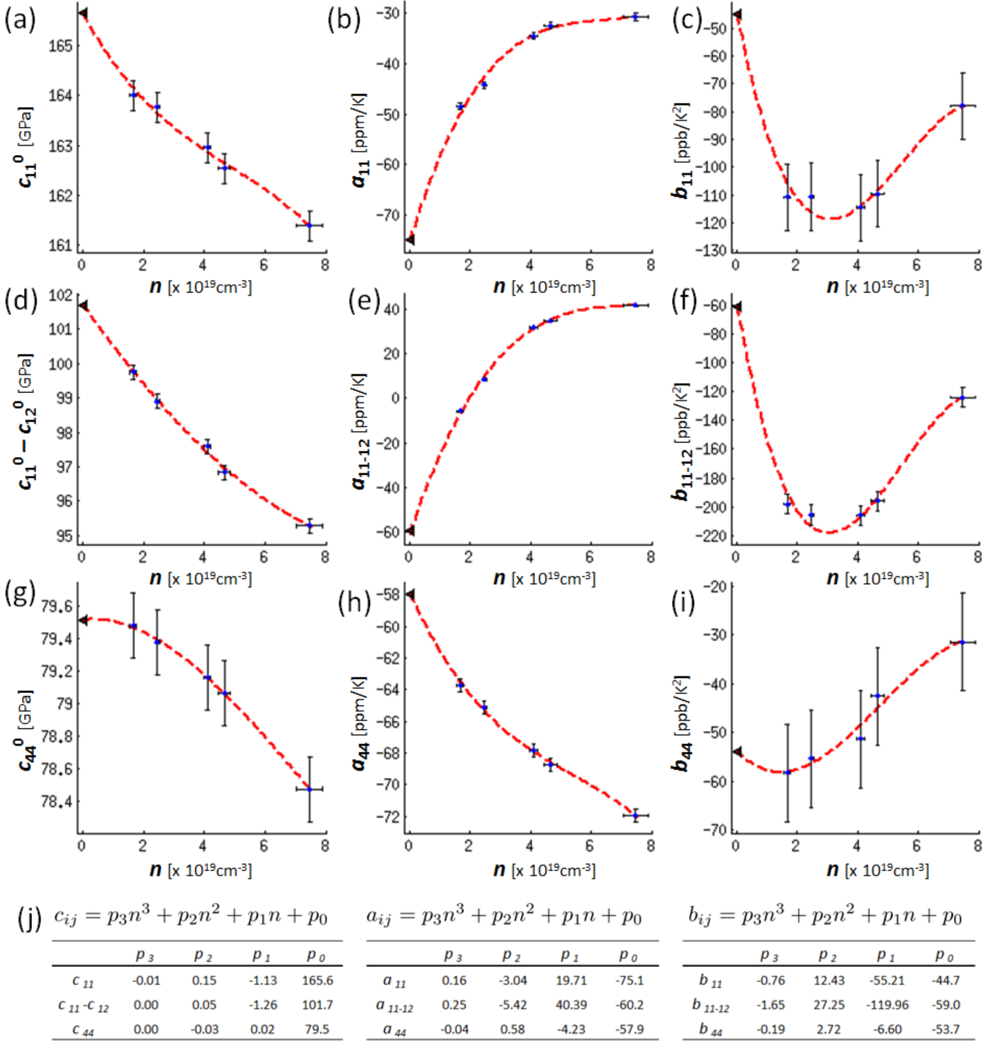

	p_3	p_2	p_1	p_0
c_{11}	-0.01	0.15	-1.13	165.6
c_{11}-c_{12}	0.00	0.05	-1.26	101.7
c_{44}	0.00	-0.03	0.02	79.5

	p_3	p_2	p_1	p_0
a_{11}	0.16	-3.04	19.71	-75.1
$a_{11\text{-}12}$	0.25	-5.42	40.39	-60.2
a_{44}	-0.04	0.58	-4.23	-57.9

	p_3	p_2	p_1	p_0
b_{11}	-0.76	12.43	-55.21	-44.7
$b_{11\text{-}12}$	-1.65	27.25	-119.96	-59.0
b_{44}	-0.19	2.72	-6.60	-53.7

Figure B.1. Third order polynomial interpolation functions for the temperature coefficients of the elastic parameters c_{ij} as a function of carrier concentration n. The dependent coefficient a_{12} is readily evaluated as $a_{12} = (a_{11}c_{11}^0 - a_{11-12}c_{11-12}^0)/c_{12}^0$, and a similar equation holds for b_{12}. Coefficients of the polynomial fits are given in (j). (Paper **III**)

C. Derivations

C.1 Change in density vs. thermal expansion

The last two terms

$$-\frac{\delta L}{L}(T) - \frac{1}{2}\frac{\delta\rho}{\rho}(T) \tag{C.1}$$

of Eq. (2.9) were expanded as

$$\frac{1}{2}(\alpha_1 \Delta T + \alpha_2 \Delta T^2) \tag{C.2}$$

to arrive at Eq. (2.11), when a second order expansion for the thermal expansion was used:

$$\frac{\delta L}{L}(T) = (\alpha_1 \Delta T + \alpha_2 \Delta T^2). \tag{C.3}$$

Justification for this is the following. Let us see what happens if second order effects are taken into account when expanding the density term

$$\delta\rho/\rho = -\delta V/V, \tag{C.4}$$

where V stands for the volume under investigation.

An infinitesimal change in volume δV relates to length changes δL through

$$\begin{aligned} V + \delta V &= (L + \delta L)^3 \\ &= L^3 + 3L^2\delta L + 3L(\delta L)^2 + \delta L^3 \\ &= L^3 + 3L^3\frac{\delta L}{L} + 3L^3(\frac{\delta L}{L})^2 + L^3(\frac{\delta L}{L})^3 \end{aligned}$$

We have of course $L^3 = V$, so

$$\begin{aligned} (V + \delta V) &= V + 3V\frac{\delta L}{L} + 3V(\frac{\delta L}{L})^2 + V(\frac{\delta L}{L})^3 \\ &\Rightarrow \\ \delta V/V &= 3\frac{\delta L}{L} + 3(\frac{\delta L}{L})^2 + (\frac{\delta L}{L})^3. \end{aligned} \tag{C.5}$$

Now, plugging Eq. (C.3) into Eq. (C.5) yields:

$$\begin{aligned}\delta V/V &= 3\alpha_1\Delta T + 3\alpha_2\Delta T^2 \\ &+3(\alpha_1^2\Delta T^2 + 2\alpha_1\alpha_2\Delta T^3 + \alpha_2^2\Delta T^4) \\ &+(\alpha_1^3\Delta T^3 + 3\alpha_1^2\alpha_2\Delta T^3 + 3\alpha_1\alpha_2^2\Delta T^3 + \alpha_2^3\Delta T^6).\end{aligned}$$

Keeping only terms up to second order in ΔT we obtain

$$\begin{aligned}\delta V/V &= 3\alpha_1\Delta T + 3\alpha_2\Delta T^2 \\ &+3(\alpha_1^2\Delta T^2) \\ &= 3[\alpha_1\Delta T + (\alpha_2 + \alpha_1^2)\Delta T^2]. \end{aligned} \tag{C.6}$$

Using values $\alpha_1 = 2.84 \times 10^{-6}\,\mathrm{K}^{-1}$ and $\alpha_2 = 8.5 \times 10^{-9}\,\mathrm{K}^{-2}$ for the thermal expansion coefficients [78], one can approximate term α_1^2 as negligible in comparison with α_2. Thus,

$$\delta\rho/\rho \sim -3[\alpha_1\Delta T + \alpha_2\Delta T^2], \tag{C.7}$$

and Eq. (2.11) results.

C.2 Model for piezoelectric transduction

The piezoelectric transduction factor η is modelled here taking the three-dimensional piezoelectric constitutive relation into account (neglecting any shear terms). The result can be compared with that derived in Section 2.4.

Suppose that the piezo film is clamped to the resonator beam. We approximate that the strains in the lateral directions are zero ($S_x = S_y = 0$), which is expected to give an upper estimate of the true coupling, and assume that the piezolayer may move freely in the z direction so the vertical stress component is zero ($T_z = 0$) [90]. When a z-directed electric field E_3 is applied, we can write the piezoelectric constitutive relation $T = eE + cS$ in matrix form [38]:

$$\begin{bmatrix} T_x \\ T_y \\ 0 \end{bmatrix} = \begin{bmatrix} 0 & 0 & e_{31} \\ 0 & 0 & e_{31} \\ 0 & 0 & e_{33} \end{bmatrix} \begin{bmatrix} 0 \\ 0 \\ E_z \end{bmatrix} + \begin{bmatrix} c_{11} & c_{12} & c_{13} \\ c_{21} & c_{22} & c_{23} \\ c_{31} & c_{32} & c_{33} \end{bmatrix} \begin{bmatrix} 0 \\ 0 \\ S_z \end{bmatrix} \tag{C.8}$$

Here we have neglected all the shear terms in e and c[1]. Only the nonzero elements $e_{31}$and e_{33} for AlN have been preserved. Solving for the unknown

[1] Simplifying the 6×1 vectors and 6×6 matrices to 3×1 and 3×3 dimensions, respectively, when the engineering notation is used [38].

lateral stresses and using elastic constant values of $c_{13} = c_{23} = 120\,\text{GPa}$ and $c_{33} = 395\,\text{GPa}$ [59] yields

$$T_x = T_y = \left(e_{31} - \frac{c_{13}}{c_{33}} e_{33}\right) E_3 \approx (e_{31} - 0.3 \times e_{33})\, E_3, \tag{C.9}$$

Following the derivation of Section 2.4, one obtains the following result for the transduction factor:

$$\eta_{pz} = w\,(e_{31} - 0.3 \times e_{33})\,. \tag{C.10}$$

Comparing with Eq. (2.32), it is seen that the z-directed electrical field couples to a lateral force also through the piezoelectric coefficient e_{33}, making the effect stronger. For AlN, the piezoelectric coefficients are $e_{33} = 1.55\ \text{Cm}^{-2}$, $e_{31} = -0.58\ \text{Cm}^{-2}$ [59].

C.3 Lamé mode and piezoelectric transduction

The elastic and piezoelectric properties of sputtered aluminum nitride are isotropic in the plane of the wafer due to the polycrystallinity of the material. Therefore, as seen in Eq. (C.9), the lateral stresses T_x and T_y are equal. The Lamé mode, being a superposition of shear waves, is isochoric, which means that each infinitesimal volume element $\mathrm{d}V$ of the material preserves its volume. The resonator thickness does not change at all during oscillation, and therefore, each area element $\mathrm{d}A$ at the top surface of the resonator preserves its area accordingly. Equal lateral stresses $T_x = T_y$ would deform an area element $\mathrm{d}A$ in a way that would contradict the element's area staying constant. Thus, piezoelectric transduction of the Lamé mode cannot be achieved with an AlN thin film.

D. List of Patents & Public Patent Applications

Table D.1. Patents and public patent applications

Patent Family	Priority date	PCT publication	Title	Granted patent & date	Pending applications
A	13.5.2010	WO2011/14134	**Microelectromechanical resonator and a method for producing the same**	US8916942 (granted 23.12.2014) EP2569862 (granted 16.4.2015)	US12/779104 EP11722749.6
B	13.8.2010	WO2012/02017	**Micromechanical resonator array and method for manufacturing thereof**	EP2603975 (granted 17.12.2014)	FI20105849, US13/209099
C	13.8.2010	WO2012/02017	**Micromechanical resonator and method for manufacturing thereof**	US20105851 (granted 30.6.2.2015)	FI20105851, US13/816493, EP11816145.4
D	17.2.2011	WO2012/11070	**Novel micromechanical devices**		FI20115151, US13/985876, EP12747759.4, JP2013553977, CN201280009253.4, KR1020137024650
E	13.5.2011	WO2012/15658	**Micromechanical device and method of designing thereof**	FI123933 (granted 31.12.2013), US 8558643 (granted 15.10.2013)	EP12786090.6, JP (no number), CN201280023350.9, KR1020137033278

Bibliography

[1] C. S. Lam, "A review of the recent development of MEMS and crystal oscillators and their impacts on the frequency control products industry," in *Proc. IEEE International Ultrasonics Symposium*, 2008, pp. 694–704. dx.doi.org/10.1109/ULTSYM.2008.0167

[2] C.-C. Nguyen, "MEMS technology for timing and frequency control," *IEEE Transactions on Ultrasonics, Ferroelectrics, and Frequency Control*, vol. 54, no. 2, pp. 251–270, 2007. dx.doi.org/10.1109/TUFFC.2007.240

[3] H. Nathanson, W. Newell, R. Wickstrom, and J. Davis, J.R., "The resonant gate transistor," *IEEE Transactions on Electron Devices*, vol. 14, no. 3, pp. 117–133, 1967. dx.doi.org/10.1109/T-ED.1967.15912

[4] K. E. Petersen, "Silicon as a mechanical material," *Proceedings of the IEEE*, vol. 70, no. 5, pp. 420–457, 1982. dx.doi.org/10.1109/PROC.1982.12331

[5] C.-C. Nguyen and R. Howe, "An integrated CMOS micromechanical resonator high-Q oscillator," *IEEE Journal of Solid-State Circuits*, vol. 34, no. 4, pp. 440–455, 1999. dx.doi.org/10.1109/4.753677

[6] K. Wang, A.-C. Wong, and C.-C. Nguyen, "VHF free-free beam high-Q micromechanical resonators," *Journal of Microelectromechanical Systems*, vol. 9, no. 3, pp. 347–360, 2000. dx.doi.org/10.1109/84.870061

[7] T. Mattila, J. Kiihamäki, T. Lamminmäki, O. Jaakkola, P. Rantakari, A. Oja, H. Seppä, H. Kattelus, and I. Tittonen, "A 12 MHz micromechanical bulk acoustic mode oscillator," *Sensors and Actuators A: Physical*, vol. 101, no. 1-2, pp. 1–9, 2002. dx.doi.org/10.1016/S0924-4247(02)00204-2

[8] T. Mattila, A. Oja, H. Seppa, O. Jaakkola, J. Kiihamaki, H. Kattelus, M. Koskenvuori, P. Rantakari, and I. Tittonen, "Micromechanical bulk acoustic wave resonator," in *Proc. IEEE International Ultrasonics Symposium*, 2002. dx.doi.org/10.1109/ULTSYM.2002.1193551

[9] T. Mattila, V. Kaajakari, J. Kiihamäki, A. Oja, H. Kattelus, H. Seppä, M. Koskenvuori, P. Rantakari, and I. Tittonen, "Silicon Micromechanical Resonators for RF-Applications," *Physica Scripta*, vol. 2004, no. T114, p. 181, 2004. dx.doi.org/10.1088/0031-8949/2004/T114/045

[10] V. Kaajakari, T. Mattila, A. Oja, J. Kiihamaki, and H. Seppa, "Square-Extensional Mode Single-Crystal Silicon Micromechanical Resonator for Low-Phase-Noise Oscillator Applications," *IEEE Electron Device Letters*, vol. 25, no. 4, pp. 173–175, 2004. dx.doi.org/10.1109/LED.2004.824840

[11] V. Kaajakari, T. Mattila, A. Oja, and H. Seppä, "Nonlinear limits for single-crystal silicon microresonators," *Journal of Microelectromechanical Systems*, vol. 13, no. 5, pp. 715– 724, 2004. dx.doi.org/10.1109/JMEMS.2004.835771

[12] V. Kaajakari, J. K. Koskinen, and T. Mattila, "Phase noise in capacitively coupled micromechanical oscillators," *IEEE Transactions on Ultrasonics, Ferroelectrics and Frequency Control*, vol. 52, no. 12, pp. 2322–2331, 2005. dx.doi.org/10.1109/TUFFC.2005.1563277

[13] V. Kaajakari, J. Kiihamaki, A. Oja, S. Pietikainen, V. Kokkala, and H. Kuisma, "Stability of wafer level vacuum encapsulated single-crystal silicon resonators," *Sensors and Actuators A: Physical*, vol. 130, pp. 42–47, 2006. dx.doi.org/10.1109/SENSOR.2005.1496567

[14] H. Lee, A. Partridge, and F. Assaderaghi, "Low jitter and temperature stable MEMS oscillators," in *Proc. IEEE International Frequency Control Symposium*, 2012, pp. 1–5. dx.doi.org/10.1109/FCS.2012.6243704

[15] J. Kuypers, G. Zolfagharkhani, A. Gaidarzhy, F. Thalmayr, A. Sparks, D. M. Chen, R. Rebel, B. Newman, M. Asmani, D. Badillo, and K. J. Schoepf, "Wafer-level chip scale MEMS oscillator for wireless applications," in *Proc. IEEE International Frequency Control Symposium*, 2012, pp. 1–5. dx.doi.org/10.1109/FCS.2012.6243689

[16] R. W. Keyes, "Electronic Effects in the Elastic Properties of Semiconductors," in *Solid State Physics: Advances in Research and Applications, ed. by F. Seitz and D. Turnbull*. Academic Press, 1967, vol. Volume 20, pp. 37–90.

[17] J. J. Hall, "Electronic Effects in the Elastic Constants of n-Type Silicon," *Physical Review*, vol. 161, no. 3, p. 756, 1967. dx.doi.org/10.1103/PhysRev.161.756

[18] A. K. Samarao, G. Casinovi, and F. Ayazi, "Passive TCF Compensation in High Q Silicon Micromechanical Resonators," in *Proc. IEEE International Conference on Micro Electro Mechanical Systems*, Hong Kong, 2010, pp. 116–119. dx.doi.org/10.1109/MEMSYS.2010.5442553

[19] G. Piazza, R. Abdolvand, G. K. Ho, and F. Ayazi, "Voltage-tunable piezoelectrically-transduced single-crystal silicon micromechanical resonators," *Sensors and Actuators A: Physical*, vol. 111, no. 1, pp. 71–78, 2004. dx.doi.org/10.1016/j.sna.2003.10.021

[20] S. Humad, R. Abdolvand, G. K. Ho, G. Piazza, and F. Ayazi, "High frequency micromechanical piezo-on-silicon block resonators," in *Proc. IEEE International Electron Devices Meeting*, 2003, pp. 39–3. dx.doi.org/10.1109/IEDM.2003.1269437

[21] G. K. Ho, R. Abdolvand, A. Sivapurapu, S. Humad, and F. Ayazi, "Piezoelectric-on-Silicon Lateral Bulk Acoustic Wave Micromechanical Resonators," *Journal of Microelectromechanical Systems*, vol. 17, no. 2, pp. 512–520, 2008. dx.doi.org/10.1109/JMEMS.2007.906758

[22] R. Abdolvand and F. Ayazi, "Enhanced power handling and quality factor in thin-film piezoelectric-on-substrate resonators," in *Proc. IEEE International Ultrasonics Symposium*, 2007, pp. 608–611. dx.doi.org/10.1109/ULTSYM.2007.158

[23] R. Abdolvand, H. Lavasani, G. Ho, and F. Ayazi, "Thin-film piezoelectric-on-silicon resonators for high-frequency reference oscillator applications," *IEEE Transactions on Ultrasonics, Ferroelectrics, and Frequency Control*, vol. 55, no. 12, pp. 2596–2606, 2008. dx.doi.org/10.1109/TUFFC.2008.976

[24] H. Bhugra, S. Lee, W. Pan, M. Pai, and D. Lei, "Commercialization of world's first piezomems resonators for high performance timing applications," in *Proc. IEEE 27th International Conference on Micro Electro Mechanical Systems (MEMS)*, 2014, pp. 204–205. dx.doi.org/10.1109/MEMSYS.2014.6765610

[25] G. Chance, T. Meyer, S. Stoeckl, B. Neurauter, G. Patane, B. Neubauer, G. Minichshofer, J. Kuypers, J. Schoepf, R. Rebel, D. Weninger, K. Chung, T. S. Chew, and O. Mendoza, "Integrated MEMS oscillator for cellular transceivers," in *Proc. IEEE International Frequency Control Symposium*, 2014, pp. 1–3. dx.doi.org/10.1109/FCS.2014.6859910

[26] J. T. M. v. Beek and R. Puers, "A review of MEMS oscillators for frequency reference and timing applications," *Journal of Micromechanics and Microengineering*, vol. 22, no. 1, p. 013001, 2012. dx.doi.org/10.1088/0960-1317/22/1/013001

[27] G. K. Fedder, C. Hierold, J. G. Korvink, and O. Tabata, *Resonant MEMS: Fundamentals, Implementation, and Application*, O. Brand, I. Dufour, S. Heinrich, and F. Josse, Eds. Weinheim: Wiley VCH, 2015.

[28] V. Kaajakari, *Practical MEMS: Design of microsystems, accelerometers, gyroscopes, RF MEMS, optical MEMS, and microfluidic systems.* Las Vegas, Nev.: Small Gear Publishing, 2009.

[29] Senturia, *Microsystem Design.* Boston: Kluwer Academic Publishers, 2002. http://link.springer.com/10.1007/b117574

[30] G. K. Ho, "Design and Characterization of Silicon Micromechanical Resonators," Ph.D. dissertation, Georgia Institute of Technology, 2008. https://smartech.gatech.edu/handle/1853/29634

[31] A. K. Samarao, "Compensation and trimming for silicon micromechanical resonators and resonator arrays for timing and spectral processing," Ph.D. dissertation, Georgia Institute of Technology, 2011. https://smartech.gatech.edu/handle/1853/39543

[32] R. Tabrizian, "Temperature-compensated silicon-based bulk acoustic resonators," Ph.D. dissertation, Georgia Institute of Technology, 2013. https://smartech.gatech.edu/handle/1853/52929

[33] B. P. Harrington, "Performance enhancement of micromachined thin-film piezoelectric-on-silicon lateral-extensional resonators through substrate and tether modifications," Ph.D. dissertation, Oklahoma state university, 2013. http://gradworks.umi.com/36/14/3614418.html

[34] J. Vig and A. Ballato, *Reference for Modern Instrumentation, Techniques, and Technology: Ultrasonic Instruments and Devices II, Chapter 4.* Elsevier, 1998. http://www.ieee-uffc.org/frequency-control/learning/pdf/fcdevices.pdf

[35] B. Neubig and W. Briese, *Das grosse Quarzkochbuch.* Feldkirchen: Franzis Verlag GmbH, 2000. http://www.axtal.com/English/TechnicalNotes/QuarzkochbuchQuarzCrystalCookbook/

[36] J. R. Vig, "Frequency Control Devices." http://www.ieee-uffc.org/frequency-control/learning-vig-tut.asp

[37] "IEEE Ultrasonics, Ferroelectrics, and frequency control society / Learning resources." http://www.ieee-uffc.org/frequency-control/learning.asp

[38] B. A. Auld, *Acoustic fields and waves in solids.* Wiley New York, 1973.

[39] R. Bechmann, A. Ballato, and T. Lukaszek, "Higher-Order Temperature Coefficients of the Elastic Stiffinesses and Compliances of Alpha-Quartz," *Proceedings of the IRE*, vol. 50, no. 8, pp. 1812–1822, 1962. dx.doi.org/10.1109/JRPROC.1962.288222

[40] H. Luoto, K. Henttinen, T. Suni, J. Dekker, J. Makinen, and A. Torkkeli, "MEMS on cavity-SOI wafers," *Solid-State Electronics*, vol. 51, pp. 328–332, 2007. dx.doi.org/10.1016/j.sse.2007.01.007

[41] J. Kiihamäki, "Fabrication of SOI Micromechanical Devices," Ph.D. dissertation, Helsinki University of Technology, 2005. http://lib.tkk.fi/Diss/2005/isbn9513864367/

[42] S. Franssila, *Introduction to microfabrication.* John Wiley & Sons, 2010.

[43] M. J. Madou, *Fundamentals of Microfabrication: The Science of Miniaturization, Second Edition.* CRC Press, 2002.

[44] J. Kuypers, C.-M. Lin, G. Vigevani, and A. Pisano, "Intrinsic temperature compensation of aluminum nitride Lamb wave resonators for multiple-frequency references," in *Proc. IEEE International Frequency Control Symposium*, 2008, pp. 240–249. dx.doi.org/10.1109/FREQ.2008.4622998

[45] G. Ho, S. Pourkamali, and F. Ayazi, "Bulk modes in silicon crystal silicon," in *Proc. Joint Conference of the IEEE International Frequency Control Symposium, the European Frequency and Time Forum*, 2011, pp. 1–6. dx.doi.org/10.1109/FCS.2011.5977882

[46] T. Pensala, M. Prunnila, and A. Jaakkola, "Bulk acoustic wave propagation characteristics in degenerately n-doped Si," in *Proc. IEEE International Frequency Control Symposium*, 2012, pp. 1–4. dx.doi.org/10.1109/FCS.2012.6243713

[47] H. A. C. Tilmans, "Equivalent circuit representation of electromechanical transducers: I. Lumped-parameter systems," *Journal of Micromechanics and Microengineering*, vol. 6, no. 1, pp. 157–176, 1996. dx.doi.org/10.1088/0960-1317/6/1/036

[48] J. Rosenbaum, *Bulk Acoustic Wave Theory and Devices.* Artech House, 1988.

[49] R. J. Matthys, *Crystal oscillator circuits.* John Wiley & Sons Australia, Limited, 1983.

[50] R. Mancini, *Op Amps for Everyone: Design Reference.* Newnes, 2003. http://www.sciencedirect.com/science/book/9780123914958

[51] E. A. Vittoz, M. G. R. Degrauwe, and S. Bitz, "High-performance crystal oscillator circuits: theory and application," *IEEE Journal of Solid-State Circuits*, vol. 23, no. 3, pp. 774–783, 1988. dx.doi.org/dx.doi.org/10.1109/4.318

[52] D. Leeson, "A simple model of feedback oscillator noise spectrum," *Proceedings of the IEEE*, vol. 54, no. 2, pp. 329–330, 1966. dx.doi.org/10.1109/PROC.1966.4682

[53] R. Lifshitz and M. L. Roukes, "Thermoelastic damping in micro- and nanomechanical systems," *Physical Review B*, vol. 61, no. 8, pp. 5600–5609, 2000. dx.doi.org/10.1103/PhysRevB.61.5600

[54] X. Zhang and W. Tang, "Viscous air damping in laterally driven microresonators," in *Proc. IEEE Workshop on Micro Electro Mechanical Systems*, 1994, pp. 199–204. dx.doi.org/10.1109/MEMSYS.1994.555623

[55] R. Tabrizian, M. Rais-Zadeh, and F. Ayazi, "Effect of phonon interactions on limiting the f.Q product of micromechanical resonators," in *Proc. International Conference on Transducers, Solid-State Sensors, Actuators and Microsystems*, 2009, pp. 2131–2134. dx.doi.org/10.1109/SENSOR.2009.5285627

[56] L. Khine, M. Palaniapan, and W. K. Wong, "12.9 MHz Lame-mode differential SOI bulk resonators," in *Proc. International Conference on Transducers, Solid-State Sensors, Actuators and Microsystems*, 2007, pp. 1753–1756. dx.doi.org/10.1109/SENSOR.2007.4300492

[57] V. Kaajakari, T. Mattila, A. Lipsanen, and A. Oja, "Nonlinear mechanical effects in silicon longitudinal mode beam resonators," *Sensors and Actuators A: Physical*, vol. 120, no. 1, pp. 64–70, 2005. dx.doi.org/10.1016/j.sna.2004.11.010

[58] C. Hayashi, *Nonlinear Oscillations in Physical Systems*. Princeton University Press, 2014.

[59] K. Tsubouchi, K. Sugai, and N. Mikoshiba, "AlN Material Constants Evaluation and SAW Properties on AlN/Al2o3 and AlN/Si," in *Proc. IEEE International Ultrasonics Symposium*, 1981, pp. 375–380. dx.doi.org/10.1109/ULTSYM.1981.197646

[60] M. Shahmohammadi, B. Harrington, and R. Abdolvand, "Zero temperature coefficient of frequency in extensional-mode highly doped silicon microresonators," in *Proc. IEEE International Frequency Control Symposium*, 2012, pp. 1 –4. dx.doi.org/10.1109/FCS.2012.6243640

[61] G. Piazza, P. Stephanou, and A. Pisano, "Piezoelectric Aluminum Nitride Vibrating Contour-Mode MEMS Resonators," *Journal of Microelectromechanical Systems*, vol. 15, no. 6, pp. 1406–1418, 2006. dx.doi.org/10.1109/JMEMS.2006.886012

[62] A. Frangi, M. Cremonesi, A. Jaakkola, and T. Pensala, "Interface dissipation in piezoelectric MEMS resonators: An experimental and numerical investigation," in *Proc. IEEE Sensors*, 2013, pp. 1–4. dx.doi.org/10.1109/ICSENS.2013.6688410

[63] J. Segovia-Fernandez and G. Piazza, "Damping in 1 GHz laterally-vibrating composite piezoelectric resonators," in *Proc. IEEE International Conference on Micro Electro Mechanical Systems*, 2015, pp. 1000–1003. dx.doi.org/10.1109/MEMSYS.2015.7051130

[64] L. Novotny, "Strong coupling, energy splitting, and level crossings: A classical perspective," *American Journal of Physics*, vol. 78, no. 11, p. 1199, 2010. dx.doi.org/10.1119/1.3471177

[65] C. v. d. Avoort, R. v. d. Hout, J. J. M. Bontemps, P. G. Steeneken, K. L. Phan, R. H. B. Fey, J. Hulshof, and J. T. M. v. Beek, "Amplitude saturation of MEMS resonators explained by autoparametric resonance," *Journal of Micromechanics and Microengineering*, vol. 20, no. 10, p. 105012, 2010. dx.doi.org/10.1088/0960-1317/20/10/105012

[66] A. H. Nayfeh and M. I. Younis, "Dynamics of MEMS resonators under superharmonic and subharmonic excitations," *Journal of Micromechanics and Microengineering*, vol. 15, no. 10, p. 1840, 2005. dx.doi.org/10.1088/0960-1317/15/10/008

[67] A. H. Nayfeh and D. T. Mook, *Nonlinear Oscillations*. John Wiley & Sons, 2008.

[68] A. Wood and A. Seed, "Activity Dips in AT-Cut Crystals," in *Proc. Annual Symposium on Frequency Control*, 1967, pp. 420–435. dx.doi.org/10.1109/FREQ.1967.199681

[69] G. K. Ho, J. K. Perng, and F. Ayazi, "Micromechanical IBARs: Modeling and Process Compensation," *Journal of Microelectromechanical Systems*, vol. 19, pp. 516–525, 2010. dx.doi.org/10.1109/JMEMS.2009.2030076

[70] "Seiko 5016 oscillator drive circuit data sheet." http://www.electronicsdatasheets.com/download/51cd7158e34e24ae1e000097.pdf?format=pdf&part=Seiko+NPC+-+5016

[71] A. K. Samarao and F. Ayazi, "Intrinsic temperature compensation of highly resistive high-Q silicon microresonators via charge carrier depletion," in *Proc. IEEE International Frequency Control Symposium*, 2010, pp. 334–339. dx.doi.org/10.1109/FREQ.2010.5556315

[72] A. Hajjam, A. Rahafrooz, and S. Pourkamali, "Sub-100ppb/C Temperature Stability in Thermally Actuated High Frequency Silicon Resonators via Degenerate Phosphorous Doping and Bias Current Optimization," in *Proc. IEEE International Electron Device Meeting (IEDM)*, 2010, pp. 7.5.1 – 7.5.4.

[73] E. Ng, V. Hong, Y. Yang, C. Ahn, C. Everhart, and T. Kenny, "Temperature Dependence of the Elastic Constants of Doped Silicon," *Journal of Microelectromechanical Systems*, vol. PP, no. 99, pp. 1–1, 2014. dx.doi.org/10.1109/JMEMS.2014.2347205

[74] C. Herring and E. Vogt, "Transport and Deformation-Potential Theory for Many-Valley Semiconductors with Anisotropic Scattering," *Physical Review*, vol. 101, no. 3, pp. 944–961, 1956. dx.doi.org/10.1103/PhysRev.101.944

[75] P. Csavinszky and N. G. Einspruch, "Effect of Doping on the Elastic Constants of Silicon," *Physical Review*, vol. 132, no. 6, p. 2434, 1963. dx.doi.org/10.1103/PhysRev.132.2434

[76] J. Wang, A. Landin, and M. Lakin, "Low Temperature Coefficient Shear Wave Thin Films for Composite Resonators and Filters," in *Proc. IEEE International Ultrasonics Symposium*, 1983, pp. 491–494. dx.doi.org/10.1109/ULTSYM.1983.198102

[77] A. Jaakkola, M. Prunnila, T. Pensala, J. Dekker, and P. Pekko, "Experimental Determination of the Temperature Dependency of the Elastic Constants of Degenerately Doped Silicon," in *Proc. Joint Conference of the IEEE International Frequency Control Symposium, the European Frequency and Time Forum*, 2013, pp. 421–424. dx.doi.org/10.1109/EFTF-IFC.2013.6702116

[78] C. Bourgeois, E. Steinsland, N. Blanc, and N. F. de Rooij, "Design of resonators for the determination of the temperature coefficients of elastic constants of monocrystalline silicon," in *Proc. IEEE International Ultrasonics Symposium*, 1997, pp. 791–799. dx.doi.org/10.1109/FREQ.1997.639192

[79] A. Jaakkola, M. Prunnila, and T. Pensala, “Temperature compensated resonance modes of degenerately n-doped silicon MEMS resonators,” in *Proc. IEEE International Frequency Control Symposium*, 2012, pp. 1 –5. dx.doi.org/10.1109/FCS.2012.6243712

[80] J. Kim, D. Cho, and R. S. Muller, “Why is (111) silicon a better mechanical material for MEMS?” *Proc. International Conference on Transducers, Solid-State Sensors, Actuators and Microsystems*, pp. 662 – 665, 2001.

[81] K. Tsubouchi and N. Mikoshiba, “Zero-Temperature-Coefficient SAW Devices on AlN Epitaxial Films,” *IEEE Transactions on Sonics and Ultrasonics*, vol. 32, no. 5, pp. 634–644, 1985. dx.doi.org/10.1109/T-SU.1985.31647

[82] M. Levy, H. Bass, and R. Stern, *Handbook of Elastic Properties of Solids, Liquids, and Gases*. Academic Press, 2000.

[83] J. M. Dickinson and P. E. Armstrong, “Temperature Dependence of the Elastic Constants of Molybdenum,” *Journal of Applied Physics*, vol. 38, no. 2, pp. 602–606, 1967. dx.doi.org/10.1063/1.1709381

[84] S. Mishin, M. Gutkin, A. Bizyukov, and V. Sleptsov, “Improving frequency control of temperature compensated surface acoustic wave devices,” in *Proc. Joint Conference of the IEEE International Frequency Control Symposium, the European Frequency and Time Forum*, 2013, pp. 111–113. dx.doi.org/10.1109/EFTF-IFC.2013.6702045

[85] M. Shahmohammadi, H. Fatemi, and R. Abdolvand, “Nonlinearity reduction in silicon resonators by doping and re-orientation,” in *Proc. IEEE International Conference on Micro Electro Mechanical Systems*, 2013, pp. 793–796. dx.doi.org/10.1109/MEMSYS.2013.6474362

[86] “MySQL Wrapper for Matlab download | SourceForge.net.” http://sourceforge.net/projects/mym/

[87] “Gmsh: a three-dimensional finite element mesh generator with built-in pre- and post-processing facilities.” http://geuz.org/gmsh/

[88] D. S. Bindel and S. Govindjee, “Elastic PMLs for resonator anchor loss simulation,” *International Journal for Numerical Methods in Engineering*, vol. 64, no. 6, pp. 789–818, 2005. dx.doi.org/10.1002/nme.1394

[89] “Standard practice for conversion between resistivity and dopant density for boron-doped, phosphorus-doped, and arsenic-doped silicon,” in *Annual Book of ASTM Standards, F 723-99*. West Conshohocken, PA: American Society for Testing and Materials, 2000, pp. 275–291. http://www.astm.org/Standards/F723.htm

[90] V. Kaajakari, A. Alastalo, and T. Mattila, “Electrostatic transducers for micromechanical resonators: free space and solid dielectric,” *IEEE Transactions on Ultrasonics, Ferroelectrics, and Frequency Control*, vol. 53, no. 12, pp. 2484–2489, 2006. dx.doi.org/10.1109/TUFFC.2006.197

Papers I—X

©2015 IEEE. Reprinted, with permission, from A. Jaakkola, M. Prunnila, T. Pensala, J. Dekker and P. Pekko, "Design Rules for Temperature Compensated Degenerately n-type Doped Silicon MEMS Resonators", IEEE Journal of Microelectromechanical Systems, 24(6), pp. 1832—1839, 2015. http://dx.doi.org/10.1109/JMEMS.2015.2443379

Design Rules for Temperature Compensated Degenerately n-Type-Doped Silicon MEMS Resonators

Antti Jaakkola, Mika Prunnila, Tuomas Pensala, James Dekker, and Panu Pekko

***Abstract*— The first- and second-order temperature coefficients and the total temperature-induced frequency deviation of degenerately n-type-doped silicon resonators are modeled. Modeling is based on finite element modelling-based sensitivity analysis of various resonator geometries combined with the experimental results on doping-dependent elastic constants of n-type-doped silicon. The analysis covers a doping range from 2.4 × 10^{17} to 7.5 × 10^{19} cm^{-3}. Families of resonance modes that can be temperature compensated via n-type doping are identified. These include bulk modes, such as the width/length extensional modes of a beam, Lamé/square extensional modes of a plate resonator, as well as flexural and torsional resonance modes. It is shown that virtually all resonance modes of practical importance can reach zero linear temperature coefficient of frequency when correctly designed. Optimal configurations are presented, where a total frequency deviation of ∼150 ppm can be reached. The results suggest that full second-order temperature compensation familiar from AT cut quartz is not possible in silicon resonators with doping below 7.5 × 10^{19} cm^{-3}. However, an analysis relying on extrapolated elastic constant data suggests the possibility of full second-order temperature compensation for a wide range of resonance modes when doping is extended beyond 10^{20} cm^{-3}. [2015-0018]**

***Index Terms*— Micromechanical devices, radiofrequency microelectromechanical systems, acoustic waves, temperature dependence, design for manufacture.**

I. Introduction

During recent years, single-crystal silicon MEMS resonators have gained a foothold in timing and frequency control applications, but the market is still dominated by quartz crystals. The main disadvantage of silicon resonators has been their high thermal drift of about -30 ppm/K, which needs to be compensated in one way or another. Typically temperature compensation of silicon MEMS resonators is achieved with active circuit level compensation techniques, often improved with passive structural compensation based on added amorphous SiO_2 structures.

In this paper, we extend our previous work [1], and identify classes of resonance modes that can be first order temperature compensated through n-type doping and correct resonator design. Passive temperature compensation through heavy doping of silicon has attracted wide attention recently [2]–[5], and experimental results have suggested that temperature stabilization with n-doping is applicable to various types of resonance modes. However, design rules and methodology for finding suitable temperature stabilized resonator designs resonators are missing thus far.

In this work, the first part of the analysis identifies a set of resonance modes that can be temperature compensated with n-type doping. To achieve this, the temperature coefficients for various resonance modes are calculated by combining a finite element modelling based sensitivity analysis with recent experimental data on doping dependent elastic constants of silicon with n-type doping in the range of $n = 1.7 \ldots 7.5 \times 10^{19}\text{cm}^{-3}$ [6]. This part of the analysis builds upon our prior results [1], which were based on a theoretical model for estimating the values of the elastic constants. After identifying modal families that could be temperature compensated by n doping, properties of these modal families are investigated in detail. First and second order temperature coefficients, and the total frequency stability, are calculated for various resonator geometries, orientations and doping levels. Optimal configurations are found, where the total frequency deviation is minimized to ∼150 ppm over the full temperature range of $T = -40... + 85$ °C.

The results suggest that full second order temperature compensation, available for certain quartz cuts, is not possible for doping levels below or equal to $7.5 \times 10^{19}\text{cm}^{-3}$, for which experimental data exists. However, elastic parameter data beyond $7.5 \times 10^{19}\text{cm}^{-3}$ is extrapolated, and it is illustrated that there is a possibility of second order temperature compensation for doping beyond 10^{20}cm^{-3}.

II. Methods

A. Temperature Coefficients of Frequency and Total Frequency Deviation

The temperature dependent frequency of a resonator is customarily expanded as a power series (up to the second order)

$$f(T) = f_0[1 + TCF_1 \times \Delta T + TCF_2 \times \Delta T^2], \qquad (1)$$

where $\Delta T = T - T_0$ is the temperature difference and f_0 is the frequency at the reference temperature T_0. TCF_1 and TCF_2 are the first and second order temperature coefficients of frequency, respectively, defined also at the reference temperature T_0. In this work, the temperature dependencies are

Manuscript received January 18, 2015; revised May 7, 2015; accepted June 3, 2015. Date of publication June 23, 2015; date of current version November 25, 2015. Subject Editor A. Holmes.

The authors are with the VTT Technical Research Centre of Finland, Espoo 02044, Finland (e-mail: antti.jaakkola@vtt.fi; mika.prunnila@vtt.fi; tuomas.pensala@vtt.fi; james.dekker@vtt.fi; panu.pekko@vtt.fi).

Color versions of one or more of the figures in this paper are available online at http://ieeexplore.ieee.org.

Digital Object Identifier 10.1109/JMEMS.2015.2443379

1057-7157 © 2015 IEEE. Personal use is permitted, but republication/redistribution requires IEEE permission.
See http://www.ieee.org/publications_standards/publications/rights/index.html for more information.

studied over the extended industrial temperature range of $T = -40... + 85$ °C, and the convention of selecting $T_0 = +25$ °C is followed. Higher-order temperature coefficients of frequency are neglected.

As a figure of merit for the temperature stability of a resonator, the total relative frequency deviation over the full temperature range is used:

$$\Delta f_{\text{total}} = \max_T (\Delta f/f_0) - \min_T (\Delta f/f_0), \quad (2)$$

where the relative frequency change is given by

$$\frac{\Delta f}{f_0} = \frac{f - f_0}{f_0} = TCF_1 \times \Delta T + TCF_2 \times \Delta T^2. \quad (3)$$

Next, typical orders of magnitude of the total frequency deviation Δf_{total} are discussed shortly. For weakly doped silicon ($n < 10^{18}\text{cm}^{-3}$), the first order temperature coefficient of frequency dominates, and typically the total frequency drift for any resonance mode is more than 3000 ppm over $T = -40... + 85$ °C. N-type doped silicon resonators with first order temperature compensation ($TCF_1 = 0$) have been demonstrated [4], [6], whereby the total frequency deviation Δf_{total} of <300 ppm comes then from TCF_2 alone. Full second order temperature compensation, i.e. where both TCF_1 and TCF_2 are simultaneously set to zero, has not been demonstrated for doped silicon resonators. This is available in certain quartz cuts, where the remaining small (∼20 ppm) total frequency deviation comes from a higher-order temperature dependency.

B. Calculation of TCF_1 and TCF_2

The frequency of an acoustic resonator is given by

$$f = \frac{1}{L}\sqrt{\frac{c}{\rho}}, \quad (4)$$

where ρ, c and L are the resonator material density, characteristic stiffness and characteristic length, respectively. The characteristic stiffness depends on the elastic parameters, and for silicon, the three independent parameters c_{11}, c_{12} and c_{44} fully describe the elastic properties. The relative frequency change due to a change in the (temperature dependent) elastic parameters $\delta c_{ij}(T)$, thermal expansion $\delta L(T)/L$ and change in density $\delta\rho(T)/\rho$ can be denoted as

$$\frac{\delta f}{f}(T) = \frac{1}{f}\sum_{ij=11,12,44} \frac{\partial f}{\partial c_{ij}} \delta c_{ij}(T) - \frac{\delta L}{L}(T) - \frac{1}{2}\frac{\delta\rho}{\rho}(T). \quad (5)$$

We assume a second order approximation for thermal expansion

$$\frac{\delta L}{L}(T) = (\alpha_1 \Delta T + \alpha_2 \Delta T^2), \quad (6)$$

where α_1 and α_2 are the first and second order thermal expansion coefficients, respectively. The last term in (5) can be expressed as

$$\frac{\delta\rho}{\rho} = -\frac{\delta V}{V} = -3\frac{\delta L}{L} - 3(\frac{\delta L}{L})^2 - (\frac{\delta L}{L})^3, \quad (7)$$

where relation to $\delta L/L$ is justified by isotropy of thermal expansion in silicon. Using (6) in (7) and keeping terms up to second order in ΔT one obtains

$$\frac{\delta\rho}{\rho} = -3[\alpha_1 \Delta T + (\alpha_2 + \alpha_1^2)\Delta T^2]. \quad (8)$$

Using values $\alpha_1 = 2.84 \times 10^{-6}\,\text{K}^{-1}$ and $\alpha_2 = 8.5 \times 10^{-9}\,\text{K}^{-2}$ for the thermal expansion coefficients [7], one can approximate term α_1^2 as negligible in (8), and express (5) as

$$\frac{\delta f}{f}(T) \approx \frac{1}{f}\sum_{ij=11,12,44} \frac{\partial f}{\partial c_{ij}} \delta c_{ij}(T) + \frac{1}{2}(\alpha_1 \Delta T + \alpha_2 \Delta T^2). \quad (9)$$

The temperature dependency of the elastic parameters for a given doping level n is given by a second order expansion such that

$$c_{ij}(T, n) = c_{ij}^0(n)[1 + a_{ij}(n)\Delta T + b_{ij}(n)\Delta T^2], \quad (10)$$

where $a_{ij}(n)$ and $b_{ij}(n)$ are the first- and second-order temperature coefficients of the elastic parameters, respectively, and $c_{ij}^0(n)$ is the constant term. The linear temperature coefficient of frequency TCF_1 is defined as the first derivative of (9)

$$TCF_1 = \frac{1}{f}\left.\frac{\mathrm{d}f}{\mathrm{d}T}\right|_{T=T_0} = \frac{1}{f}\sum_{ij} \frac{\partial f}{\partial c_{ij}} c_{ij}^0 a_{ij} + \alpha_1/2, \quad (11)$$

and the second order temperature coefficient of frequency TCF_2 is obtained as

$$TCF_2 = \frac{1}{2f}\left.\frac{\mathrm{d}^2 f}{\mathrm{d}T^2}\right|_{T=T_0} = \frac{1}{f}\sum_{ij} \frac{\partial f}{\partial c_{ij}} c_{ij}^0 b_{ij} + \alpha_2/2. \quad (12)$$

C. Numerical Sensitivity Analysis

Linear sensitivities $\partial f/\partial c_{ij}$ of the resonance frequencies to the elastic parameters are needed for evaluation of (11) and (12); these derivatives were calculated using finite element modelling with Comsol Multiphysics. Eigenfrequency analyses were used for calculating $\partial f/\partial c_{ij}$ for the resonance modes. Two routines of parametric sweeps for geometry variation were performed. A starting point for the parametric variations was a beam resonator having dimensions of $W \times L \times H = 40 \times 320 \times 10\,\mu\text{m}^3$ on a 100 oriented silicon wafer with its length aligned along the 100 direction (see Fig. 1(a)). In simulation S1, the in-plane rotation angle θ of the beam was varied from 0° to 45° so that the beam alignment changed from 100 to 110 (Fig. 1(b)). In simulation S2 (Fig. 1(c)), the beam width W was increased from $40\,\mu$m to $640\,\mu$m so that the aspect ratio W/L changed from ∼ 0.1 to 2. No boundary conditions were applied to the model in order to allow an unrestricted appearance of resonance modes in the modal analysis.

D. Interpolation of Elastic Parameter Data

Elastic constants that were used as input for the calculations over the full doping range of $n = 0 \ldots 7.5 \times 10^{19}\text{cm}^{-3}$ were based on recent experimentally determined data set for heavily-doped ($n > 1.7 \times 10^{19}\text{cm}^{-3}$) silicon [6]

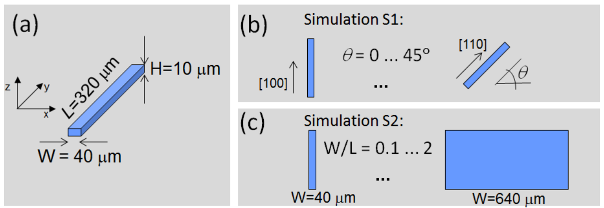

Fig. 1. Parametrically varied resonator geometry used for finite element modelling. (a) Basic geometry used as a starting point of the simulations. (b) In simulation S1, the orientation of the beam was varied from 100 to 110. (c) The in-plane aspect ratio was varied from ~0.1 to 2 in simulation S2.

(supported by results in [8]), and on the data for relatively weakly-doped ($n = 2.4 \times 10^{17}\text{cm}^{-3}$) silicon [7]. Third order polynomials were fitted to the data to form the doping dependent functions $c^0_{ij}(n)$, $a_{ij}(n)$ and $b_{ij}(n)$. The data points, the interpolation functions used in the simulations and the associated coefficients are shown in Fig. 2(a)–(j).

E. Analysis Procedure

The following analysis concentrates first on identifying the resonance modes that have a potential for (at least) first order temperature compensation. This is achieved by evaluating TCF_1 for all resonance modes that were obtained from simulations S1 and S2. Evaluation of TCF_1 is done at $n = 7.5 \times 10^{19}\text{cm}^{-3}$, where the elastic parameters are maximally deviated from their original values at low doping levels. Resonance modes with $TCF_1 \geq 0$ are searched for, since they can be temperature compensated to first order by decreasing the doping level.

After identifying the interesting resonance modes, we investigate the whole parameter space of orientation, in-plane aspect ratio and doping to find optimal combinations producing the lowest total frequency deviations.

III. Results

A. Identification of Modal Branches Which Can Be Temperature Compensated

Fig. 3(a) shows the dispersion of the modal frequencies as a function of the parametric variations. Results of simulations S1 and S2 are combined in the same plot. The linear temperature coefficient TCF_1, calculated at the doping level of $n = 7.5 \times 10^{19}\text{cm}^{-3}$, is illustrated with color coding for each resonance mode. TCF_1 of selected resonance mode branches are plotted in detail in Fig. 3(b), and representative mode shapes from important branches are shown in 3(c).

The following five modal families fulfilling the criterion $TCF_1 \geq 0$ can be identified in the dispersion plot. The branch labels in parentheses correspond to those in Fig. 3, and the subscript indices stand for overtones of the modal branches.

1) *Out-of-Plane Flexural Modes ($OPF_1 \ldots OPF_5$):* At $\theta = 0$, $W/L \sim 0.1$ these modes have their TCF_1 in the range of +8 ppm/K…+14 ppm/K (decreasing with increasing overtone order). Within the OPF_1 branch, TCF_1 is observed to peak at +20 ppm/K near $W/L = 1$, where the mode shape has evolved into a saddle mode.
2) *In-Plane Flexural Modes ($IPF_1 \ldots IPF_2$):* The behavior of these modes in terms of TCF_1 is largely similar to the OPF modes.
3) *Torsional Modes ($T_1 \ldots T_3$):* These modes have a clearly positive TCF_1 with a maximum value of +18 ppm/K, which is is attained when the resonator beam is aligned with the 110 direction. TCF_1 slightly decreases with increasing overtone order. Branch T_1 is coupled to OPF_3, resulting in branch splitting near $\theta = 10°$. Therefore, the T_1 curve in plot 3(b) is missing at the splitting region. Similar coupling occurs between T_2/OPF_4 and T_3/OPF_5 branches, respectively.
4) *Width-Extensional/Square Extensional Mode Resonance Branch (WE/SE):* the mode shape evolves from an x-directed WE mode at low in-plane aspect ratios W/L (not shown in the the dispersion plot due to the high modal frequency) to an SE mode of a square plate ($W = L$), and then again to a y-directed WE mode at $W/L > 1$. The WE modes approach a TCF_1 of approximately +8 ppm/K, while TCF_1 of the SE mode is close to zero.
5) *Length-Extensional/Lamé Mode Resonance Branch ($LE/Lamé$):* This branch has a clearly positive TCF_1 for all aspect ratios and for θ deviating from zero by less than approximately 20°. The mode shape evolves from a y-directed length extensional (LE) mode into the Lamé (or wineglass) mode of a square resonator ($W/L = 1$), and then further to an x-directed LE mode as the resonator in-plane aspect ratio is further increased. For 100 alignment, maximal TCF_1 of slightly more than +20 ppm/K occurs with the pure Lamé mode, while TCF_1 of the length extensional modes approaches +14 ppm/K when the resonator geometry becomes more beam-like.

Fig. 3(b) shows that the TCF_1 curves for the OPF_1, IPF_1 and LE branches are very similar to each other for $\theta = 0° \ldots 45°$. The characteristic stiffness, introduced in Eq. (4), for an LE or flexural mode of a beam resonator is given by the Young's modulus in the direction of the beam, which, for example, in the [100] direction can be approximated by

$$Y_{[100]} = c_{11} - 2c_{12}^2/(c_{11} + c_{12}). \tag{13}$$

This approximation was calculated numerically for all orientations θ and applied to solve the linear sensitivities $\partial f/\partial c_{ij}$ of (11). The obtained approximate TCF_1 curve has been plotted in Fig. 3(b), and it is seen to follow the OPF_1, IPF_1 and LE branches rather well.

In Fig. 3(b), values of TCF_1 at doping level of $n = 2.4 \times 10^{17}\text{cm}^{-3}$ have been plotted as well, in addition to the corresponding values calculated at the maximum doping level. TCF_1 was found to be near −30 ppm/K for all cases.

B. Detailed Temperature Behavior

In this Section, branches $LE/Lamé$, T_1 and WE/SE are investigated in more detail. First, results from simulation

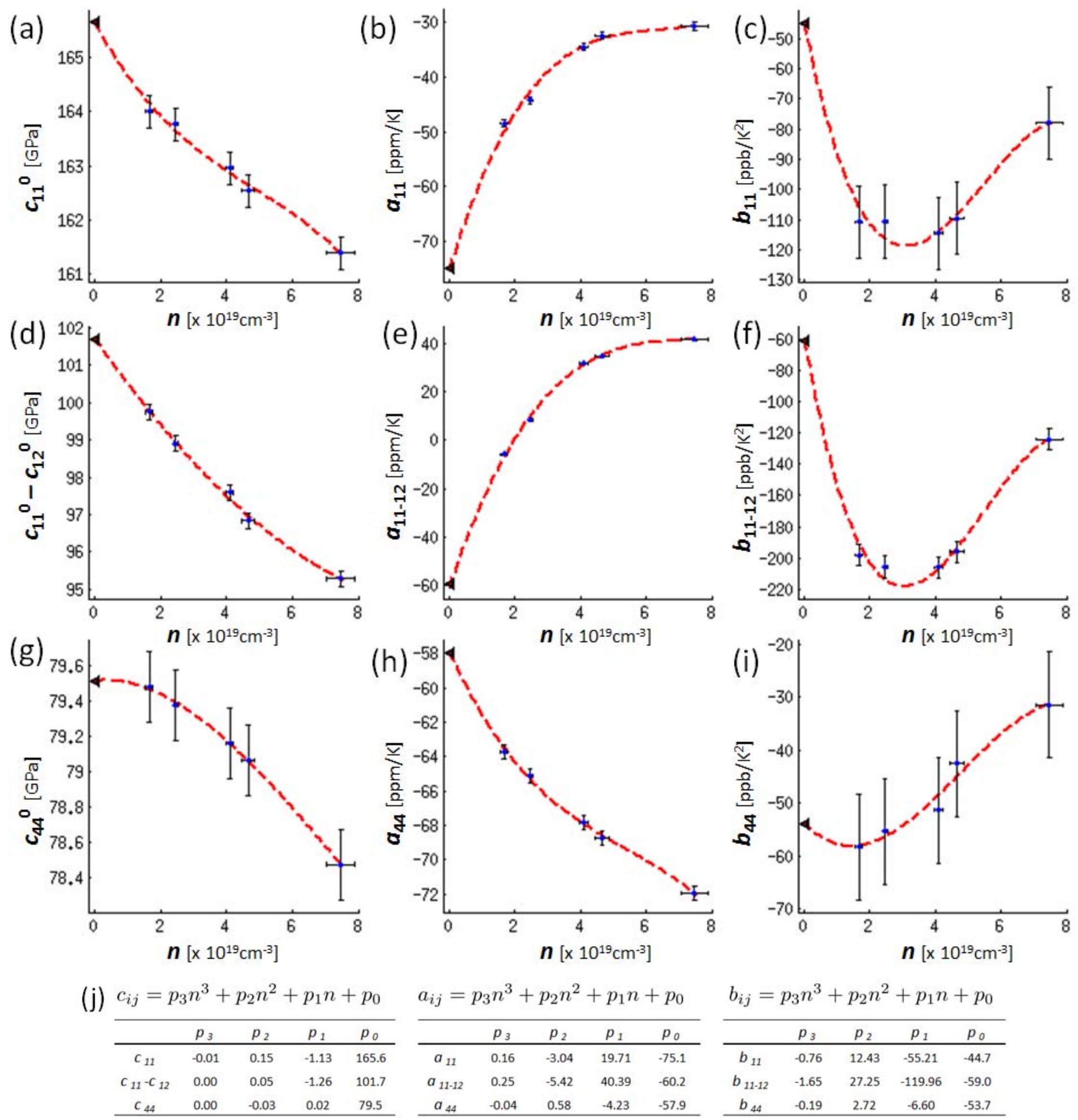

(j)

$c_{ij} = p_3n^3 + p_2n^2 + p_1n + p_0$

	p_3	p_2	p_1	p_0
c_{11}	-0.01	0.15	-1.13	165.6
c_{11}-c_{12}	0.00	0.05	-1.26	101.7
c_{44}	0.00	-0.03	0.02	79.5

$a_{ij} = p_3n^3 + p_2n^2 + p_1n + p_0$

	p_3	p_2	p_1	p_0
a_{11}	0.16	-3.04	19.71	-75.1
a_{11-12}	0.25	-5.42	40.39	-60.2
a_{44}	-0.04	0.58	-4.23	-57.9

$b_{ij} = p_3n^3 + p_2n^2 + p_1n + p_0$

	p_3	p_2	p_1	p_0
b_{11}	-0.76	12.43	-55.21	-44.7
b_{11-12}	-1.65	27.25	-119.96	-59.0
b_{44}	-0.19	2.72	-6.60	-53.7

Fig. 2. (a)–(i) Temperature coefficients of the elastic parameters c_{ij} as a function of carrier concentration n. Blue dots with error bars represent experimental data from [6] and the black triangles at the lowest doping level represent data from [7]. Red dashed lines are third order polynomial fits to the experimental data; these fits were used in the simulations to evaluate (11), (12) and (2) with varying n. The first, second and third column represent the constant terms c_{ij}^0, linear coefficients a_{ij}, and second-order coeffients b_{ij} at $T = 25$ °C, respectively, see (10). c_{11-12}^0, a_{11-12} and b_{11-12} are shorthands for the coefficients of $c_{11} - c_{12}$. The dependent coefficient a_{12} is readily evaluated as $a_{12} = (a_{11}c_{11}^0 - a_{11-12}c_{11-12}^0)/c_{12}^0$, and a similar equation holds for b_{12}. (j) Coefficients of the polynomial fits.

S1 are used to find optimal configurations which minimize the total frequency deviation Δf_{total} (Eq. (2)) on the $LE/Lamé$ and T_1 branches when the resonator orientation θ and doping n are varied (simulation S1). Then, optimal combinations of the in-plane aspect ratio W/L and doping n are searched from the WE/SE and $LE/Lamé$ branches using data from simulation S2.

Figure 4 shows the results for the $LE/Lamé$ and torsional T_1 branches, respectively, when θ is varied. It is found in Figs. 4(a),(e) that the lowest carrier concentration that yields $TCF_1 = 0$ within the $LE/Lamé$ branch is $n_{0,\text{LE}} \sim 2.4 \times 10^{19}\text{cm}^{-3}$, while the corresponding limit for the T_1 branch is slightly smaller $n_{0,\text{T}_1} \sim 2.1 \times 10^{19}\text{cm}^{-3}$. Above these carrier concentration limits, there always exists an angle at which zero TCF_1 can be obtained. The second order coefficient TCF_2 (Figs. 4(b),(f)) is most negative between $n \sim 2 \ldots 4 \times 10^{19}\text{cm}^{-3}$ for both modal branches, and its magnitude is decreased towards low and high doping concentrations. The total frequency deviation Δf_{total} is dominated by the non-zero linear coefficient TCF_1 below

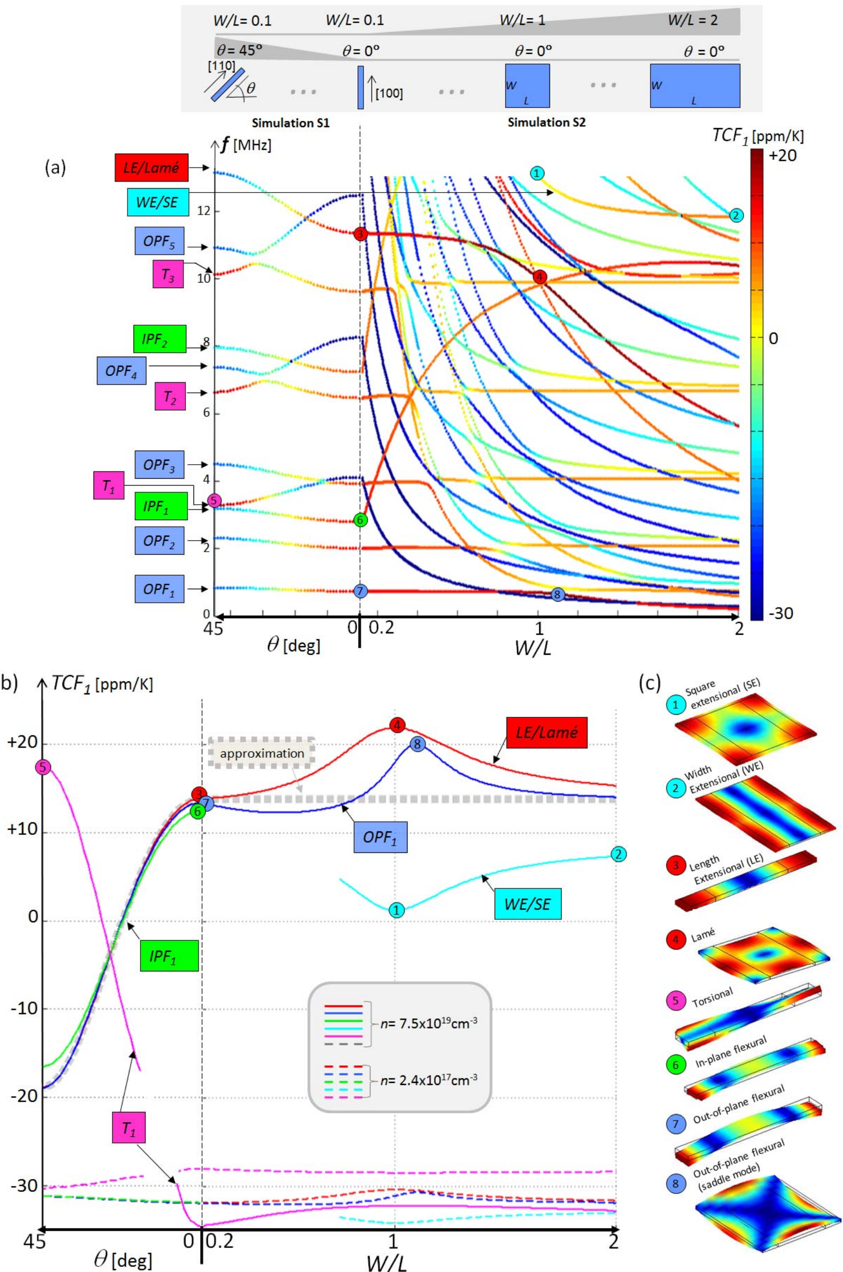

Fig. 3. (a) Resonance frequencies and their linear temperature coefficients TCF_1 (color coding) as a function of the resonator orientation θ (Simulation S1) and in-plane aspect ratio W/L (Simulation S2). The top illustrations show how the geometry is modified in parametric simulations S1 and S2, respectively. Dopant concentration of $7.5 \times 10^{19}\text{cm}^{-3}$ has been assumed for evaluating TCF_1. Modes with $TCF_1 \geq 0$ (from yellow to red) are desired ones, since their TCF_1 can be set to zero by lowering the doping. Following modal branches and their overtones (denoted by subscripts) are identified in the plot: out-of-plane flexural modes (OPF), in-plane flexural modes (IPF), torsional modes (T), width extensional/square extensional modes (WE/SE), and length extensional/Lamé modes. ($LE/Lam\acute{e}$). (b) TCF_1 for selected branches plotted in detail. Solid lines show TCF_1 evaluated at a doping level of $n = 7.5 \times 10^{19}\text{cm}^{-3}$, while their dashed counterparts denote the corresponding TCF_1 evaluated at $n = 2.4 \times 10^{17}\text{cm}^{-3}$. The grey dashed line represents the TCF_1 based on the approximation discussed in the context of Eq. (13). (c) Illustrations of the mode shapes of selected modes from the modal branches. Labels 1-8 correspond to those found in plots (a) and (b).

the limits $n_{0,\text{LE}}$ or n_{0,T_1}, respectively. At higher doping levels, travelling along the "valleys" of Figs. 4(c),(g), it is found that the total frequency variation deviation Δf_{total} steadily decreases on both branches to $\sim$150 ppm, reached at the maximal doping level of $n_{max} = 7.5 \times 10^{19}\text{cm}^{-3}$. Optimal orientations at this doping level are $\theta \sim 23°$ and $\theta \sim 28°$ degrees for the $LE/Lam\acute{e}$ and T_1 branches, respectively. The paths for minimum total frequency variation coincide with the $TCF_1 = 0$ curves. As discussed in previous section, the behavior of the IPF_1 and OPF_1 branches was very similar

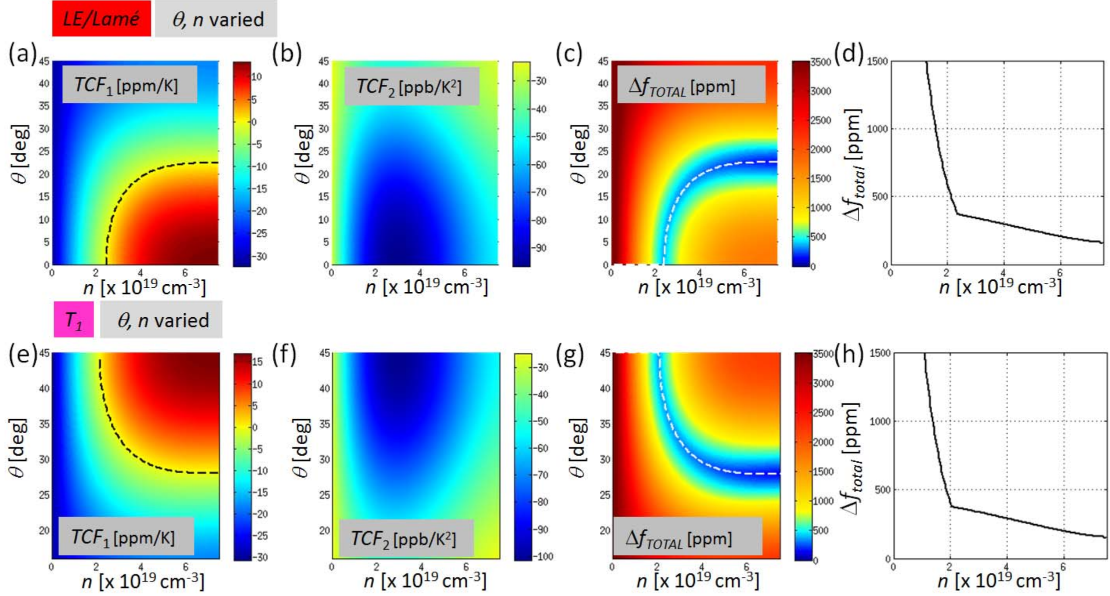

Fig. 4. Details of temperature dependent behavior within the $LE/Lam\acute{e}$ branch [(a)–(d)] and the T_1 branch [(e)–(h)] as a function of doping level n and resonator orientation θ. $\theta = 0°/45°$ correspond to alignment with 100/110. Color coding of (a)/(e) and (b)/(f) illustrate the first and second order temperature coefficients of frequency. The dashed lines of (a)/(e) denote the locus of points (n, θ) for which TCF_1 equals to zero. The total frequency variation Δf_{total} over the full temperature range of $T = -40 \ldots +85$ °C is shown in (c)/(g). The dashed lines of (c)/(g) denote the in-plane rotation angle θ which minimizes Δf_{total} for each n. Figs. (d)/(h) are plots of Δf_{total} along this line. Note that orientations of θ below 16° have been omitted for the T_1 branch due to coupling with the OPF_3 branch (see discussion in Section III-A).

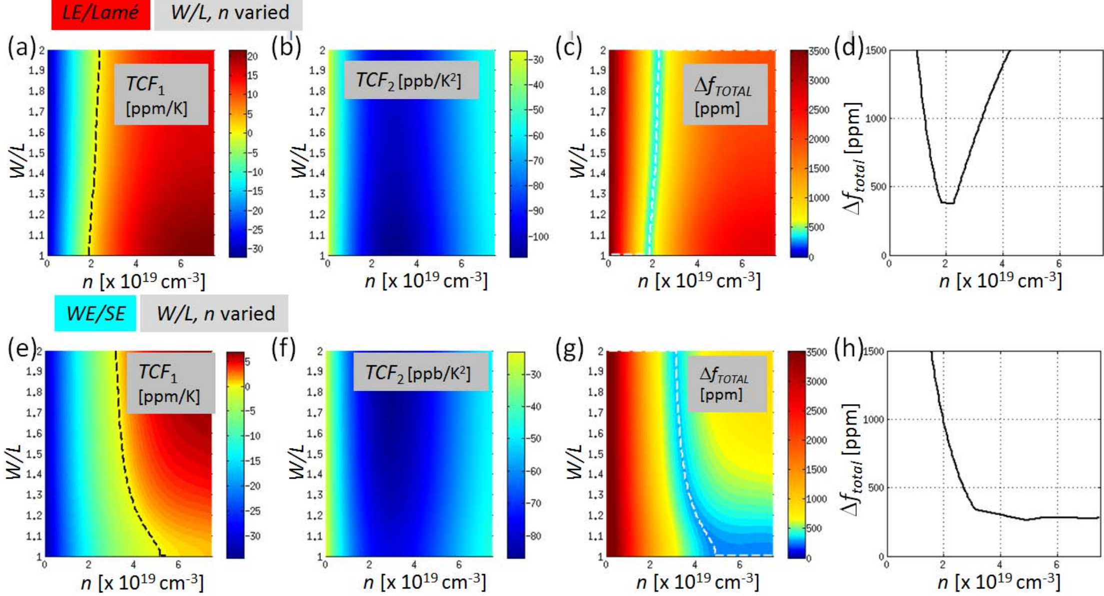

Fig. 5. Details of temperature behavior within the $LE/Lam\acute{e}$ branch [(a)–(d)] and the WE/SE branch [(e)–(h)] as a function of doping level n and resonator in-plane aspect ratio W/L. Color coding of (a)/(e) and (b)/(f) illustrate the first and second order temperature coefficients of frequency. The dashed lines of (a)/(e) denote the locus of points $(n, W/L)$ for which TCF_1 equals to zero. The total frequency variation Δf_{total} over the full temperature range of $T = -40 \ldots +85$ °C is shown in (c)/(g). The dashed lines of (c)/(g) denote the in-plane aspect ratio W/L which minimizes Δf_{total} for each n. Figs. (d)/(h) are plots of Δf_{total} along this line.

to the $LE/Lam\acute{e}$ branch characteristics when θ was varied. Therefore, one can expect the results of Fig. 4(a)-(d) to describe the behavior of these modes as well.

Fig. 5 illustrates TCF_1, TCF_2 and Δf_{total} for the $LE/Lam\acute{e}$ and WE/SE branches, respectively, when the aspect ratio W/L is varied. With increasing doping,

$TCF_1 = 0$ is first attained at the doping level of $n_{0,Lam\acute{e}} \sim 1.9 \times 10^{19}\text{cm}^{-3}$ on the $LE/Lam\acute{e}$ branch, and on the WE/SE branch the corresponding threshold is $n_{0,WE} \sim 3.1 \times 10^{19}\text{cm}^{-3}$. The second order coefficient TCF_2 stays below zero for all n and W/L, and its magnitude is again most negative for $n \sim 2 \ldots 4 \times 10^{19}\text{cm}^{-3}$. Since the zero-$TCF_1$ region for the $LE/Lam\acute{e}$ branch is limited to the doping range of $n \sim 1.9 \ldots 2.3 \times 10^{19}\text{cm}^{-3}$(which coincides with the most negative region for TCF_2), the minimal total frequency deviation remains at a comparatively high level of ~380 ppm. For the WE/SE branch, The region with $TCF_1 = 0$ is found at a doping range of $n \sim 3.1 \ldots 5.1 \times 10^{19}\text{cm}^{-3}$, and a minimum total frequency deviation of ~250 ppm is reached with a square geometry ($W/L = 1$) at the end of this doping range.

IV. Discussion

Five modal families were identified by inspecting the dispersion curves in Figs. 3. As discussed in [4], shear modes whose dependency on elastic parameters c_{ij} is a function of only the $(c_{11} - c_{12})$ term are maximally affected by n-doping. This was exemplified by the behavior within the LE/Lamé modal branch, where the largest TCF_1 was found for the Lamé mode and a lower TCF_1 was found for the LE modes. The reason for the difference can be illuminated by inspecting the formulas of the modal frequencies. Closed form expression for the Lamé mode frequency exists and the following relationship holds:

$$f_{\text{Lamé}} \sim \sqrt{c_{11} - c_{12}}.$$

Using the approximation of Eq. (13) to evaluate the resonance frequency of an LE mode resonator, and linearizing it with respect to the changes in the elastic parameters δc_{ij}, one finds the relationship

$$\delta f_{LE} \sim (\delta c_{11} - \delta c_{12}) + 0.2\delta c_{12}.$$

It is apparent that the functional dependence of the LE mode on the c_{ij} parameters is to a large part similar to that of the Lamé mode - except for the added term $0.2\delta c_{12}$.

The WE/SE-branch is of special practical interest due to the fact that the WE and SE bulk mode silicon resonators have shown good performance in terms of phase noise as well as good electromechanical coupling [9], [10]. Additionally, these resonance modes can be effectively transduced with piezoelectric thin films, see Refs. [11], [12]. These modes, with their TCF_1 in the range 0...+ 8 ppm/K, can still take full advantage of n-doping for temperature stabilization, although the WE/SE bulk modes have clearly less shear-mode character than the LE/Lamé modes.

It is an anticipated outcome of the analysis that the torsional modes with evident shear character belong to the group of modes that can be temperature stabilized. However, the fact that the maximum TCF_1 (Fig. 3(b), label "5") of the torsional mode branch T_1 is slightly smaller than that of the pure shear Lamé mode (Fig. 3(b), label "4") shows that the dependency on the elastic parameters is not of pure $(c_{11} - c_{12})$ form.

In addition to the five highlighted modal families one can pinpoint other branches in Fig. 3(a) that fulfil the $TCF_1 \geq 0$ criterion. Typically these are overtone modes of the five identified modal families or coupled modes having combined characteristics.

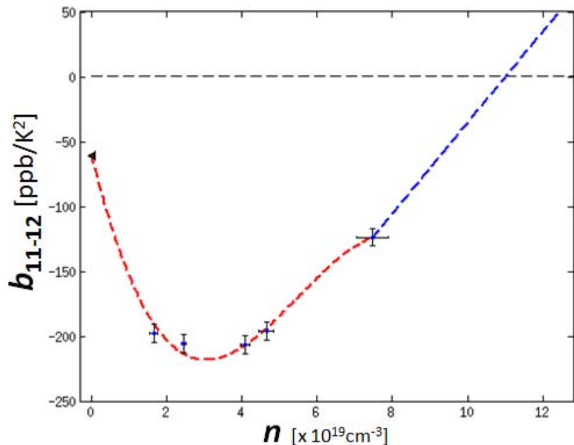

Fig. 6. Extrapolation (blue dashed line) for $b_{11-12}(n)$ used for calculation of the results of Fig. 7.

Temperature compensated behavior of the presented modal branches can be found also in resonators fabricated on 110 oriented wafers. The presented parametric geometry sweeps on a 100 oriented silicon wafer were chosen, since they portrayed the temperature compensated behavior of all five modal families. A calculation similar to simulation S2 was presented in [1], but with geometry aligned with the 110 direction. There it was observed that neither the $LE/Lam\acute{e}$ branch nor the WE/SE branch could be temperature compensated by n type doping when using this alignment.

V. Possibility of Second Order Temperature Compensation With Increased Doping

It was seen in Section III-B that the total frequency deviation Δf_{total} can be minimized at the highest doping level of $n_{max} = 7.5 \times 10^{19}\text{cm}^{-3}$ for certain modal branches. The decreasing nature of the total frequency deviation Δf_{total} of Figs. 4(d),(h) and 5(h) raises the question of whether this trend would be continued at even increased doping. Most of the contribution to the remaining (non-zero) second order coefficient TCF_2 comes from the second order temperature coefficient b_{11-12} (see Fig. 2(f)), which has a decreasing magnitude for $n > 4 \times 10^{19}\text{cm}^{-3}$. To illustrate the possibility of the existence of a resonance mode with full second order temperature compensation, we assume $b_{11-12}(n)$ to grow linearly so that it crosses zero at $n \sim 11 \times 10^{19}\text{cm}^{-3}$, Fig. 6. To simplify the treatment, all other temperature constants c_{ij}^0, a_{ij}^0 and b_{ij}^0 of Fig. 2 are assumed to remain unchanged from the values they have at $n_{max} = 7.5 \times 10^{19}\text{cm}^{-3}$. Using these assumptions, calculations for the $LE/Lam\acute{e}$ mode branch (Fig. 4(a)-(d)) for $\theta = 0° \ldots 45°$ were repeated, now extending the doping level to $n = 13 \times 10^{19}\text{cm}^{-3}$. The results are shown in Fig. 7.

It is found in Fig. 7(b) that TCF_2 approaches zero with increasing doping, and, finally reaches zero at $n \sim 11.3 \times 10^{19}\text{cm}^{-3}$. Fig 7(e) shows that the curves for

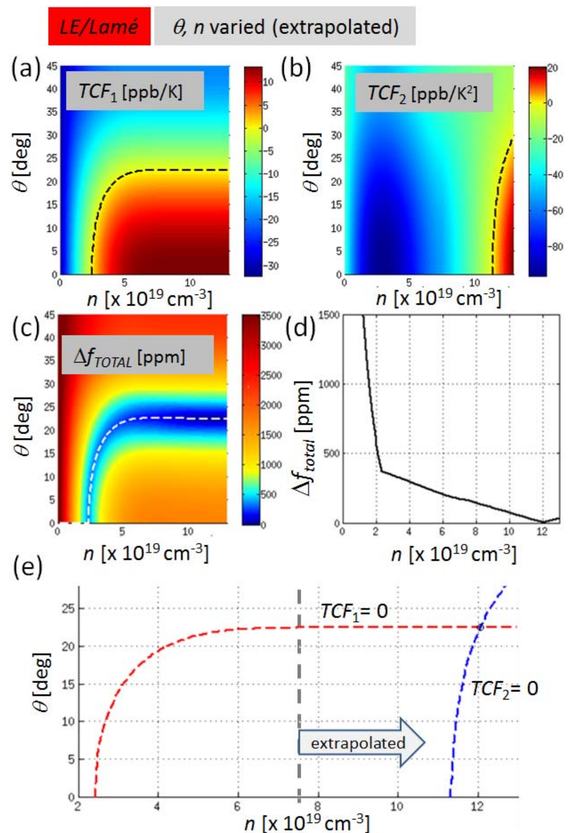

Fig. 7. Extrapolated temperature behavior of the $LE/Lam\acute{e}$ branch, when orientation θ and doping n are varied. (a)-(d) are similar to Fig. 4(a)-(d). (e) reproduces $TCF_1 = 0$ and $TCF_2 = 0$ curves from plots (a) and (b) and highlights their crossing.

$TCF_1 = 0$ and $TCF_2 = 0$ intersect each other at $\theta = 22.5°$ when the doping level is $n \sim 12 \times 10^{19}\text{cm}^{-3}$. At this point the total frequency deviation Δf_{total} reaches zero, as seen in Fig. 7(d).

Again, due to the similarity of the IPF, OPF and $LE/Lam\acute{e}$ branches (with θ variation), the qualitative result obtained here can be expected to apply among all of these branches. This, on the other hand, implies that resonators covering a wide range of frequencies from <100 kHz (flexural modes) to 100 MHz (overtone length extensional) could potentially be second order temperature compensated.

VI. Conclusions

First and second order temperature coefficients and the total temperature induced frequency deviation of degenerately n-type doped silicon resonators were modelled covering a doping range from $2.4 \times 10^{17}\text{cm}^{-3}$ to $7.5 \times 10^{19}\text{cm}^{-3}$.

Families of resonance modes that can be temperature compensated via n-type doping were identified: These included bulk modes such as the width/length extensional modes of a beam, Lamé/square extensional modes of a plate resonator, as well as flexural and torsional resonance modes. It is shown that virtually all resonance modes of practical importance can reach zero linear temperature coefficient of frequency when correctly designed. Optimal configurations were found, where a total frequency deviation of ∼150 ppm can be reached.

The results indicated that full second order temperature compensated familiar from AT cut quartz crystals is not possible in silicon resonators with doping below $7.5 \times 10^{19}\text{cm}^{-3}$. However, an analysis relying on extrapolated elastic parameter data suggests this could be possible if doping is extended beyond 10^{20}cm^{-3}.

Acknowledgements

A.J. wishes to thank Juho Luomahaara and Jyrki Kiihamäki for their help with the manuscript.

References

[1] A. Jaakkola, M. Prunnila, and T. Pensala, "Temperature compensated resonance modes of degenerately n-doped silicon MEMS resonators," in *Proc. IEEE Int. Freq. Control Symp. (FCS)*, May 2012, pp. 1–5.

[2] A. K. Samarao, G. Casinovi, and F. Ayazi, "Passive TCF compensation in high Q silicon micromechanical resonators," in *Proc. IEEE 23rd Int. Conf. Micro Electro Mech. Syst. (MEMS)*, Hong Kong, Jan. 2010, pp. 116–119.

[3] A. Hajjam, A. Rahafrooz, and S. Pourkamali, "Sub-100 ppb/°C temperature stability in thermally actuated high frequency silicon resonators via degenerate phosphorous doping and bias current optimization," in *Proc. IEEE Int. Electron Device Meeting (IEDM)*, Dec. 2010, pp. 7.5.1–7.5.4.

[4] T. Pensala, A. Jaakkola, M. Prunnila, and J. Dekker, "Temperature compensation of silicon MEMS resonators by heavy doping," in *Proc. IEEE Int. Ultrason. Symp.*, Oct. 2011, pp. 1952–1955.

[5] M. Shahmohammadi, B. P. Harrington, and R. Abdolvand, "Zero temperature coefficient of frequency in extensional-mode highly doped silicon microresonators," in *Proc. IEEE Int. Freq. Control Symp. (FCS)*, May 2012, pp. 1–4.

[6] A. Jaakkola, M. Prunnila, T. Pensala, J. Dekker, and P. Pekko, "Determination of doping and temperature-dependent elastic constants of degenerately doped silicon from MEMS resonators," *IEEE Trans. Ultrason., Ferroelectr., Freq. Control*, vol. 61, no. 7, pp. 1063–1074, Jul. 2014.

[7] C. Bourgeois, E. Steinsland, N. Blanc, and N. F. de Rooij, "Design of resonators for the determination of the temperature coefficients of elastic constants of monocrystalline silicon," in *Proc. IEEE Int. Freq. Control Symp.*, May 1997, pp. 791–799.

[8] E. J. Ng, V. A. Hong, Y. Yang, C. H. Ahn, C. L. M. Everhart, and T. W. Kenny, "Temperature dependence of the elastic constants of doped silicon," *J. Microelectromech. Syst.*, vol. 24, no. 3, pp. 730–741, Jun. 2015.

[9] V. Kaajakari, T. Mattila, A. Oja, J. Kiihamaki, and H. Seppa, "Square-extensional mode single-crystal silicon micromechanical resonator for low-phase-noise oscillator applications," *IEEE Electron Device Lett.*, vol. 25, no. 4, pp. 173–175, Apr. 2004.

[10] G. K. Ho, S. Pourkamali, and F. Ayazi, "Bulk modes in silicon crystal silicon," in *Proc. Joint Conf. IEEE Int. Freq. Control Eur. Freq. Time Forum (FCS)*, May 2011, pp. 1–6.

[11] A. Jaakkola *et al.*, "Piezoelectrically transduced single-crystal-silicon plate resonators," in *Proc. IEEE Ultrason. Symp.*, Beijing, China, Nov. 2008, pp. 717–720.

[12] G. K. Ho, R. Abdolvand, and F. Ayazi, "High-order composite bulk acoustic resonators," in *Proc. IEEE 20th Int. Conf. Micro Electro Mech. Syst.*, Jan. 2007, pp. 791–794.

Authors' photographs and biographies not available at the time of publication.

Paper II

©2015 IEEE. Reprinted, with permission, from A. Jaakkola, P. Pekko, J. Dekker, M. Prunnila, T. Pensala, "Second Order Temperature Compensated Piezoelectrically Driven 23 MHz Heavily Doped Silicon Resonators with ±10 ppm Temperature Stability", Proc. IEEE International Frequency Control Symposium , 2015, pp. 420—422.
http://dx.doi.org/10.1109/FCS.2015.7138871

Second Order Temperature Compensated Piezoelectrically Driven 23 MHz Heavily Doped Silicon Resonators with ±10 ppm Temperature Stability

Antti Jaakkola, Panu Pekko, James Dekker, Mika Prunnila and Tuomas Pensala
VTT Technical Research Centre of Finland
Espoo, Finland
antti.jaakkola@vtt.fi

***Abstract*—We report quartz level temperature stability of piezoelectrically driven silicon MEMS resonators. Frequency stability of better than ±10 ppm is measured for 23 MHz extensional mode resonators over a temperature range of $T = -40 \ldots +85°$C. The temperature compensation mechanism is entirely passive, relying on the tailored elastic properties of heavily doped silicon with a doping level of $n > 10^{20}$cm^{-3}, and on an optimized resonator geometry. The result highlights the potential of silicon MEMS resonators to function as pin-to-pin compatible replacements for quartz crystals without any active temperature compensation.**

I. Introduction

While silicon MEMS based solutions have well known advantages to offer to the timing and frequency control applications, the market is still dominated by quartz devices. The adoption of silicon MEMS resonator technology could be greatly enhanced if the devices could be made pin-to-pin compatible with quartz crystals through the combination of piezoelectric actuation and fully passive doping based temperature compensation. This paper reports progress towards this goal: we have designed and fabricated piezoelectrically driven 23-MHz silicon MEMS resonators, which have a ±10 ppm temperature stability corresponding to that of an AT cut quartz crystal, and whose electrical characteristics approach those of quartz at the same frequency.

Recent research has shown that heavy phosphorus doping (10^{19}cm^{-3} -range) of silicon can be used for reducing the thermal drift of a MEMS resonator frequency from over 3000 ppm to less than 300 ppm over the industrial temperature range [1]. It has been identified that further doping to carrier concentrations above 10^{20}cm^{-3} has the potential to reduce the temperature dependency through its effect on the 2nd order temperature coefficient TCF_2 [2]. Recently, we have verified this to be true with ultra heavily doped (UHD) capacitively coupled (bare silicon) resonators, illustrated in Fig 1. This data leads to two observations:

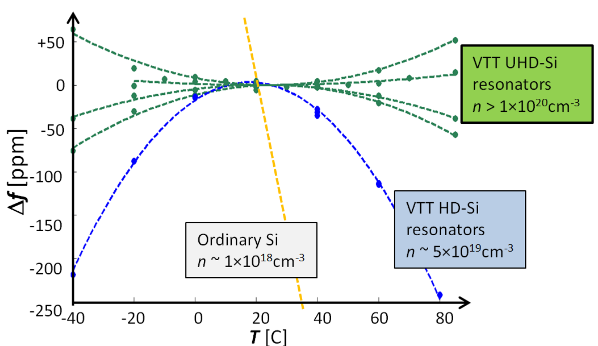

Figure 1. Temperature characteristics of capacitively coupled (bare silicon) extensional mode resonators made at VTT. Resonators made of ordinary silicon ($n \sim 10^{18}$cm^{-3}), heavily doped silicon (HD-Si, $n \sim 5 \times 10^{19}$cm^{-3}), and ultra heavily doped silicon (UHD-Si, $n > 10^{20}$cm^{-3}) are compared. With optimized doping and resonator design a stability of ±10 ppm has been reached. In UHD-Si devices, the initially negative second order temperature coefficient can be made positive, up to $TCF_2 \sim +15\,$ppb/$°C^2$.

		Typical AT-cut quartz	VTT HD Si AlN-driven MEMS - doping ~ 5x1019cm-3	VTT UHD Si AlN-driven MEMS - doping above 10^{20}cm^{-3}
Δf	frequency stability over T=-40...+85°C	±10 ppm	±150 ppm	±10 ppm
Q	Quality factor	100 000	15 000 (*)	4 000 (*)
ESR (R_m)	Equivalent series resistance (motional resistance)	50 Ω	50 Ω	100 Ω
C_0	Shunt capacitance	4 pF	4 pF	11 pF

(*) In open air

this work (VTT UHD Si AlN-driven MEMS)

Table I
Performance comparison of quartz and VTT UHD/HD Si AlN-driven MEMS resonators at $\sim 24\,$MHz.

1) There is an optimal doping level which, together with a correct design, produces near zero TCF_2, and yields quartz level temperature stability. The best experimen-

978-1-4799-8866-2/15/$31.00 ©2015 IEEE

tally demonstrated level of stability is ± 10 ppm for $T = -20 \ldots +85°C$.

2) The usually negative second order temperature coefficient TCF_2 can be made positive, up to $TCF_2 \sim +15\,\text{ppb}/°C^2$.

Observation 1 leads to attractive possibilities for realizing various types of passively temperature compensated bare silicon resonators, but observation 2 is the key for realizing *piezoelectrically driven* silicon MEMS resonators with quartz class temperature stability: Piezoelectric actuation requires addition of piezoelectric and metal (electrode) layers to the resonator device, and, practically all such materials (typically AlN + Mo/Al) have negative first- and second order temperature coefficients TCF_1 and TCF_2, respectively [3], [4], [5]. By balancing the positive contribution from the UHD silicon resonator body and the negative effect from the piezoelectric and metallic layers to both TCF_1 and TCF_2 by correct composition of the resonator, it is possible to reach quartz level frequency stability.

II. Methods

A. Resonator design and fabrication

The resonators were fabricated using the VTT cavity-SOI based process platform, see Fig. 2. First, SOI wafers featuring ultra heavily doped (doping in excess of 10^{20}cm^{-3}) Si device layers, including pre-etched cavities were prepared (steps 1,2). Next, AlN was deposited and patterned (3) right onto the Si device layer acting as a substrate and as the bottom electrode for device operation. SiO2 was deposited on the wafer (4). AlN was located only on top of the resonator, while SiO_2 was used as the insulator between the top and bottom electrodes elsewhere. Openings were etched to the SiO_2 layer, one onto the AlN layer and another onto the place where the bottom electrode contact would be formed (5). Aluminum was deposited and patterned as the top electrode material (6). Deep reactive ion etching was used to define the device geometry and to release the resonator (7).

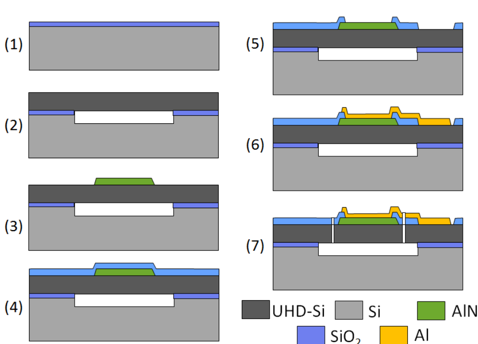

Figure 2. Fabrication process. UHD-Si refers to ultra heavily doped silicon with n-type carrier concentration above 10^{20}cm^{-3}.

B. Measurements

The frequency-vs-temperature curve measurements were performed on wafer level under atmospheric pressure on a Cascade Summit probe station using a HP 4294A impedance analyzer. The resonance frequencies were extracted by fitting the response of a BVD equivalent circuit to the measured admittance traces spanning the resonance peak (see Fig. 4). The wafer was held on a temperature-controlled chuck, whose temperature was varied from −40°C to +85°C with seven steps. A flow of dry air was used to prevent condensation of moisture on the non-packaged resonators. A total of $\sim$ 30 resonators were characterized on a wafer.

III. Results

A frequency stability better than ±10 ppm was measured for several devices over a temperature range of $T = -40 \ldots + 85°C$. The frequency-vs-temperature curves of three resonators are shown in Figure 3. Typical resonator performance parameters were: $R_m \sim 100\,\Omega$, C_0 ~11 pF, $Q \sim 4000$, $f_p - f_s$ ~750 ppm, and k^2 ~0.15% — a frequency response of a resonator is shown in Fig. 4. The scatter between the $f-\text{vs}-T$ curves of the set of $\sim$ 30 resonators spanning the whole wafer are shown in Fig. 5.

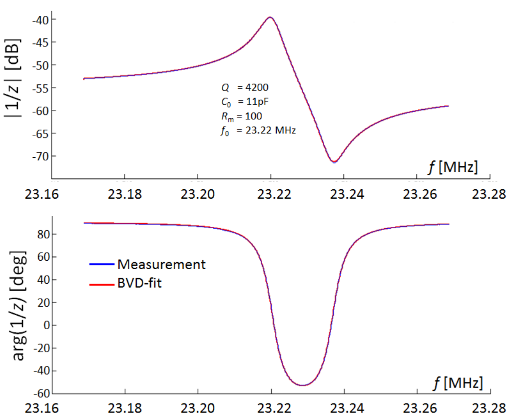

Figure 4. Frequency response of the resonator. Q, C_0, R_m and f_0 were obtained by fitting a BVD equivalent circuit to the data.

IV. Discussion

The result of $\pm 10\,\text{ppm}$ frequency stability shows that passively temperature compensated piezoelectrically coupled silicon MEMS resonators can reach a similar performance to AT cut quartz crystals. With further optimization (reduction of TCF_2), there is a potential for even better stability.

It can be seen in Fig. 3 that the measured data points do not accurately lay on top of the quadratic fit for the f-vs-T curve. At maximum, a fit error of $\sim$ 5 ppm is observed. The measurement was done in open air, which could cause instability of the resonance frequency at this level. Encapsulation of the devices is needed for performing more accurate measurements.

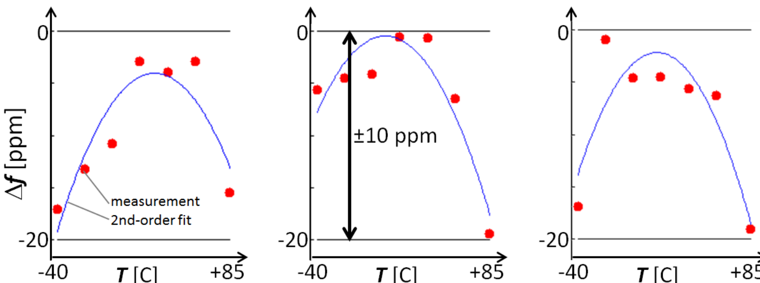

Figure 3. $f-\text{vs}-T$ curves of three 23 MHz extensional mode resonators. Data points are shown as red circles, and the blue line is a 2nd order polynomial fit. The scatter between measured data and the fit is expected to be caused by the fact that the measured resonators were non-packaged and measured in open-air.

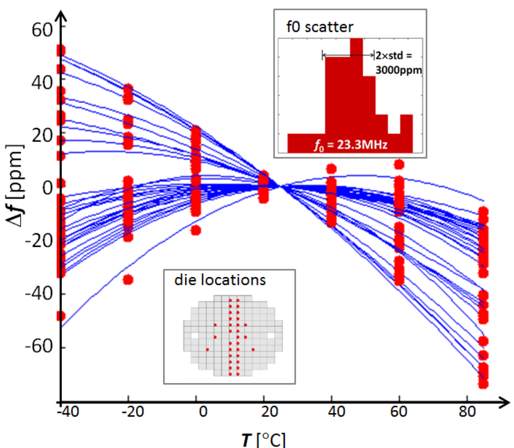

Figure 5. f-vs-T curves from $\sim$ 30 resonators spanning the wafer on the south-north direction. Note that the Δf is given in relative units, and hence the initial frequency error is absent. The top inset shows the initial frequency f_0 error, which has a standard deviation of 1500 ppm. Bottom inset illustrates the location of the measured dies on the wafer.

The performance parameters of two types of VTT MEMS resonators (HD-Si and UHD-Si) and a typical quartz crystal at the same frequency are compared in Table I. It can be seen that the electrical performance in terms of the equivalent series resistance (ESR) and shunt capacitance C_0 corresponds to that of quartz for the case of HD-Si resonators, however, in this case the frequency instability is an order-of-magnitude too high (see Fig. 1 as well). For the UHD-Si resonator of this work, frequency stability is sufficient, but the electrical performance parameters do not yet quite reach those of quartz, and thus complete pin-to-pin compatibility is not yet realized for these devices. Our further work includes reduction of ESR (through increased Q) by more optimized anchoring of the resonator. Reduction of the shunt capacitance will be assessed in particular by using thicker AlN layer on the resonator. The target is that the resonator can be driven with a standard oscillator IC intended for quartz crystals.

Figure 5 illustrates the scatter between the f-vs-T curves as well as the initial accuracy error of resonators on a wafer. For approximately two thirds of the resonators, the frequency stability is within ± 20 ppm. The distribution of the initial accuracy has a standard deviation of 1500 ppm. It is of paramount importance to develop an economically viable way of reducing the scatter of these properties. Both the temperature characteristics as well as the frequency of the resonator are functions of the Si/AlN/Al stack. Thus, selective addition or removal of material can be used for their fine tuning. Mapped ion beam trimming is a particularly promising technique for assessing this problem [6].

V. Conclusion

Piezoelectrically driven 23-MHz silicon MEMS resonators having a ± 10 ppm temperature stability and electrical characteristics approaching those of quartz crystals were demonstrated. The presented result greatly improves the competitiveness of silicon based resonator technology in timing and frequency reference applications, and presents an attractive alternative to current silicon MEMS approaches using active (PLL-based) temperature compensation. The work suggests that eventual pin-to-pin compatibility between silicon MEMS resonators and quartz is within reach.

References

[1] T. Pensala, A. Jaakkola, M. Prunnila, and J. Dekker, "Temperature compensation of silicon MEMS resonators by heavy doping," in *Proc. IEEE International Ultrasonics Symposium*, 2011, pp. 1952–1955.

[2] A. Jaakkola, M. Prunnila, T. Pensala, J. Dekker, and P. Pekko, "Determination of doping and temperature-dependent elastic constants of degenerately doped silicon from MEMS resonators," *IEEE Transactions on Ultrasonics, Ferroelectrics, and Frequency Control*, vol. 61, no. 7, pp. 1063–1074, Jul. 2014.

[3] K. Tsubouchi and N. Mikoshiba, "Zero-Temperature-Coefficient SAW Devices on AlN Epitaxial Films," *IEEE Transactions on Sonics and Ultrasonics*, vol. 32, no. 5, pp. 634–644, Sep. 1985.

[4] M. Levy, H. Bass, and R. Stern, *Handbook of Elastic Properties of Solids, Liquids, and Gases*. Academic Press, 2000.

[5] J. M. Dickinson and P. E. Armstrong, "Temperature Dependence of the Elastic Constants of Molybdenum," *Journal of Applied Physics*, vol. 38, no. 2, pp. 602–606, Feb. 1967.

[6] S. Mishin, M. Gutkin, A. Bizyukov, and V. Sleptsov, "Improving frequency control of temperature compensated surface acoustic wave devices," in *European Frequency and Time Forum International Frequency Control Symposium (EFTF/IFC), 2013 Joint*, Jul. 2013, pp. 111–113.

©2014 IEEE. Reprinted, with permission, from A. Jaakkola, M. Prunnila, T. Pensala, J. Dekker, and P. Pekko, "Determination of Doping and Temperature Dependent Elastic Constants of Degenerately Doped Silicon from MEMS Resonators", IEEE Transactions on Ultrasonics Ferroelectrics and Frequency Control, 61(7), pp. 1063-1074, 2014.
http://dx.doi.org/10.1109/TUFFC.2014.3007

Determination of Doping and Temperature-Dependent Elastic Constants of Degenerately Doped Silicon From MEMS Resonators

Antti Jaakkola, Mika Prunnila, Tuomas Pensala, James Dekker, and Panu Pekko

***Abstract*—Elastic constants c_{11}, c_{12}, and c_{44} of degenerately doped silicon are studied experimentally as a function of the doping level and temperature. First- and second-order temperature coefficients of the elastic constants are extracted from measured resonance frequencies of a set of MEMS resonators fabricated on seven different wafers doped with phosphorus (carrier concentrations 4.1, 4.7, and 7.5 × 10^{19} cm^{-3}), arsenic (1.7 and 2.5 × 10^{19} cm^{-3}), or boron (0.6 and 3 × 10^{19} cm^{-3}). Measurements cover a temperature range from −40°C to +85°C.**

It is found that the linear temperature coefficient of the shear elastic parameter $c_{11} - c_{12}$ is zero at n-type doping level of $n \sim 2 \times 10^{19}$ cm^{-3}, and that it increases to more than 40 ppm/K with increasing doping. This observation implies that the frequency of many types of resonance modes, including extensional bulk modes and flexural modes, can be temperature compensated to first order. The second-order temperature coefficient of $c_{11} - c_{12}$ is found to decrease by 40% in magnitude when n-type doping is increased from 4.1 to 7.5 × 10^{19} cm^{-3}.

Results of this study enable calculation of the frequency drift of an arbitrary silicon resonator design with an accuracy of ±25 ppm between the calculated and real(ized) values over T = −40°C to +85°C at the doping levels covered in this work. Absolute frequency can be estimated with an accuracy of ±1000 ppm.

I. Introduction

Single-crystal silicon MEMS resonators are challenging quartz devices in timing and frequency control applications. The main disadvantage of silicon resonators is their high frequency drift of about −30 ppm/K, which must be compensated to make a stable reference. Heavy doping of silicon has recently been found as an attractive way to significantly reduce this temperature dependency. Doping dependency of the elastic constants of silicon can be explained as a free carrier effect. The band structure of Si depends on strain and, therefore, the charge carriers (introduced to the silicon crystal lattice with doping) redistribute between different bands under strain [1], [2]. This leads to strain dependency of the carriers' free energy and introduces doping-dependent correction terms to the elastic constants. In n + Si (p + Si) the redistribution involves electrons (holes) that redistribute between different conduction band minima (valence band maxima).

Doping-based temperature compensation of silicon resonators started with p-type doping [3], but n-type doping soon appeared as a viable alternative [4]. Our work with bulk mode resonators has shown that n-type doping is an effective and versatile way of tailoring the temperature behavior of silicon resonators; we have demonstrated resonators with their f-versus-T turnover point near room temperature, overcompensated devices (+18 ppm/K) [5], and shown that n-type doping is applicable to virtually all resonance modes of practical importance [6]. Recently, resonators made of strongly n-type doped epitaxially grown silicon [7] have been reported.

The main contribution to the temperature-dependent frequency drift of a resonator comes from the elastic constants of the resonator material. Thus, to optimize the thermal stability of a silicon MEMS resonator, a designer needs to know the temperature behavior of the elastic parameters of silicon; in particular, the first- and second-order thermal derivatives of the elastic constants are of interest. However, experimental data on the temperature dependency of the elastic parameters of heavily doped silicon is limited; most usable results of n-type doped silicon have been published by Hall [8] for carrier concentration of 2 × 10^{19} cm^{-3}.

In this work, silicon elastic constants c_{11}, c_{12}, and c_{44} are studied experimentally as a function of doping level and temperature. First- and second-order temperature coefficients of the elastic constants are extracted from the resonance frequencies of a set of MEMS resonators fabricated on seven different wafers with varied doping. In Section II, the analysis method for extracting the unknown elastic parameters from the measured f-versus-T curves of the resonators is introduced. The fabrication of the devices and the measurements are covered in Section III. Results are presented in Section IV. Implications of the results are discussed in Section V, concentrating on the aspects important for temperature compensation of MEMS resonators. Reliability of the elastic parameter extraction procedure is assessed, and this provides a way to estimate how accurately the frequency and its thermal drift of an arbitrary resonator design can be calculated. An error analysis of the extracted elastic parameters is presented, and, additionally, MEMS resonator manufacturability aspects are covered.

Manuscript received September 19, 2013; accepted April 2, 2014. The authors acknowledge the Finnish Funding Agency for Technology and Innovation (Tekes), Okmetic Oyj, Murata Electronics, and Micro Analog Systems for providing funding. A. Jaakkola acknowledges funding from the Academy of Finland.

The authors are with the VTT Technical Research Centre of Finland, Espoo, Finland (e-mail: Antti.Jaakkola@vtt.fi).

DOI http://dx.doi.org/10.1109/TUFFC.2014.3007

II. Methods

A. Extraction of Elastic Constants From Resonance Frequencies

The frequency of an acoustic resonator is given by

$$f = 1/L \times \sqrt{c/\rho}, \tag{1}$$

where ρ, c, and L are the resonator material density, characteristic stiffness, and characteristic length, respectively. The characteristic stiffness depends on the elastic constants c_{11}, c_{12}, and c_{44}, which can be solved from a set of measured resonance frequencies of different resonance modes when their functional dependency on constants c_{ij} varies among the modes, and when there are three or more modes within the set. In our case, the set of two Lamé mode resonators and five length-extensional (LE) modes in different orientations fulfill these conditions. The test resonator set, and their exemplary sensitivities on the c_{ij} parameters are illustrated in Fig. 1, and micrographs of the two types of resonators are shown in Fig. 2(a). Additional constraints that led to the selection of this particular set of devices were: 1) the resonators had to be actuated electrostatically over vertical coupling gaps; 2) air damping needed to be low enough to allow detection of resonances in atmospheric pressure; 3) the resonators had to be relatively large in lateral dimensions to minimize effects from processing inaccuracies; 4) the resonance frequencies and their sensitivities on c_{ij} should be insensitive to device thickness variations (see error E_5 in Section V-D); and 5) the number of different resonator types had to be relatively large in comparison with the three unknowns c_{ij} to allow assessment of the reliability of the results (Section V-C).

The experimental data consists of measured resonance frequencies at different temperatures for all seven resonance modes $f_k^{\exp}(T)$ $(k = 1, \ldots, 7)$. Let us denote the corresponding theoretical estimates containing the c_{ij} dependencies—obtained through FEM modeling—as $f_k^{\mathrm{th}}(c_{11}, c_{12}, c_{44})$. We use an approach of first matching $f_k^{\exp}$ and f_k^{th} at $T_0 = 20°\mathrm{C}$ by numerical minimization of

$$g(c_{ij}) = \sum_k [f_k^{\exp} - f_k^{\mathrm{th}}(c_{ij})]^2 \tag{2}$$

to find elastic parameters $c_{ij}(T_0)$, and then linearize (1) to obtain the relation

$$\frac{\delta f_k^{\exp}(T)}{f_{k0}^{\exp}} = \frac{1}{f_{k0}^{\mathrm{th}}} \sum_{ij} \frac{\partial f_k^{\mathrm{th}}}{\partial c_{ij}} \delta c_{ij}(T) + \frac{1}{2}\frac{\delta L}{L}(T). \tag{3}$$

Here, $\delta c_{ij}(T)$ are the unknown changes in elastic parameters, $\delta f_k^{\exp}(T)$ are the measured frequency differences, and $f_{k0}^{\exp}$ and f_{k0}^{th} are shorthands for $f_k^{\exp}(T_0)$ and $f_k^{\mathrm{th}}(c_{ij}(T_0))$. Sensitivities $\partial f_k^{\mathrm{th}}/\partial c_{ij}$ are calculated from the theoretical estimates. The last term accounts for thermal expansion,

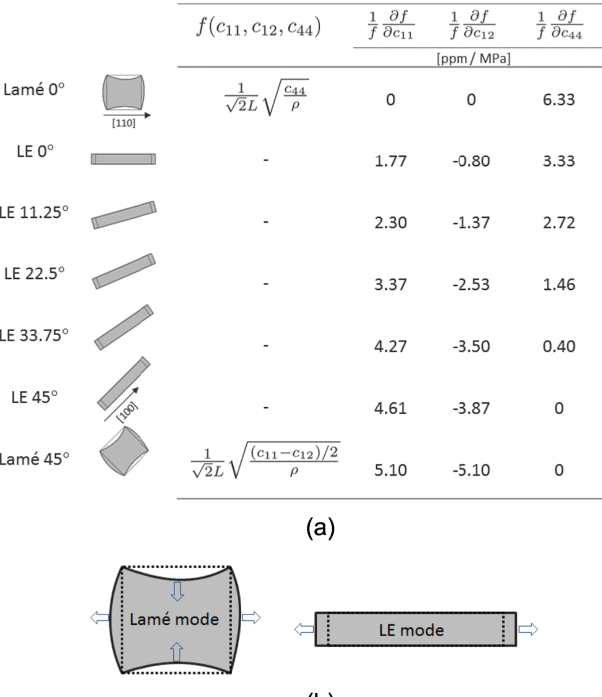

	$f(c_{11}, c_{12}, c_{44})$	$\frac{1}{f}\frac{\partial f}{\partial c_{11}}$	$\frac{1}{f}\frac{\partial f}{\partial c_{12}}$	$\frac{1}{f}\frac{\partial f}{\partial c_{44}}$
		[ppm / MPa]		
Lamé 0°	$\frac{1}{\sqrt{2}L}\sqrt{\frac{c_{44}}{\rho}}$	0	0	6.33
LE 0°	-	1.77	-0.80	3.33
LE 11.25°	-	2.30	-1.37	2.72
LE 22.5°	-	3.37	-2.53	1.46
LE 33.75°	-	4.27	-3.50	0.40
LE 45°	-	4.61	-3.87	0
Lamé 45°	$\frac{1}{\sqrt{2}L}\sqrt{\frac{(c_{11}-c_{12})/2}{\rho}}$	5.10	-5.10	0

Fig. 1. (a) Determination of the elastic constants c_{11}, c_{12}, and c_{44} is based on seven resonance modes whose frequencies have different dependencies on the c_{ij} parameters. Alignment of the resonators is varied from [110] to [100]. The table contains the analytical formulas for the resonance frequency $f(c_{11}, c_{12}, c_{44})$—which exist only for the two Lamé modes—and the sensitivities $1/f \times \partial f/\partial c_{ij}$ for each mode. These exemplary sensitivities have been calculated at a linearization point of $(c_{11}, c_{12}, c_{44}) = (163, 25, 79)$ GPa using the finite element approach outlined in Section II-B (zero angular alignment error and device layer thickness 15 μm of has been assumed). The listed numbers only illustrate the character of the variation of the sensitivies within the set of modes. For individual wafers, the sensitivities differ because of the different linearization points, device layer thicknesses, and angular misalignments, respectively. (b) Illustration of the mode shapes of the Lamé/LE resonances.

and it has been obtained by employing the isotropic nature of length changes for silicon. We use a third-order expansion for this term

$$\frac{1}{2}\frac{\delta L}{L}(T) = (\alpha_1 \Delta T + \alpha_2 \Delta T^2 + \alpha_3 \Delta T^3)/2, \tag{4}$$

where values of $\alpha_1 = 2.84 \times 10^{-6}\mathrm{K}^{-1}$, $\alpha_2 = 8.5 \times 10^{-9}\mathrm{K}^{-2}$, and $\alpha_3 = -32 \times 10^{-12}\mathrm{K}^{-3}$ are assumed. These expansion coefficients are based on the values reported for undoped silicon in [9]; thus, it is assumed that thermal expansion is not affected by doping. The assumption is supported by our measurements with mechanical dilatometry (see Section V-E).

In matrix form, (3) can be rewritten as

$$\delta \mathbf{f}^{\exp}(T) = A \cdot \delta \mathbf{c}(T) + \beta(T), \tag{5}$$

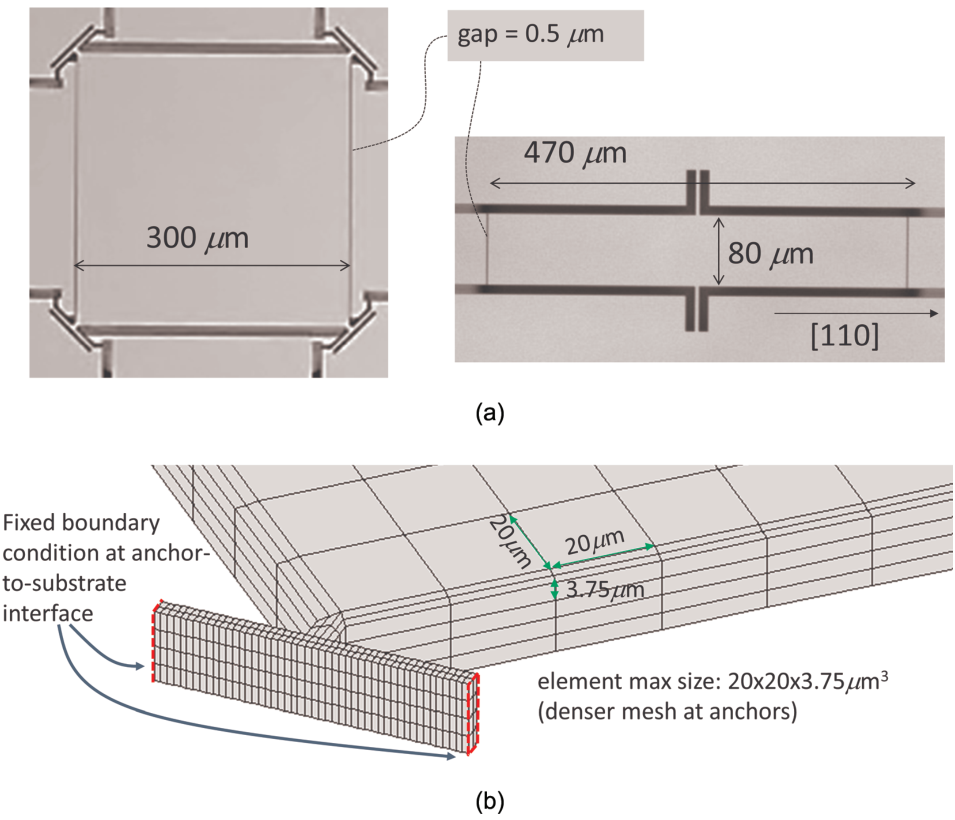

Fig. 2. (a) Micrographs of Lamé- and LE-mode resonators. (b) Illustration of the finite element mesh at one corner of the Lamé-mode resonator. Meshing was done in similar fashion for the LE-mode resonator models.

where $\delta \mathbf{f}^{\mathbf{exp}}$ contains the relative frequency changes and elements of the sensitivity matrix A are defined as

$$a_{kn} = \frac{1}{f_{k0}^{\mathrm{th}}} \frac{\partial f_k^{\mathrm{th}}}{\partial c_n}, \quad n = 11,12,44; \quad k = 1,...,7. \qquad (6)$$

Sensitivity matrix elements are illustrated in Fig. 1. One should note that (6) depends on the linearization point at which it is evaluated.

The changes in elastic parameters $\delta \mathbf{c}(T)$ can be solved as a least-squares fit from (5):

$$\delta \mathbf{c}(T) = (A^T A)^{-1} A^T [\delta \mathbf{f}^{\mathbf{exp}}(T) - \beta(T)]. \qquad (7)$$

B. Numerical Modeling

Numerical estimates of the modal frequencies $f_k^{\mathrm{th}}(c_{11}, c_{12}, c_{44})$ were calculated by finite element analysis with Comsol Multiphysics (Comsol Inc., Burlington, MA). Resonance frequencies were obtained with modal analysis of full 3-D geometries of the devices including the anchoring regions; see illustration of the finite element mesh in Fig. 2(b). Nominal thicknesses of 15 or 24 μm of the wafers were used in the calculations, see Table I. The maximum size of the mesh elements was 20 × 20 × 4 μm.

Calculation was performed for parameters c_{11}, c_{12}, and c_{44} spanning ranges of 160 to 168 GPa, 63 to 68 GPa, and 70 to 80 GPa, respectively. The ranges were discretized to a grid of 5 × 5 × 5 points. Values were stored in tables, and later retrieved for evaluation of (2) and (6). Cubic interpolation was used for evaluation of $f_k^{\mathrm{th}}(c_{11}, c_{12}, c_{44})$ between grid points. The discretization was verified to be dense enough for accurate evaluation of the derivatives of (6). Simulations took into account different angular misalignments of the wafers.

C. Measurement of Angular Misalignment

In practice, fabrication of the devices results in a small deviation of the resonator orientation from the intended alignment with the crystal axes, which can affect accuracy of the extraction of elastic parameters. This deviation, or angular misalignment $\Delta\theta$, was determined using the method illustrated in Fig. 3. Because of silicon anisotropy, the resonance frequency of an LE-mode beam resonator increases by ~10% when resonator alignment is rotated from [100] to [110]. Between these directions, i.e., at ±22.5° from [110], the resonance frequency is most sensitive to angular misalignment with $\Delta f/\Delta\theta \sim \pm 460$ ppm/0.1°. Copies of two LE resonators identical in dimensions, but oriented 45° to each other, both at the

TABLE I. Details of the Wafers for the Silicon Device Layers.

Wafer ID	Dopant	Specified resistivity (mΩ·cm) Min	Max	Calculated carrier concentration (10^{19} cm^{-3}) Min	Max	Avg	Angular alignment error (°)	Device layer thickness (μm)	Total thickness variation (μm)
B3	B	3.49	3.66	2.88	3.04	2.96	−0.6	23.8	3.1
B0.6	B	10	20	0.33	0.86	0.60	−0.1	15.6	3.5
As1.7	As	3.96	4.36	1.55	1.77	1.66	0.3	15.4	2.7
As2.5	As	2.94	3.08	2.39	2.52	2.46	−0.6	14.5	2.5
P4.1	P	1.67	1.76	3.98	4.22	4.10	0.0	14.6	2.6
P4.7	P	1.47	1.59	4.45	4.86	4.66	1.6	14.5	3.7
P7.5	P	0.95	1.05	7.05	7.89	7.47	0.5	14.5	1.7

Carrier concentrations were calculated from the resistivity specification using [11]. Carrier concentration ranges are included as error bars in Fig. 8. Angular misalignment was measured using the method described in Section II-C.

most sensitive orientation of ±22.5°, were included on the wafers. The angular misalignment could be deduced from the up/down frequency shifts $\pm\Delta f$ of these resonators.

III. Experimental

The resonators [Fig. 2(a)] were fabricated on seven different 150-mm C-SOI wafers (silicon-on-insulator wafers with pre-etched cavities [10]) manufactured in co-operation with Okmetic Oyj (Vantaa, Finland). The handle wafers with DRIE-etched cavities were thermally oxidized before they were fusion bonded to the device wafers. Device layers were fabricated from 100-oriented wafers grown with the Czochralski method. The resonator fabrication process started with the C-SOI wafers with circular cavities of a diameter of 500 μm for each resonator. The process flow consisted of two lithographic layers: 1) Al contact metallization and patterning, and 2) DRIE release etch, producing vertical gaps of minimum nominal width of 0.5 μm.

Dopant (B, P, and As) concentrations of the wafers for the silicon device layer were varied according to Table I. Carrier concentration range for each wafer was calculated from the specified resistivity range using the conversion method of [11]. Device layer nominal thickness was 15 μm (24 μm for wafer B3), and the manufacturer-specified C-SOI stack total thickness variation (including the handle wafer) was within ±2 μm for all wafers.

Because the wafers featured pre-etched cavities, it was possible to fabricate monolithic resonators without a grid of release etch holes within the devices, and thus the elastic properties of the resonators could be accurately modeled. In our previous studies [5], existence of release etch holes was a source of uncertainty for the determination of the elastic constants.

The resonators were measured on wafer level in atmospheric pressure on a Cascade Summit probe station (Cascade Microtech Inc., Beaverton, OR) using a HP 4294A impedance analyzer (Agilent Technologies Inc., Santa Clara, CA). A two-needle probe card was used for the measurements, and an open-short-load calibration was performed at $T = 40$°C at the beginning of the measurement. Measurements were done in the four-terminal pair configuration with four 2-m BNC cables, and the two end connections to the probe needles were ~15 cm long. A dc bias voltage of 40 V was applied between the resonator and the electrodes for electromechanical coupling. The effect on the resonance frequencies from the dc bias was negligible because of the relatively wide coupling gaps and the high mechanical spring constant of the resonance modes. The excitation ac voltage level was set to 1 V to maximize signal-to-noise ratio. The resonators still operated at their linear regime because of the weak electromechanical coupling. The measured devices were located near the wafer center. Quality factors of $Q \sim 10\,000$ were measured for all resonance modes, and the resonance frequencies were extracted by fitting a BVD equivalent circuit to the measured admittances. Example traces are shown in Fig. 4.

The wafer was held on a temperature-controlled chuck, whose temperature was varied from −40°C to +85°C with seven steps (for wafer As1.7, the highest temperature was

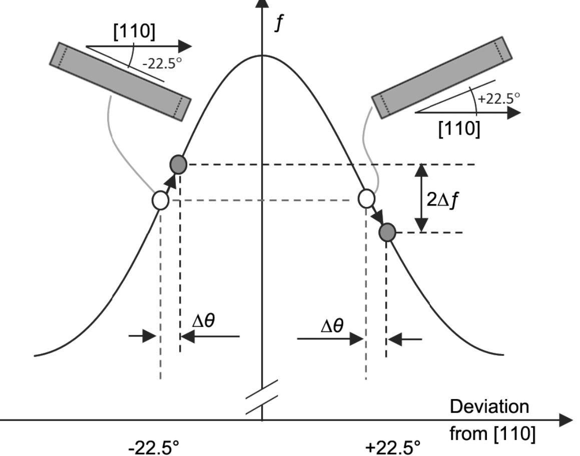

Fig. 3. In-plane angular misalignment of the wafers can be deduced from the difference of the resonance frequencies of two types of LE beam resonators, which are designed at an angle of ±22.5° from the [110] direction. In-plane rotation of the resonators shifts the resonance frequencies up/down by ±460 ppm/0.1°.

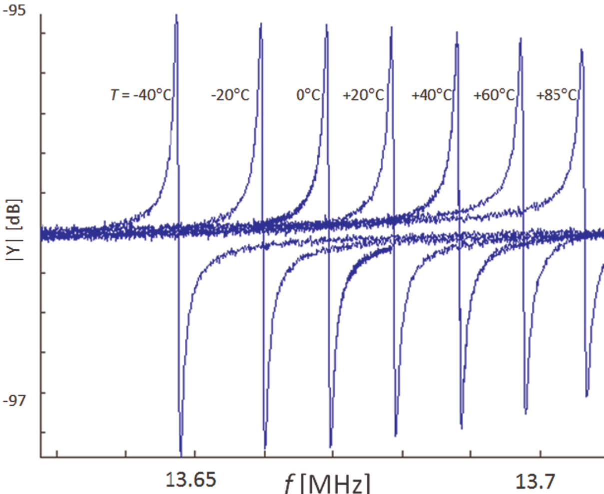

Fig. 4. Measured admittance traces of the Lame-45° resonators on wafer P7.5 measured at different temperatures.

80°C). The specified temperature accuracy of the system (Temptronic TP3200A) including the temperature controller and the chuck was ±0.5°C. A 15 min stabilization period followed after each temperature change before probing of the resonators was started; the chuck temperature was well stabilized in less than 10 min for all temperature steps. Clean dry air flow at a rate of 30 L/min was used for purging. The effect from room-temperature gas flow to resonator temperature was found to be smaller than the specified uncertainty of ±0.5°C by the following comparison: Lamé-45° resonator f-versus-T curves on wafer B0.6 were compared with corresponding data from a similar wafer that was wafer-level encapsulated by a silicon/glass wafer (the encapsulation method is described in [12]). Encapsulated resonators can be assumed to be free from thermal gradients caused by the gas flow, but it could potentially affect temperature of resonators on uncapped wafers like B0.6. f-versus-T curves of resonators near the wafer center on these two wafers were found to overlap with each other within 15 ppm, implying that device temperatures were within ~0.5°C with each other [assuming identical temperature coefficients for the resonators on both wafers (see Table II)].

IV. Results

Measured f-versus-T curves are shown for all modes on all wafers in Fig. 5, and the related temperature coefficients are collected in Table II.

On the weakest doped wafer, B0.6, all f-versus-T curves lie almost on top of each other, and the linear temperature coefficients are near −30 ppm/K. On wafer B3, the slopes of the curves are decreased in magnitude, and the biggest change is observed for the Lamé-0° mode. On n-type doped wafers larger effects are observed. The slope of the f-versus-T curve of the Lamé-45° mode is gradually increased with increasing doping, and above 2×10^{19} cm^{-3}, the slopes are positive. Lame-0° mode is almost unaffected by doping, and the f-versus-T curves of the LE modes span the region between the two Lamé modes.

Frequencies of more than 20 LE beam resonators were measured on each wafer for determination of the angular misalignment, as described in Section II-C. The results are tabulated in Table I. Fig. 6 shows an example of the resonance curves for wafer P7.5.

The elastic parameters $c_{ij}(T)$ were extracted from the measured frequency data using the least squares method of Section II-A. Results are shown in Fig. 7. The magnitude of the elastic constants is observed to decrease upon increased doping, except for the c_{12} elastic constant, which gets larger with increasing n-type doping.

For closer investigation of the thermal dependency of the $c_{ij}(T)$ curves, second-order polynomials centered at T_0 = 25°C were fitted to the elastic parameter data as

$$c_{ij}(T) = c_{ij}^0[1 + a_{ij}(T - T_0) + b_{ij}(T - T_0)^2], \qquad (8)$$

where a_{ij} and b_{ij} are the first-order and second-order temperature coefficients, respectively, and c_{ij}^0 is the constant term.[1] A second-order expansion of $c_{ij}(T)$ was found to be valid to within ±20 ppm for all $c_{ij}(T, n)$. The results are collected in Figs. 8(a)–(l) and in Table III. One should note that, in Fig. 8, we have chosen to accommodate data points from both n- and p-type doped wafers within same axes by representing p/n type doping with negative/positive carrier concentrations. Observations are discussed in the following section.

V. Discussion

A. Comparison to the Literature

Temperature coefficients measured in this work are compared with previously reported values in Fig. 8. Values for relatively weakly n- or p-doped silicon, reported by Bourgeois *et al.* [13], appear to be in satisfactory agreement with our data; the data points near zero carrier concentration follow the trends observable from our data points. Data by Hall [8] differs somewhat from our results, in particular for the second-order temperature coefficients. However, it should be noted that the temperature coefficients for Hall's data are based on graphical extraction of the published $c_{ij}(T)$ curves.

[1] Note that the least squares method of Section II-A uses $T = 20$°C as the linearization point, because it was one of the measurement points. However, expansions of (8) and that of Table II are customarily centered at 25°C.

TABLE II. Temperature Coefficients of Frequency (f_0, a, and b) of the Resonance Modes of Fig. 5.

Mode	Wafer B3 f_0 (MHz)	Wafer B3 a (ppm/K)	Wafer B3 b (ppb/K^2)	Wafer B0.6 f_0 (MHz)	Wafer B0.6 a (ppm/K)	Wafer B0.6 b (ppb/K^2)	Wafer As1.7 f_0 (MHz)	Wafer As1.7 a (ppm/K)	Wafer As1.7 b (ppb/K^2)	Wafer As2.5 f_0 (MHz)	Wafer As2.5 a (ppm/K)	Wafer As2.5 b (ppb/K^2)
Lamé 0°	13.68	−8.3	−64	13.77	−24.5	−37	13.76	−30.4	−25	13.75	−31.1	−23
LE 0°	9.02	−16.6	−52	9.07	−27.8	−33	9.04	−24.0	−44	9.03	−22.2	−43
LE 11.25°	8.81	−17.3	−50	8.87	−28.0	−33	8.85	−20.8	−49	8.80	−17.9	−53
LE 22.5°	8.39	−18.8	−49	8.45	−28.3	−34	8.41	−14.4	−66	8.36	−9.9	−69
LE 33.75°	8.04	−19.9	−47	8.09	−28.6	−34	8.03	−8.9	−78	7.99	−3.0	−83
LE 45°	7.92	−20.4	−47	7.95	−28.7	−34	7.88	−6.7	−85	7.86	−0.8	−85
Lamé 45°	10.96	−17.2	−52	11.02	−27.1	−37	10.91	−1.8	−94	10.86	5.6	−98

Mode	Wafer P4.1 f_0 (MHz)	Wafer P4.1 a (ppm/K)	Wafer P4.1 b (ppb/K^2)	Wafer P4.7 f_0 (MHz)	Wafer P4.7 a (ppm/K)	Wafer P4.7 b (ppb/K^2)	Wafer P7.5 f_0 (MHz)	Wafer P7.5 a (ppm/K)	Wafer P7.5 b (ppb/K^2)
Lamé 0°	13.74	−32.5	−20	13.72	−32.7	−17	13.68	−34.5	−12
LE 0°	9.00	−19.5	−42	8.99	−19.0	−39	8.95	−18.9	−26
LE 11.25°	8.79	−14.1	−51	8.83	−14.7	−46	8.75	−13.2	−31
LE 22.5°	8.34	−3.0	−68	8.39	−3.7	−62	8.30	−0.8	−41
LE 33.75°	7.96	5.8	−82	7.98	6.4	−77	7.89	9.6	−48
LE 45°	7.81	9.4	−87	7.80	10.6	−84	7.74	13.7	−52
Lamé 45°	10.79	17.2	−98	10.75	18.6	−94	10.66	22.1	−57

Fit was done to polynomial $f(T) = f_0[1 + a(T - T_0) + b(T - T_0)^2]$, which was centered at $T_0 = 25°C$. The fits reproduced the f versus T curves to within ±10 ppm for all cases.

B. Behavior of Elastic Coefficients With Doping

Figs. 8(a), 8(d), 8(g), and 8(j) show that the magnitude of the elastic parameters, i.e., the constant terms c_{ij}^0, are affected to within a few percent by increased doping over the tested wafers. These changes should be taken into account when dimensioning resonator designs targeting a specific resonance frequency. Although the offsets have a negligible effect for temperature compensation purposes, the effect has the potential to degrade the initial frequency accuracy within a set of devices on a single wafer or within a batch of wafers.

In general, it is seen that arsenic (data points with $0 < n < 4 \times 10^{19}$ cm^{-3}) and phosphorus ($n > 4 \times 10^{19}$ cm^{-3}) as dopants do not stand out from the plots as separate groups, which supports the view of the effects being of mainly electronic origin [1].

The effects on silicon elastic properties from n-type doping are best observed in the shear elastic constant $c_{11} - c_{12}$ and, in particular, in its temperature coefficients a_{11-12} and b_{11-12}. Fig. 8(k) shows that the linear temperature coefficient a_{11-12} crosses zero at approximately $n = 2 \times 10^{19}$ cm^{-3}. This is the effect of most practical importance for temperature compensation of MEMS applications, because many shear-type resonance modes are purely dependent on the $c_{11} - c_{12}$ term, and hence the linear temperature coefficient of frequency of such resonators can be brought to zero at this doping level. For example, the Lame 45° mode of Fig. 1(a) is a mode whose frequency depends solely on $c_{11} - c_{12}$. When doping is further increased, a_{11-12} reaches a level of more than +40 ppm/K. The effect appears to saturate with increasing doping. A wide class of resonance modes, such as torsional, flexural, and extensional modes have an amount of shear mode character, i.e., their frequency depends on $c_{11} - c_{12}$ with a large weight factor. Thus, their f-versus-T curves are largely determined by the behavior of the $c_{11} - c_{12}$ term. The fact that a_{11-12} attains relatively large positive values enables first-order temperature compensation of such modes. These aspects are discussed in more detail in [6].

Fig. 8(l) shows that the second-order coefficient b_{11-12} is negative for all studied doping levels, with a maximum deviation from zero of approximately −200 ppb/K^2. This would translate to a 250 ppm frequency deviation over a range of 100°C. Importantly, one finds that the second-order coefficient b_{11-12} appears to approach zero when the n-type doping level is above $n = 4.1 \times 10^{19}$ cm^{-3}. This suggests a possibility of a flat or positive second-order response at high enough doping, motivating further investigation of n-type doping beyond 10^{20} cm^{-3}.

The key effect on temperature compensation with p-type doping is observable in Fig. 8(h). The linear temperature coefficient a_{44} approaches zero with increasing p-type dopant concentration. However, the zero level has not yet been crossed with the highest doping level of 3×10^{19} cm^{-3}. The second-order coefficient b_{44} is seen to grow in magnitude with increased p-type doping. N-type doping

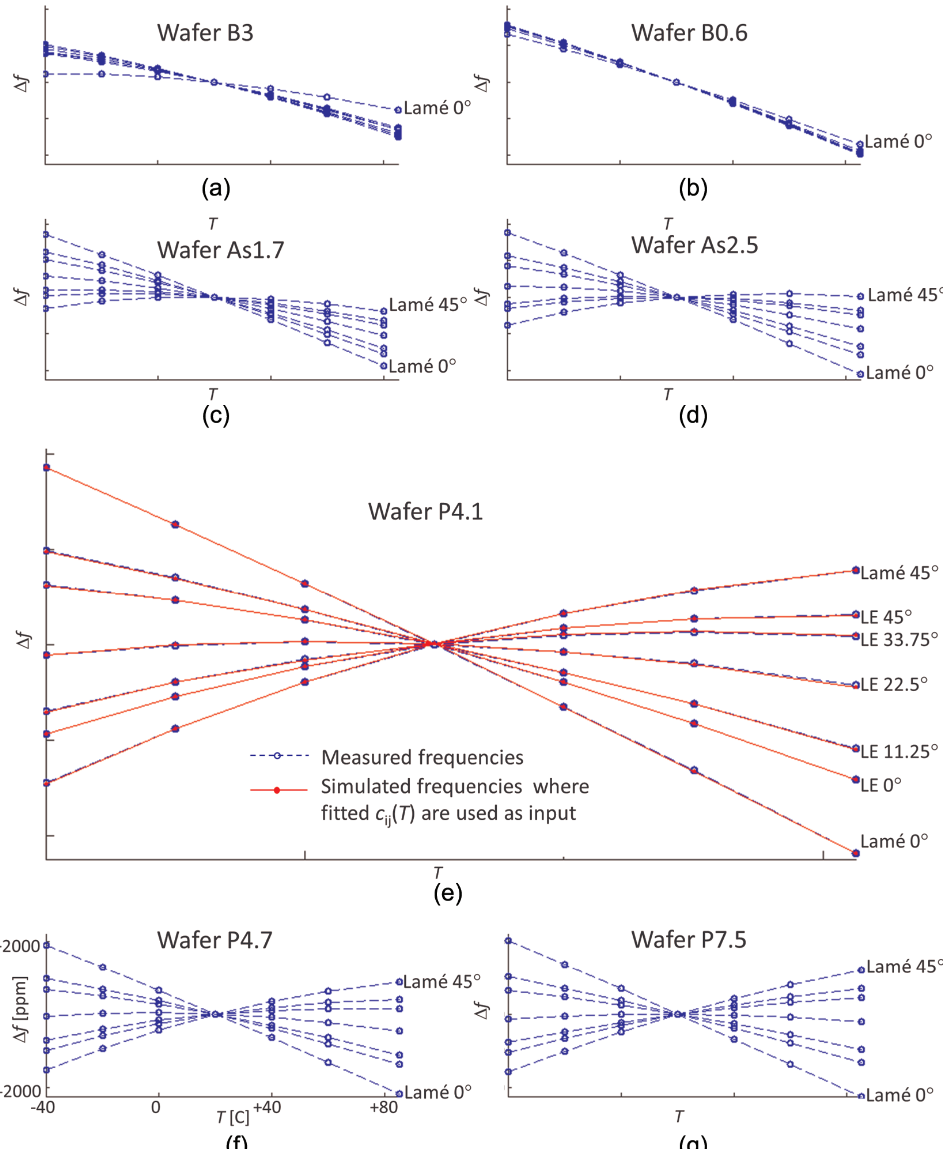

Fig. 5. (a)–(g) Measured f versus T data of all resonance modes on all wafers is shown with blue open circles. Dashed blue lines are second-order polynomial fits to the data; fit coefficients are collected in Table II. All plots have similar scaling of axes. (e) Experimental data from wafer P4.1 has been overlaid with corresponding numerical estimates $f_k^{\mathrm{th}}(T)$ which use the fitted parameters $c_{ij}(T)$ as an input (red lines with dots). The overlap is shown in more detail in Fig. 9(b).

is observed to have a relatively small effect on coefficients a_{44} and b_{44}

C. Reliability of Elastic Parameter Extraction

Seven data points were used for the extraction of the three unknown elastic parameters $c_{ij}(T)$ at each temperature. Hence, the reliability of the method can be assessed by comparing the measured frequency data to the corresponding numerical estimates obtained from FEM simulations which use the solved parameters $c_{ij}(T)$ as an input. First, Fig. 9(a) shows the correspondence of measured and simulated resonance frequencies at $T_0 = 20°\mathrm{C}$, where $c_{ij}(T_0)$ has been obtained from a fit to (2). The difference is within ±1000 ppm.

Correspondingly, the quality of the least-squares fit of (7) can be judged from the overlap of the measured and simulated data, exemplified in Fig. 5(e). This is seen in closer detail in Fig. 9(b), where the difference between the measured relative frequency changes $\delta f_k^{\mathrm{exp}}(T)$ and the corresponding theoretical estimates $\delta f_k^{\mathrm{th}}(c_{ij}(T))$ has been plotted for all modes on all wafers. Maximum deviation between the measured and simulated data points was less than 25 ppm for all seven resonance modes on all wafers,

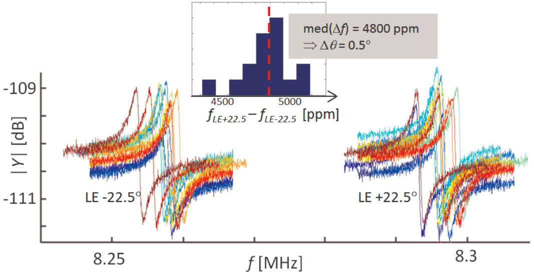

Fig. 6. Admittance traces of 32 LE mode beam resonators (16 pairs) on wafer P7.5 at ±22.5° offset from the [110] direction. Closest pairs (one resonator with +22.5° offset and the other with −22.5°) have been colored similarly, and all pairs have different colors. Inset: Distribution of the frequency differences between the closest pairs. Angular misalignment is calculated from the median of this distribution (see Section II-C).

which speaks for the reliability of the extraction method. It should be noted that without correction of the angular misalignments (Section II-C), the least-squares method would have resulted in errors up to 60 ppm.

Validity of the linearization step needed for the least-square method was confirmed. Frequency changes from approximation of (3) were calculated for each of the extracted elastic parameters $c_{ij}(T)$, and compared with the nonlinearized counterpart $\delta f_k^{\mathrm{th}}(c_{ij}(T))$. Linearization error was found to be less than 5 ppm for all cases.

Based on the preceding analysis, we expect that by using the extracted elastic parameters, one can estimate the frequency of an arbitrary resonance mode, fabricated on a wafer with similar carrier concentration as in our experiments, with the following accuracies:

- Absolute frequency of a resonator can be predicted with ±1000 ppm accuracy.
- Thermal drift over a temperature range of T −40°C to +85°C can be predicted with ±25 ppm accuracy.

D. Accuracy of Temperature Coefficients of c_{ij} Parameters

Although the analysis of the previous section provides a way to establish a confidence level on the resonance frequencies that can be calculated from the extracted elastic parameters of this work, one can also obtain estimates for the accuracy of the temperature coefficients of elastic constants. Let us denote these confidence intervals as Δc_{ij}^0, Δa_{ij}, and Δb_{ij}. They are listed in Table III and are shown as vertical error bars in Fig. 8.

For Δc_{ij}^0, an upper limit of ±2000 ppm is obtained by starting from the previously discussed absolute frequency accuracy of ±1000 ppm, and by applying (1). Other potential error sources of smaller magnitude are:

- The mass of dopant atoms differs from that of silicon. Assuming that the volume of the crystal stays con-

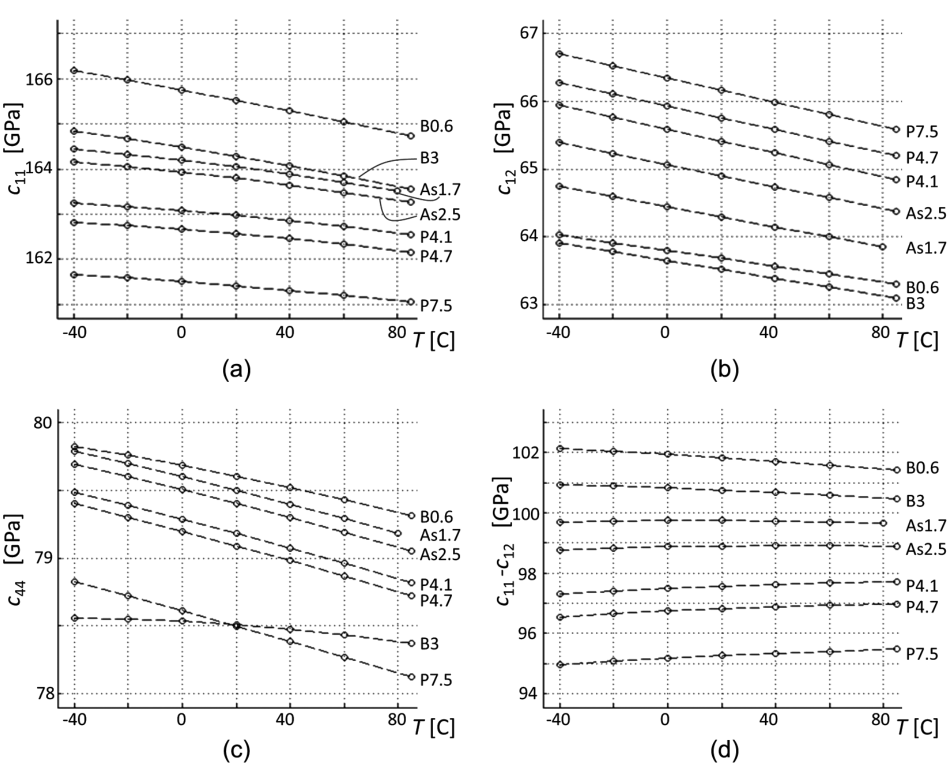

Fig. 7. Elastic parameters c_{11}, c_{12}, c_{44}, and $c_{11} - c_{12}$ as a function of temperature and doping. The legends denote the dopant element types and the doping level, see Table I. Dashed lines are second-order fits to the c_{ij}-versus-T data, and the fit coefficients are displayed in Fig. 8 and in Table III.

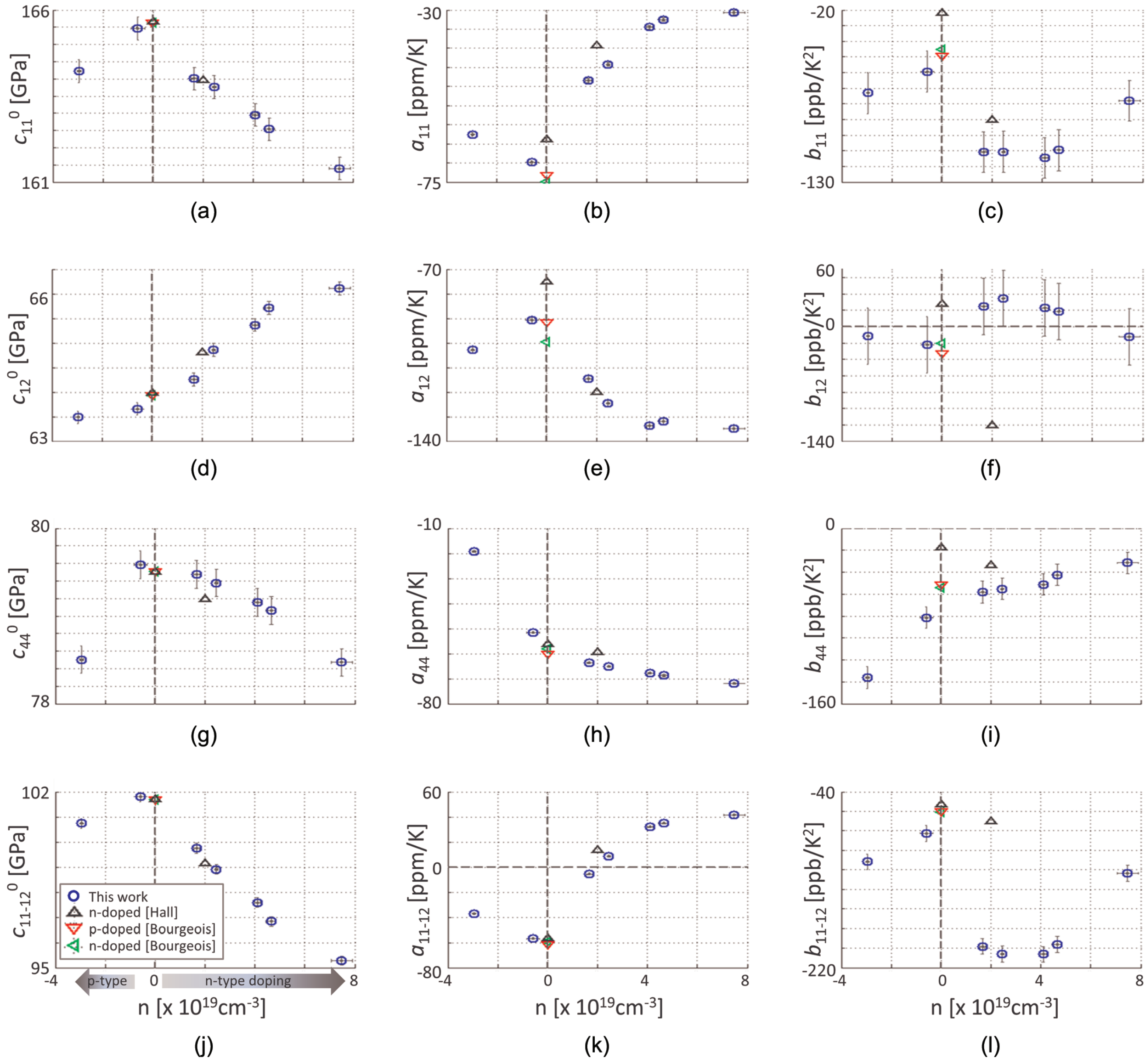

Fig. 8. Temperature coefficients of the elastic parameters c_{ij} as a function of carrier concentration n. Data from p-type doped wafers is represented with negative carrier concentrations. First, second and third columns represent the constant terms c_{ij}^0, linear coefficients (a_{ij}), and second-order coeffients (b_{ij}) at $T = 25$°C, respectively, see (8). c_{11-12}^0, a_{11-12}, and b_{11-12} are shorthands for the coefficients of $c_{11} - c_{12}$. Open blue circles are the experimentally determined values of this work. Numerical values are given in Table III. Values reported in [13] are shown as red triangles pointing down (weak p-type doping) and as green triangles pointing left (weak n-type doping). Data reported by Hall [8] were used for calculating data points shown as black triangles pointing up. Horizontal error bars indicate the carrier concentration ranges calculated from the resistivity specification for each wafer (see Table I). Vertical error bars are based on the error analysis of Section V-D.

stant, the maximal density change is less than 200 ppm, which would be reflected as a similar inaccuracy in c_{ij}^0.

- The dimensions of the resonators may vary slightly from the designed measures because of potential mask bias and imperfections in DRIE etching. A conservative estimate for the lateral dimension change of ± 0.1 µm of the resonators would cause deviation of the resonance frequency by approximately ± 300 ppm, and thus have an effect of ± 600 ppm on c_{ij}^0.
- A thickness variation of ± 2 µm of the device layer would have a very small effect on frequencies of the resonators: FEM analysis indicated that the frequencies of the LE modes stay within ± 20 ppm, and changes are even smaller for the Lamé modes.

To assess the inaccuracy of the first- and second-order temperature coefficients of the elastic parameters, a Monte Carlo approach was used to simulate the effect of several error sources. A large number of copies of the experimen-

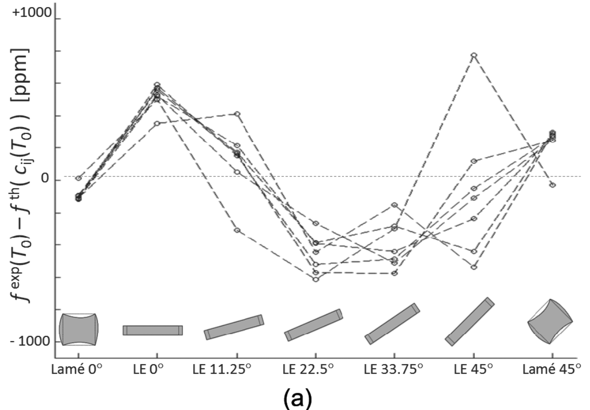

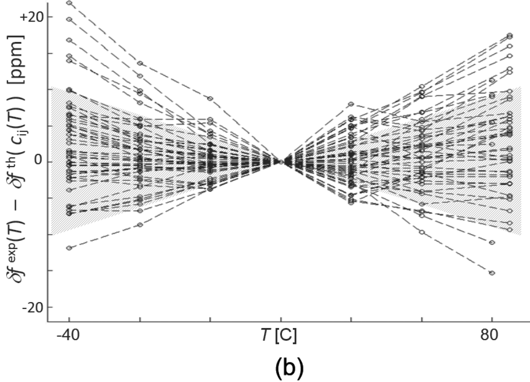

Fig. 9. (a) Difference between measured frequencies $f_k^{\exp}(T_0)$ and theoretical estimates $f_k^{\rm th}(c_{ij}(T_0))$ at $T_0 = 20°$C for all resonance modes on all wafers. Theoretical estimates are based on $c_{ij}(T_0)$, which are the fitted elastic parameters obtained through numerical minimization of (2). (b) Difference between the measured relative frequency changes $\delta f_k^{\exp}(T)$ and the corresponding theoretical estimates $\delta f_k^{\rm th}(c_{ij}(T_0) + \delta c_{ij}(T))$ for all resonance modes on all wafers. Theoretical estimates are calculated using $\delta c_{ij}(T)$ that have been fitted using (7). The shaded region illustrates the frequency measurement uncertainty that has been assumed in error analysis of Section V-D.

tal data sets (of Fig. 5) were taken, and perturbed according to the following sources of uncertainty, labeled as E_1 through E_5:

- E_1: Relative frequencies were varied by $\delta f \times |\Delta T| / \Delta T_{\max}$, where δf was taken from a normally distributed population with a standard deviation of 10 ppm, ΔT was defined as $T - 20°$C, and $\Delta T_{\max}$ was set to 65°C. The distribution is visualized by the shaded region of Fig. 9(b). In this way, a distribution corresponding to the observed errors in relative frequencies was reproduced.
- E_2: The accuracy specified for the temperature controller and chuck was taken into account by varying the temperature points by δT taken from a normally distributed population with a standard deviation of 0.5°C.
- E_3: Sensitivities of (6) were evaluated at the linearization points c_{ij}^0, which was estimated previously to have

TABLE III. Values of Temperature Coefficients of the Elastic Parameters c_{ij}.

Dopant	n ($\times 10^{19}$ cm^{-3})	c_{11}^0 (GPa)	a_{11} (ppm/K)	b_{11} (ppb/K^2)	c_{12}^0 (GPa)	a_{12} (ppm/K)	b_{12} (ppb/K^2)	c_{44}^0 (GPa)	a_{44} (ppm/K)	b_{44} (ppb/K^2)	$c_{11}^0 - c_{12}^0$ (GPa)	a_{11-12} (ppm/K)	b_{11-12} (ppb/K^2)
B	3.0	164.2	−62.5	−73	63.5	−102.9	−11	78.5	−19.3	−136	100.7	−37.1	−112
B	0.6	165.5	−69.9	−59	63.7	−90.6	−22	79.6	−51.7	−81	101.8	−56.9	−83
As	1.7	164.0	−48.5	−111	64.3	−114.7	25	79.5	−63.7	−58	99.7	−5.8	−198
As	2.5	163.8	−44.2	−111	64.9	−124.6	34	79.4	−65.1	−55	98.9	8.5	−206
P	4.1	163.0	−34.5	−115	65.4	−133.7	22	79.2	−67.8	−51	97.6	31.9	−206
P	4.7	162.5	−32.5	−110	65.7	−131.8	18	79.1	−68.7	−43	96.8	34.9	−196
P	7.5	161.4	−30.7	−78	66.1	−134.9	−12	78.5	−71.9	−31	95.3	41.6	−124
		Δc_{11}^0	Δa_{11}	Δb_{11}	Δc_{12}^0	Δa_{12}	Δb_{12}	Δc_{44}^0	Δa_{44}	Δb_{44}	$\Delta(c_{11}^0 - c_{12}^0)$ (GPa)	Δa_{11-12} (ppm/K)	Δb_{11-12} (ppb/K^2)
Total uncertainty (rms sum)		±0.3	±0.7	±12	±0.1	±1.5	±33	±0.2	±0.4	±10	±0.2	±0.3	±7
E_1: frequency error		±0.3	±0.39	±9.4	±0.1	±1.20	±28.5	±0.2	±0.16	±3.6	±0.2	±0.16	±3.5
E_2: temperature error			±0.26	±6.6		±0.64	±17.1		±0.34	±9.1		±0.20	±5.6
E_3: linearization point error			±0.54	±0.8		±0.69	±1.1		±0.01	±0.0		±0.02	±0.0
E_4: thermal expansion error			±0.09			±0.09			±0.09			±0.09	
E_5: thickness variation error			±0.02	±0.0		±0.04	±0.0		±0.00	±0.0		±0.00	±0.0

Corresponding data points are plotted in Fig. 8. Confidence intervals Δc_{ij}^0, Δa_{ij}, and Δb_{ij} are based on the error analysis of Section V-D.

an uncertainty within ±2000 ppm. Error caused by this was simulated by perturbing the linearization points accordingly.

- E_4: Thermal expansion was assumed constant in the calculations, and our measurements suggested this to hold for linear thermal expansion within a ±7% error margin (Section V-E). The thermal expansion effect in (4) was perturbed to take this uncertainty into account.
- E_5: Thickness of the devices deviated from the nominal thicknesses used in the simulations. Sensitivities of (6) were perturbed to take into account a thickness variation of ±2 µm.

Extraction of the elastic parameters $c_{ij}(T)$ was performed on the perturbed data sets in the same way as it was done on the real measurement data and distributions of a_{ij} and b_{ij} were obtained. Confidence intervals Δa_{ij} and Δb_{ij} were calculated for each error source E_1 to E_5 separately, and the total effect was estimated as the rms sum. Values for E_1 and E_2 were obtained as standard deviations of the a_{ij}/b_{ij} distributions, whereas the full range was used for E_3 to E_5. Inaccuracy of the first-order coefficient a_{ij} was found to range from $\Delta a_{11-12} = \pm 0.3$ ppm/K to $a_{12} = \pm 1.5$ ppm/K. Correspondingly, error of the second-order coefficient was seen to vary from $\Delta b_{11-12} = \pm 7$ ppb/K^2 to $\Delta b_{12} = \pm 33$ ppb/K^2. Error in measured frequencies (E_1) and inaccuracy of temperature (E_2) were major sources of uncertainty for all a_{ij}/b_{ij} parameters, and the linearization point error (E_3) was a top contributor for a_{11} and a_{12}.

E. Doping Independency of Thermal Expansion

The procedure for extracting the elastic parameters relied on the assumption that thermal expansion of (4) would be insensitive to doping. To our knowledge, effects from heavy doping on thermal expansion of silicon have not been studied experimentally. For verification, mechanical dilatometry was used for measuring the thermal expansion of samples with doping levels similar to wafers B3, As1.7, and P7.5. The linear thermal expansion coefficient α_1 was found to be constant within the ±7% error margin of the measurement.

F. Manufacturability of Temperature-Compensated MEMS Resonators

Eventual manufacturability of silicon resonators whose temperature compensation is based on degenerate doping crucially depends on the statistical variations of the *f*-versus-T curves among devices fabricated on a single wafer or on a batch of wafers. This aspect was addressed by studying a set of 30 square extensional mode resonators of [5], which were fabricated on a wafer with a specification similar to that of wafer P4.7 of this work. The *f*-versus-T curves of the devices are shown in Fig. 10. These devices were temperature compensated to first-order with their turnover temperatures near 20°C. The overall frequency drift over the whole temperature range of 120°C stays within 250 ppm, and maximum deviation between samples is approximately 20 ppm. One should note that the data of this example is from devices on a Czochralski-grown wafer, where the doping level may vary ±5% within the wafer. A better control of doping level is achievable with diffusion-based doping, or with epitaxially grown silicon, for which doping can be controlled during the crystal growth process.

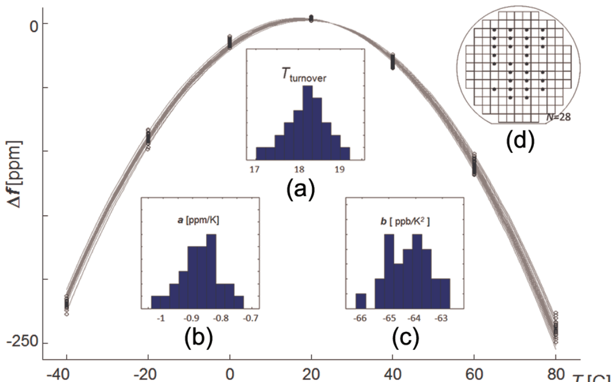

Fig. 10. Superposed f versus T curves of 28 square extensional resonator samples similar to those of [5]. Measurements are shown as black open circles, whereas second-order polynomial fits to the data are shown with gray lines. The wafer has been doped with phosphorus to a concentration of $n \sim 5 \times 10^{19}$ cm^{-3}. Histograms (a), (b), and (c) illustrate the distribution of the turnover temperature, and the first-/second-order temperature coefficients of frequency, respectively. Wafer map (d) shows the location of the measured devices on the wafer.

VI. Conclusion

Elastic constants c_{11}, c_{12}, and c_{44} of degenerately doped silicon were studied experimentally as a function of the doping level and temperature. First- and second-order temperature coefficients of the elastic constants were extracted from measured resonance frequencies of a set of MEMS resonators fabricated on wafers with varied doping.

The linear temperature coefficient of the shear elastic parameter $c_{11} - c_{12}$ was found to be zero at n-type doping level of $n \sim 2 \times 10^{19}$ cm^{-3}. It was observed to increase to more than +40 ppm/K with higher level of doping, which implies that the frequency of many types of resonance modes, including extensional bulk modes and flexural modes, can be temperature compensated to first order. The second-order temperature coefficient of $c_{11} - c_{12}$ was found to decrease by 40% in magnitude when n-type doping was increased from 4.1 to 7.5 × 10^{19} cm^{-3}, suggesting a further reduction of the second-order effect with increased doping.

It was found that the frequency drift of an arbitrary silicon resonator design, fabricated on a wafer with doping level similar to those investigated in this work, can be es-

timated with an accuracy of ±25 ppm over a temperature range of $T = -40°C$ to 85°C using the elastic parameters of this work. Absolute frequency can be calculated with an accuracy of ±1000 ppm.

Acknowledgments

Okmetic Oyj is acknowledged for providing the silicon wafers. A. Jaakkola thanks A. Nurmela for help in the measurements. R. Morrell is thanked for performing the thermal expansion measurements.

References

[1] R. W. Keyes, "Electronic effects in the elastic properties of semiconductors," in *Solid State Physics: Advances in Research and Applications*, F. Seitz and D. Turnbull, Eds., New York, NY: Academic Press, 1967, vol. 20, pp. 37–90.

[2] F. S. Khan and P. B. Allen, "Temperature dependence of the elastic constants of p+ silicon," Phys. Status Solidi B, vol. 128, no. 1, pp. 31–38, 1985.

[3] A. K. Samarao, G. Casinovi, and F. Ayazi, "Passive TCF compensation in high q silicon micromechanical resonators," in *IEEE Int. Conf. Micro Electro Mechanical Systems*, 2010, pp. 116–119.

[4] A. Hajjam, A. Rahafrooz, and S. Pourkamali, "Sub-100ppb/°C temperature stability in thermally actuated high-frequency silicon resonators via degenerate phosphorous doping and bias current optimization," in *Proc. IEEE Int. Electron Device Meeting*, 2010, pp. 7.5.1–7.5.4.

[5] T. Pensala, A. Jaakkola, M. Prunnila, and J. Dekker, "Temperature compensation of silicon MEMS resonators by heavy doping," in *Proc. IEEE Int. Ultrasonics Symp.*, 2011, pp. 1952–1955.

[6] A. Jaakkola, M. Prunnila, and T. Pensala, "Temperature compensated resonance modes of degenerately n-doped silicon MEMS resonators," in *IEEE Int. Frequency Control Symp.*, 2012, pp. 1–5.

[7] E. J. Ng, C. H. Ahn, Y. Yang, V. A. Hong, C.-F. Chiang, E. Ahadi, M. W. Ward, and T. W. Kenny, "Localized, degenerately doped epitaxial silicon for temperature compensation of resonant MEMS systems," in *Transducers 2013*, pp. 2419—2422.

[8] J. J. Hall, "Electronic effects in the elastic constants of n-type silicon," *Phys. Rev.*, vol. 161, no. 3, pp. 756–761, 1967.

[9] K. G. Lyon, G. L. Salinger, C. A. Swenson, and G. K. White, "Linear thermal expansion measurements on silicon from 6 to 340 k," *J. Appl. Phys.*, vol. 48, no. 3, pp. 865–868, Mar. 1977.

[10] H. Luoto, K. Henttinen, T. Suni, J. Dekker, J. Mäkinen, and A. Torkkeli, "MEMS on cavity-SOI wafers," *Solid-State Electron.*, vol. 51, no. 2, pp. 328–332, 2007.

[11] "Standard practice for conversion between resistivity and dopant density for boron-doped, phosphorus-doped, and arsenic-doped silicon," in *Annual Book of ASTM Standards, F 723–99.* West Conshohocken, PA: American Society for Testing and Materials, 2000, pp. 275—291.

[12] V. Kaajakari, J. Kiihamäki, A. Oja, S. Pietikäinen, V. Kokkala, and H. Kuisma, "Stability of wafer level vacuum encapsulated single-crystal silicon resonators," *Sens. Actuators A*, vol. 130, pp. 42–47, Aug. 2006.

[13] C. Bourgeois, E. Steinsland, N. Blanc, and N. F. de Rooij, "Design of resonators for the determination of the temperature coefficients of elastic constants of monocrystalline silicon," in *IEEE Int. Frequency Control Symp.*, 1997, pp. 791–799.

Antti Jaakkola was born in Juva, Finland, in 1978. He received the M.Sc. degree in engineering physics from the Helsinki University of Technology in 2003. He has worked for the VTT Technical Research Centre of Finland since 2006, where he currently holds the position of research scientist in the MEMS sensors team. His current research interests include silicon MEMS resonators and piezo-MEMS devices.

Mika Prunnila was born in 1974 in Helsinki. He received his Ph.D. degree in the field of semiconductor physics from the Helsinki University of Technology (Aalto University) in 2006. Currently, he works at the VTT Technical Research Centre of Finland, where he holds the Principal Scientist position and leads the nanoelectronics team. His research topics have included micro/nano device physics and fabrication, electron and heat transport, energy harvesting, electron-phonon interaction, double-gate MOSFETs, and micro coolers.

Tuomas Pensala was born in Helsinki, Finland, in 1972. He received the M.Sc. degree in engineering physics from the Helsinki University of Technology in 2000 and the D. Sc.(Tech.) degree from Aalto University in 2011. Since 1998, he has worked for the VTT Technical Research Centre of Finland, where he currently holds the position of research team leader of the Thin Film Devices team. His interests include piezoelectric thin film devices and piezo-MEMS.

James Dekker received his bachelor's degree in mechanical engineering in 1990 and his doctoral degree in materials science in 1997, both from the University of California, Davis in 1997. In 1998, he began work at the Optoelectronic Research Centre in Tampere, Finland, and then moved to the Helsinki University of Technology, studying defect structures in semiconductors, primarily III-V materials, using DLTS. In 2001, he began work at VTT in the MEMS fabrication group, developing particular expertise in wafer bonding and dry-etch technologies.

Panu Pekko was born in Mikkeli, Finland, in 1970. He received his M.Sc. and Ph.D. degrees in physics from the University of Helsinki in 1997 and 2000, respectively. He conducted his thesis work on properties of tetrahedral amorphous carbon coatings. He has worked at the VTT Technical Research Centre of Finland since 2001, and currently holds a position of senior scientist. His research interests include MEMS fabrication technologies, process integration, and sensor applications.

©2014 IEEE. Reprinted, with permission, from A. Jaakkola, S. Gorelick, M. Prunnila, J. Dekker, T. Pensala, P. Pekko, "Long term stability and quality factors of degenerately n-type doped silicon resonators", Proc. IEEE International Frequency Control Symposium, 2014, pp. 1-5. http://dx.doi.org/10.1109/FCS.2014.6859866

Long Term Stability and Quality Factors of Degenerately n-type Doped Silicon Resonators

Antti Jaakkola, Sergey Gorelick, Mika Prunnila, James Dekker, Tuomas Pensala and Panu Pekko
VTT Technical Research Centre of Finland
Espoo, Finland
antti.jaakkola@vtt.fi

***Abstract*—Effect of degenerate doping on the long term stability and quality factors of silicon resonators was studied. The long term stability of electrostatically coupled tuning fork and width extensional mode resonators was found to be better than 1 ppm during a measurement spanning 220 days. Resonators were phosphorus doped to a carrier concentration of 4.1×10^{19}cm^{-3}. Quality factors of ~10-MHz Lamé mode resonators on wafers doped up to a concentration of 7.5×10^{19}cm^{-3} were found to range from 900,000 to 1,500,000, which is comparable to that reported for similar resonators with moderate doping. The results indicate that the effect from heavy phosphorus doping on resonator stability or on silicon intrinsic losses is low at the studied doping levels.**

I. Introduction

Degenerate doping of silicon has been found as a viable way of reducing the temperature dependency of the frequency of MEMS resonators, and, in particular, n-type doping up to 7.5×10^{19}cm^{-3} has been shown to be applicable to temperature compensation of a variety of flexural and bulk resonance modes [1], [2], [3], [4].

However, it has remained largely uncovered whether the performance of resonators is affected by doping in terms of their aging behavior and quality factors. In this work, the long term stability and quality factors of heavily doped MEMS resonators are studied experimentally.

II. Methods

A. Resonator fabrication and encapsulation

Electrostatically coupled silicon resonators were fabricated on SOI wafers with heavily phosphorus/boron doped Czochralski-grown device wafers with 100 orientation. Resonator wafer process was similar to that discussed in [5], [6]. Device wafers were vacuum encapsulated on wafer level using anodic bonding with a glass/silicon cap wafer [7]. Several types of bulk and flexural mode resonators were included in the measurements, see Fig. 1. Resonator frequencies ranged from 1 MHz to 20 MHz , and the temperature coefficients spanned a range of $TCF = -32 \ldots +16\,\text{ppm/K}$ (see Fig. 4(c)).

B. Long term stability measurement

Encapsulated resonator wafer stacks were diced into 1×1 mm^2 dies. A set of these dies were picked and attached with Electrolube silver conductive paint onto carrier boards (Fig. 2(a)) each accommodating four resonators. Electrical

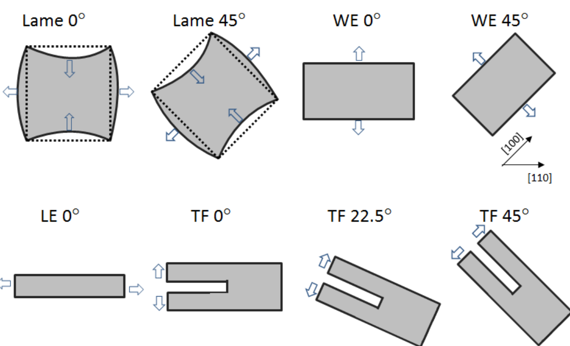

Figure 1. Illustration of the geometries and mode shapes of Lamé, width extensional (WE), length extensional (LE) and tuning fork (TF) resonators used in the study. The arrows indicate the 100 and 110 crystal orientations. Rotation angles 0°, 22.5°and 45° have been defined relative to the 110 direction. Temperature coefficients and resonance frequencies are listed in Fig. 4(c).

connections were made with wire bonding. The carrier boards included a Maxim DS600 temperature sensor which was in good electrical contact with the resonators through the ground plane. The specified accuracy of the temperature sensor was ± 0.5°C. Carrier boards were connected to a circuit board, which contained ADG1206 multiplexers for selection of a single active resonator at a time.

The approach that was used to measure the frequency response of the resonators is illustrated in Fig. 2(b). A HP4195A network analyzer was used for measuring the forward transmission coefficient $S_{21} = v_{out}/v_{in}$ across the resonator and amplifier (AD825), whose function was to perform the current-to-voltage conversion. A constant bias of 10 volts was applied to all measured resonators to achieve electromechanical coupling.

Circuit boards containing the resonator dies were placed into a climate chamber (Weiss WKL 34/70), whose temperature profile was varied as shown in Fig. 4(a). The profile consisted of sections, where the temperature was ramped over $T = -20 \ldots +60$°C at a pace of approximately one full ramp per day, and of sections where the temperature was held constant at $T = +30/+40$°C. The purpose of the temperature ramps was twofold: to determine the f vs.

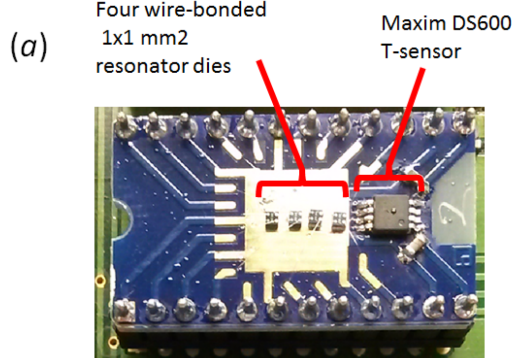

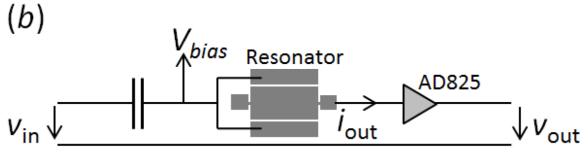

Figure 2. (a) Carrier board used in the long term stability measurement. (b) The frequency response accross the resonator and amplifier was recorded as the transmission coefficient $S_{21} = v_{out}/v_{in}$.

T curves of the resonators (used in (1)) and to accelerate resonator aging. Sections with constant temperature served for eventual determination of the long term stability itself. At each temperature point, the frequency responses of the resonators were measured successively, one resonator at a time.

During the course of the measurement, it turned out that the temperature control of the climate chamber was deficient: the DS600 sensors indicated that the temperature drifted by approximately one centigrade during the constant temperature sections (from $t = -220\,\text{d}$ to $t = 0\,\text{d}$), even though the temperature setpoint was kept unchanged. As a result, the frequency deviation with time at constant temperature could not be followed anymore. However, one could monitor if the frequency drifts off from the f vs. T curve of the device at *any* temperature, and this could then be used as a measure of (in)stability. Therefore, in this work, the frequency drift is defined as

$$\text{drift}(t) = \frac{f_{exp}(t) - f_{theo}(T)}{f_0}, \tag{1}$$

where $f_{exp}(t)$ is the measured frequency at time t, $T = T(t)$ is the measured temperature at this point of time, and $f_{theo}(T)$ is the value from the f vs. T curve in temperature point $T(t)$. f_{theo} was as obtained as a 3rd order polynomial fit to all (f_{exp}, T) data pairs measured for a resonator. The denominator is given by $f_0 = f_{theo}(T = 25°\text{C})$.

Resonators from two phosphorus doped wafers were included in stability measurements. First, measurements were started with seven samples from a wafer with a doping level of $4.1 \times 10^{19}\text{cm}^{-3}$ and later five more samples were added from a wafer with doping of $7.5 \times 10^{19}\text{cm}^{-3}$.

C. Quality factor measurement

Resonators were probed on wafer level before dicing of the encapsulated wafer stacks. The impedances of the resonators were measured with an impedance analyzer HP4294A using the procedure described in [6]. In addition to the two phosphorus doped wafers discussed above, a boron-doped wafer with doping level of $0.6 \times 10^{19}\text{cm}^{-3}$ was characterized as well. Quality factors of the resonators were extracted by fitting the frequency responses to a BVD equivalent circuit (an example is shown in Fig.3). In this paper the focus is on the quality factor of the Lamé mode resonators, since these designs are known to have minimal anchor losses, and therefore the quality factor conveys information about the intrinsic losses in doped silicon (assuming air damping is at a negligible level due to vacuum encapsulation).

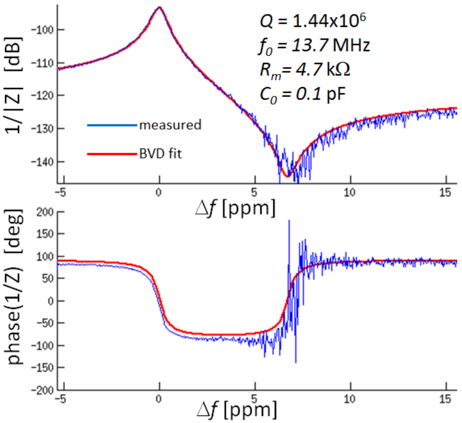

Figure 3. Example frequency response of a Lamé-0° resonator on wafer with $4.1 \times 10^{19}\text{cm}^{-3}$ phosphorus doping. Z denotes the resonator impedance. Q is the quality factor, R_m is the electromechanical resistance and C_0 is the parallel capacitance of the device (obtained from the BVD fit).

III. Results and Discussion

A. Long term stability

Figure 4 shows the frequency drift of the tested resonators over a period of 220 days (70 days for the samples that were added later). The following observations can be made:

1) The frequency drift is less than 1 ppm for resonators with a small temperature coefficient ($|TCF| < 10$) during the observation periods where the temperature is held constant.
2) The frequency drift is degraded with increasing magnitude of resonator TCF.
3) Noise in the frequency drift signal (in particular during the constant temperature phases) is smallest with lowest magnitude of TCF.
4) Frequency drift is larger during the temperature ramps.

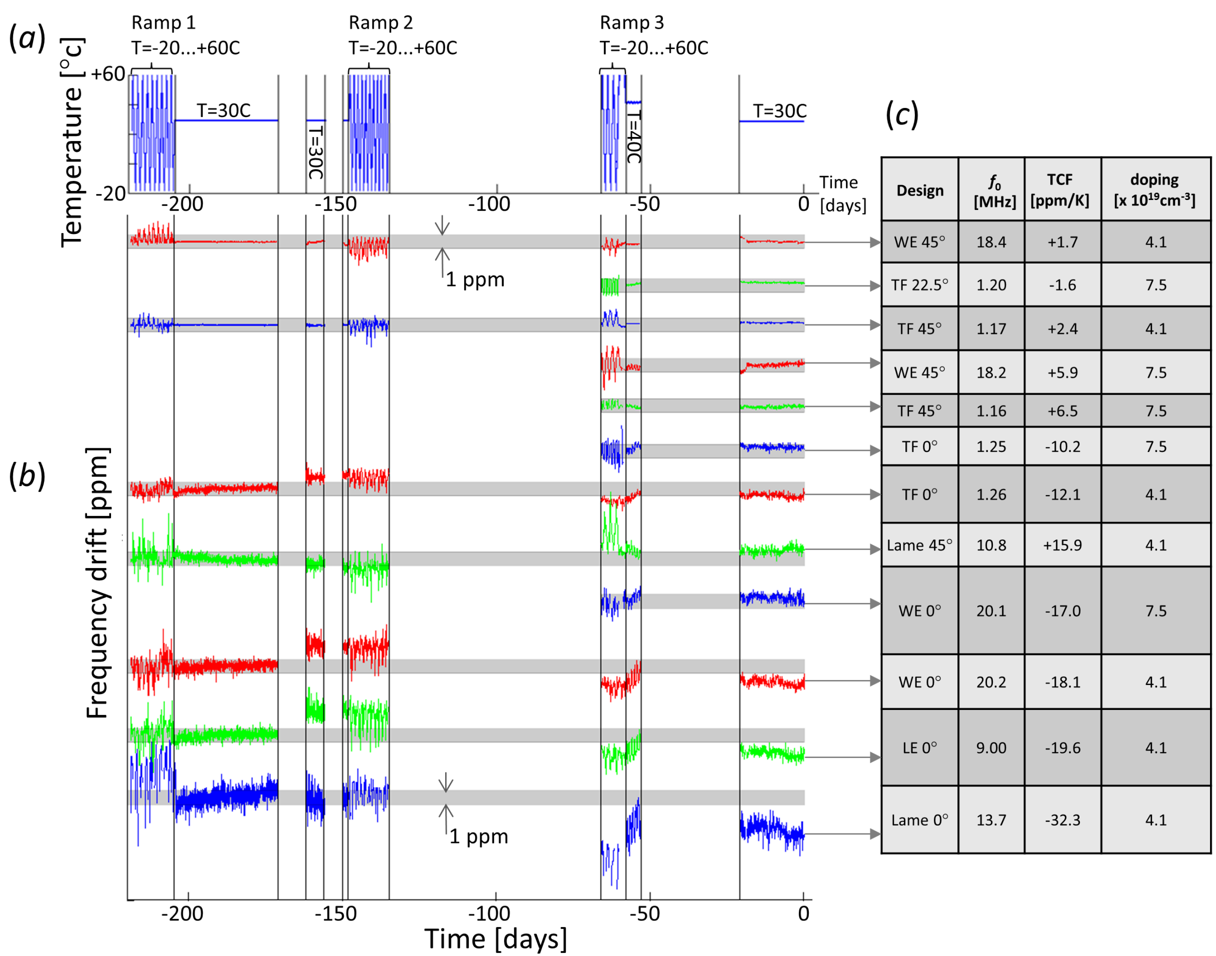

Design	f_0 [MHz]	TCF [ppm/K]	doping [x 10^{19}cm^{-3}]
WE 45°	18.4	+1.7	4.1
TF 22.5°	1.20	-1.6	7.5
TF 45°	1.17	+2.4	4.1
WE 45°	18.2	+5.9	7.5
TF 45°	1.16	+6.5	7.5
TF 0°	1.25	-10.2	7.5
TF 0°	1.26	-12.1	4.1
Lame 45°	10.8	+15.9	4.1
WE 0°	20.1	-17.0	7.5
WE 0°	20.2	-18.1	4.1
LE 0°	9.00	-19.6	4.1
Lame 0°	13.7	-32.3	4.1

Figure 4. (a) Temperature of the climate chamber during the stability measurement. The profile consisted of repeated temperature ramps on a range of $T = -20 \ldots + 60°\text{C}$ and sections where the temperature was held constant at $T = +30/+40°\text{C}$. Samples were removed from the climate chamber for periods with no data (for example $t = -130 \ldots - 70$ days). (b) Frequency drift (see (1) for the definition) of the resonators. The greyed out regions represent 1-ppm corridors. Rows of data have been ordered according to the magnitude of the TCF of the resonators. (c) Design type, resonance frequency, TCF and doping level of the resonators.

The observation that the frequency drift and its noise level increase with growing magnitude of resonator TCF can be explained by the drift and noise from the used temperature sensor, which had a limited accuracy of $\pm 0.5°\text{C}$, and/or by temperature fluctuations during the measurement leading to temperature differences between the resonators and the temperature sensors. Increased sensitivity to temperature error (through increased magnitude of the TCF) is propagated to apparent frequency drift through the definition of (1). Thus, it could be that the real stability is better than what is shown in Fig. 4(b).

In any case, regardless of potential error sources in temperature measurement (and in temperature control, see discussion in Section II-B), the fact that many resonators showed less than 1 ppm drift is a strong indication that degenerate phophorus doping does not affect the stability of silicon resonators detrimentally at the studied doping levels.

The relatively large frequency drifts observed during the temperature ramp periods can be explained by the fact that the 3rd order fits for obtaining $f_{theo}(T)$ of (1) do not fully represent the real f vs. T curves of the resonators, and, also by the possibility of increased temperature gradients in the climate chamber during the ramps.[1]

[1]The originally submitted pre-conference abstract for this paper discussed a frequency jump observed for certain devices at a time $t < -220$ days. This was erroneously identified as a burn-in effect, and in reality the reason was a change in the drive amplitude of these resonators. In this paper the first month of data (with different drive level for some resonators) has been excluded for consistency.

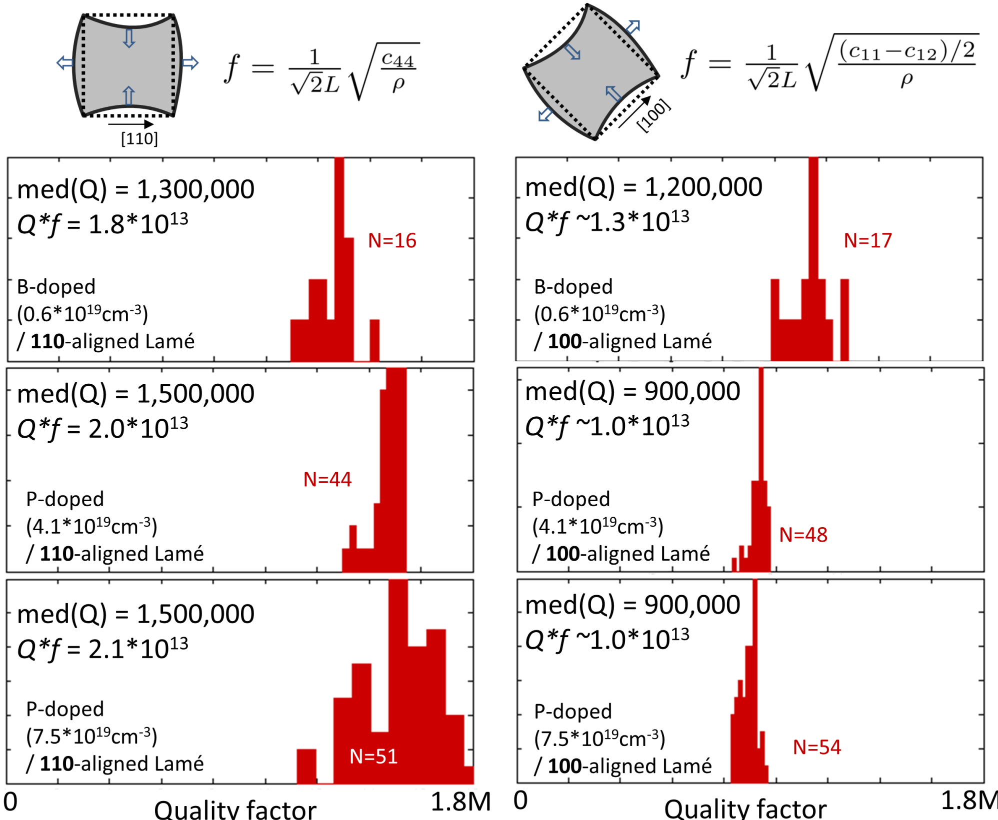

Figure 5. Quality factors of sets of two types of Lamé mode resonators on a moderately boron-doped wafer and on two heavily phosphorus-doped wafers.

B. Quality factors

Figure 5 shows histograms of the quality factors for the 100/110 aligned Lamé mode resonators on three different wafers. Quality factors were seen to range from 900,000 to 1,500,000. The corresponding $Q \times f$ product was found to be within the range of $Q \times f = 1 \ldots 2.1 \times 10^{13}$. These findings match well with previously published results of similar silicon resonators with considerably weaker doping, where the Akhiezer effect losses have been considered to be the major loss mechanism [8], [9].

Evidence for the negligible role of air damping is given by the observation that the average quality factors for the 100/110 oriented Lamé modes differ from each other on the same wafer, while air damping for both modes should be essentially the same due to similar geometries and modeshapes.

IV. Conclusions

A frequency drift below 1 ppm over 220 days of observation was found for several types of heavily phosphorus doped MEMS resonators. The results confirm that heavy n-type doping of silicon does not degrade the long term stability of resonators at the studied doping levels. The stability appears on par or better than that of previously reported for weakly doped silicon resonators, e.g. in [7]. The aging requirement for TCXOs in 3G/LTE/4G phones is less than 1 ppm/year, and this work suggests it could be met with solutions based on heavily doped silicon resonators.

The quality factor measurements indicate that the impact from heavy doping to silicon intrinsic losses is very small. Losses were found to be of a similar order of magnitude when compared to silicon resonators with considerably weaker doping. For most silicon resonator designs of practical importance, the quality factors are limited by other loss mechanisms such as thermoelastic damping or anchor losses.

V. Acknowledgements

The authors would like to acknowledge the Finnish Funding Agency for Technology and Innovation (Tekes), Okmetic Oyj, Murata Electronics and Micro Analog Systems for funding. Jérôme Lamy is acknowledged for the development and construction of the electronics used in the stability measurements.

References

[1] A. K. Samarao, G. Casinovi, and F. Ayazi, “Passive TCF compensation in high q silicon micromechanical resonators,” in *IEEE International Conference on Micro Electro Mechanical Systems (MEMS 2010)*, Hong Kong, Jan. 2010, pp. 116–119.

[2] A. Hajjam, A. Rahafrooz, and S. Pourkamali, “Sub-100ppb/C temperature stability in thermally actuated high frequency silicon resonators via degenerate phosphorous doping and bias current optimization,” in *Proc. IEEE International Electron Device Meeting (IEDM)*, 2010, pp. 7.5.1 – 7.5.4.

[3] T. Pensala, A. Jaakkola, M. Prunnila, and J. Dekker, “Temperature compensation of silicon MEMS resonators by heavy doping,” in *Proc. IEEE International Ultrasonics Symposium*, 2011, pp. 1952–1955.

[4] A. Jaakkola, M. Prunnila, and T. Pensala, “Temperature compensated resonance modes of degenerately n-doped silicon MEMS resonators,” in *Frequency Control Symposium (FCS), 2012 IEEE International*, May 2012, pp. 1 –5.

[5] A. Jaakkola, M. Prunnila, T. Pensala, J. Dekker, and P. Pekko, “Experimental determination of the temperature dependency of the elastic constants of degenerately doped silicon,” in *Joint European Frequency and Time Forum / International Frequency Control Symposium (EFTF/IFC)*, Jul. 2013, pp. 421–424.

[6] ——, “Determination of doping and temperature dependent elastic constants of degenerately doped silicon from MEMS resonators,” *arXiv:1401.1363 [cond-mat]*, Jan. 2014. [Online]. Available: http://arxiv.org/abs/1401.1363

[7] V. Kaajakari, J. Kiihamaki, A. Oja, S. Pietikainen, V. Kokkala, and H. Kuisma, “Stability of wafer level vacuum encapsulated single-crystal silicon resonators,” *Sensors and Actuators A: Physical*, vol. 130, pp. 42–47, 2006.

[8] C. Tu and J. E. Y. Lee, “Thermoelastic dissipation in etch-hole filled lame bulk-mode silicon microresonators,” *IEEE Electron Device Letters*, vol. 33, no. 3, pp. 450–452, 2012.

[9] L. Khine, M. Palaniapan, and W. K. Wong, “12.9 MHz lame-mode differential SOI bulk resonators,” in *Solid-State Sensors, Actuators and Microsystems Conference, TRANSDUCERS 2007.*, 2007, pp. 1753–1756.

Paper V

Reproduced with permission from L. Lipiäinen, A. Jaakkola, K. Kokkonen, M. Kaivola, "Frequency splitting of the main mode in a microelectromechanical resonator due to coupling with an anchor resonance". Applied Physics Letters, 100(1), 013503, pp. 013503-1—3, 2012. Copyright 2012, AIP Publishing LLC. http://dx.doi.org/10.1063/1.3673558

APPLIED PHYSICS LETTERS **100**, 013503 (2012)

Frequency splitting of the main mode in a microelectromechanical resonator due to coupling with an anchor resonance

Lauri Lipiäinen,[1,a)] Antti Jaakkola,[2] Kimmo Kokkonen,[1] and Matti Kaivola[1]
[1]*Department of Applied Physics, Aalto University, P.O. Box 13500, FI-00076 AALTO Espoo, Finland*
[2]*VTT Technical Research Centre of Finland, P.O. Box 1208, FI-02044 VTT Espoo, Finland*

(Received 23 August 2011; accepted 9 December 2011; published online 4 January 2012)

We present an experimental study of the frequency scaling of the main, square-extensional mode in a piezoelectrically actuated plate resonator. The studied set consists of resonators of different plate sizes with identical anchors. The behavior of the square-extensional mode is analyzed using electrical impedance measurements and optical characterization of the mechanical vibration fields. The results reveal a detrimental anchor effect, where for certain plate sizes the square-extensional mode branch is split into two due to a coupled oscillation of the resonator plate and the anchors. © *2012 American Institute of Physics*. [doi:10.1063/1.3673558]

Recent progress in microelectromechanical systems (MEMS) technology has opened up possibilities for the use of single-crystal silicon resonators in frequency control and timing applications, dominated for decades by quartz crystal based components. The foreseen benefits of MEMS resonators include, e.g., low cost, compact size, low power consumption, and added functionality due to compatibility with complementary metal-oxide-semiconductor (CMOS) processing. It has already been demonstrated that capacitively driven square-extensional (SE) mode MEMS resonators can fulfill the performance requirements for frequency reference applications.[1] There is a further interest to excite MEMS resonators piezoelectrically[2,3] in order to avoid the need for bias voltage and sub-100-nm sized gaps as in capacitive excitation.

In a MEMS resonator, the energy has to be mechanically well confined within the resonating structure. Since anchoring is needed to support the resonator, the whole device structure, including the anchors, should be carefully designed to minimize the leakage of acoustic energy to the surroundings. Both analytical[4] and numerical[5] methods exist to calculate such structures, but in practice, empirical testing is often required to truly optimize a device. Experimental studies of the anchoring geometry of bulk mode MEMS resonators[6–8] suggest that in order to minimize the acoustic loss, the anchors should be flexible and preferably be located at the nodal points of the vibration mode.

In SE-mode operation, the resonator plate expands and contracts, while preserving its shape and, therefore, does not have a nodal point at the plate perimeter. As the in-plane (IP) vibration component of the SE mode contains most of the vibration energy, the existing nodal point of the IP vibration at the center of the plate would be an optimal anchor site. Unfortunately, anchoring at this point is challenging in the type of resonators discussed here,[3] in which the SE mode is excited using a piezoelectric thin film on top of the resonator plate, see Fig. 1(a). In our resonators, the anchors are therefore placed at the plate corners. Even though in this design the SE mode vibration maxima fall at the anchor positions, it has been demonstrated that a high quality-factor SE resonance ($Q \approx 130\ 000$) can be achieved in a capacitively excited SE mode resonator, using such an anchor structure.[1]

In this letter, we present an experimental study of the frequency scaling of the SE vibration mode as a function of the resonator plate size. A starting point for the analysis was the measurements of the electrical response of a set of 1200 MEMS resonators.[9] It was observed that, at certain device sizes, the SE mode branch appeared to split into two distinct frequency branches. In order to gain physical insight into

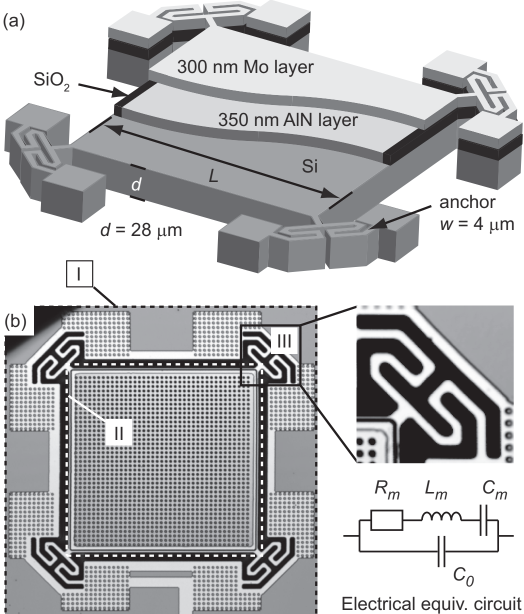

FIG. 1. (a) Structure of the square-plate resonator. The 28-μm-thick, single-crystalline silicon resonator plate is attached to the substrate at the plate corners with 4-μm-wide meander anchors. A 350-nm-thick piezoelectric AlN layer is deposited on top of the plate. A 300-nm Mo layer on top of the AlN layer acts as a top electrode, and the Si resonator plate itself acts as a bottom electrode. (b) Photograph of the $L = 209\,\mu$m resonator sample and the rectangular scan areas I (scan step 1.54 μm), II (0.44 μm), and III (0.44 μm) used for laser probe measurements. To enable in-plane laser probe measurements, the top-electrode Mo layer is patterned with a 5-μm grid of circular 2.5-μm-diameter holes. The electrical equivalent circuit model of the resonator is shown at the bottom-right corner.

a)Electronic mail: lauri.lipiainen@tkk.fi.

 © 2012 American Institute of Physics

This article is copyrighted as indicated in the article. Reuse of AIP content is subject to the terms at: http://scitation.aip.org/termsconditions. Downloaded to IP: 130.188.235.206 On: Sun, 06 Sep 2015 07:56:31

this adverse behavior, 8 devices of different plate sizes were selected for optical characterization of the IP and out-of-plane (OP) vibration fields (preliminary findings reported in Ref. 10). The results of the optical measurements indicate a coupled resonance between the resonator plate and the anchors. This finding is further supported by a good fit of an analytic model of two coupled resonators with the experimental data.

The resonator structure is illustrated in Fig. 1(a). The fabricated set consists of resonators of 64 different sizes; the side length of the plate is varied from $L = 131\,\mu$m to $L = 320\,\mu$m in steps of $3\,\mu$m. This plate size range corresponds to a designed SE frequency range from 13 to 32 MHz. The design and the dimensions of the anchors were kept the same in all resonators. Each size variation was replicated 10 times on a single wafer, and the replicas were distributed over the whole wafer. The fabrication process is described in Ref. 3.

The electrical responses of approximately 1200 resonators from two wafers were measured with an impedance analyzer (Agilent Technologies A4294). The resonance frequency f_0, motional resistance R_m, quality factor Q, and the parallel capacitance C_0 were determined by fitting an electrical equivalent circuit model of the resonator [see inset in Fig. 1(b)] to the measured impedance data.

Eight devices with L ranging from 137 μm to 305 μm (in steps of 24 μm) were selected for laser probe measurements. The laser probing was carried out using a scanning Michelson laser interferometer.[11] The instrument enables amplitude and phase measurements of both the OP[12] and IP components[13,14] of the surface vibrations.

The OP and IP scan areas and their relation to the sample geometry are depicted in Fig. 1(b). To get an overview of the acoustic behavior of the sample, the OP data were first measured over the whole resonator [scan area I in Fig. 1(b)] including the resonator plate, anchors, and a part of the substrate. The IP vibration fields were then obtained from the resonator plate (scan area II). In addition, both vibration components were measured over the top-right anchor and a part of the resonator plate (scan area III). All the optical measurements were carried out at low pressure (<0.2 mbar) and at room temperature.

An analytic spring-mass model of the resonator, in which the contribution of the anchors is excluded (see inset A in Fig. 2), predicts that the resonance frequency of the SE mode is inversely proportional to the plate side length L. In the electrical characterization results, however, a deviation from the expected $1/L$ frequency scaling is observed, see Fig. 2. In particular, at the intermediate plate sizes, $160\,\mu\text{m} < L < 260\,\mu$m, instead of a single resonance, two strong resonances are observed above and below the predicted SE resonance frequency such that the SE mode branch appears to split into two distinct frequency branches. In addition, for these plate dimensions, the spread of the resonance frequencies between samples of the same plate size increases when the upper or lower resonance frequency branches diverges away from the expected $1/L$ scaling.

In the eight optically measured samples, despite of the frequency splitting, the IP vibration field of the two branches corresponds to what is characteristic to the SE mode, except for the $L = 185\,\mu$m plate size at the lower frequency branch and for the $L = 233\,\mu$m and $L = 257\,\mu$m plate sizes at the higher frequency branch (see the symbolic representation in Fig. 2). These three non-SE modes are observed to vibrate strongly in the OP direction, indicating that another mode, with a strong OP component, is excited instead of the SE mode at these plate dimensions.

It is also observed that the IP vibration amplitudes and the electrically characterized resonances are stronger for the branch that is closer to the predicted frequency of the SE mode. The electrical Q values of the resonances on the stronger branch are typically between 12 000 and 18 000 and R_m between 80 and 200 Ω at a pressure of <10 mbar, whereas on the weaker branch they are significantly worse, $Q \sim 100$–1000 and $R_m > 1$ kΩ.

The laser probing measurements reveal an increased vibration activity at the anchors within the 20–22 MHz frequency range for all plate sizes. In this frequency range, several resonances are observed that feature stronger IP and OP vibration amplitudes at the anchors than at the resonator plate. An example of the frequency response of such a resonance is illustrated in Fig. 2 (enlarged in the inset E).

The IP phase data give further evidence on the role of the increased anchor activity at the 20–22 MHz frequency range to the splitting of the SE mode. The phase data in insets C and D of Fig. 2 show that the resonator plate and the anchor are moving in opposite phase on the higher-frequency branch, whereas on the lower-frequency branch, they vibrate in phase. This would indicate that the resonances on the upper and lower branches are the two eigenmodes of a coupled oscillation between the SE mode and a parasitic anchor mode. The trends of the behavior of the two frequency branches also suggest that this anchor mode exists between 20 and 22 MHz.

A coupled two-resonator model, depicted in inset B of Fig. 2, was used to give further support to our conclusion. A spring-mass system with an effective mass m_1 and a spring constant k_1 describes the SE mode of the resonator plate. When another spring-mass system (k_2, m_2) is introduced in the model to take into account the anchor, this coupled resonator model results in a good fit to the electrically measured resonance frequency data.

The extensive electrical and laser probe characterizations of this study have provided us with valuable information on the anchor resonance effects to the operation of the MEMS plate resonator. It is evident that even small and flexible anchors may have a significant impact on the resonance behavior of the massive plate (relative to the anchors), at least in the case when the resonator plate is not anchored at a nodal point of the plate's vibrational motion. As seen from the electrical data in Fig. 2, the deviation of the stronger SE resonance branch from the $1/L$ scaling starts already at around $L = 170\,\mu$m (upper branch) and $L = 230\,\mu$m (lower branch), although the resonance frequencies are more than 1 MHz away from the 20 to 22 MHz frequency range where the anchors are active.

The coupling between the SE mode and a parasitic anchor resonance leads to unwanted consequences. First of all, certain operation frequencies cannot be achieved by simply scaling the size of the resonator plate unless the anchor design is changed accordingly. More importantly, the spread of the SE

This article is copyrighted as indicated in the article. Reuse of AIP content is subject to the terms at: http://scitation.aip.org/termsconditions. Downloaded to IP: 130.188.235.206 On: Sun, 06 Sep 2015 07:56:31

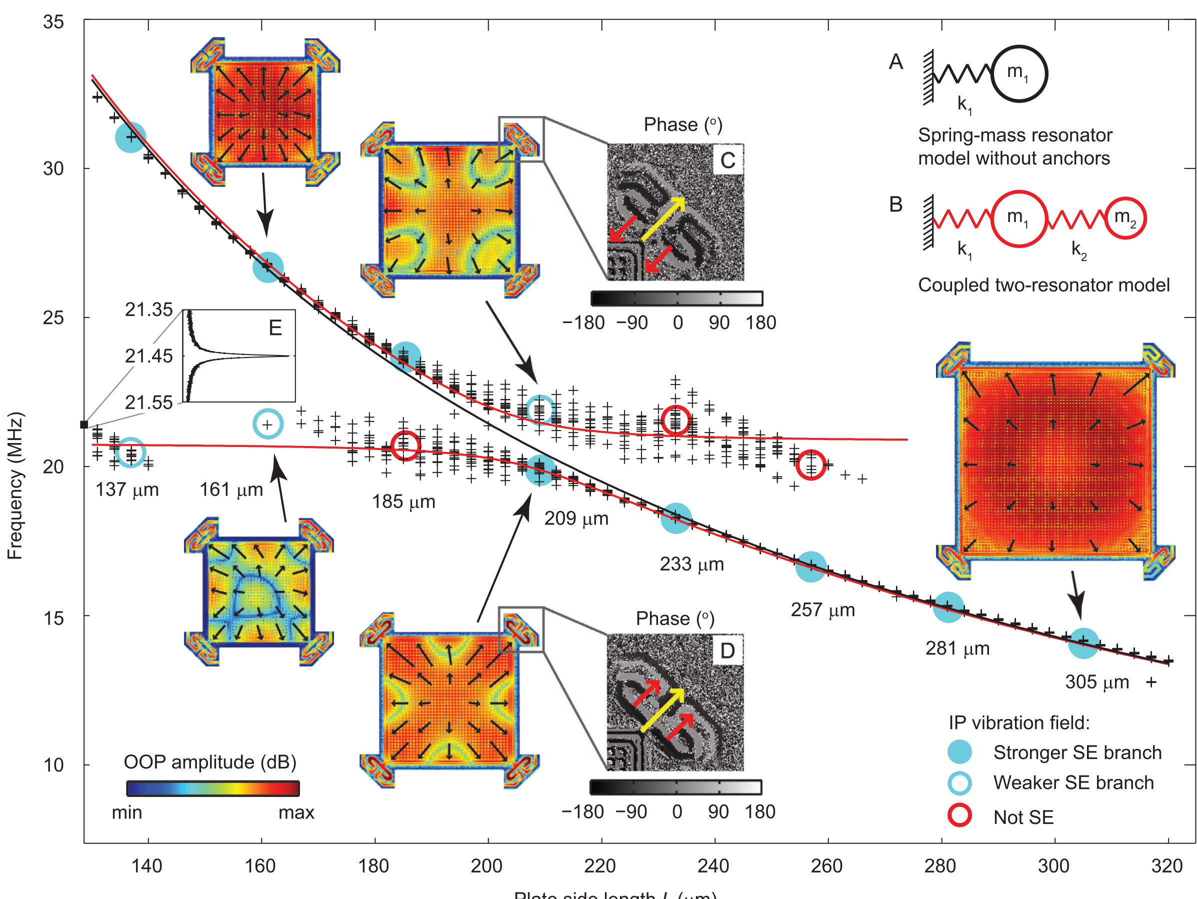

FIG. 2. (Color) The electrical characterization and laser probing results. The electrically characterized resonance frequencies (black "+") are plotted as a function of the plate side length L. Only the resonances corresponding to the two frequency branches closest to the pure SE mode frequency curve (black line) predicted by the single spring-mass model (shown in inset A) are presented. The red curves represent the least squares fit of the coupled resonator model (shown in inset B) to the electrical data. The measured OP (colormap) and IP amplitude data (black arrows on the OP data) of selected plate sizes are shown as insets. To visualize the vibration fields, each OP data figure has a separate logarithmic scaling normalized to its maximum OP amplitude, and also the lengths of the arrows indicating the IP fields have a separate linear scaling for each data figure. Insets C and D: The IP phase data of the top-right anchor of the $L = 209\,\mu$m resonator. The instantaneous movement directions of the anchor and the resonator plate are depicted with red and yellow arrows. Inset E: Frequency sweep of the IP vibration amplitude of a selected resonance within the 20-22 MHz range, in which increased anchor activity is observed (measured from the top-right anchor).

resonance frequencies between resonator samples of the same size is too high for frequency control and timing applications in the region where the SE frequency deviates from the $1/L$ relationship due to the mode coupling. In this study, this frequency spread is unsatisfactorily high over an operational frequency range of 19–25 MHz. To avoid the adverse effects of the anchor-plate coupling, a large frequency margin between the main and anchor resonance is therefore required.

L.L. acknowledges Aalto University School of Science and Technology for scholarships.

[1] V. Kaajakari, T. Mattila, A. Oja, J. Kiihamäki, and H. Seppä, IEEE Electron Device Lett. **25**, 173 (2004).

[2] G. K. Ho, R. Abdolvand, A. Sivapurapu, S. Humad, and F. Ayazi, J. Microelectromech. Syst. **17**, 512 (2008).

[3] A. Jaakkola, P. Rosenberg, S. Asmala, A. Nurmela, T. Pensala, T. Riekkinen, J. Dekker, T. Mattila, A. Alastalo, O. Holmgren, and K. Kokkonen, in *Proceedings of the IEEE Ultrasonics Symposium*, Beijing, China, November 2–5, 2008 (IEEE, New York, 2008), pp. 717–720.

[4] Z. Hao, A. Erbil, and F. Ayazi, Sens. Actuators, A **109**, 156 (2003).

[5] D. S. Bindel, E. Quévy, T. Koyama, S. Govindjee, J. W. Demmel, and R. T. Howe, in *Proceedings of the IEEE MEMS 2005* (IEEE, Inc., Miami, Florida, U.S, 2005), pp. 133–136.

[6] J. E.-Y. Lee, J. Yan, and A. A. Seshia, in *Proceedings of Eurosensors XXII*, Dresden, Germany, September 7–10, 2008, pp. 536–539.

[7] L. Khine, M. Palaniapan, and W -K. Wong, in *Proceedings of the Solid-State Sensors, Actuators and Microsystems Conference*, Lyon, France, June 10–14, 2007, pp. 1753–1756.

[8] L. Khine and M. Palaniapan, J. Micromech. Microeng. **19**, 015017 (2009).

[9] A. Jaakkola, J. Lamy, J. Dekker, T. Pensala, L. Lipiäinen, and K. Kokkonen, in *Proceedings of the IEEE International Frequency Control Symposium*, Newport Beach, California, USA, June 1–4, 2010 (IEEE, New York, 2010), pp. 410–414.

[10] L. Lipiäinen, K. Kokkonen, O. Holmgren, and M. Kaivola, in *Proceedings of the IEEE Ultrasonics Symposium*, San Diego, California, USA, October 11–14, 2010 (IEEE, New York, 2010), pp. 416–419.

[11] J. V. Knuuttila, P. T. Tikka, and M. M. Salomaa, Opt. Lett. **25**, 613 (2000).

[12] L. Lipiäinen, K. Kokkonen, and M. Kaivola, J. Appl. Phys. **108**, 114510 (2010).

[13] O. Holmgren, K. Kokkonen, T. Mattila, V. Kaajakari, A. Oja, J. Kiihamäki, J. V. Knuuttila, and M. M. Salomaa, Electron. Lett. **41**, 16 (2005).

[14] O. Holmgren, K. Kokkonen, T. Veijola, T. Mattila, V. Kaajakari, A. Oja, J. V. Knuuttila, and M. Kaivola, J. Micromech. Microeng. **19**, 015028 (2009).

This article is copyrighted as indicated in the article. Reuse of AIP content is subject to the terms at: http://scitation.aip.org/termsconditions. Downloaded to IP: 130.188.235.206 On: Sun, 06 Sep 2015 07:56:31

Reproduced with permission from L. Lipiäinen, A. Jaakkola, K. Kokkonen, M. Kaivola, "Nonlinear excitation of a rotational mode in a piezoelectrically excited square-extensional mode resonator". Applied Physics Letters, 100(15), pp. 153508-1—4, 2012. Copyright 2012, AIP Publishing LLC. Reprinted with permission. http://dx.doi.org/10.1063/1.3703119

APPLIED PHYSICS LETTERS **100**, 153508 (2012)

Nonlinear excitation of a rotational mode in a piezoelectrically excited square-extensional mode resonator

Lauri Lipiäinen,[1] Antti Jaakkola,[2] Kimmo Kokkonen,[1] and Matti Kaivola[1]
[1]*Department of Applied Physics, Aalto University, P.O. Box 13500, 00076 Aalto, Finland*
[2]*VTT Technical Research Centre of Finland, Espoo, Finland*

(Received 18 January 2012; accepted 24 March 2012; published online 12 April 2012)

We present an experimental study of the nonlinear behavior of a square-extensional (SE) mode microelectromechanical resonator, actuated with a piezoelectric AlN thin film. The acoustic vibration fields of the device are characterized using laser probing. A nonlinear vibration behavior of the SE mode is observed above a drive power level of −10 dBm such that the vibration amplitude of the SE mode saturates and a rotational in-plane vibration mode is excited at a significantly lower frequency (0.725 MHz) than the SE mode (16.670 MHz). Interestingly, the measured ∼10 nm saturation amplitude of the SE mode is more than a decade below the amplitude value at which mechanical or electromechanical nonlinearities are estimated to become significant. © *2012 American Institute of Physics*. [http://dx.doi.org/10.1063/1.3703119]

Microelectromechanical system (MEMS) silicon resonators are considered as potential alternatives to quartz crystals in timing and frequency control applications. Compared to quartz crystals that have dominated these markets over decades, the foreseen benefits of MEMS resonators include low cost, small size, low power consumption, and integrability with CMOS processing.[1] Piezoelectric thin-film actuation is a promising transduction method for MEMS silicon resonators.[2,3] While the more commonly used capacitive transduction provides resonances with a higher quality factor, even as high as $Q \sim 100000$ in the 10–100 MHz range[4,5] and $Q \sim 10000$ in the GHz range,[6] piezoelectric thin-film excitation can offer a better electromechanical coupling and, moreover, no DC bias or sub-100 nm gap structures are required as in capacitive coupling.

Compared to quartz crystals, the desirable smaller size of MEMS resonators unavoidably results in poorer energy storage, making it challenging to achieve an adequate phase noise performance.[7] Hence, the MEMS resonator should provide a vibration amplitude as high as possible for the best performance. In capacitively actuated Si resonators, the power handling capacity in linear operation is limited by both the nonlinear nature of the transduction method and the mechanical structure of the resonator.[7] The nonlinearity of the transduction is often the dominant one in capacitively driven resonators, but the effect can be reduced, e.g., by a more dedicated electrode configuration such as those used in comb-drive structures. The main mechanical nonlinearities are typically the nonlinearity of the resonator materials and the nonlinear geometrical effects caused by dynamic shape variations during vibration.

In the case of piezoelectric AlN thin-film-actuated MEMS Si resonators discussed here, the power handling capacity in linear operation is ultimately limited by the mechanical nonlinearities of the vibrating AlN-Si structure[8] and by the electromechanical nonlinearity of the AlN thin film. In a recent study,[9] the most dominant nonlinearity of AlN was shown to be the electromechanical nonlinearity, which, however, was observed to be nearly negligible at electric field strengths below 10 V/μm. In our experiments, the electric field strength was < 1V/μm, and hence, the nonlinearities of the AlN layer are expected to be small compared to the mechanical nonlinearities of the Si resonator structure.

The mechanical nonlinearities (and transduction nonlinearities in capacitive resonators) cause vibration amplitude dependent changes to the center frequency of the resonance, so-called spring-softening or spring-hardening effects (a.k.a. duffing effect). Increasing the vibration amplitude either decreases (spring softening) or increases (hardening) the center frequency of the resonance, and eventually, above a critical vibration amplitude A_c, the amplitude-frequency curve shows hysteresis (bifurcation). Although there have been some ideas of taking advantage of the bifurcation effect,[10–12] this effect is usually considered detrimental to resonators designed for linear operation, which in practice limits their power handling capacity.

In this letter, we have experimentally studied the acoustic behavior of a piezoelectrically driven square-extensional (SE) mode MEMS silicon resonator as a function of the input power. The in-plane (IP) and out-of-plane (OP) acoustic vibration fields of the device are characterized using optical probing. It is observed that when linearly increasing the drive power, the vibration amplitude of the 16.670-MHz SE mode first linearly increases and then, above a drive power level of $P_{TH} = -10$ dBm, saturates to a nearly constant value. The corresponding saturation amplitude of the IP vibration is measured to be approximately 10 nm, which is more than an order of magnitude below the anticipated critical amplitude of bifurcation resulting from the mechanical nonlinearities of the resonator structure. Furthermore, the results show that, by driving the SE mode into the nonlinear regime where its vibration amplitude is saturated, a very pure rotational IP vibration mode is excited at 0.725 MHz, corresponding to the 23rd subharmonic frequency of the SE mode.

The structure of the square-plate resonator is illustrated in Fig. 1(a). The resonator is designed to operate in the SE mode at 16.670 MHz. The electrically measured quality factor for the SE mode operation (in vacuum, < 1 mBar) is $Q = 18\,000$ and the motional resistance is $R = 80\,\Omega$. The electrical characterization method is described in Ref. 13.

This article is copyrighted as indicated in the article. Reuse of AIP content is subject to the terms at: http://scitation.aip.org/termsconditions. Downloaded to IP: 130.188.235.206 On: Sun, 06 Sep 2015 08:02:09

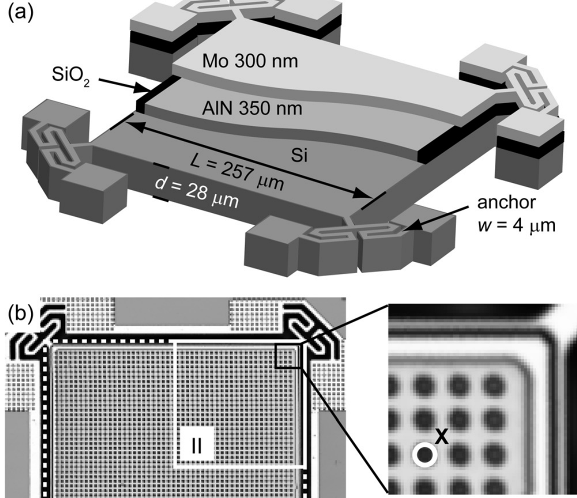

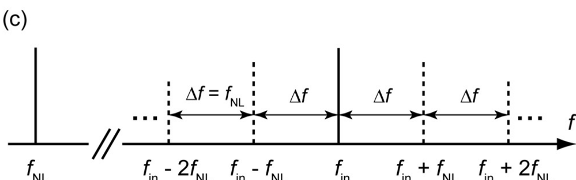

FIG. 1. (a) Schematic view of the sample. The 257 μm × 257 μm × 28 μm, single-crystalline Si resonator plate is piezoelectrically actuated with an AlN thin film. The Mo layer on top of the AlN layer acts as the top electrode, and the Si plate itself is used as the bottom electrode. The resonator is attached to the substrate at its corners with 4-μm-wide, meander anchors. (b) A microscope image of the resonator and illustration of the measurement areas used for optical characterization of the vibration fields. The top-electrode Mo layer is patterned with a 5-μm-period grid of circular, 2.5-μm-diameter holes in order to create reflectivity variations for IP detection. (c) Schematic representation of the frequency spectrum of the measurement signal, including signal artifacts caused by the nonlinearity of the optical detection (dashed lines) and the signals from the real acoustic modes (solid lines). The resonator is driven at f_{in}, resulting in the excitation of one vibration mode at f_{in} and another at f_{NL}.

The acoustic vibration fields were measured using a scanning homodyne Michelson interferometer,[14] which is capable of amplitude and phase measurements of IP (Refs. 15 and 16) and OP (Ref. 17) surface vibration fields. The setup enables the use of different excitation and detection frequencies for studies of nonlinear acoustic phenomena.

The measurement areas in the sample geometry are depicted in Fig. 1(b). First, the amplitude of the IP and OP vibrations were measured at a single point as a function of the drive power of the single-frequency excitation. Care was taken to choose the measurement position in such a way that all relevant acoustic modes were detected. The OP measurement point, marked with "X" in Fig. 1(b), is located on the metal surface between the holes at the top-right corner of the resonator plate. The IP measurement point is at the right-hand side edge of the hole depicted with a white circle in Fig. 1(b). For each IP vibration mode, only the most sensitive point at the edge of the hole, i.e., the point where the normal of the edge is collinear with the direction of the vibration, is selected as the IP detection point. Areal measurements were then carried out on the resonator plate at selected excitation and detection frequency combinations in which the nonlinear acoustic behavior was observed. The OP measurement area I (267 μm × 267 μm) covers the whole resonator plate with a scan step of 1.54 μm. Due to the symmetry of the IP modes obtained in this study, the IP vibration field was measured only at the top-right quarter of the plate (scan area II: 134 μm × 134 μm, scan step 0.44 μm). The measurements were carried out in a low pressure environment ($<$0.2 mBar) at room temperature.

It should be noted that the laser interferometric OP and the vectorial IP detection methods are themselves nonlinear in nature. Consequently, all the acoustic modes which simultaneously exist in the sample at different resonance frequencies are mixed in the detection, leading to artifacts in the detected signal. A schematic spectrum of such a measurement signal is depicted in Fig. 1(c) for the case of a MEMS resonator that features one mode at the input drive frequency f_{in} and one nonlinearly excited mode at $f_{NL} \ll f_{in}$. In our experiments, we utilize the IP data of the areal measurements to identify the true acoustic modes based on the fact that, contrary to the laser interferometric OP data, the artifacts result in a different spatial content in the IP data than the real acoustic fields.

In the sample resonator, a nonlinear acoustic behavior was observed which was similar to the illustrative case of Fig. 1(c). When driving the sample at the SE mode excitation frequency of $f_{in} = f_{SE} = 16.670$ MHz above a threshold power of $P_{TH} = -10$ dBm, another mode gets nonlinearly excited at $f_R = 0.725$ MHz. The f_R mode could not be electrically detected with this electrode geometry, but it was readily observed with the optical detection.

The detected IP vibration amplitudes of the two modes are presented in Fig. 2(a) as a function of the input drive power P_{in}, when the sample is driven at $f_{SE} = 16.670$ MHz. The nominal drive power P_{in} is swept in the range from -41 to -6 dBm with 0.5 dBm steps. The mode at f_R abruptly emerges at $P_{TH} = -10$ dBm. Above P_{TH}, the IP amplitude of the SE mode saturates, whereas the IP amplitude of the f_R mode starts to increase with a slope approaching unity at $P_{in} > -9$ dBm. This indicates that above $P_{in} = -9$ dBm all the added power goes to the f_R mode. Importantly, it should be noted that the f_R mode cannot be directly excited via piezoelectric actuation at f_R in this electrode geometry. Hence, the f_R mode is a result of a truly nonlinear effect, emerging only by actuating the resonator at f_{SE} with $P_{in} > P_{TH}$.

The IP vibration amplitudes of the SE and f_R modes are illustrated in Fig. 2(b) as a function of the drive frequency, using three different drive power levels in the nonlinear regime ($P_{in} > P_{TH}$) and one in the linear regime. The drive frequency is swept both into increasing (f_{in-up} sweep) and decreasing frequency ($f_{in-down}$ sweep) with 100 Hz frequency steps. In the nonlinear regime, the SE mode data clearly show the amplitude cutoff effect. However, the behavior is different for the f_{in-up} and $f_{in-down}$ sweeps. For the up sweeps, the resonances extend higher in frequency, until, at certain drive frequencies depending on the power level, the

This article is copyrighted as indicated in the article. Reuse of AIP content is subject to the terms at: http://scitation.aip.org/termsconditions. Downloaded to IP: 130.188.235.206 On: Sun, 06 Sep 2015 08:02:09

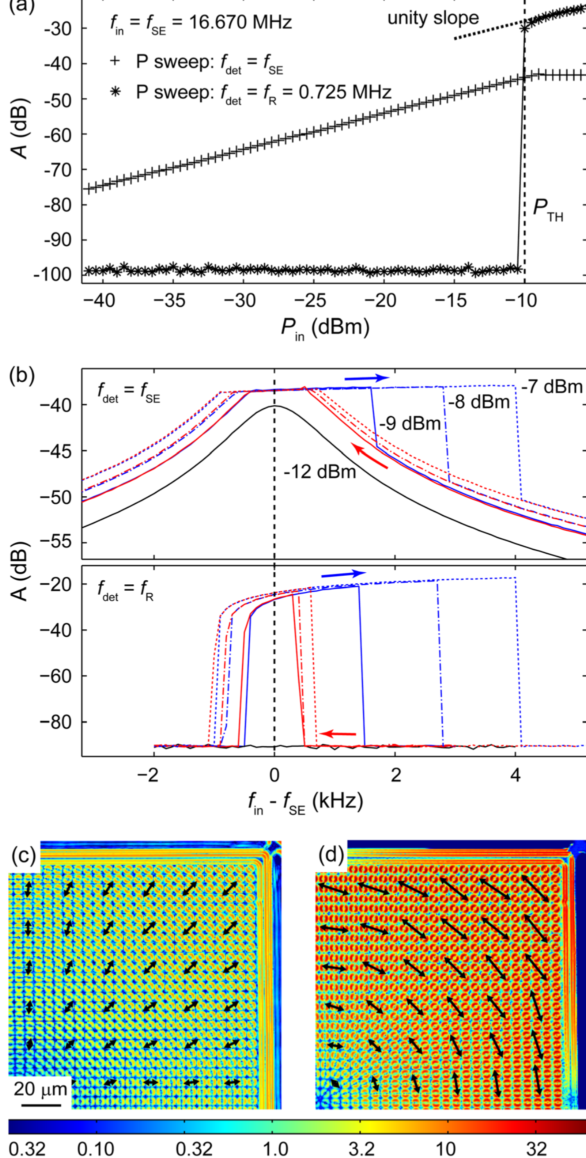

FIG. 2. (a) Measured relative IP vibration amplitude A at $f_{SE} = 16.670$ MHz ("+") and at $f_R = 0.725$ MHz ("∗") as a function of the input drive power ($f_{in} = f_{SE} = 16.670$ MHz). (b) The relative IP vibration amplitude detected at f_{SE} (top) and at f_R (bottom) as a function of f_{in}, using four different P_{in} levels (-12 dBm solid black line, -9 dBm solid, -8 dBm dashdotted, and -7 dBm dotted blue/red line). In the nonlinear regime, $P_{in} > -10$ dBm, the drive frequency f_{in} is swept both upward (blue lines) and downward (red) in frequency. (c) IP vibration amplitude A_{vib} and vector fields of the $f_{SE} = 16.670$ MHz and the (d) $f_R = 0.725$ MHz mode, when the sample is driven with $P_{in} = -8$ dBm at $f_{in} = 16.670$ MHz.

amplitude abruptly drops down. No such asymmetric broadening of the resonance is observed for the down sweeps. Similar broadening behavior for the f_{in-up} sweeps is observed also for the f_R mode. In addition, the f_{in-up} and $f_{in-down}$ sweeps of the f_R mode show hysteresis effect which is characteristic for spring hardening.

The measured IP vibration fields of the f_{SE} mode and the f_R mode are illustrated in Figs. 2(c) and 2(d). In these areal scans, the resonator is driven in the nonlinear regime with $P_{in} = -8$ dBm at f_{SE}. Although the IP vibration amplitude of the SE mode is saturated to a maximum of ~ 10 nm in this regime, its vibration field pattern is still characteristic to the SE mode, similar to the one obtained in the linear operation range, $P_{in} < P_{TH}$. Also the shape of the OP SE vibration field was found to stay unchanged in the nonlinear range, but the amplitude saturates.

The IP data of the f_R mode correspond to an IP vibration mode with radially symmetric rotational vibration of the resonator plate with the corner anchors acting as springs. Interestingly, there is no detectable OP component, indicating the mode to be purely rotational. The measured maximum IP amplitude of this rotational mode is even higher than that of the SE mode, see Figs. 2(c) and 2(d). It was also confirmed using FEM simulations that such a f_R mode indeed can exist in this resonator structure at this frequency.

The nonlinearity observed in this study severely degrades the power handling capacity of the resonator sample. The obtained IP saturation amplitude for the SE mode is approximately 10 nm, whereas the bifurcation amplitude due to mechanical nonlinearities has been estimated to be > 300 nm in this resonator structure. This estimation is based on a limit obtained previously in a capacitive SE mode resonator with a similar Si resonator structure,[7] which is scaled to the dimensions and the Q value of our resonator. Hence, the mechanical nonlinearity of the resonator structure does not explain the low nonlinearity limit obtained.

Avoort *et al.*[18] have reported a nonlinear behavior in capacitively actuated MEMS resonators, which shows similarities to the observations of our study, such as the amplitude saturation and the excitation of another acoustic mode at a different frequency than the excitation frequency. They proposed the nonlinear behavior to be related to an autoparametric resonance. However, we observe an amplitude-frequency hysteresis in our sample resonator, a feature not explained by the autoparametric resonance in a linear system. The 1:23 frequency ratio between the f_R and f_{SE} modes would indicate that they may be mechanically coupled, thus resulting in a nonlinear parametric excitation.[19] Dedicated simulations and further experiments in varying dimensions are needed to explain in detail the nonlinear effects observed.

A.J. acknowledges funding from the Academy of Finland.

[1] C. T.-C. Nguyen, IEEE Trans. Ultrason. Ferroelectr. Freq. Control. **54**, 251–270 (2007).
[2] R. Abdolvand, H. Lavasani, G. Ho, and F. Ayazi, IEEE Trans. Ultrason. Ferroelectr. Freq. Control **55**, 2596–2606 (2008).
[3] A. Jaakkola, P. Rosenberg, S. Asmala, A. Nurmela, T. Pensala, T. Riekkinen, J. Dekker, T. Mattila, A. Alastalo, O. Holmgren, and K. Kokkonen, in *Proceedings of the IEEE Ultrasonics Symposium*, Beijing, China, 2-5 November 2008 (IEEE, New York, 2008), pp. 717–720.
[4] V. Kaajakari, T. Mattila, A. Oja, J. Kiihamäki, and H. Seppä, IEEE Electron Device Lett. **25**, 173–175 (2004).
[5] N. D. Badilaf-Ciressan, M. Mazza, D. Grogg, and A. M. Ionescu, Solid-State Electron. **52**, 1394–1400 (2008).
[6] J. Wang, J. E. Butler, T. Feygelson, and C. T. C. Nguyen, in *Proceedings of the IEEE 17th International Conference on MEMS*, Maastricht, The Netherlands, 25–29 January 2004 (IEEE, New York, 2004), pp. 641–644.
[7] V. Kaajakari, T. Mattila, A. Oja, and H. Seppä, J. Microelectromech. Syst. **13**, 715–724 (2004).
[8] C. Zuo, N. Sinha, J. Van der Spiegel, and G. Piazza, J. Microelectromech. Syst. **19**, 623–627 (2010).

This article is copyrighted as indicated in the article. Reuse of AIP content is subject to the terms at: http://scitation.aip.org/termsconditions. Downloaded to IP: 130.188.235.206 On: Sun, 06 Sep 2015 08:02:09

[9]W. Sahyoun, J.-M. Duchamp, and P. Benech, IEEE Trans. Ultrason. Ferroelectr. Freq. Control **58**, 2162–2170 (2011).
[10]M. Pardo, L. Sorenson, and F. Ayazi, in *Proceedings of the IEEE International Symposium on Circuits and Systems*, Rio de Janeiro, Brazil, 15-18 March 2011 (IEEE, New York, 2011), pp. 221–224.
[11]V. Kumar, J. W. Boley, Y. Yang, H. Ekowaluyo, J. K. Miller, G. T.-C. Chiu, and J. F. Rhoads, Appl. Phys. Lett. **98**, 153510 (2011).
[12]A. Hajati, S. P. Bathurst, H. J. Lee, and S. G. Kim, in *Proceedings of the IEEE 24th International Conference on MEMS 2011, Cancun, Mexico, 23-27 Jan 2011* (IEEE, New York, 2011), pp. 1301–1304.
[13]A. Jaakkola, J. Lamy, J. Dekker, T. Pensala, L. Lipiäinen, and K. Kokkonen, in *Proceedings of the IEEE International Frequency Control Symposium*, Newport Beach, California, USA, 1–4 June 2010 (IEEE, New York, 2010), pp. 410–414.
[14]J. V. Knuuttila, P. T. Tikka, and M. M. Salomaa, Opt. Lett. **25**, 613–615 (2000).
[15]O. Holmgren, K. Kokkonen, T. Mattila, V. Kaajakari, A. Oja, J. Kiihamäki, J. V. Knuuttila, and M. M. Salomaa, Electron. Lett. **41**, 16–17 (2005).
[16]O. Holmgren, K. Kokkonen, T. Veijola, T. Mattila, V. Kaajakari, A. Oja, J. V. Knuuttila, and M. Kaivola, J. Micromech. Microeng. **19**, 015028 (2009).
[17]L. Lipiäinen, K. Kokkonen, and M. Kaivola, J. Appl. Phys. **108**, 114510 (2010).
[18]C. van der Avoort, R. van der Hout, J. J. M. Bontemps, P. G. Steeneken, K. L. Phan, R. H. B. Fey, J. Hulshof, and J. T. M. van Beek, J. Micromech. Microeng. **20**, 105012 (2010).
[19]W. K. Tso and T. K. Caughey, J. Appl. Mech. **32**, 899–902 (1965).

This article is copyrighted as indicated in the article. Reuse of AIP content is subject to the terms at: http://scitation.aip.org/termsconditions. Downloaded to IP: 130.188.235.206 On: Sun, 06 Sep 2015 08:02:09

©2011 IEEE. Reprinted, with permission, from T. Pensala, A. Jaakkola, M. Prunnila, J. Dekker, "Temperature compensation of silicon MEMS resonators by heavy doping", Proc. IEEE International Ultrasonics Symposium, 2011, pp. 1952-1955.
http://dx.doi.org/10.1109/ULTSYM.2011.0486

10.1109/ULTSYM.2011.0486

Temperature Compensation of Silicon MEMS Resonators by Heavy Doping

Tuomas Pensala, Antti Jaakkola, Mika Prunnila, and James Dekker
VTT Technical Research Centre of Finland
Espoo, Finland
Email: tuomas.pensala@vtt.fi

***Abstract*—Passive temperature compensation of silicon MEMS resonators based on heavy n- and p-type doping is studied. Resonators are fabricated utilizing silicon with phosphorus doping level of $5 \cdot 10^{19}\ \mathrm{cm}^{-3}$ and boron doping levels of $5 \cdot 10^{19}\ \mathrm{cm}^{-3}$ and $2 \cdot 10^{20}\ \mathrm{cm}^{-3}$, the latter being stress compensated with germanium. The temperature behavior of the resonance frequencies of Lamé and square extensional (SE) modes is measured. Depending on the vibration mode and crystal orientation, significant temperature compensation effects are observed: as a result of heavy n-type doping the temperature coefficient of frequency (TCF) of the SE mode is reduced from -32 ppm/K to ca. -1 ppm/K, while a Lamé mode resonator exhibits an overcompensated TCF of +18 ppm/K. In p-type resonators a TCF of ca. -2 ppm/K is observed in a Lamé-mode. Keyes' [1] theory of free carrier contribution to the elastic constants of many-valley semiconductors is used to predict the temperature behavior of the n-type resonators. Good agreement is obtained between predicted and observed temperature behavior. The n-type doping can be applied to the TCF reduction of a large class of resonators and shows great potential in improving Si resonator performance.**

I. INTRODUCTION

Silicon based MEMS resonators have been investigated for a long time as a replacement for quartz resonators in oscillators and timing circuits. The driving forces have been miniaturization further than possible with quartz, integration with CMOS, manufacturing cost reduction, and potentially better noise performance. One of the most serious challenges of the technology has been the temperature coefficient of frequency (TCF), typically around -30 ppm/K for silicon [2], whereas quartz achieves essentially zero linear TCF. A Si MEMS resonator exhibits a frequency drift of over 3000 ppm over the temperature range from -40 to +80 C, while an AT cut quartz crystal stays within ± 10 ppm of the frequency at room temperature.

Methods of compensation of the large intrinsic TCF of Si MEMS resonators include addition of amorphous SiO_2 structures having an opposite sign of temperature drift, external electronic compensation via phase-locked-loop (PLL) techniques, electrostatic spring stiffening, and doping.

Application of SiO_2 makes the structure more complicated. In order to be effective in compensation, the oxide needs to be placed in a position of large stress in the resonator. Certain flexural mode resonators may be compensated by oxidation of the surfaces but an extensional mode resonator would need significant amount of SiO_2 to be placed preferably in the depth of the device leading to complicated processing.

Although the PLL based solution adds noise and jitter and consume power, it has been successfully applied in certain timing products of e.g. companies SiTime and Discera. Adjusting the stiffness of the electrostatic spring by DC bias in electrostatically actuated devices is applicable only to resonators whose mechanical spring constant is low, that is, flexural mode devices.

Intrinsic passive compensation by doping of Si has been reported in [3], [4], [5], [6]. The advantages include keeping the manufacturing process and the structure simple and removed or relaxed requirements for the external compensation oscillator circuitry.

In the approach of this paper, there is no need for additional process steps for doping, since homogenously doped material is used for the device layers. Even overcompensation by a large margin is demonstrated with reasonable doping concentration. Moreover, a modeling method for predicting the TCF of a resonator as function of n-type doping concentration, resonance mode, and crystal orientation has been developed.

II. THEORY

A. Temperature coefficient of frequency of a mechanical resonator

The frequency of an acoustic $\lambda/2$-resonator with characteristic dimension L is given by

$$f = \frac{v}{2L} = \frac{1}{2L}\sqrt{\frac{c}{\rho}}, \tag{1}$$

where the acoustic velocity is given by $v = \sqrt{\frac{c}{\rho}}$, c being the stiffness of the material and ρ its density. The linear temperature coefficient of frequency of the resonator is given by

$$\begin{aligned} \mathrm{TC}_f &= \frac{1}{f}\frac{\mathrm{d}f}{\mathrm{d}T} \qquad (2)\\ &= \frac{1}{f}\frac{\mathrm{d}f}{\mathrm{d}L}\frac{\partial L}{\partial T} + \frac{1}{f}\frac{\mathrm{d}f}{\mathrm{d}c}\frac{\partial c}{\partial T} + \frac{1}{f}\frac{\mathrm{d}f}{\mathrm{d}\rho}\frac{\partial \rho}{\partial T} \\ &= -\mathrm{TC}_L + \mathrm{TC}_c - \frac{1}{2}\mathrm{TC}_\rho \\ &= \frac{1}{2}(\mathrm{TC}_c + \alpha) \end{aligned}$$

where TC_L is the linear coefficient of thermal expansion α and $\mathrm{TC}_\rho = -3\alpha$. For silicon and many other materials TC_c

is much larger than α and thus forms the primary source of temperature drift. In order to intrinsically temperature stabilize a resonator, this coefficient must be reduced or counteracted.

B. Effect of Doping

Doping affects the elastic constants of semiconductors by two main mechanisms: dissimilarity of the doping atom with respect to the host lattice and free charge carriers introduced by the doping. Here we will focus on the latter effect, which is assumed dominant at least below doping concentrations of 10^{21} cm^{-3}.

In a many-valley semiconductor such as Si, certain strain components lift the conduction band valley degeneracy changing the energy of the free electron system. Since the elastic constants c_{ij} are second derivatives of the free energy,

$$c_{ij} = \frac{1}{V_0}\frac{\partial^2 G}{\partial S_i \partial S_j}, \tag{3}$$

where V_0 is the volume of the non-deformed crystal, G the Gibbs free energy, and S is the strain (in the contracted notation), a coupling between the charge carrier concentration and the elastic constants is established. A similar mechanism applies for the free holes.

For free electrons Keyes [1] presents an expression for the free energy based on which electronic contributions to the elastic constants can be derived. In the case of n-type Si we have

$$\begin{aligned} \delta c_{11} &= -\Phi\frac{4}{3}\Xi_u^2 \qquad (4)\\ \delta c_{12} &= \Phi\frac{2}{3}\Xi_u^2 \\ \delta c_{44} &= 0, \end{aligned}$$

where Ξ_u is the uniaxial deformation potential constant [7],

$$\Phi = -\int dEN_i(E)\frac{\partial}{\partial E}f_0(E), \tag{5}$$

$N_i(E)$ is the density of states for valley i, and $f_0(E)$ is the Fermi-Dirac distribution

$$f_0 = \left[e^{(E-E_F)/k_BT}+1\right]^{-1} \tag{6}$$

from which the temperature dependence arises. With parabolic bands and deformation potential constant of $\Xi_\mathrm{u} = 9.6$ eV obtained from a fit to the measurement data of Hall [8] (using the data at range $T = 100\ldots308$ K), the electronic contributions (Eq. 4) can be calculated.

C. Mode frequencies

The Lamé-mode is a pure shear mode present in square plates. Its frequency is given by

$$f_\mathrm{L} = \frac{1}{\sqrt{2}L}\sqrt{\frac{c_{xy,\mathrm{shear}}}{\rho}}, \tag{7}$$

where L is the plate side length and $c_{xy,\mathrm{shear}}$ is c_{44} for plates with sides oriented along 110 and $\frac{1}{2}(c_{11}-c_{12})$ for plates with sides oriented along 100 directions. Other modes such as the SE mode have a more complicated dependence on the elastic parameters with usually no exact analytic expression available. In such a case one can perform a sensitivity analysis by numerical FEM simulation to obtain a linearized function for the frequency of the form

$$f(\delta c_{11}, \delta c_{12}, \delta c_{44}) = f_0\left(1+\sum_{ij}\frac{1}{f_0}\frac{\partial f}{\partial c_{ij}}\delta c_{ij},\right) \tag{8}$$

where $ij = 11, 12, 44$. Differentiating this with respect to T using the temperature derivatives of c_{ij} from calculation described in Sec. II-B and assuming a doping independent thermal coefficient of expansion $\alpha = 2.84$ ppm/K [2] one can calculate the TCF of a resonance mode according to Eq. (2).

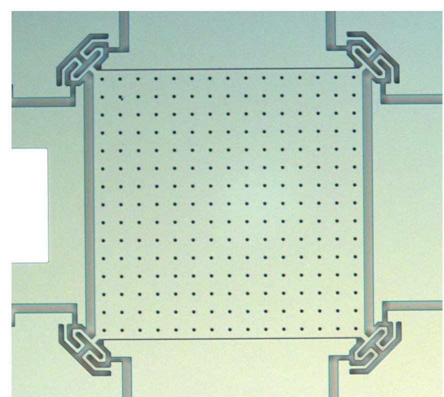

Fig. 1. Photograph of a resonator. The 0.5 μm actuation gaps are at the top and bottom sides of the square plate to facilitate excitation of both SE and Lamé modes. The dots in the resonator are the 3 μm holes for the HF vapor release etch.

III. Experimental

Silicon-On-Insulator wafers with heavily doped device layer were fabricated in three different types:

1) n-type Czochralski wafers with phosphorus doping concentration of $5\cdot10^{19}\mathrm{cm}^{-3}$.
2) p-type Czochralski wafers with boron doping concentration of $5\cdot10^{19}\mathrm{cm}^{-3}$.
3) p-type epitaxially grown wafers with boron concentration of $2\cdot10^{20}\mathrm{cm}^{-3}$ and Ge of $1.6\cdot10^{21}\mathrm{cm}^{-3}$ (stress compensation).

The doping concentrations were chosen to be maximal without expecting fabrication complications. The device layer orientation was 100 and thickness was 10 μm in all samples.

Resonators were fabricated by a process including Al contact metallization and patterning, DRIE etching of vertical gaps (width 0.5 μm) and release etch holes (diam. 3 μm), and finally release etching by HF vapor. A photograph of a resonator is shown in Fig. 1. The samples included square plate resonators in different orientations on the wafer which could be electrostatically actuated to resonate both in the square extensional and the Lamé modes.

The resonators were measured in atmospheric pressure on wafer level with an impedance analyzer while applying a

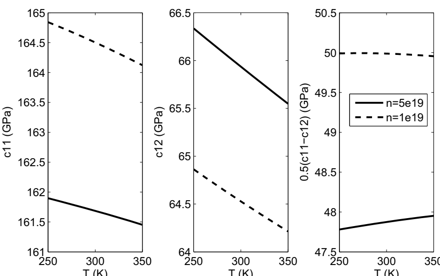

Fig. 2. The elastic constants c_{11}, c_{12}, and $0.5(c_{11} - c_{12})$ calculated for the n-type doping concentration $5 \cdot 10^{19}$ cm^{-3} of the experimental samples and for a lower level of $1 \cdot 10^{19}$ cm^{-3} for reference.

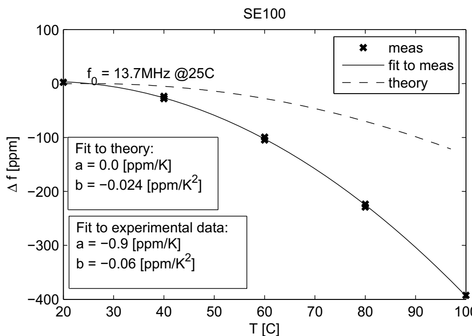

Fig. 3. Measured and predicted resonance frequency f_0 vs. T of the n-type doped SE(100)-mode. The coefficients a and b are the fitted linear and 2nd order TCFs, respectively. The dependence is quadratic with a small negative slope at RT.

DC bias of 40 V over the gaps. The wafers were held on a temperature controlled chuck, the temperature of which was varied from 20 °C to 100 °C (n-type wafers) and 40 °C to 80 °C (p-type wafers). The Lamé and SE resonances were identified and their frequency was tracked over temperature. A second-order polynomial centered at $T = 25$ °C was fitted to the frequency vs. temperature data to obtain the linear and second-order TCFs.

IV. Results

The temperature behavior of the elastic constants c_{ij} predicted by the calculation described in II-B are presented in Fig. 2 for the case of n-type doping with doping concentration $5 \cdot 10^{19}$ cm^{-3} of the experimental samples and for a lower level of $1 \cdot 10^{19}$ cm^{-3} for reference. Doping is seen to both change the absolute value of c_{ij} at given T but also to affect the shape of the $c_{ij}(T)$ curves. Most remarkably, the slope of the shear elastic constant $\frac{1}{2}(c_{11} - c_{12})$ changes sign from negative to positive between the two doping levels.

Measured resonance frequency vs. T data and the 2nd order polynomial fits for the n-type doped 100-oriented SE mode and the 100-oriented Lamé modes are shown in Figs. 3 and 4, respectively.

The linear TCFs extracted from measurements are presented in Table I. For reference, with standard doping level in the range below $5 \cdot 10^{18}$ cm^{-3} all modes exhibit a TCF in the range -32 $\cdots$ -29 ppm/K.

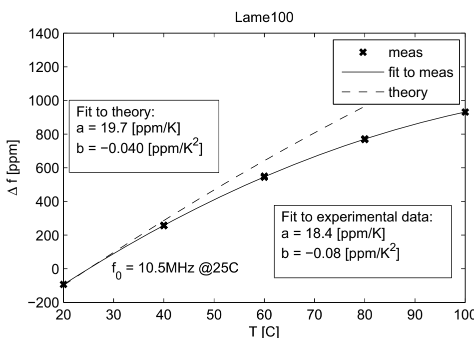

Fig. 4. Measured and predicted resonance frequency f_0 vs. T of the n-type doped Lamé(100)-mode. The coefficients a and b are the fitted linear and 2nd order TCFs, respectively. The curve is quadratic with a large positive slope at RT.

TABLE I
Measured linear TCF for the Lamé and Square Extensional plate modes. Plate side crystal orientation is indicated.

	Lamé 110	Lamé 100	SE 110	SE 100
n (P)	-32 ppm/K	+18 ppm/K	-6.5 ppm/K	-0.9 ppm/K
p (B)	-3.0 ppm/K	-14 ppm/K	-21 ppm/K	-22 ppm/K
p (B+Ge)	-1.8 ppm/K	-14 ppm/K	-21 ppm/K	-22 ppm/K

The phosphorus doped n-type devices show remarkable thermal compensation effects. The strongest effect is seen in the $\frac{1}{2}(c_{11} - c_{12})$ -characterized 100-oriented Lamé mode, which exhibits a large positive TCF of +18 ppm/K. The TCF of the 100-SE mode is -0.9 ppm/K, more than one decade below the starting point, while the c_{44} characterized Lamé mode is practically unaffected. It is to be noted that this is in harmony with the last row of Eq. (4).

The p-type boron doping results in a reduction of the TCF of the 110-oriented Lamé mode characterized by the shear elastic constant c_{44} by one full decade to -3 ppm/K. The TCF of the $\frac{1}{2}(c_{11} - c_{12})$ -characterized 100-oriented Lamé-mode is reduced in magnitude to -14 ppm/K, and the TCF of the SE modes for the two resonator orientations are -21 ppm/K and -22 ppm/K, respectively.

With even heavier p-type doping with boron associated with Ge doping for stress compensation, the TCF of the 110 oriented Lamé mode is reduced further to -1.8 ppm/K but no changes are observed in the 100 Lamé nor the SE mode as compared to the first p-type case.

Table II compares the measured and calculated TCFs of the three vibration modes in the case of n-type doping. The values show good agreement.

In 1 atm the Q-values of the devices are limited by air damping to $\sim 10\,000$. The p-type devices were also measured in vacuum and exhibited Q-values above 100 000.

V. Discussion

The TCF of the resonators was measured with only the wafer bottom contacted to the heat sink at the desired temper-

TABLE II
MEASURED VS. CALCULATED LINEAR TCF FOR THE LAMÉ AND SQUARE EXTENSIONAL PLATE MODES IN PHOSPHORUS DOPED (N-TYPE) SI RESONATORS. PLATE SIDE CRYSTAL ORIENTATION IS INDICATED.

	Lamé 110	Lamé 100	SE 110	SE 100
calc.	-26 ppm/K	+20 ppm/K	-4.9 ppm/K	+0.0 ppm/K
meas.	-32 ppm/K	+18 ppm/K	-6.5 ppm/K	-0.9 ppm/K

ature. Finite element method thermal simulations of the SOI wafer stack and of that of the resonator were performed to estimate the temperature error caused by the ambient room-temperature air. An upper limit estimate of 2K difference between the chuck and the resonator element was obtained assuming a highly overestimated convection coefficient of $H_{\rm air} = 50{\rm W}/({\rm m}^2{\rm K})$ for the ambient air. This would lead to less than 1 ppm/K underestimation of the magnitude of the linear TCFs reported in Table I. Furthermore, TCF measurement of conventionally doped resonators with the same setup yielded the same TCF as that obtained in an oven within 1 ppm/K.

Some uncertainty exists in the actual doping concentration of the devices under test. Variation in the order of several percents over the wafer is known to exist, depending on the manufacturing method and level of doping. In the quest for repeatable minimization of the TCF of resonators, this matter needs attention.

In the n-type devices the agreement between the theoretical prediction due to free carrier contribution is good in qualitative sense as the c_{44} is only weakly affected (Eq. (4). Furthermore, good quantitative agreement is obtained using the deformation potential constant fitted to the data of Hall [8]. This forms strong evidence for the fact that the effect of doping on the elastic constants is mainly of electronic origin.

For n-type doped Si resonators, a modeling method for predicting the TCF of a resonator as function of doping concentration, resonance mode and crystal orientation has thus been established. For p-type Si the modeling is more demanding due to a more complex band structure of the free holes, but should be possible. It is to be noted that a doping independent thermal expansion coefficient has been assumed for calculated TCFs (Table II) while it is possible that the heavy doping does have an effect on it.

The n-type doped 100 SE-mode shows an extrapolated total frequency drift of below 300 ppm in the range of -20 $\cdots$ 80 $^\circ$C as compared to a typical $\sim$ 3000 ppm of conventional MEMS resonators - an improvement by one decade. The 100 Lamé-mode shows overcompensation at +18 ppm/K showing that there is large margin of compensation available by n-type doping.

Most importantly, n-type compensation affects most effectively the elastic constant $\frac{1}{2}(c_{11} - c_{12})$ which contributes to a large class of resonance modes. This makes the range of applicability of n-type doping wide while p-type doping is limited more special modes characterized by the pure shear elastic constant c_{44}.

It is foreseen that heavy n-type doping of Si allows for developing resonators approaching quartz in intrinsic temperature stability.

In further work we plan to study the accuracy, repeatability, and $2^{\rm nd}$ order effects of the temperature compensation by doping, in addition to extracting elastic constants from measurements as function of both doping concentration and temperature varied in wider ranges.

VI. CONCLUSION

Si MEMS resonators were manufactured using SOI wafers with heavily p- and n-type doped device layers. It was demonstrated that doping of Si can be used to reduce temperature drift of MEMS resonators significantly via electronic effects. By n-type doping the TCF of a resonance with dependency only on the shear elastic constant $\frac{1}{2}(c_{11} - c_{12})$ can be made positive, while the TCF of certain other modes can be reduced in magnitude.

By p-type doping the temperature drift of the elastic constant c_{44} is reduced most significantly. A model developed based on Keyes' theory on free electron contribution to the elastic constants allows for prediction of the of the TCF of n-type doped Si resonators with good agreement with experiment. Especially the n-type doping is found very versatile and shows great promise in improving the Si resonator performance for the timing and frequency reference applications.

ACKNOWLEDGMENT

The work was funded by TEKES, VTI Technologies, and Okmetic Oyj. Okmetic is acknowledged for their important contribution in fabricating the highly doped Si wafers. The authors would like to thank S. Gorelick for his help in thermal FEM modelling

REFERENCES

[1] R.W. Keyes, “Electronic effects in the Elastic Properties of Semiconductors”, Solid State Physics: Advances in Research and Applications, ed. by F. Seitz and D. Turnbull, Academic Press, New York, 1967, vol 20, pp 37-90.
[2] C. Bourgeois et al., “Design of resonators for the determination of the temperature coefficients of elastic constants of monocrystalline silicon”, Proc. IEEE International Frequency Control Symposium, 1997, pp. 791–799.
[3] J.S. Wang et al., “Low Temperature Coefficient Shear Wave Thin Films for Composite Resonators and Filters”, Proc. IEEE International Ultrasonics Symposium, 1983, pp. 491–494.
[4] A. Hajjam et al., “Sub-100ppb/C Temperature Stability in Thermally Actuated High Frequency Silicon Resonators via Degenerate Phosphorous Doping and Bias Current Optimizations”, Proc. IEEE International Electron Device Meeting, 2010.
[5] A. Hajjam et al., “Temperature compensated single-device electromechanical oscillators”, Proc. IEEE 24th International Conference on Micro Electro Mechanical Systems (MEMS), 2011, pp. 801–804.
[6] A. K. Samarao et al., “Passive TCF Compensation in High Q Silicon Micromechanical Resonators”, Proc. IEEE International Conference on Micro Electro Mechanical Systems (MEMS 2010), 2010, pp. 116–119.
[7] C. Herring et al., “Transport and Deformation-Potential Theory for Many-Valley Semiconductors with Anisotropic Scattering”, Phys. Rev. 101, 1956, pp. 944-961.
[8] J.J. Hall, “Electronic Effects in the Elastic Constants of n-Type Silicon”, Physical Review, vol. 161, no. 3, 1967, pp. 756-761.

©2010 IEEE. Reprinted, with permission, from A. Jaakkola, J. Lamy, J. Dekker, T. Pensala, L. Lipiäinen, K. Kokkonen, (2010, June). "Experimental study of the effects of size variations on piezoelectrically transduced MEMS resonators", Proc. IEEE International Frequency Control Symposium, 2010, pp. 410-414. http://dx.doi.org/10.1109/FREQ.2010.5556299

Experimental Study of the Effects of Size Variations on Piezoelectrically Transduced MEMS Resonators

Antti Jaakkola, Jérôme Lamy,
James Dekker and Tuomas Pensala
VTT Technical Research Centre of Finland
Espoo, Finland
antti.jaakkola@vtt.fi

Lauri Lipiäinen and Kimmo Kokkonen
Aalto University
Department of Applied Physics
Espoo, Finland

***Abstract*—We report results of a parametric study on a set of single-crystal-silicon plate resonators, whose lateral dimensions are varied so that the main resonance mode occurs at a range of f = 13. . .30 MHz. The resonator transduction is based on a piezoelectric AlN thin film. Measurements spanning >1000 devices and two wafers indicate that with certain device dimensions the square extensional resonance mode and a higher-order extensional mode are excited with a relatively low frequency scatter of $\triangle f \sim$ 2 000 ppm (full range). Other resonance modes typically have a frequency scatter larger than 15 000 ppm, which we interpret to be an indication of their flexural character. Additionally, we observe a splitting of the main resonance mode branch at intermediate device dimensions.**

I. Introduction

Single-crystal silicon (SCS) MEMS resonators are being considered as potential alternatives for quartz crystals in timing and frequency control applications due to their small size, good noise performance and compatibility with CMOS processing. SCS MEMS resonators transduced with a piezoelectric thin film deposited on top of the resonator bulk have been studied with increasing interest [1], [2], [3]. Main merits of piezoelectric transduction — as compared to the traditional method of capacitive transduction — are the inherently stronger electromechanical coupling and the fact that no DC bias is needed. Additionally, processing of narrow gaps is not needed. On the other hand, the piezoelectric stack may degrade resonator quality factor, and it may affect resonator frequency repeatability. Additionally, with piezoelectric transduction, parasitic resonance modes are often relatively easily excited; to create a successful design it is important to identify the unwanted resonances in the vicinity of the intended main resonance mode, and to minimize their effects.

In this work we report experimental results of a statistical parametric study on a set of piezoelectrically transduced plate resonators, whose lateral dimensions are varied so that the main resonance mode occurs at a frequency range of f = 13. . .30 MHz. The study extends our previous work with plate resonators [4], [5]. The objective is to experimentally probe the limits of the resonator design by mapping the resonance mode branches and their properties as a function of the resonator size, and, in particular, to investigate whether the bulk extensional modes of the resonators are excited "cleanly", i.e., with a relatively low frequency scatter. Furthermore, the extensive experimental data set allows a comprehensive comparison with simulated data, which helps us to evaluate whether the simplifications in our finite element models are justified.

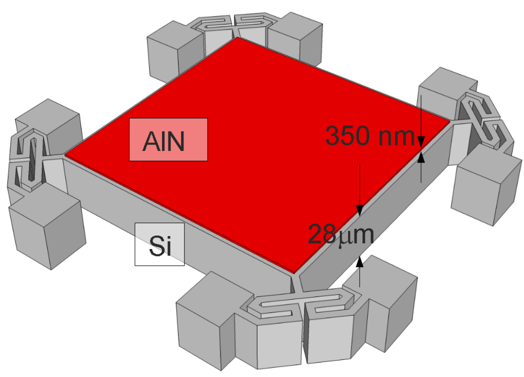

Figure 1. Schematic representation of a plate resonator (SiO_2 and Mo layers have been excluded from the image).

II. Plate resonator design

The schematic structure of the plate resonator design is shown in Figure 1. The resonator is comprised of a 30-μm-thick square-shaped block of single-crystalline strongly p-doped silicon, which is attached to the substrate at its corners with flexible anchors (Figure 2b). Electromechanical coupling is achieved with a 350-nm thin film of AlN deposited on top of the resonator plate. A 300-nm layer of molybdenum acts as the top electrode, and the silicon device layer serves as the bottom electrode. AlN is patterned to cover only the resonator plate: a SiO_2 layer provides insulation between the electrodes elsewhere.

The studied set of devices consisted of 64 variations, where the resonator plate lateral dimension L was varied from 131 μm to 320 μm with 3-μm steps. Micrographs of the biggest and smallest device variation are shown in Figure 2a. Each variation had similar corner anchors (Figure 2b). The resonators were designed to be connected electrically as one-port devices.

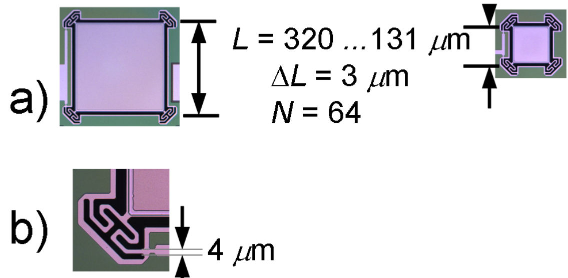

Figure 2. a) Micrographs of the largest and smallest resonator variation. b) Corner anchor design used in all of the variations.

The main vibration mode of the resonators is the square-extensional (SE) mode, which is characterized by the contraction/expansion of the plate. Neglecting the effects of the piezo stack and of the anchors, the SE mode frequency is given by $f = \sqrt{Y_{2D}/\rho}/(2L)$, where ρ and L are the silicon density and the length of the plate side, respectively. Y_{2D} is the effective Young's modulus for the SE mode, and it is given by $Y_{2D} = c_{11} + c_{12} - 2c_{12}^2/c_{11} =$ 181 GPa [4], where c_{11} and c_{12} are the elastic matrix elements of silicon.

The transduction principle is described briefly with the help of the following approximative model: Suppose that the AlN film is clamped to the resonator plate. We approximate that the strains in the lateral directions are zero ($S_x = S_y = 0$) — which is expected to overestimate the transduction strength to some extent — and assume that the piezoelectric layer may move freely in the z direction so the vertical stress component is zero ($T_z = 0$) [6]. When a z-directed electric field E_z is applied, we can solve the piezoelectric constitutive relation $T = eE + cS$ [7] for the unknown lateral stresses:

$$T_x = T_y = \left(\frac{\nu}{1-\nu} e_{33} - e_{31} \right) E_z, \tag{1}$$

where ν is the Poisson ratio of AlN, and e_{31} and e_{33} are the AlN piezoelectric coupling constants. We observe that the out-of-plane electric field results in lateral forces by direct coupling via the piezoelectric constant e_{31}, and by indirect coupling through the term e_{33}.

The resonators were fabricated with our cavity-SOI based process, which is described in more detail in References [8] and [5]. To enable optical detection of the in-plane vibrations, the top metal layer of every second variation was patterned with a grid of circular holes (see discussion in Section III-B).

III. Measurements and Modelling

A. Wafer level electrical characterization

A total of ~1200 devices were electrically characterized from two wafers: each of the 64 variations was replicated 10 times on a wafer, and the locations of these devices spanned the central region as well as the edges. The electrical impedance Z of the resonators was measured with Agilent

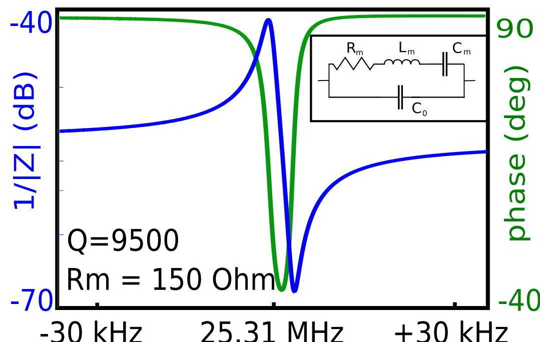

Figure 3. SE mode resonance of a resonator with plate side length $L = 181\mu$m measured in ambient air. Inset: equivalent circuit which was fitted to the measured data.

4294A impedance analyzer. The following automatic measurement scheme was implemented to gather the resonance data of each device: First, a relatively coarse scan was performed at a frequency range of $f = 5 \ldots 80$ MHz. Then the trace was analyzed and the resonances were identified. Subsequently, five strongest resonances were measured using a narrower frequency span. The equivalent circuit (see Figure 3 inset) response was then fitted to the measured data, and the motional resistance R_m, resonance frequency f_0, quality factor Q and parallel capacitance C_0 were obtained for the top five resonances. Figure 3 shows example trace of the SE resonance of a resonator with $L = 181\mu$m. The wafer level characterization was done in ambient air pressure, and as a consequence air damping is a prominent loss mechanism. Some devices were afterwards measured in vacuum: typically the Q factors were enchanced by a factor of 2 under $p <$0.1 mbar.

B. Optical probing

After the wafer-level electrical measurements, a set of resonators was selected for optical probing. Vibration fields in the resonators were measured using a scanning Michelson laser interferometer [9]. Both in-plane and out-of-plane vibrations were measured. The lateral resolution of the setup is better than 1 μm and the minimum detectable out-of-plane vibration amplitude is typically less than 1 pm. With a small modification to the setup also in-plane vibrations can be measured [10], [11]. Utilizing the circular holes in the metal layer, a vectorial detection of the in-plane vibration was accomplished. It should be noted, however, that the in-plane and out-of-plane vibration amplitudes cannot be directly compared to each other due to the different detection methods. Measured out-of-plane and in-plane vibration patterns of selected modes are shown in Figures 6. . . 8 and they are discussed in more detail in Section IV.

C. Finite element modelling

The vibration modes of the resonator plate were solved with Comsol Multiphysics using the eigenfrequency analysis mode. The model geometry was simplified by excluding the corner

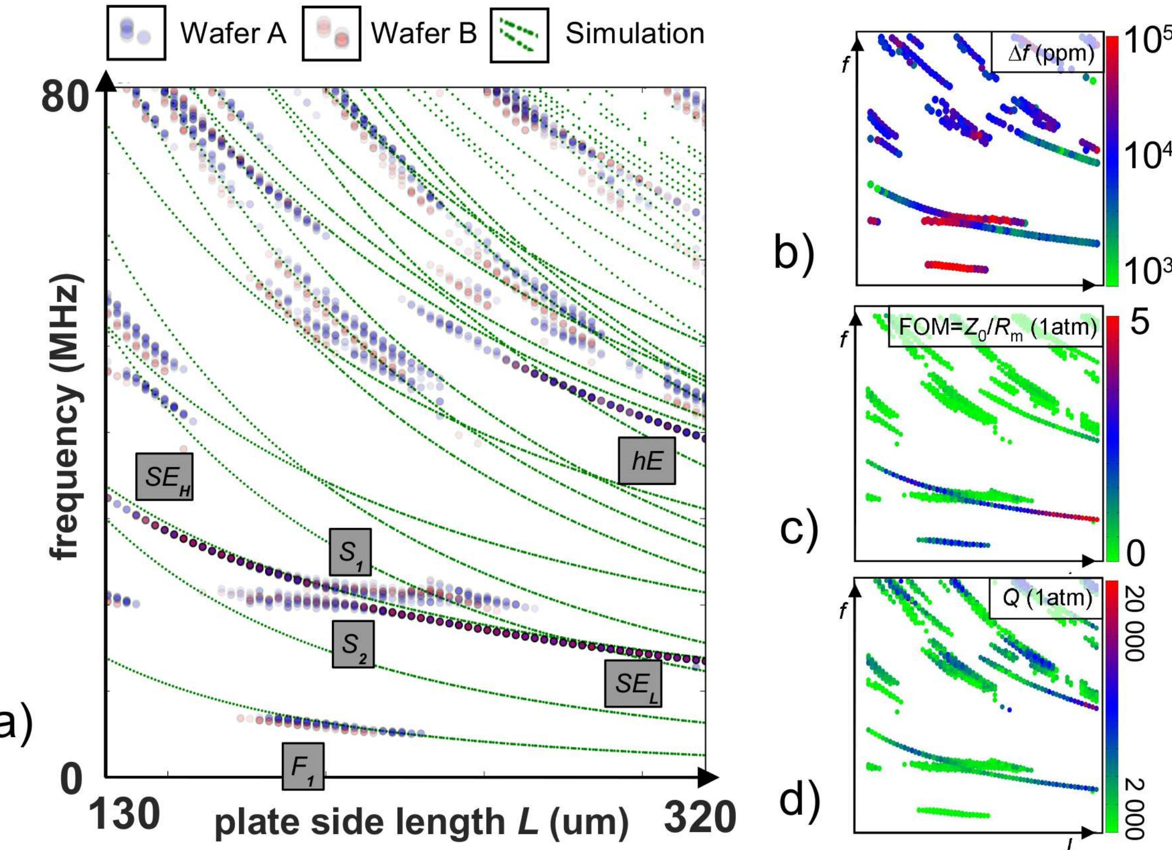

Figure 4. a) Dispersion of the resonance frequency as a function of resonator size: experimental data and simulation. Note that the data points are semitransparent, and hence the colors are stronger for data points stacked on top of each other. For the same reason, the blue and red colors mix to make purple for overlying data from wafers A and B. b) Frequency scatter of the resonances modes. We have defined the frequency scatter Δf as the full range of frequencies measured for the mode under investigation. c) $FOM = Z_0/R_m$, i.e., the ratio of impedances at the shunt capacitance branch and the motional branch of the equivalent circuit. d) Quality factor of the measured resonances. The measurements have been done at atmospheric pressure.

anchors and the top metal layer. The modal frequencies are plotted in Fig. 4a along with the experimental data. It should be noted that the plot contains only modes, whose symmetry allows piezoelectric coupling with a piezo that covers the whole resonator plate. The mode shapes of selected modes are shown in Figures 5, 6, 7 and 8 together with the optical probing data.

IV. Results and discussion

The dispersion curves of the measured and simulated resonance frequencies as a function of the resonator size are shown in Figure 4a. For most of the measured modal branches the frequency scatter is noticeable, typically more than 15 000 ppm. We interpret this to be attributed to the flexural character of these modes: The resonance frequency of a flexural mode is sensitive to the device thickness, and the SOI device layer thickness variation across a wafer is seen as corresponding resonance frequency variations. Additionally, a systematic difference of resonance frequencies is observed for the high-scatter branches between wafers A and B. Wafer A resonance frequencies tend to be slightly lower than those for devices from wafer B, which we attribute to a device layer thickness difference between wafers A and B. Figure 4b illustrates the frequency scatter in more detail. Figure 5a shows the mode shape of the low-frequency flexural mode F_1. For this mode, match between simulation and measurement is excellent.

On the other hand, it is evident from the dispersion plot that the spread of measured resonance frequencies is very small for certain resonances. Comparing with data from simulation, one finds that the low-scatter branches correspond to the SE mode and to a higher-order extensional mode — we have labeled these branches as SE_H , SE_L and hE according to their mode type (subindices H and L denote the high/low-frequency region of the SE branch, respectively). The frequency scatter within the SE_H , SE_L and hE branches is typically $\Delta f \sim$ 2000 ppm. We have defined the frequency scatter Δf as the

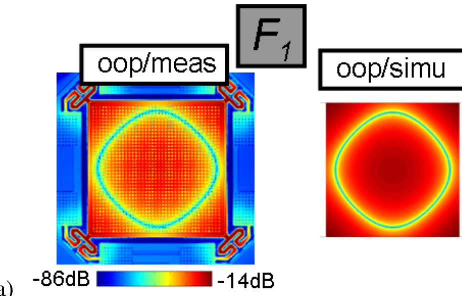

Figure 5. Measured and simulated out-of-plane (oop) vibration field of the low-frequency flexural mode F_1.

full range of frequencies measured for the mode under investigation[1]. We interpret the relatively small frequency scatter to indicate that these bulk extensional modes have been excited "cleanly", i.e., with a very small flexural component. The frequency of an extensional mode is only weakly dependent on the resonator thickness, and the SOI device layer thickness variations do not affect the resonator frequency repeatibility. Our working hypothesis is that the frequency scatter of these modes originates mainly from variations of the resonator lateral dimensions. Figures 6 and 7 show in-plane and out-of-plane vibration fields of these low-scatter modes. Side-to-side comparison of the experimental and simulated data yields a relatively good match for the vibration fields.

For certain branches, such as F_1, SE_H , SE_L and hE, simulated data from the FEM modal analysis and the experimental data match well with each other (Fig. 4a). The few percent difference in resonance frequencies can be explained by the difference in real stiffness parameters and those used in the simulation, and by the exclusion of the top metal layer from simulation model. However, some of the experimentally observed resonances do not overlap with the simulated data. Most strikingly, simulation fails to capture SE resonance branch splitting at intermediate plate dimensions (regions S_1 and S_2): each sample from the splitting region has two separate resonances, instead of a single SE resonance peak. Optical probing data of these resonance modes (Figure 8) reveals that the in-plane vibration field of both of the modes have the SE resonance characteristics, while the out-of-plane vibration pattern is somewhat different for the two modes. We refrain from an attempt to explain the SE resonance splitting by these observations from optical probing alone; we are currently working on a refined FEM model, which will capture the resonator geometry more accurately by containing the corner anchors.

The ratio of the shunt impedance $Z_0 = 1/2\pi f C_0$ and the motional resistance R_m is a figure of merit from the point of view of building an oscillator circuit based on the resonator. $FOM = Z_0/R_m \sim 10$ or more is needed for a realization

[1]Standard deviation was not used due to relatively small number ($N = 20$) of measured samples of each variation type.

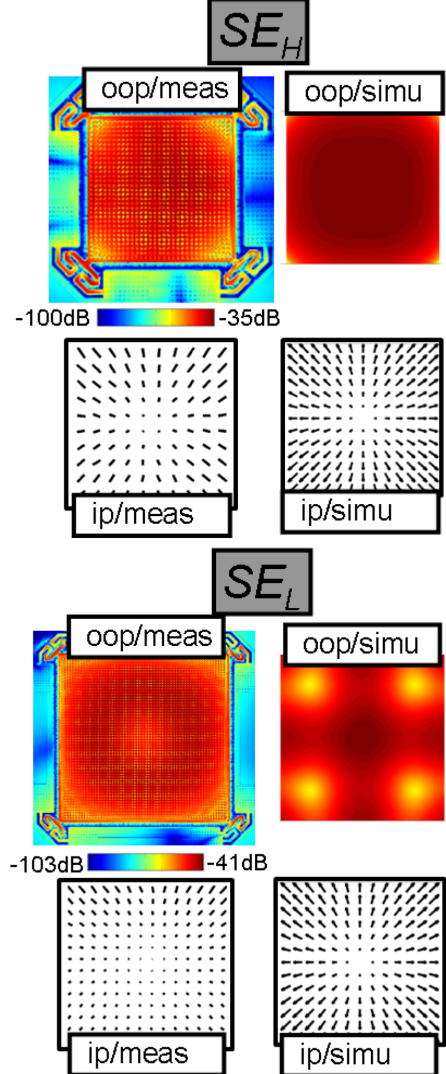

Figure 6. Measured and simulated out-of-plane (oop) and in-plane (ip) vibration fields of the resonance modes of branches SE_H and SE_L.

based on a simple oscillator topology, e.g., the Pierce topology. Figure 4c indicates that in atmospheric pressure $FOM \sim 5$ is reached for the SE resonance — in vacuum the Q values are typically doubled and $FOM \sim 10$ would be reached. It is also observed, that at intermediate dimensions also the flexural mode F_1 is relatively strongly coupled, and that at the SE resonance splitting region the performance degrades. All other modes appear to be weakly coupled with $FOM \lesssim 1$. In general, we notice that a 2-port realization of the piezoactuated plate resonator design would be more practical for oscillator applications since the feedthrough capacitance is reduced and, consequently, FOM is increased.

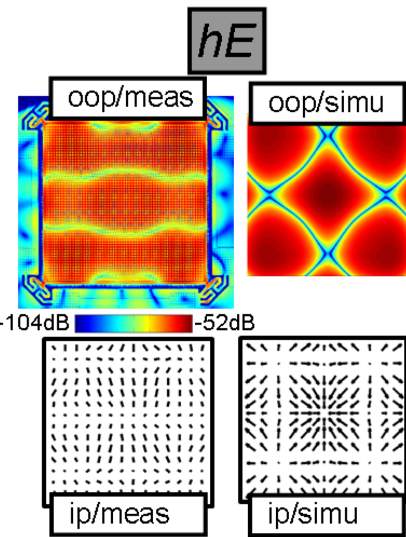

Figure 7. Measured and simulated out-of-plane (oop) and in-plane (ip) vibration fields of the resonance modes of branch hE_L.

Figure 4d illustrates the quality factors of the resonances. Air damping in atmospheric pressure masks other damping mehcanisms to some extent but some observations can be made: The losses are observed to increase, when approaching the splitting region along the SE resonance branches. At SE_L and SE_H regions we observe Q ∼10 000. Interestingly, the highest quality factors of Q ∼20 000 are measured at the hE region.

V. Conclusions

The parametric study of this work with statistics from over 1000 devices has given valuable new insight to plate resonator operation. It was observed, that with certain device dimensions bulk extensional modes can be excited with a relatively low frequency scatter of $\Delta f \sim$ 2 000 ppm (full range), as opposed to the flexural resonance modes, whose frequency scatter was seen to be larger than 15 000 ppm. Modal analysis of a simplified FEM model reproduces relatively well the resonance frequencies observed in the measurements. The mode shapes of selected modes were probed optically, and good correspondence with simulated mode shapes was found. However, importantly, the experimentally observed clear splitting of the main resonance branch was not reproduced by the FEM model. As a consequence, we are currently working on a refined FEM analysis which includes the corner anchors.

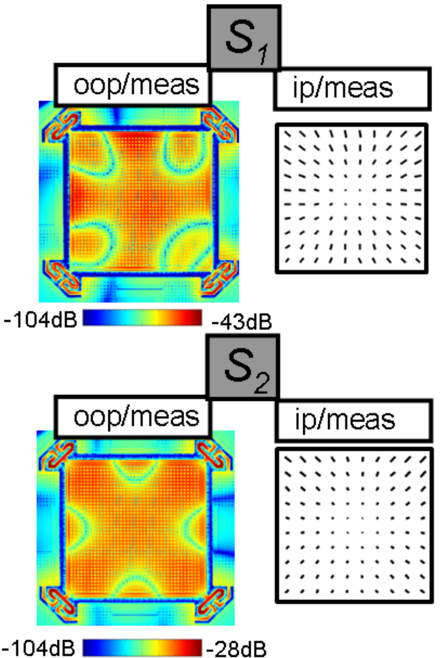

Figure 8. Measured out-of-plane (oop) and in-plane (ip) vibration field of the splitting-region modes S_1 and S_2.

References

[1] R. Abdolvand and F. Ayazi, "Enhanced power handling and quality factor in thin-film piezoelectric-on-substrate resonators," in *IEEE Ultrasonics Symposium*, 2007, pp. 608–611.

[2] J. Baborowski, C. Bourgeois, A. Pezous, C. Muller, and M. A. Dubois, "Piezoelectrically activated silicon resonators," in *IEEE Ultrasonics Symposium*, 2007, pp. 1210–1213.

[3] G. Ho, R. Abdolvand, A. Sivapurapu, S. Humad, and F. Ayazi, "Piezoelectric-on-Silicon Lateral Bulk Acoustic Wave Micromechanical Resonators," *Journal of microelectromechanical systems*, vol. 17, no. 2, pp. 512–520, 2008.

[4] V. Kaajakari, T. Mattila, A. Oja, J. Kiihamäki, and H. Seppa, "Square-Extensional mode Single-Crystal silicon micromechanical resonator for Low-Phase-Noise oscillator applications," *IEEE Electron Device Letters*, vol. 25, no. 4, pp. 173–175, 2004.

[5] A. Jaakkola, P. Rosenberg, S. Asmala, A. Nurmela, T. Pensala, T. Riekkinen, J. Dekker, T. Mattila, A. Alastalo, O. Holmgren, and K. Kokkonen, "Piezoelectrically transduced single-crystal-silicon plate resonators," in *IEEE Ultrasonics Symposium*, Beijing, China, 2008, pp. 717–720.

[6] V. Kaajakari, A. T. Alastalo, and T. Mattila, "Electrostatic transducers for micromechanical resonators: free space and solid dielectric," *IEEE Transactions on Ultrasonics, Ferroelectrics and Frequency Control*, vol. 53, no. 12, pp. 2484–2489, 2006.

[7] B. A. Auld, *Acoustic fields and waves in solids*. Wiley New York, 1973.

[8] H. Luoto, K. Henttinen, T. Suni, J. Dekker, J. Mäkinen, and A. Torkkeli, "MEMS on cavity-SOI wafers," *Solid-State Electronics*, vol. 51, pp. 328–332, 2007.

[9] J. V. Knuuttila, P. T. Tikka, and M. M. Salomaa, "Scanning Michelson interferometer for imaging surface acoustic wave fields," *Optics Letters*, vol. 25, no. 9, pp. 613–615, 2000.

[10] O. Holmgren, K. Kokkonen, T. Mattila, V. Kaajakari, A. Oja, J. Kiihamäki, J. V. Knuuttila, and M. M. Salomaa, "Visualization of in-and out-of-plane vibrations in a micromechanical RF-resonator," in *2004 IEEE Ultrasonics Symposium*, vol. 2, 2004.

[11] O. Holmgren, K. Kokkonen, T. Mattila, V. Kaajakari, A. Oja, J. Kiihamäki, J. Knuuttila, and M. Salomaa, "Imaging of in- and out-of-plane vibrations in micromechanical resonator," *Electronics Letters*, vol. 41, no. 3, p. 121, 2005.

Paper IX

©2008 IEEE. Reprinted, with permission, from A. Jaakkola, P. Rosenberg, S. Asmala, A. Nurmela, T. Pensala, T. Riekkinen, J. Dekker, T. Mattila, A. Alastalo, O. Holmgren, K. Kokkonen, "Piezoelectrically transduced single-crystal-silicon plate resonators", Proc. IEEE International Ultrasonics Symposium, 2008, pp. 717-720.
http://dx.doi.org/10.1109/ULTSYM.2008.0171

Piezoelectrically transduced Single-Crystal-Silicon Plate Resonators

Antti Jaakkola, Piia Rosenberg, Samuli Asmala
Arto Nurmela, Tuomas Pensala, Tommi Riekkinen,
James Dekker, Tomi Mattila, and Ari Alastalo
VTT Technical Research Centre of Finland
P.O. Box 1000, FI-02044 VTT, Finland
antti.jaakkkola@vtt.fi

Olli Holmgren and Kimmo Kokkonen
Department of Applied Physics
Helsinki University of Technology
Espoo, Finland

***Abstract*—We report on the design, fabrication and characterization of piezoelectrically actuated single-crystal silicon plate resonators vibrating mainly in their bulk acoustic wave modes. Two resonator types are presented: one operates in the square extensional mode at 26 MHz with $Q \sim 18000$ and motional resistance $R_m \sim 0.24$ kΩ, while the other resonator features a resonance at 22 MHz with $Q \sim 51000$ and $R_m \sim 1.5\,\mathrm{k}\Omega$. The resonators are characterized electrically and by scanning laser interferometry. Measured vibration fields are compared to simulated eigenmodes.**

I. Introduction

Micromechanical resonators are considered as candidates for replacing quartz crystals used as frequency reference components in modern wireless applications. Typically MEMS resonators rely on capacitive transduction. For good electromechanical coupling, sub-100 nm capacitive gap sizes and biasing voltages in excess of 10 V are needed. Especially the latter need is problematic to meet with low cost integrated circuits.

To overcome these problems we have studied single-crystal silicon (SCS) BAW plate resonators, which are transduced using a piezoelectric aluminum nitride (AlN) layer grown on top of the resonator. SCS resonators based on a similar transduction principle have been reported, e.g., in [1], however, for beam resonators operating in 1D length-extensional vibration modes. In this paper, we extend our previous work with beam resonators [2] to plate resonators, motivated by the good stability and noise properties observed in capacitively coupled resonators of this type [3], [4]. Two resonator designs are studied. Device A operates in the square extensional mode at 26 MHz with $Q \sim 18000$ and has motional resistance $R_m \sim 0.24\,\mathrm{k}\Omega$. Device B features a resonance at 22 MHz with $Q \sim 51000$ and motional resistance $R_m \sim 1.5\,\mathrm{k}\Omega$, and also two other well-coupled high-Q resonances. In addition to electrical characterization, the vibration fields in the resonators were measured with a scanning laser interferometer [5]. Measured mode shapes are found to correspond well with finite element method simulations.

II. Resonator design

A micrograph of resonator A is shown in Fig. 1a. The resonator is designed to be connected electrically as a one-port device, and the intended vibration mode of the resonator is the square-extensional (SE) mode [4] at 26 MHz. The SE mode occurs when the resonator plate side length is half of the acoustic wavelength, and its frequency is given by $f = \sqrt{Y_{2D}/\rho}/(2L)$, where ρ and L are the plate material density and the length of the plate side, respectively. Y_{2D} is the effective Young's modulus for the SE mode, and it is given by $Y_{2D} = c_{11} + c_{12} - 2c_{12}^2/c_{11} = 181$ GPa, where c_{11} and c_{12} are silicon elastic matrix elements.

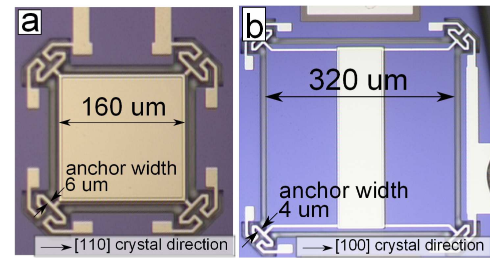

Figure 1. Micrographs of resonators A and B. The thickness of the resonators is 20 μm.

The in-plane mode shape can be approximated by a superposition of two orthogonal acoustic waves with displacements

$$u_x = A\sin(\pi x/L) \quad \text{and} \quad u_y = A\sin(\pi y/L), \quad (1)$$

where A is the vibration amplitude and x and y denote the coordinates on the plate with the origin located in the center of the plate.

The principle of exciting in-plane vibration modes by a piezoelectric thin film located on top of the resonator body can be described with the help of an approximative model. Suppose that the AlN film is clamped to the resonator plate. We approximate that the strains in the lateral directions are zero ($S_x = S_y = 0$) — which is expected to overestimate the transduction strength to some extent — and assume that the piezoelectric layer may move freely in the z direction so the vertical stress component is zero ($T_z = 0$) [6]. When a z-directed electric field E_z is applied, we can solve the piezoelectric constitutive relation $T = eE + cS$ [7] for the unknown lateral stresses:

$$T_x = T_y = \left(\frac{\nu}{1-\nu}e_{33} - e_{31}\right)E_z, \quad (2)$$

where ν is the Poisson ratio of AlN, and e_{31} and e_{33} are the AlN piezoelectric coupling constants. We observe that the out-of-plane electric field results in lateral forces by direct coupling via the piezoelectric constant e_{31}, and by indirect coupling through the term e_{33}.

Fig. 1b shows a micrograph of resonator B. As compared to resonator A, the plate is doubled in size, and the resonator is aligned with the [100] crystal direction. In order to better excite other than the SE mode the piezo geometry is modified to cover the plate only partially.

III. Resonator fabrication

In the fabrication process, special attention was paid for the creation of narrow anchoring tethers for the resonators: the narrowest meander anchors measured 4 microns in width (Fig. 1b). Figure 2 illustrates the processing steps. SOI wafers with pre-etched cavities [8] were first prepared (steps 1,2). Highly boron doped, (100) oriented silicon wafers were used for the device layer, and therefore no metallization was needed for forming the piezo bottom electrode. Next, AlN was deposited and patterned (3). SiO_2 was deposited on the wafer, and thinned with chemical mechanical polishing (4). AlN was located only on top of the resonator plate, while SiO_2 was used as the insulator between the top and bottom electrodes elsewhere. Openings were etched to the SiO_2, one onto the AlN layer and another onto the place where the bottom electrode contact would be formed (5). Molybdenum was deposited and patterned so that the bottom and top electrode contacts were electrically isolated (6). The last etch step (7) consisted of successive etches, where Mo and SiO_2 were first removed around the resonator plate and the anchors, and, finally, the resonator was released and the electrode pad areas were defined using deep reactive ion etching.

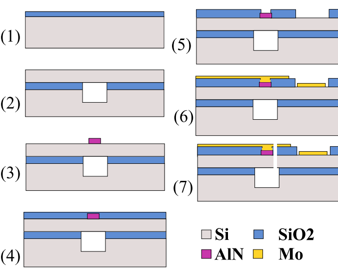

Figure 2. The fabrication process.

IV. Experimental results

The electrical transmission response of the resonators was measured with a network analyzer (HP4195A). The samples were measured in a vacuum chamber with pressure $p < 0.1$ mbar in order to reduce the air-damping effects to a negligible level. The resonator current was detected using a transresistance amplifier with a low input resistance to avoid loading of the resonator quality factor. The resonator parameters f_0, Q, R_m and C_0 were obtained by fitting the simulated response of an equivalent circuit (inset in Fig. 3) to the measurements. Modal analysis with Comsol Multiphysics 3.4 was used for simulating the resonance modeshapes.

Vibration fields in the resonators were measured using a scanning Michelson laser interferometer [5]. Both in- and out-of-plane vibrations were measured. The out-of-plane vibration was measured using the setup in its original Michelson interferometer configuration. The lateral resolution of the setup is better than 1 μm and the sensitivity of the interferometer is 10^{-4} Å/$\sqrt{\text{Hz}}$, corresponding to minimum detectable vibration amplitude of 0.35 pm with the 1 kHz measurement bandwidth used. With a small modification to the setup, also

in-plane vibrations can be measured [9], [10]. In this work, a grid of circular holes was etched to the top metal electrode to enable detection of the in-plane vibrations. Utilizing the circular holes in the metal layer, a vectorial detection of the in-plane vibration can be accomplished. It should be noted, however, that the in-plane and out-of-plane vibration amplitudes cannot be directly compared to each other due to the different detection methods.

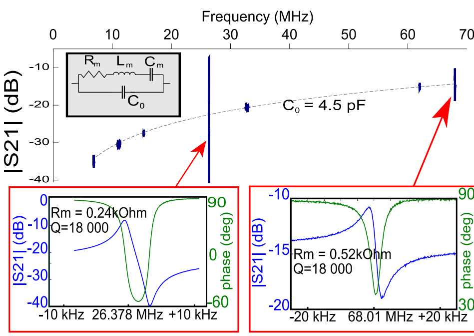

Figure 3. Measured transmission response of resonator A. The grey (dashed) line indicates the signal baseline level resulting from the feedthrough capacitance C_0. The upper-left inset shows the resonator equivalent circuit.

Resonator A transmission response is shown in Fig. 3. The SE mode occurs at $f = 26$ MHz and it is the strongest resonance with $R_m = 0.24\,\mathrm{k}\Omega$ and $Q = 18000$. The interferometric image of the out-of-plane vibration (Fig. 4) indicate that the SE mode is excited rather cleanly. In particular, it should be observed that parasitic out-of-plane modes are absent, unlike in the capacitively coupled SE plate resonator discussed in [10]. The other strong resonance at $f = 68$ MHz ($R_m = 0.52\,\mathrm{k}\Omega$ and $Q = 18000$) was observed to have a prominent out-of-plane character in its vibration (Fig. 5). All other resonances up to 70 MHz were found to be electrically relatively weak.

The transmission response of resonator B (Fig. 6) is observed to be somewhat richer than that of resonator A. Strongly coupled high-Q resonances occur at 9 MHz, 22 MHz and 36 MHz. For the measurement of in-plane vibrations, a replica of resonator B was fabricated, however with a grid of holes added to the top metal electrode. The modified resonator B, denoted hereafter B2 featured similar transmission response to that of resonator B. The 9-MHz resonance ($R_m = 1.6\,\mathrm{k}\Omega$ and $Q = 17000$) was found to be a flexural resonance

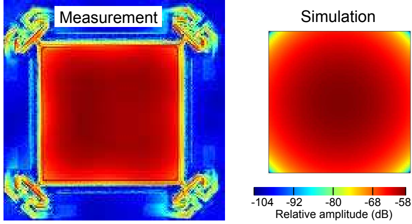

Figure 4. Relative amplitudes of the out-of-plane vibration of resonator A at 26 MHz. The measurement was done in vacuum (p <1 mbar).

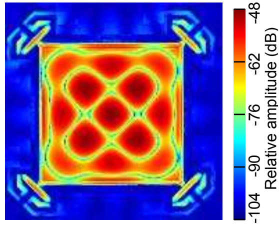

Figure 5. Relative amplitudes of the out-of-plane vibration of resonator A at 68 MHz.

mode with dominant out-of-plane character. The simulated modeshape agrees well with the measured one (Fig. 7). The 22-MHz resonance has the highest quality factor of the three main resonances: $R_m = 1.5\,\mathrm{k}\Omega$ and $Q = 51000$. Fig. 8 shows that the out-of-plane component of the vibration mode is relatively weak while the resonance has a strong in-plane character. The measured in-plane vector field has a vortex in the center of the plate, which we have not yet reproduced in our simulations. The 36-MHz resonance has the best electromechanical coupling with $R_m = 0.6\,\mathrm{k}\Omega$ and $Q = 27000$. The vibration mode has prominent in-plane and out-of-plane components, and the measurements and simulations correspond to each other fairly well.

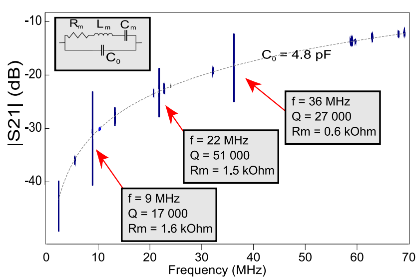

Figure 6. Measured transmission response of resonator B.

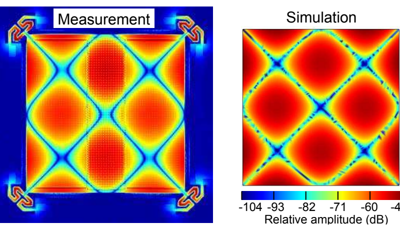

Figure 7. Relative amplitudes of the out-of-plane vibration of resonator B2 at 9 MHz. The measurement was done in atmospheric pressure..

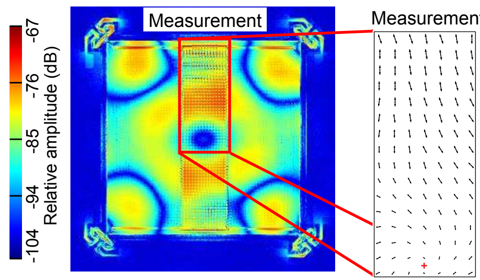

Figure 8. The out-of-plane and in-plane vibration modes of resonator B2 at 22 MHz.

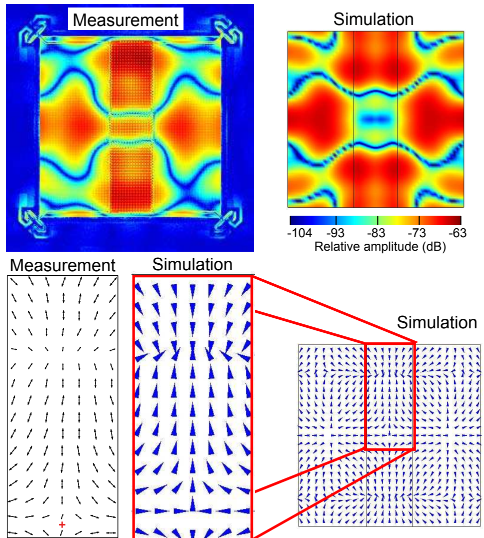

Figure 9. The out-of-plane (top row) and in-plane (bottom row) vibration fields of resonator B2 at 36 MHz.

V. Conclusions

We have designed, fabricated and characterized single crystal silicon plate resonators, which are transduced by a piezoelectric AlN thin film grown on top of the resonator. High quality factor resonances with good electromechanical coupling were observed. Furthermore, by using optical probing, we have shown that resonance modes vibrating mainly in the resonator plane can be successfully excited with the transduction method.

Our future work on the subject contains more accurate numerical modelling of the resonators, and the optimization of anchoring and top electrode geometries.

References

[1] R. Abdolvand and F. Ayazi, "Enhanced power handling and quality factor in thin-film piezoelectric-on-substrate resonators," in *IEEE Ultrasonics Symposium*, pp. 608–611, 2007.

[2] A. Jaakkola, P. Rosenberg, A. Nurmela, T. Pensala, T. Riekkinen, J. Dekker, T. Mattila, and A. Alastalo, "Piezotransduced Single-Crystal Silicon BAW Resonators," in *IEEE Ultrasonics Symposium*, pp. 1653–1656, 2007.

[3] V. Kaajakari, J. Kiihamäki, A. Oja, S. Pietikäinen, V. Kokkala, and H. Kuisma, "Stability of wafer level vacuum encapsulated single-crystal silicon resonators," *Sensors & Actuators: A. Physical*, vol. 130, pp. 42–47, 2006.

[4] V. Kaajakari, T. Mattila, A. Oja, J. Kiihamäki, and H. Seppä, "Square-extensional mode single-crystal silicon micromechanical resonator for low-phase-noise oscillator applications," *IEEE Electron Device Letters*, vol. 25, no. 4, pp. 173–175, 2004.

[5] J. Knuuttila, P. Tikka, and M. Salomaa, "Scanning Michelson interferometer for imaging surface acoustic wave fields," *Optics Letters*, vol. 25, no. 9, pp. 613–615, 2000.

[6] V. Kaajakari, A. Alastalo, and T. Mattila, "Electrostatic transducers for micromechanical resonators: free space and solid dielectric," *IEEE Transactions on Ultrasonics, Ferroelectrics and Frequency Control*, vol. 53, no. 12, pp. 2484–2489, 2006.

[7] B. Auld, *Acoustic fields and waves in solids*. Wiley New York, 1973.

[8] H. Luoto, K. Henttinen, T. Suni, J. Dekker, J. Mäkinen, and A. Torkkeli, "Mems on cavity-soi wafers," *Solid-State Electronics*, vol. 51, pp. 328–332, 2007.

[9] O. Holmgren, K. Kokkonen, T. Mattila, V. Kaajakari, A. Oja, J. Kiihamaki, J. Knuuttila, and M. Salomaa, "Visualization of in-and out-of-plane vibrations in a micromechanical RF-resonator," in *IEEE Ultrasonics Symposium*, vol. 2, 2004.

[10] O. Holmgren, K. Kokkonen, T. Mattila, V. Kaajakari, A. Oja, J. Kiihamaki, J. Knuuttila, and M. Salomaa, "Imaging of in-and out-of-plane vibrations in micromechanical resonator," *Electronics Letters*, vol. 41, no. 3, pp. 121–122, 2005.

Paper X

©2007 IEEE. Reprinted, with permission, from A. Jaakkola, P. Rosenberg, A. Nurmela, T. Pensala, T. Riekkinen, J. Dekker, T. Mattila, A. Alastalo. "Piezotransduced Single-Crystal Silicon BAW Resonators", Proc. IEEE International Ultrasonics Symposium, 2007, pp. 1653-1656. http://dx.doi.org/10.1109/ULTSYM.2007.416

Piezotransduced Single-Crystal Silicon BAW Resonators

Antti Jaakkola, Piia Rosenberg, Arto Nurmela, Tuomas Pensala,
Tommi Riekkinen, James Dekker, Tomi Mattila, and Ari Alastalo
VTT Technical Research Centre of Finland
P.O. Box 1000, FI-02044 VTT, Finland

***Abstract*—We report on the design, fabrication and measurement of 13-MHz piezoelectrically actuated single-crystal silicon beam resonators operating in the first length-extensional mode. The transduction mechanism is based on an aluminum nitride layer grown on top of the resonator beam. The resonators are measured to have a quality factor of $Q \sim 20000$ at $p < 1$ mbar and typical motional resistance of $R_m \sim 3$ kΩ. The electromechanical transduction factor is $\eta \sim$20 μN/V, representing a coupling of the same order as produced by 20 V over a 100-nm gap for capacitively coupled resonators. The quality factor is observed to be dependent on the crystal direction of the resonator beam. A qualitative explanation for this effect is given.**

I. Introduction

Micromechanical resonators offer a promise of compact size, low power consumption, integrability with IC electronics, and a price advantage. They are thus considered as candidates for replacing bulky off-chip quartz devices used as filter and frequency reference components in modern wireless applications. Capacitively coupled MEMS resonators need sub-100 nm gap sizes and bias voltages in excess of 10 V in order to reach a good electromechanical coupling. Especially the latter need is problematic to meet with low cost integrated circuits.

To overcome these problems we have studied single-crystal silicon (SCS) BAW resonators, which are transduced with a piezoelectric aluminum nitride layer grown on top of the resonator beam. SCS resonators based on a similar transduction principle have been reported [1], [2], however, using ZnO as the piezoelectric material. In this paper, we present measurement results of 13-MHz piezoelectrically actuated SCS beam resonators operating in their first length-extensional mode. Quality factors of $Q \sim 20000$ at $p < 1$ mbar are observed, and a typical motional resistance is $R_m \sim 3$ kΩ. A model of the piezoelectric transduction is derived, and it is found that the measured transduction factor $\eta \sim 20\,\mu$N/V is ~70% of the value obtained from the model using bulk AlN piezoelectric coefficients. The quality factor is observed to be dependent on the crystal direction of the resonator beam. This effect is modelled as anchor loss by using a 2D finite element model featuring a perfectly matched layer boundary condition, and a qualitative match with measurements is found.

II. Resonator design

The dimensioning of the 13-MHz resonator is shown in Fig. 1. The resonator is designed to be connected electrically as a one-port device, and the desired operation mode of the resonator is the first lateral length-extensional mode [3]. This mode occurs when the resonator length is half of the acoustic wavelength, and its frequency is given by $f = \sqrt{Y/\rho}/(2L)$, where Y and ρ are the Young's modulus in the x direction and the material density, respectively. The mode shape can be approximated by $X(x,t) = X_0(t)\sin(\pi x/L)$, where x denotes the position along the resonator arm, and X_0 is the resonator endpoint displacement. We have assumed that the piezolayer and the top electrode do not have any other parasitic effects than to slightly change the effective Young's modulus and density of the silicon resonator, and hence alter the mode frequency.

By integrating the wave equation over the mode shape we arrive at a 1D model of the resonator [4]:

$$M\ddot{X}(t) + \frac{\sqrt{KM}}{Q}\dot{X}(t) + KX(t) = F(t). \quad (1)$$

Here Q denotes the quality factor of the resonator, and the generalized mass and spring constant are given by

$$M = \rho AL/2,\ K = \pi^2 YA/(2L), \quad (2)$$

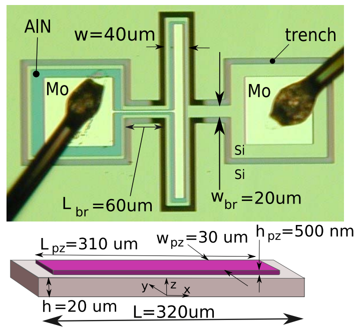

Figure 1. Micrograph of a wire-bonded resonator. The beam dimensions are $L \times w \times h$, and the piezolayer size is $L_{pz} \times w_{pz} \times h_{pz}$. $L_{br}$and w_{br} denote the anchor dimensions.

where A is the cross sectional area of the resonator beam. The force term on the right-hand side is given by

$$F(t) = \int_{-L/2}^{L/2} \frac{\partial F_e(x,t)}{\partial x} \sin\left(\frac{\pi}{L}x\right) dx, \quad (3)$$

where F_e is the excitation force within the beam.

Now, we assume that the electromechanical coupling to voltage U and current I is described by the transduction factor η as

$$F(t) = \eta U(t), \; I(t) = \eta \dot{X}(t). \quad (4)$$

Here we assume a symmetry of drive and sense coupling. Using (1) and (4) we obtain

$$\frac{M}{\eta^2}\dot{I}(t) + \frac{\sqrt{KM}}{Q\eta^2}I(t) + \frac{K}{\eta^2}\int I(t)\mathrm{d}t = U(t). \quad (5)$$

This can be identified with a series RLC circuit with motional equivalent parameters

$$R_m = \sqrt{KM}/(Q\eta^2),\; L_m = M/\eta^2,\; C_m = \eta^2/K. \quad (6)$$

The electrical-equivalent circuit of the resonator consists of an RLC branch connected in parallel with the capacitance C_0 between the piezo electrodes (see the inset in Fig. 3).

The piezoelectric transduction factor η is modelled next. Suppose that the piezo film is clamped to the resonator beam. We approximate that the strains in the lateral directions are zero ($S_x = S_y = 0$), which is expected to give an upper estimate of the true coupling, and assume that the piezolayer may move freely in the z direction so the vertical stress component is zero ($T_z = 0$) [4]. When a z-directed electric field E_z is applied, we can write the piezoelectric constitutive relation $T = eE + cS$ in matrix form [5]:

$$\begin{bmatrix} T_x \\ T_y \\ 0 \end{bmatrix} = \begin{bmatrix} 0 & 0 & e_{31} \\ 0 & 0 & e_{31} \\ 0 & 0 & e_{33} \end{bmatrix} \begin{bmatrix} 0 \\ 0 \\ E_z \end{bmatrix} + \begin{bmatrix} c_{11} & c_{12} & c_{12} \\ c_{12} & c_{11} & c_{12} \\ c_{12} & c_{12} & c_{11} \end{bmatrix} \begin{bmatrix} 0 \\ 0 \\ S_z \end{bmatrix} \quad (7)$$

Here we have neglected all the shear terms in e and c, and the isotropic form of c has been used. Only the nonzero elements $e_{31}$and e_{33} for AlN have been preserved. Solving for the unknown lateral stresses yields

$$T_x = T_y = \left(\frac{\nu}{1-\nu}e_{33} - e_{31}\right)E_z. \quad (8)$$

where ν is the Poisson ratio of AlN.

Because the length-extensional resonance of the beam is in the x direction, only T_x is of interest for further analysis. Expressing the electric field as $E_z(t) = U(t)/h_{pz}$, where $U(t)$ is the voltage across the piezolayer, we obtain an expression for the force exerted on the resonator by the piezolayer at their interface, i.e., for $-L_{pz}/2 < x < L_{pz}/2$:

$$\begin{aligned} F_e(x,t) &= T_x w_{pz} h_{pz} \\ &= \left(\frac{\nu}{1-\nu}e_{33} - e_{31}\right) w_{pz} U(t). \quad (9) \end{aligned}$$

We can now solve (3):

$$F(t) = \left(e_{31} - \frac{\nu}{1-\nu}e_{33}\right) 2w_{pz}U(t)\sin\left(\frac{\pi}{2}\frac{L_{pz}}{L}\right). \quad (10)$$

Comparing the result with (4) we obtain

$$\eta = \left(e_{31} - \frac{\nu}{1-\nu}e_{33}\right) 2w_{pz}\sin\left(\frac{\pi}{2}\frac{L_{pz}}{L}\right). \quad (11)$$

The electromechanical coupling to the resonator is at maximum when the piezoelectric layer covers the whole beam: $\eta_{max} = \left(e_{31} - \frac{\nu}{1-\nu}e_{33}\right) 2w_{pz}$. Humad *et al.* [2] arrived at a similar result, however, neglecting the effect of the term e_{33}.

The validity of the model was verified by modelling the piezoelectric transduction mechanism in 3D with ANSYS finite element package. It was found, as expected, that (11) overestimates the transduction factor by ~20%. This discrepancy between the simulation and our model is well explained by the approximation, where the lateral strains were set to zero.

Using (11) with the geometry in Fig. 1 we obtain a transduction factor $\eta_{theor} = 28\,\mu$N/m, when values $e_{33} = 1.55$ Cm^{-2}, $e_{31} = -0.58$ Cm^{-2} [6], and $\nu = 0.2$ are used, and a correction factor of 0.8 suggested by the simulation is applied. We stress that with capacitive coupling a gap size of 100 nm and a bias voltage of 20 V would be required to reach a corresponding strength of coupling.

III. Resonator fabrication

The resonators were fabricated on silicon-on-insulator (SOI) wafers featuring pre-etched cavities [7], see Fig. 2. The used wafers were (100)-oriented highly boron-doped silicon wafers. The device layer thickness was 20 μm. AlN and Mo were sputtered on top of the silicon layer and patterned by wet etching. The resonators were released using deep reactive-ion etching. Resonators aligned in the [110] and [100] crystal directions were produced.

IV. Experimental results

The transmission response of the resonators was measured with a standard network analyzer (HP4195A). To reduce the air-damping effects to a negligible level, the measured samples were placed in a vacuum chamber with pressure $p < 0.1$ mbar. The resonator current was detected with an amplifier block with a capacitive input to avoid loading of the resonator quality factor.

A typical response of a resonator with beam orientation in the [110] crystal direction is shown in Fig. 3. Quality factors of $Q \sim 20000$ were measured. The four-parameter equivalent-circuit response was fitted to the measured data: the motional resistance level of the resonators was $R_m \sim 3$ kΩ. Assuming an effective mass $M = 3 \times 10^{-10}$ kg and using (6), a transduction factor of $\eta \sim 20\,\mu$N/V was obtained. This is ~70% of the modelled coupling strength η_{theor} calculated in section II. Also resonators with the beam orientation in the [100]

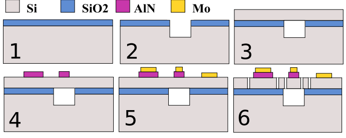

Figure 2. Resonator fabrication process flow: 1) — 3) the SOI wafer with pre-etched cavities is formed. 4) Aluminum Nitride deposition and patterning. 5) Molybdenum deposition and patterning. 6) Release etch using DRIE.

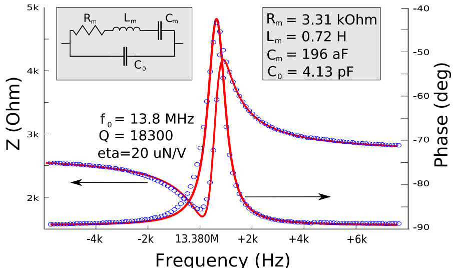

Figure 3. The resonator impedance calculated from the transmission data. Blue markers denote measured data, and the line is the fitted equivalent circuit response. The insets show the resonator equivalent circuit and its parameter values.

crystal direction were measured. Measurements indicate a clear difference in Q factors in comparison with their [110]-oriented counterparts: the Q factors were limited to ~3500.

V. Anchor loss simulation

The dependence of the Q factor on the resonator beam orientation can be explained by anchor losses. Due to the anisotropy of SC silicon, the in-plane Poisson ratio ν_{xy} varies: For the (100) plane, the maximal mechanical coupling of $\nu_{max} = 0.28$ occurs between the $[100]$ and $[010]$ directions, whereas the minimum value of $\nu_{min} = 0.06$ appears between crystal directions $[110]$ and $[\bar{1}10]$ [8]. Resonators with their beam in the [100] direction should thus have larger anchor losses than the corresponding [110]-oriented resonators, since more resonator energy would be "pumped" through the anchor bridges.

The anchor losses were modelled using the open-source finite-element simulation tool HiQLab [9], [10]. The resonator energy leakage through the anchors to the substrate can be modelled in HiQLab by employing a *perfectly-matched-layer* (PML) boundary condition [11]: at a PML boundary waves are absorbed from any angle of incidence with no impedance mismatch. A 2D simulation model was used (see the inset in Fig. 4). The resonator was modelled as isotropic silicon, and the plane-stress approximation was used. The quality factors were extracted from the eigenfreqency analysis of the model. The PML boundary conditions lead to complex-valued eigenfrequencies ω_i of the system, from which the quality factor of the mode under interest is readily calculated: $Q = \text{Re}(\omega)/(2\text{Im}(\omega))$.

Fig. 4 shows a simulation result, where the silicon Poisson ratio is varied. The result matches

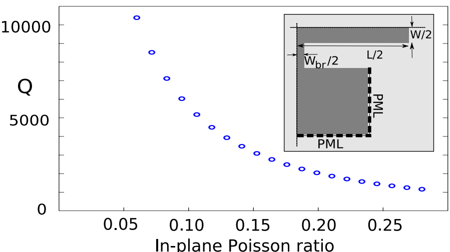

Figure 4. Quality factor as the function of the in-plane Poisson ratio. Inset: 2D resonator model. The thin dashed lines denote the symmetry axis, and the thick dashed lines show the boundaries at which the PML boundary condition is applied.

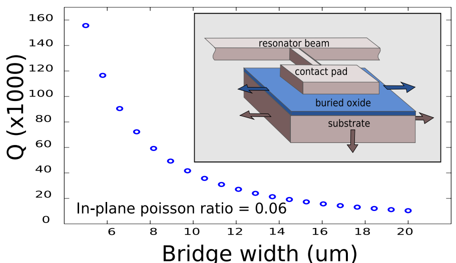

Figure 5. Quality factor value as a function of the anchor bridge width. Inset: resonator anchoring in 3D. The arrows indicate where the buried oxide (SiO_2) layer and the silicon substrate extend and into which directions the acoustic energy thus "leaks".

qualitatively with the measurements. The simulated Q factors for Poisson ratios 0.06 and 0.28 were approximately 10000 and 1000, respectively, whereas the corresponding measured figures were 20000 and 3500. The lack of a quantitative agreement can be attributed to the simplifications of the model. In reality, the anchor bridge is connected to a contact pad, and some of the acoustic energy coming through the anchor is reflected back by the contact pad vertical edges and by the material layer interfaces (see the inset in Fig. 5). Thus the measured Q factors should indeed be larger than those of the simulations. Some effects can be missed also by the fact that silicon was modelled as an isotropic material, and the anisotropy of silicon was mimicked by varying the Poisson ratio directly.

Also the relation between the bridge width and the Q factor was studied (Fig. 5). A clear increase of the Q factor is observed as the anchor bridge is thinned. The results of Mattila *et al.* [3] match qualitatively with the simulation: a [110]-oriented beam resonator reminiscent of ours — but featuring bridge width below 10 μm — was measured to have a quality factor of 180000.

VI. Conclusions

Piezoelectrically transduced beam resonators were designed, fabricated and tested. A good electromechanical coupling was observed, and Q factors of $\sim$ 20000 were measured. The losses were observed to depend on the resonator orientation. With numerical simulation, this effect was explained at a qualitative level as anchor loss.

In our future experiments, we plan to investigate dissipations related to the piezolayer and to the top metal electrodes, since our modified process allows fabrication of narrower anchor bridges and consequently a suppression of the anchor losses.

References

[1] G. Piazza, R. Abdolvand, and F. Ayazi, "Voltage-tunable piezoelectrically-transduced single-crystal silicon resonators on SOI substrate," *IEEE The Sixteenth Annual International Conference on Micro Electro Mechanical Systems, 2003. MEMS-03 Kyoto.*, pp. 149–152, 2003.

[2] S. Humad, R. Abdolvand, G. Ho, G. Piazza, and F. Ayazi, "High frequency micromechanical piezo-on-silicon block resonators," *IEEE International Electron Devices Meeting, 2003. IEDM'03 Technical Digest.*, pp. 39–3, 2003.

[3] T. Mattila, A. Oja, H. Seppa, O. Jaakkola, J. Kiihamaki, H. Kattelus, M. Koskenvuori, P. Rantakari, and I. Tittonen, "Micromechanical bulk acoustic wave resonator," in *2002 IEEE Ultrasonics Symposium, 2002. Proceedings.*, vol. 1, pp. 945–948vol.1, 8-11 Oct. 2002.

[4] V. Kaajakari, A. Alastalo, and T. Mattila, "Electrostatic transducers for micromechanical resonators: free space and solid dielectric," *IEEE Transactions on Ultrasonics, Ferroelectrics and Frequency Control*, vol. 53, no. 12, pp. 2484–2489, 2006.

[5] B. Auld, *Acoustic fields and waves in solids*. Wiley New York, 1973.

[6] L. Xinjiao, X. Zechuan, H. Ziyou, C. Huazhe, S. Wuda, C. Zhougcai, Z. Feng, and W. Enguang, "On the properties of AlN thin films grown by low temperature reactive rf sputtering," *Thin Solid Films*, vol. 139, pp. 261–274, 1986.

[7] H. Luoto, K. Henttinen, T. Suni, J. Dekker, J. Mäkinen, and A. Torkkeli, "Mems on cavity-soi wafers," *Solid-State Electronics*, vol. 51, pp. 328–332, 2007.

[8] J. J. Wortman and R. A. Evans, "Young's modulus, shear modulus, and Poisson's ratio in silicon and germanium," *Journal of Applied Physics*, vol. 36, no. 1, pp. 153–156, 1965.

[9] D. S. Bindel, *Structured and Parameter-Dependent Eigensolvers for Simulation-Based Design of Resonant MEMS*. PhD thesis, EECS Department, University of California, Berkeley, Aug 2006.

[10] HiQLab is available at http://www.cims.nyu.edu/~dbindel/hiqlab.

[11] U. Basu and A. Chopra, "Perfectly matched layers for time-harmonic elastodynamics of unbounded domains: theory and finite-element implementation," *Comput. Methods Appl. Mech. Eng*, vol. 192, pp. 1337–1375, 2003.

Aalto-DD 6/2016
VTT SCIENCE 122

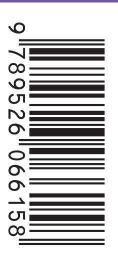

ISBN 978-952-60-6615-8 (printed)
ISBN 978-952-60-6616-5 (pdf)
ISSN-L 1799-4934
ISSN 1799-4934 (printed)
ISSN 1799-4942 (pdf)

978-951-38-8388-1 (printed)
978-951-38-8387-4 (pdf)
2242-119X
2242-119X (printed)
2242-1203 (pdf)

Aalto University
School of Science
Department of Applied Physics
www.aalto.fi

BUSINESS +
ECONOMY

ART +
DESIGN +
ARCHITECTURE

SCIENCE +
TECHNOLOGY

CROSSOVER

DOCTORAL
DISSERTATIONS